Influence of Conductivity Additives on the Performance of Lithium-Ion Batteries

Zur Erlangung des akademischen Grades eines
DOKTORS DER INGENIEURWISSENSCHAFTEN (Dr.-Ing.)

von der KIT-Fakultät für Chemieingenieurwesen und Verfahrenstechnik
des Karlsruher Instituts für Technologie (KIT)
genehmigte

DISSERTATION

von
Anshuman Chauhan, M.Sc.
aus Shimla

Tag der mündlichen Prüfung: 10.04.2025
Erstgutachter: Prof. Dr.-Ing. habil. Hermann Nirschl
Zweitgutachter: Prof. Dr.-Ing. Marc Kamlah

Dedicated to those
who made me capable of it.

On the shoulders of giants...

Acknowledgement

The following work is the outcome of my four and a half year tenure as a Research Associate, in the Process Machines group, at the Institute of Mechanical Process Engineering and Mechanics (MVM), Karlsruhe Institute of Technology (KIT). First and foremost, I would like to thank my doctoral advisor, Prof. Dr.-Ing. habil. Hermann Nirschl, for putting his faith in my abilities, for the academic freedom he granted me and his support over the years. I also wish to extend my gratitude to Prof. Dr.-Ing. Marc Kamlah, for obliging to review this work. Moreover, I wish to thank him and Prof. Dr.-Ing. Thomas Wetzel for the discussions and guidance at the meetings organized in the framework of our research training group, *Simulation mechanisch-elektrisch-thermischer Vorgänge in Lithium-Ionen-Batterien* (SiMET), of which I was fortunate to be a part of.

It was also my fortune, to be part of our congenial institute where, there was always a helping hand to be found. I thank the departments of our institute (*Werkstatt, Vewaltung, PMT and Technik*), for always having an open ear for my concerns. Particularly, Amuthavalli Schnepf and Andreas Baum for guiding me through numerous organisational and technical hurdles.

A large contribution to the amicable environment at work was ensured by my fellow doctoral candidates, many of whom have turned into good friends, who consistently engaged in curricular as well as non-curricular activities to boost my moral. I will always cherish the annual *wander*- seminars and conferences as well as the daily coffee-break(s) and other memories, we made together at and outside the institute. In this regard, I wish to specially thank my office colleagues over the years, Lucas Jakob and Nikolai Erhardt. Lucas for offering me to share the office with him and guiding me through thick and thin over the years and Nikolai for his patience during the countless white-board sessions, during the final stages of the completion of this work and for proofreading the very first draft. Moreover, I thank Dr.-Ing. Benjamin Radel, for resolving the endless software issues, I had as a new doctoral candidate. Amadeus Wolf, Timo Dobler, Tolga Yildiz and Felix Reinke, were the perfect lunch companions towards the end of my time at the institute, with whom I could share the joy and the inevitable pain of writing a doctoral dissertation. Further, I specially wish to mention Felix Gerbig and Marvin Winkler for assisting me in the corrections necessary to improve the quality of this work.

During this time, I had the opportunity to supervise Rafdian Nahri and Salvatore Vella, both of whose diligent efforts contributed to this work.
My loved ones have always played a significant role in my achievements. I am particularly grateful for the love, dedication and support from my parents, Geeta and Manohar Lal Chauhan. It's their encouragement in the pursuit my dreams and ambitions, as well as influence of the members of my family like my grandfather Bhagat Ram Tajta and my brother Karan Chauhan, that inspired me to strive for academic excellence.
At last I thank you, my partner, Victoria Nicole Lang, for being by my side through all these years and taking the burdens off my shoulders, particularly towards the end of this massive endeavour. Moreover, for being supportive, when I prioritized the completion of this work. You and Theo, were a constant source of motivation and the occasional respite, during this time.
Thank you! for all the guidance, love, patience and support. It is for all of you, that I was able to see further. For that, I shall remain forever in your debt.

Zusammenfassung

Die Forschung zu Lithium-Ionen-Batterien hat sich von den frühen Fortschritten bei hochkapazitiven Aktivenmaterialien hin zu einem Schwerpunkt auf die Optimierung der Elektrodenmikrostruktur entwickelt. Die Mikrostruktur, die während des Herstellungsprozesses durch die Leitfähigkeitsadditive beeinflusst wird, ist zu einem zentralen Forschungsbereich geworden. Diese Additive spielen eine wesentliche Rolle bei der Verbesserung der Stabilität und Leitfähigkeit der Elektroden. Digitale Methoden sind entscheidend, um die Auswirkungen mikrostruktureller Variationen auf die Batterieleistung zu erfassen. Diese Arbeit untersucht daher den Einfluss des Leitfähigkeitsadditives *Carbon Black* (Ruß) auf die Leistung von Lithium-Ionen-Batterien durch aufgelöste elektrochemische Simulationen. Hierzu wurde ein dreistufiger numerischer Ansatz entwickelt: Zunächst werden stochastische partikuläre Kathodenhalbzellen erstellt, die den mikrostrukturellen Wandel durch die Verarbeitung von Ruß während des Mischvorgangs nachbilden. Anschließend wird der Effekt dieser mikrostrukturellen Änderungen anhand von Leistungsindikatoren (z.B. ionische und elektrische Leitfähigkeit) analysiert. Abschließend werden elektrochemische Simulationen durchgeführt, um den Einfluss auf die Leistung mittels Leistungskennzahlen (z.B. Energie- und Leistungsdichte) zu quantifizieren.
Anfangs wurden grundlegende Untersuchungen zum Einfluss der Größe und Form von Rußpartikeln präsentiert. Diese Untersuchungen basieren auf einem konventionellen Nassverfahren, das es ermöglicht, Ruß- und Binderpartikel gemeinsam als *Cluster*, die als *Carbon-Binder-Domain* (CBD) bezeichnet werden, zu modellieren. Die Untersuchungen zeigen, dass eine Verringerung der Größe der CBD-Cluster zu einer Erhöhung ihrer Dispersion führt. Diese Erhöhung hat verschiedene Auswirkungen auf die Transportprozesse. Eine erhöhte Dispersion führt zu einer Verbesserung der elektrischen Leitfähigkeit, geht jedoch zulasten der Ionenleitung, die mit steigender Tortuosität abnimmt. Daher sind die Leitphänomene als wechselseitig abhängig anzusehen. Zudem wird gezeigt, dass die erhöhte Dispersion des CBD die verfügbare aktive Oberfläche für die Interkalation reduziert.
Im Gegensatz dazu zeigt die Untersuchung der Form von Rußpartikeln mittels der fraktalen Dimension, dass eine höhere elektrische Leitfähigkeit nicht nur durch eine erhöhte Dispersion erreicht werden kann, sondern auch durch die Präsenz von weniger dispergierten, hoch-fraktalen Rußpartikeln. Zudem deutet die Studie darauf hin, dass die Struktur des

Rußes die Qualität der gebildeten elektrischen Verbindungen bestimmt, die nur quantitativ durch Kompression verbessert werden kann.
Bei den Leistungsbewertungen im Rahmen von Untersuchungen zu Größe und Form führt die beste Kombination von Leistungsindikatoren zu der höchsten Leistung. Die Bedeutung dieser Indikatoren ändert sich jedoch mit zunehmendem Entladestrom, da sich die Faktoren, die die Leistung der Kathode begrenzen, ändern.
Um diesen Aspekt weiter zu untersuchen, wurden verschiedene Dispersionsgrade, die durch den *Erosion* und *Rupture* Bruchmechanismus der CBD-Cluster im konventionellen Nassmischprozess entstehen, hinsichtlich ihrer Eignung für Designstrategien von *High-Power*- und *High-Energy* Kathoden analysiert. Die Untersuchungen zeigen, dass sich bei zunehmender Entladerate der limitierende Faktor für die Kathodenperformance von der Verfügbarkeit der aktiven Oberfläche auf die Transportprozesse verlagert, unabhängig von der gewählten Designstrategie. Diese Ergebnisse wurden zusammengefasst, um eine anwendungsabhängige optimale aktive Oberfläche vorzuschlagen. Für *High-Power* Kathoden, die Transportbeschränkungen aufgrund erhöhter Porosität und höherem Rußgehalt bewältigen, erweist sich eine höhere Verfügbarkeit der Oberfläche bei geringerer Dispersion als optimal. Im Gegensatz dazu wird für *High-Energy* Kathoden eine höhere Dispersion empfohlen, um die niedrige elektrische Leitfähigkeit auszugleichen. Die Verfügbarkeit der aktiven Oberfläche hingegen wird als weniger entscheidend angesehen.
Schließlich wurde zur Berücksichtigung der Zerkleinerung von Ruß durch *Shattering* im intensiven Trockenmischprozess die Schüttdichte der trockenen Kathodenmischungen mit der Halbzellenporosität und letztlich mit der Performance korreliert. Die Untersuchungen identifizieren eine optimale Porosität für die Kathode, die von der spezifischen Anwendung abhängt. Diese optimale Porosität wird unter Berücksichtigung sowohl des begrenzten Halbzellenvolumens als auch der begrenzten Kathodenmasse in der Halbzelle bestimmt. Bei begrenztem Halbzellenvolumen und niedrigen Strömen zeigt sich, dass geringere Porosität zu einer besseren Kathodenperformance führt. Dies ist auf die minimalen Transportbeschränkungen und auf die höheren Mengen Aktivmaterial in der Halbzelle züruckzuführen. Bei höheren Strömen, bei denen die Transportprozesse dominieren, muss jedoch ein Gleichgewicht zwischen Energie- und Leistungsfähigkeit gefunden werden, wobei eine hohe Porosität die Energie und eine niedrige Porosität die Leistung begünstigt. Im Gegensatz dazu ergibt sich die beste Kathodenperformance bei begrenztem Material in der Halbzelle stets bei höherer Porosität.
Daher vertieft die vorliegende Arbeit durch eine systematische Untersuchung der komplexen Zusammenhänge zwischen den Eigenschaften von Ruß, der Mikrostruktur der Kathode und der elektrochemischen Leistung das Verständnis dieser Beziehungen und bietet Richtlinien für die Entwicklung fortschrittlicher Lithium-Ionen-Batterien.

Abstract

Lithium-ion battery research has transitioned from early strides in high-capacity active materials to a focus on optimizing the electrode microstructure. The microstructure, shaped significantly during the manufacturing processes by the conductivity additives essential for enhancing electrode stability and conductivity, has become a key area of study. Digital methods are instrumental in comprehending how microstructural variations impact battery performance. Therefore, this work investigates the impact of conductivity additive: carbon black on lithium-ion battery performance through resolved electrochemical simulations. To achieve this, a three-step numerical approach has been devised: initially, generating stochastic particulate cathode half-cells that mimic microstructural changes caused by processing of carbon black during mixing; then, analyzing the effect of these microstructural modifications using performance indicators (e.g. ionic & electrical conductivity); and finally, conducting electrochemical simulations to quantify the influence on performance using performance determinants (e.g. energy & power density).

To begin with, fundamental investigations on the impact of carbon black size and shape have been presented. These investigations assume a conventional-wet process, allowing for the modelling of carbon black and binder together as clusters called the carbon binder domain (CBD). The investigations show, that a decrease in the size of the CBD clusters leads to an increase in their dispersion, which in turn has contrasting consequences for the different transport processes. Increased dispersion leads to an increase in the electrical conductivity at the cost of the ionic conduction, which decreases with the rising tortuosity. Hence, the conduction phenomena in a lithium-ion battery cathode are interdependent. Moreover, it is shown that the increased dispersion of the CBD results in a loss of the active surface area available for intercalation.

In contrast, the study of carbon black's shape using fractal dimension reveals that higher electrical conductivity can be achieved not only through increased dispersion but also through the presence of less dispersed, highly fractal-shaped carbon black. Additionally, the study suggests that the structure of carbon black dictates the quality of the electrical connections formed, which is only quantitatively enhanced under compression.

In the performance evaluations made in the investigations of size and shape, the best combination of performance indicators translate into the highest performance. However, the significance of these indicators changes with increasing discharge current, as the factors limiting cathode performance change.
To examine this aspect further, different degrees of dispersion resulting from the erosion and rupture cluster breakage mechanism in the conventional-wet mixing process have been examined with regard to their suitability for high-power and high-energy cathode design strategies. The investigations reveal that as the discharge rate increases, the limiting factor for cathode performance shifts from active surface availability to the transport processes, irrespective of the design strategy. These findings have been summarized to suggest an application-dependent optimal active surface. For high-power cathodes, which effectively manage transport limitations due to increased porosity and higher carbon black content, a higher surface availability with less dispersion is found to be optimal. Conversely, for high-energy cathodes with lower carbon black content, higher dispersion is recommended to counter their low electrical conductivity. While active surface availability is found to be not as critical in their design.
Lastly, to account for carbon black comminution through shattering in an intensive-dry mixing process, the bulk density of dry cathode mixtures has been correlated with their half-cell porosity and ultimately to their performance. The investigations identify an optimal porosity for the cathode, dependent on its application. This optimal porosity is determined considering both limited half-cell volume and limited cathode mass in the half-cell. With limited half-cell volume and lower currents, it is shown that lower porosity leads to better cathode performance. This is due to the minimal transport restrictions and the higher amounts of active material in the half-cell. However, at higher currents where transport processes dominate, a balance between energy and power capability must be found, with high porosity favoring energy and low porosity favoring power. In contrast, the best cathode performance with limited material in the half-cell is always achieved with higher porosity.
Therefore, through a methodical examination of the intricate link between carbon black characteristics, cathode microstructure, and electrochemical performance, this dissertation deepens the understanding of these relationships and offers practical guidelines for developing advanced lithium-ion batteries.

Contents

Chapter 1

Introduction

The global shift towards sustainable energy sources has significantly amplified the demand for lithium-ion batteries (LIBs), which are essential for advancing the energy transition. As the industrial and transportation sectors undergo rapid electrification, LIBs have emerged as pivotal components, extending their applications from consumer electronics to electric vehicles. This growing diversity in applications necessitates the development of lithium-ion batteries that are specifically tailored to meet varying demands, balancing energy and power density to fulfill future requirements.
While extensive research in the past has focused on new energy storage materials, optimizing the lithium-ion battery as a whole is crucial. Moreover, a comprehensive understanding of the influence of the manufacturing processes is fundamental to developing the next generation of batteries. This approach not only facilitates the engineering of battery electrodes for specific applications but also aims to reduce production costs and explore sustainable alternatives to conventional manufacturing methods. The employment of digital means is crucial in this approach as it streamlines the battery performance informed development of manufacturing processes, by establishing a directly link between the microstructure and the electrochemical performance of the battery.

1.1 Motivation

The development of lithium-ion batteries initially spurred intense material research, aiming to meet their surging demand. However, progress has slowed as efforts to innovate new battery chemistries for enhanced battery performance have plateaued, diverging from the rapid advancements dictated by the Moore's Law, applicable to the semiconductor industry. Challenges include inherent chemical limitations and safety concerns associated especially with nickel-rich compositions (state-of-art cathode active materials), despite their performance benefits.

While advances in new materials for LIBs have diminished, significant strides have been made in enhancing battery performance through improvements in microstructure of porous electrodes. Central to these improvements is the optimization of conductivity additives and binders, which play a pivotal role in shaping the microstructural integrity of LIBs. Particularly, carbon black has emerged as a crucial conductivity additive. Due to its high specific surface area, when integrated with binders during LIB fabrication, carbon black forms composite clusters that contribute to the formation of electrically conductive and rheologically stable cathode mixtures. During the manufacturing process, these clusters organize into a percolating network within the cathode, significantly boosting the electrical conductivity. Moreover, they passively contribute to the formation of the pore network, which develops around them. This pore network, upon being filled by the electrolyte, facilitates the transport of lithium-ions, essential for electrochemical reactions. The distribution of pores, alongside the arrangement of carbon black and binder clusters, profoundly impacts the rate and efficiency of electrochemical processes within the cathode. Excessive presence of carbon black and binder can reduce pore volume as well as the availability of the active surface, impairing ion intercalation and ionic diffusion, especially under high discharge rates. Conversely, overly porous structures may compromise electrical conductivity and stability. Thus, achieving an optimal distribution of these clusters is imperative to realize high-performance LIB cathodes.

A profound understanding of how lithium-ion battery manufacturing processes impact the distribution of conductivity additive and binder, is a key step in this direction. The mixing process, which is the first in the series of processes involved in the manufacturing of lithium-ion batteries, has a significant impact on its microstructure. The foundations of the percolating electrical network as well as the pore network establishment in the cathode take place during this process. Although the percolation behaviour of the conductivity additive in the cathode microstructure on a global scale has been well documented through an analysis of globally measured parameters like effective electrical conductivity in the past, localized effects of the conductivity additive on the contacting in the cathode have not been sufficiently quantified. This includes the influence of its distribution on the availability of the active surface, its impact on the quality of the pore space, and the consequences thereof for the transport processes at the microscale.

The application of digital methods is particularly advantageous in this context. Scale-resolving electrochemical simulations facilitate the quantification of microstructural changes and their impact on performance determining processes at the microscale, which are typically challenging to investigate through experimental means. Additionally, unlike experimental battery performance studies that necessitate costly and complex pilot-scale fabrication, digital models enable feasible exploration of numerous variations in the microstructure, along with the ability to isolate the impact of an individual processes.

1.2 Objectives

The central objective of this dissertation is to quantify the impact of conductivity additives on the performance of lithium-ion batteries through resolved electrochemical simulations. The work highlights alterations in the cathode microstructure induced by the conductivity additives, particularly during the mixing process and examines the subsequent effects on cathode performance. In this regard, three key objectives have been identified:

Influence of Size and Shape

The alteration in size and shape of the conductivity additive during cathode manufacturing results in contrasting implications for the transport of reactants involved in the performance dictating electrochemical reactions within the cathode, affecting both electronic and ionic pathways. This dependency of the conduction characteristics and hence performance of the cathode on the conductivity additive, can only be quantified through its explicit consideration in the cathode microstructure. To achieve this, measures to quantify the size as well as the shape of the conductivity particles during the mixing process must be devised. For the size, the outer diameter of the conductivity additive and binder agglomerates will be utilized, while the fractal dimension is to be employed as a measure of the conductivity additive shape. These measures are then to be integrated into a method to generate digital representations of the cathode microstructure that accurately capture the structure of the conductivity additives resulting from the mixing process. Subsequently, the digital microstructures are to be characterized through numerical evaluation of performance indicators like electrical conductivity and tortuosity. Ultimately, the resolved electrochemical model from the preliminary work [1] is to be extended to explicitly account for the conductivity additive and implemented on the digital representations revealing the link between the attained cathode microstructure and its performance.

Application Dependent Optimal Available Active Surface Area

The rate of electrochemical reactions at the active material surface is constrained either by the availability of the active surface area or by the transport of reactants to these sites. Ionic conduction, being inherently slower than electronic conduction due to the substantial differences in the mechanisms of ion and electron transport, often represents the most significant limitation to cathode performance. However, depending on the application represented by contrasting cathode design strategies (high-energy cathode and high-power cathode) and discharge current variation, the primary constraints can shift to other limiting parameters, electrical conductivity and the specific active surface area available for intercalation. Therefore, the aim is to, at first identify the dominant limiting

factor for a given application. Subsequently, the influence of the transport phenomena and the active surface on the cathode performance are to be unified in the form of the an application dependent optimum for the active surface area. Finally, this optimal active surface availability is to be correlated to the degree of conductivity additive dispersion achieved in the mixing process.

Application Dependent Optimal Porosity

The optimal porosity of a lithium-ion battery cathode is a function of the transport limitations in the pores space under varying application, the constraints on total battery volume and the mass of the cathode components. To study this interdependence, the bulk density of dry cathode mix is to be used as a measure of the relationship between the mass of the cathode components and the occupied battery volume while variation in the discharge current serves to represent the contrasting application scenarios. Based on the application dependent performance determinant i.e. utilizable energy density for the high-energy application and utilizable power density for the high-power application, the significance of the aforementioned constraints for an optimal porosity may vary. Hence, the aim here is, to achieve an application dependent optimum porosity encompassing the constraints on total battery volume as well as mass of the cathode components. This optimum will ultimately be correlated with the bulk density, which can be adjusted through the comminution of the conductivity additive in the intensive-dry mixing process.

1.3 Structure

In the pursuit of the objectives mentioned in Section 1.2, different mechanisms of conductivity additive particle and cluster breakage during the mixing of cathode components: *erosion, rupture* and *shattering* [2], were investigated in this work. Herein, the first two mechanisms of breakage occur under the influence of hydrodynamic forces overcoming weak forces of attraction between conductivity additive partilces and the binder, while shattering involves high energy input during the mixing process, leading to comminution of the conductivity additive particles. Given that these breakage mechanisms occur under considerably different conditions, both conventional-wet processing and the modern solvent-free manufacturing method using intensive-dry mixing were taken into account. Moreover, modern cathodes are specifically designed to cater to their intended application. This aspect has also been addressed in this work. This section serves to provide an overview of the parts of this dissertation wherein these topics were handled.

Mechanisms of Particle and Cluster Breakage

Chapters 4 and 5, include investigation covering conductivity additive cluster erosion and rupture. In these chapters, it is assumed that the energy input in mixing is sufficient to break the agglomerates formed between the conductivity additive and the binder, but not enough to breakdown the elementary aggregate structure of the conductivity additive. Only with the increased energy input associated with intensive-dry mixing can the aggregate bonds be broken, leading to the investigations presented in Chapter 6.

Wet and Solvent-Free Processing

Since the breakage mechanisms are closely related to the forces to which the conductivity additive particles and clusters are subjected to during mixing, processing with and in the absence of the solvent have been considered in this work. In Chapter 4 and 5, it is presumed that during wet processing the shearing forces predominantly lead to erosion and rupturing of the clusters, supported by the Reference [3]. In these investigations the binder it modelled together with the conductivity additive as a composite, with the dispersion of this composite being the central theme. While, in case of intensive-dry mixing the high intensity collisions in the mixer lead to comminution of the conductivity additive particles, investigated in Chapter 6. Here, the binder has not been explicitly modelled due to its sparse usage and state of total fibrillation dictated by the solvent-free fabrication process.

Cathode Design

In the framework of this dissertation, the dimensions of the half-cell as well as the composition of the cathodes was informed by cathode design, engineered to catered to a specific purpose. In Chapter 5, a clear distinction has been made between the two contrasting design strategies studying them separately. On the other hand in Chapter 4 a design balancing both design strategies was chosen, while in Chapter 6 with variant in the cathode mass and porosity the entire range of cathode design strategies were investigated together.

Chapter 2

Theoretical Foundations

2.1 Basics of Lithium-Ion Batteries

This section is aimed at the familiarization with the basics of the lithium-ion battery. To begin with, the fundamental processes involved in converting chemical energy to electrical energy are explained. Various devices can achieve this energy conversion. This work focuses on secondary batteries, which are designed for reuse. Specifically, it examines the class of secondary batteries that use lithium-transition-metal-oxide as the intercalation electrode. Subsequently, the modes under which LIBs are commonly operated have been listed. Finally, a description on the composition of modern LIBs along with the means to manufacture them has been elaborated.

2.1.1 Working Principles

The following explanation derives from the macroscopic description of porous electrodes proposed by Newman et al. [4]. Figure 2.1, shows two porous electrodes, with their pores flooded by an electrolyte. The more noble of these electrodes is called the positive electrode and the lesser, the negative electrode. As the electrodes come in contact with the electrolyte, ions from the electrolyte solution get adsorbed onto its surface, as shown by the zoomed-in surface of the negative electrode in the latter figure. The layer closest to the electrode contains only solvent molecules of the electrolyte and is known as the inner Helmholtz plane (IHP), while the next layer comprises ions covered in a layer of the solvent molecules, called the outer Helmholtz plane (OHP). Together the two planes comprise the double-layer, leading to the creation of a potential difference across the surface of the electrode, in a so called *capacitive process*. In the investigations presented in this work the capacitive processes have not been simulated. Rather the potential difference $\Delta\phi$, that develops across the double-layer is modelled as a discontinuity.

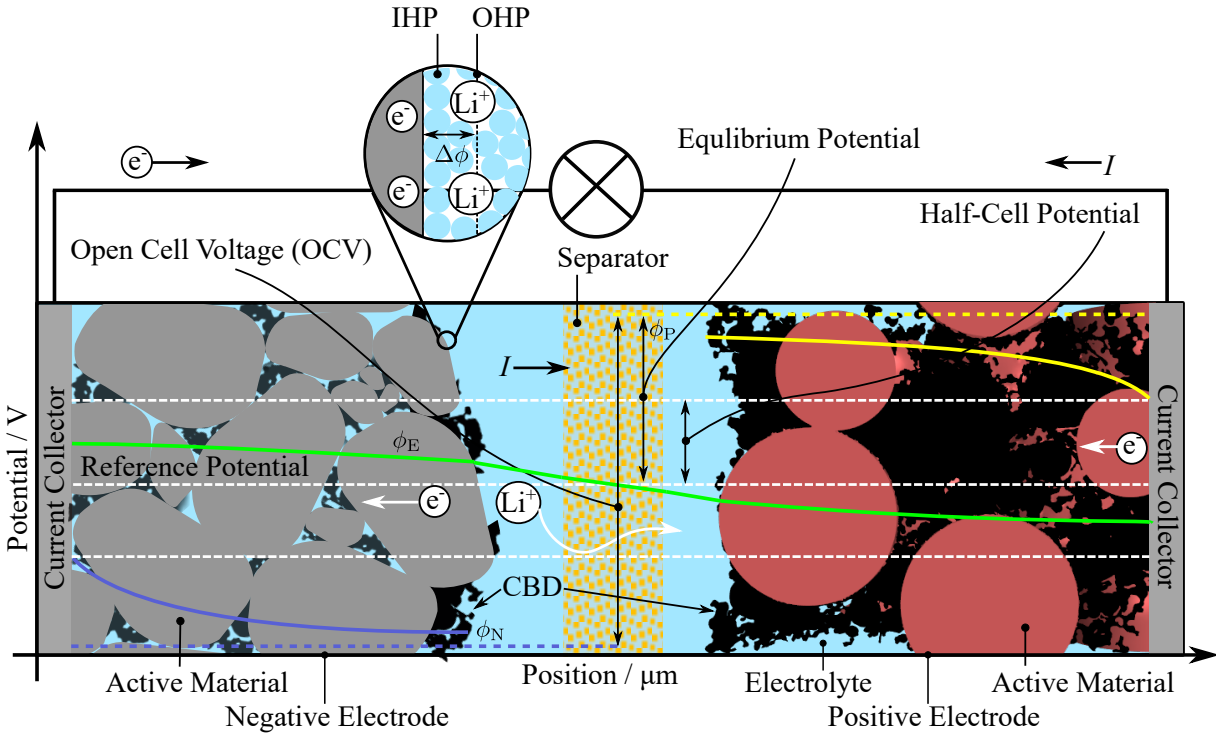

Figure 2.1: A depiction of the fundamental processes and the spatial potential progression in a lithium-ion battery during discharge.

Without any connection between the electrodes, the potential of the positive electrode ϕ_{P}, is represented by the straight-dashed-yellow line and that of the negative electrode ϕ_{N}, by the straight-dashed-purple line in the potential vs position graph embedded in Figure 2.1. The difference in these potentials is just enough to avoid any net current from following in the system. This potential difference is known as the open cell voltage (OCV). For an individual electrode, this potential measured against a reference is called the *equilibrium potential*. When the electrodes are connected to each other over a load, the potential of the positive electrode is decreased and the potential of the negative electrode increased, as indicated in the figure. This drives the equilibrium redox reaction taking place at the surface of the electrodes [5]

$$\text{Negative Electrode}: \ \mathrm{Li[A]} \underset{\text{Charge}}{\overset{\text{Discharge}}{\rightleftharpoons}} \mathrm{[A]} + \mathrm{Li^+} + \mathrm{e^-} \ , \tag{2.1}$$

$$\text{Positive Electrode}: \ \mathrm{[C]} + \mathrm{Li^+} + \mathrm{e^-} \underset{\text{Charge}}{\overset{\text{Discharge}}{\rightleftharpoons}} \mathrm{Li[C]} \ , \tag{2.2}$$

thermodynamically in direction of the discharge [6]. According to convention, under such circumstances the positive electrodes is referred to as the cathode, represented by [C]. The negative electrode on the other hand is called anode, denoted by [A]. Subsequently,

(in case of a lithium-ion battery) under the influence of increased positive potential at the anode, positive lithium-ions are released into the electrolyte and the freed electrons are conducted over the external circuit. At the cathode, the decreased positive potential helps to attract the lithium-ions carrying a positive charge, from the electrolyte, that receive the electron conducted over the external circuit and get stored in the cathode in a process called *intercalation*. Hence, at the cathode the positive-ion and the electron come from separate sources and are combined in a charge transfer reaction, leading to the generation of an charge exchange current. This process is labelled as the *faradaic process* and the entailing current is driven by the difference in the potential across the cathode surface in the absence of current ($\Delta\phi_{\text{eq}}$) and in its presence, by the quantity *overpotential*

$$\eta = \Delta\phi - \Delta\phi_{\text{eq}} \ . \tag{2.3}$$

The current density at the cathode surface, which serves as the measure of the electrons transferred in the charge transfer reaction is proportional to the overpotential. Modelling of the faradaic process using this proportionality, with help of the Butler-Volmer equation has been discussed in detail in Section 3.3.1. In the case of charging, an external voltage must be applied in place of the load to reverse the direction of the exchange current, by reversing the overpotential. This drives the reactions stated by the Equations 2.1 and 2.2 in the charging direction. As, a result lithium-ions are stripped-off the positive electrode and intercalated back into the negative electrode.
As was mentioned previously, during discharge, electrons are released at the anode and get conducted to the cathode over the external circuit, while lithium-ions are released into the electrolyte. At the same time lithium-ions are extracted from the electrolyte close to the cathode surface, as they take up electrons conducted through the cathode. Thus, a gradient in the lithium concentration is established in the electrolyte, driving the movement of the lithium-ions from the anode to the cathode, across the separator (see Figure 2.1). The transport of both these species i.e. electrons in the anode and cathode as well as the movement of the lithium-ion in the electrolyte comprises the *transport-process* in the porous electrodes, simulated explicitly in this work. As can be seen from Figure 2.1, the potential of the electrolyte ϕ_{E} (shown in green) decreases in the direction opposite to the movement of the electrons i.e. in the direction of the current I, as dictated by convention. This drop is not linear, as the current density is not a constant function of the position[1], but dictated by the transport phenomenon. In addition, the slope of the potential drop is higher across the separator, due to the increased resistance to the following current. Similarly, for ϕ_{P} at the cathode and ϕ_{N} at the anode a position dependent drop, in the direction of the following current is observed.

[1]Inspired from the COMSOL Blog by Ed Fontes [7].

2.1.2 Modes of Operation

Electrochemical cells are classified as *galvanic cells* and *electrolytic cells*. A lithium-ion battery under discharge behaves like a galvanic cell, such that spontaneous electrical work is produced upon connecting the positive and negative electrode. Conversely, under charging the behaviour of lithium-ion battery is described by that of an electrolytic cell. Such that, an external potential must be applied to oppose the thermodynamically viable process, forcing the electrochemical reactions in the opposite direction to store energy [6]. In this work, lithium-ion batteries are exclusively investigated under discharging conditions. The discharge behavior of LIBs is often the primary concern, especially in the case of consumer electronics and electric vehicles. Moreover, the discharging behavior of an LIB is frequently more directly linked to the electrode microstructure, which is influenced by the conductivity additive—an aspect that is the focus of this dissertation—compared to the charging process. The latter may be dominated by degradation phenomena such as lithium plating and solid electrolyte interphase (SEI) growth.
Principally, two operational discharge regimes are possible for a LIB. In case, a constant discharge current follows through the terminals of the battery, it is considered to be in *galvanostatic operation*. Conversely, LIBs can also subjected to *potentiostatic operation*, by keeping the voltage across the terminals constant. In this work, solely the galvanostatic operation has been investigated. Further, a current based classification of the galvanostatic discharge has been made to give rise to two application types: high-power application and high-energy application. Since lithium-ion batteries comprise of a wide range of active materials as well as numerous variation in composition and construction, a common metric to access the rate of galvanostatic discharge, called the C-rate, is adopted. The C-rate is based on the evaluation of the current necessary to discharge a cell completely in unit time, defined in hours. Thus, 1C represents the current that discharges the cell in an hour. Further multiples x, of the C-rate imply a proportional decrease in time such that xC is the current need to discharge the cell in $\frac{1}{x}$ hours. Consequently, investigation involving the galvanostatic operation of LIB at a C-rate $>$ 1C are considered to be high-current or high-power applications. The higher current is linked to higher power on account of the derivation of electrical power from the ohm's law

$$P = V \cdot I \ . \tag{2.4}$$

Conversely, below 1C, the operation of the LIB is considered to be in low current or high-energy application. Lower current leads to a lower overpotential on account of the proportionality discussed previously. This allows for operation closer to the equilibrium (i.e. no current), allowing for the maximum possible extraction of the chemical energy stored in the electrode.

2.1.3 Composition

The schematic representation of the lithium-ion battery, as illustrated in Figure 2.1, depicts a singular layer of battery components. This layer can be configured in various forms: it may be wound into a spiral to produce a cylindrical configuration, or alternatively, multiple layers can be stacked to form prismatic or pouch configuration. This layer of components represents an electrochemical cell comprising two particulate, porous electrodes with their respective current-collectors, an electrolyte that fills up the pores spaces and a separator needed to isolate the two half-cells (composed of the combination of the respective electrode and the electrolyte). Each electrode further consists of three essential components: active material, conductivity additive and binder. Herein, the active material is the substance that actively participates in the electrochemical reaction, while the conductivity and binder constitute the passive materials added to improve electrode characteristics. The nomenclature adopted in this work, follows the convention defined under consideration of electrochemical discharge, such that the electrode with the more positive potential is considered to be the cathode.
The active material of a LIB cathode is composed of a lithium-transition-metal-oxide. Lithium (Li) is an ideal choice in this matter as it is the lightest metal, hence it exhibits high specific energy storage capacity. Moreover, due to its high electrochemical potential, high cell-voltage can be achieved. Lithium-transition-metal-oxides used in LIB have been developed in recent years to optimize capacity as well as cell voltage. In this regard initially, $LiNi_{1-x}Co_xO_2$ (NC) emerged as an alternative to $LiCoO_2$, but despite better performance than the latter, NC was found to be structurally unstable during electrochemical cycling. Subsequently Manganese (Mn), which is electrochemically inactive in the operational voltage window of NC was used in partial substitution of NC giving rise to modern materials like $LiNi_{0.33}Mn_{0.33}Co_{0.33}O_2$ (NMC 333) [8]. With further advancement in material research, in a bid to raise the cell voltage, the Nickel (Ni) content in the lithium-transition-metal-oxide could be increased further while maintaining adequate structural integrity, leading to the cathode active material (CAM) investigated in this work, $LiNi_{0.60}Mn_{0.20}Co_{0.20}O_2$ (NMC 622) [9].
On the other hand, for the anode of a LIB, materials that can store lithium under low potentials are preferred. In this regard, Graphite is a viable choice. Its layered structure is particular favourable w.r.t. to the structural changes caused during the de-/intercalation of lithium. Moreover, it is chemically stable during the dis-/charging process. In recent years silicon has been suggested an alternative anode active material, owing to its higher capacity compared to the latter. However, silicon is prone to stability issues owing to the significant volume expansion during the de-/intercalation process. This dissertation focuses on the investigation of the positive half-cell of lithium-ion batteries (LIBs), driven by several critical considerations. First, the escalating demand for enhanced energy and

power densities necessitates an in-depth exploration of cathode materials, given their intrinsic ties to safety and economic implications. Second, emerging trends suggest a potential shift towards pure metal anodes in future technologies, which could render current anode alternatives obsolete.

As previously mentioned, conductivity additives and binders constitute the passive materials in lithium-ion batteries (LIBs). Commonly used conductivity additive in LIBs are graphite and carbon black, while common binders include Polyvinylidene fluoride (PVDF), carboxymethylcellulose (CMC) and Styrene-Butadiene Rubber (SBR). A detailed review of the significance of these materials, particularly the conductivity additive in the cathode, is presented in Section 2.2. Since these materials do not participate in the electrochemical reaction, they are considered dead weights in the LIB and reduce the overall energy density. As a result, the mass fraction of these materials in the electrode mix is carefully monitored and optimized to minimize their usage. The electrode mix comprising both the active and passive materials is coated on a conducting metal foil called the current-collector. In case of the anode the foil is made of Copper (Cu), while for the cathode, Aluminum (Al) is applied.

Once the electrode mixtures have been coated on their respective current-collectors, they are assembled together and the pore space is filled up with an electrolyte. Commonly used electrolytes in LIBs comprise of a lithium-salt dissolved in an organic solvent. An example of a LIB electrolyte is the completely dissociated lithium salt hexafluorophosphate $LiPF_6$, in a mixture of organic carbonates ethylene carbonate (EC) and ethyl-methyl carbonate (EMC). The electrolyte is responsible for the transport of lithium-ions. While, the dissociated lithium salt serves as the source of lithium-ions, the solvent helps in the mobility of these ions by forming a shell around it. The electrolyte only conducts ions, forcing electrons to flow over an external circuit, thus generating electricity. Moreover, to avoid a short-circuit between the two half-cell of a LIB, a porous separator is but into place that is permeable to lithium-ions, but physically separates the two electrodes. Typical materials used for LIB separator are either polymeric or ceramic in nature. During the first charging process of a LIB called *forming*, the solvent covered lithium-ions react with the anode surface leading to the formation of the protective layer called the SEI (solid electrolyte interface).

2.1.4 Means of Production

In the current work, a distinction has been made between *wet processes* and *dry processes* involved in the production of lithium-ion batteries. Herein, wet refers to use of an organic solvent typically N-Methyl-2-pyrrolidone (NMP), in the manufacturing process and dry indicates the processing using only solid constituents. Moreover, wet processing has been branded as conventional, as it is the established means of mass production [10].

A conventional lithium-ion battery electrode production process comprises of four steps. In the first-step, the components of the electrode are dispersed in a solvent using a dissolver (a stirring device commonly equipped with a blade shaped mixing element, rotating about its axis) leading to the formation of a slurry. Conventionally, the binder is initially dissolved in the solvent, after which the dry powders are directly introduced into the solvent, followed by subsequent dispersion. However, in recent years the dry components: active material and the conductivity additive are dry mixed in advance, owing to the merits of homogeneity achieved during this pre-mixing process [11]. Moreover, intensive-dry mixing has been used to pre-treat the dry mix of the active material and carbon black, inducing carbon black aggregate comminution, which further facilitates the homogeneity as well as allows for the coating of the active material with the conductivity additive. This process is carried out in specialized batch mixers designed for the task eg. Eirich-Intensive-Mixer, Maschinenfabrik Gustav Eirich GmbH and Nobilta®, Hosokawa Alpine AG. Apart from discontinuous batch mixing applied in the conventional process, twin-screw extruders have emerged as a viable continuous processing alternative [12]. These extruders facilitate enhanced dispersion of electrode constituents due to the higher shearing forces, which are achieved through the ability to process higher solid content. As a result, the extrusion process significantly reduces the usage of the expensive solvent [13].
In the second-step, the prepared slurry is coated onto a current-collector. The most common technique used in this process involves the use of a slot-die [14]. The coating on the current-collector is subsequently dried in the third-step. In the conventional process chain, large quantities of solvent have to be eliminated from the slurry using large ovens, rendering the process highly energy-intensive and costly. Drying alone consumes over 50% of the total energy required in this process [9]. Additionally, N-Methyl-2-pyrrolidone (NMP), which is toxic, must be recovered post-drying through intricate procedures due to its environmental hazards. In the fourth-step, the films produced in the conventional method are calendered using calender rolls to increase the adhesion to the current-collector, improve the contacting of particles and increase the volumetric energy density.
In light of the discussion on solvent usage, modern electrode production methods are advancing towards solvent-free processes [9]. In these methods, slurry preparation is replaced by dry mixing [15, 16]. With regard to coating and calendering, two process routes have gained particular importance: powder-spraying and binder fibrillation. Powder spraying involves the electrostatic application of the dry electrode mixture onto a binder-coated current-collector, followed by compaction under elevated temperatures through a hot pressing process [17]. While, binder fibrillation is typically executed via a roll-to-roll calendering technique. In this method, cylindrical calender rolls shear the dry constituents of the cathode, promoting the formation of binder filaments. This process results in the creation of a self-supporting film, which is subsequently laminated onto the current-collector [18].

2.2 Significance of Conductivity Additives

As the name suggests, conductivity additives refers to the substances added to lithium-ion battery electrodes, to improve their electrical conduction. Conductivity additives are added to both the LIB electrodes: cathode and anode, primarily in a bid to improve their ability to conduct electrons. In addition to the conduction phenomenon however, these additives also influence the thermal [19] and mechanical [20] properties of the LIB electrodes. Within the scope of this work, emphasis will be placed exclusively on their significance for cathodes, particularly w.r.t. impact on electrochemical performance.
The incorporation of conductivity additives is especially crucial for the cathode, due to the inherently low electrical conductivity of the cathode active material (CAM). The search for enhanced battery materials in recent years, has lead to improvement in the electrical conductivity of CAMs e.g. $Li_{1-x}Ni_{0.33}Mn_{0.33}Co_{0.33}O_2$ (NMC 333) achieving, 10^{-2} S m^{-1} at the lowest lithium content [8], in comparison to older materials like $LiFePO_4$ (LFP), which almost act as insulators with an electrical conductivity of 10^{-7} S m^{-1} [21]. Nevertheless, a close correlation is seen between the critical volume fraction of the conductivity additive and binder needed to establish a percolating electrical network in the cathode and its performance [22]. Guy et al. [23], showed that the variation in the electrical conductivity of the conductivity additive and binder composite with volume fraction of the conductivity additive is similar to a percolating system [24]. Wherein the composite exhibits the conductivity of the binder matrix, until a critical value called the *percolation threshold* is reached, beyond which a sharp increase in the conductivity followed by an asymptotic convergence to a fixed value below the intrinsic electrical conductivity of the conductivity additive is seen. Beyond the percolation threshold, the conductivity was found to be function of the ratio of binder and conductivity additive content with significant impact on the cell capacity.
In addition to the impact on the conduction of electrons through the cathode, the presence of the conductivity additive in combination with the binder also has a significant impact on the ionic conduction in the electrolyte, present in pores of the cathode. Bauer et al. [25] demonstrated that in an ideal scenario the conductivity additive in not only responsible for the improvement in the electrical contacting in the cathode, but also for the immobilization of the binder. This absorption of the binder by the conductivity additive is crucial for the formation of the electrical network as well as for the prevention of excess binder from covering the active surface and thus hindering ionic movement at the cathode-electrolyte interface. Similarly, Li et al. [26], found that the ratio of conductivity additive and the binder was closely linked to the interfacial impedance and the capacity of cathodes. Additionally, morphology of the conductivity additive was found to impact the electrical as well ionic conduction in the cathode microstructure [27].

In the porous cathode of a lithium-ion battery, performance optimization necessitates balancing electrical and ionic conduction [28]. Electrical conduction within the cathode: active material highlighted in red in Figure 2.2 and the combination of conductivity additive and binder, is facilitated by the conductivity additive and binder, which enables electron transport to the sites of the redox surface reactions involved in the electrochemical charge and discharge processes, as depicted in Figure 2.2. Concurrently, lithium-ions are conveyed to the same interfacial sites via the liquid electrolyte within the pore network surrounding the solid material, highlighted in blue in the same figure. Given that the rate of the redox reaction is dependent on the transport rate of both of these reactants and that the networks responsible for transport share spatial domains within the battery, achieving enhanced performance is contingent on an optimized synergy between these conduction phenomena and networks. The distribution of the conductivity additive is particularly crucial in this context, as its modification can impact the quality of both networks and the available surface area for redox reactions [29, 30, 31].

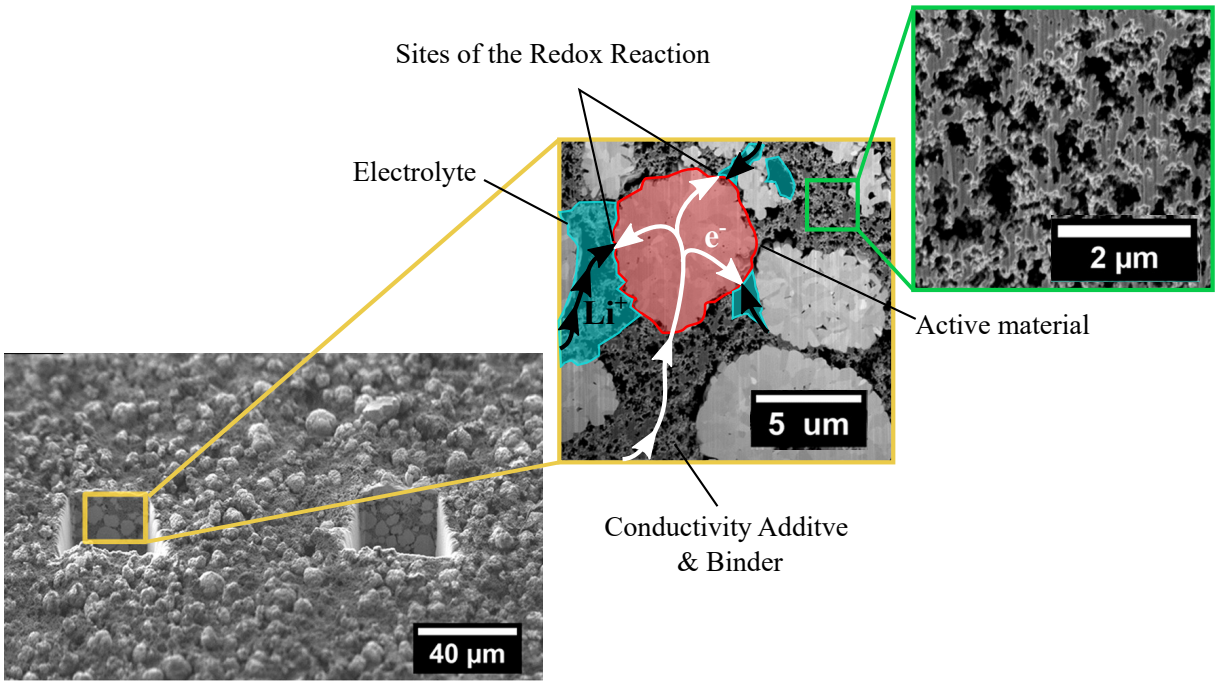

Figure 2.2: Visualization of trenches milled into a LIB cathode at various levels of magnification, adapted from scanning electron microscope (SEM) micrographs published by Daemi et al. [32]. The original image has been modified under the license CC-BY 4.0.

Due to their high charge mobility and specific active surface area, carbon based conductivity additives are widely used in energy storage devices [33]. The most common of this category of additives is carbon black. Carbon black is produced by the partial thermal decomposition of hydrocarbons [34]. The particles of carbon black grow as hierarchical structures or aggregates in their combustion synthesis, as shown in Figure 2.3. Hereafter, carbon black will be referred to synonymously as the conductivity additive.

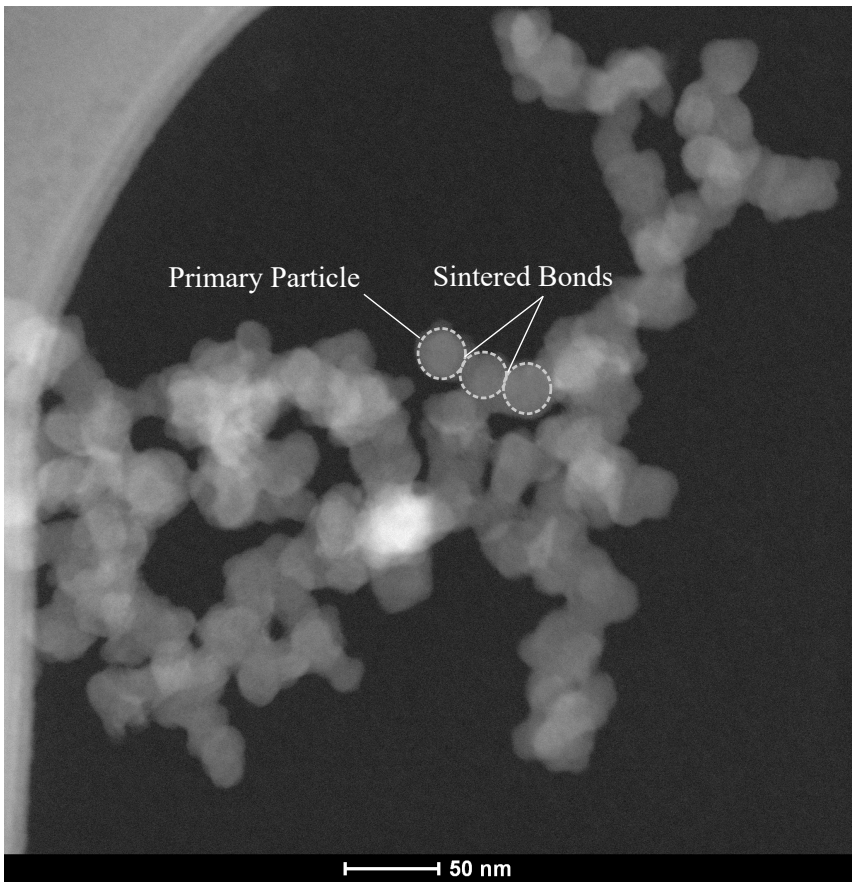

Figure 2.3: High-angle annular dark-field scanning transmission electron microscopy (HAADF-STEM) image of a carbon black aggregate. The image was kindly provided by Mr. Simon Buchheiser, M.Sc., Institute of Mechanical Process Engineering and Mechanics, Karlsruhe Institute of Technology.

The smallest unit of carbon black aggregates called *primary particles*, highlighted in Figure 2.3, are sintered together under the influence of high temperatures. The shape of these aggregates is often characterized using the concept of fractal dimension [35], as will be discussed in detail, in Chapter 4. Finally, owing to their high specific surface area carbon black aggregates agglomerate with polymers during the mixing process of lithium-ion battery manufacturing, leading to the formation of a foam-like composite, as shown in Figure 2.2, responsible for the electrical conduction in the cathode.
In the following parts of this section, contemporary research w.r.t. conductivity additives is addressed. To begin with, the influence of the LIB manufacturing processes on the combination of carbon black and binder, is elaborated. Subsequently, the means of numerical and experimental representation of the conductivity additive and binder combination in the cathode microstrucutre are discussed. Further, key indicators of cathode performance are identified to quantify the entailing consequences on the cathode performance. Finally, the state of the art hence established, is summarized in form of the **challenges** faced in the field and the **opportunities** available for subsequent research.

2.2.1 Influence of Manufacturing Processes

The mixing process in LIB manufacturing is accountable for two tasks with respect to the conductivity additive, its dispersion and its distribution. In this context, degree of dispersion refers to the degree to which the conductivity additive particles and their clusters are deagglomerated in the cathode mixture. While, distribution refers to the spatial spread of these passive materials [36]. In the investigations presented in the following chapters of this work, emphasis will be laid on the former, as the basis for a homogeneous distribution of the conductivity additive in the lithium-ion battery is formed by the achieved degree of dispersion in the mixing process.
Rwei et al. laid the foundation of the dispersion of carbon black in fluid media. Their investigations [3, 37] on the deagglomeration of the conductivity additive in simple shear flows, reveal two essential mechanisms of cluster breakage namely erosion and rupture, depicted in Figure 2.4. Herein, erosion is defined as the mechanism of particle cluster breakage [2], wherein small fragments of large clusters are gradually sheared off under the influence of hydrodynamic forces, resulting in smaller fragments that cannot be broken further, while rupture refers to the breakage of clusters into several smaller clusters of comparable size, which can be broken down further.

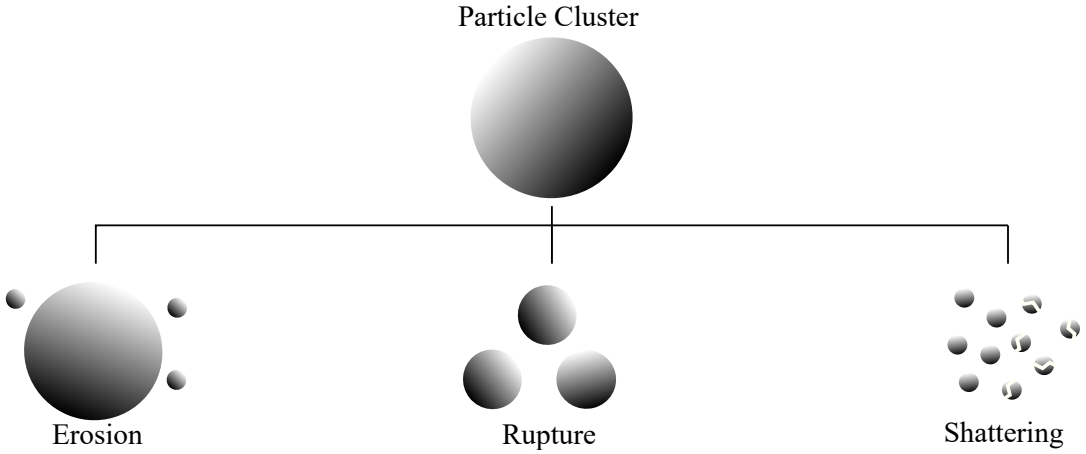

Figure 2.4: Mechanisms of nanoparticle cluster breakage following Özcan-Taşkin et al. [2].

Identical trends were also observed by the same group [38] while analysing the dispersion of carbon black in polymeric melts, characteristic of the conventional-wet mixing process. Consequently, numerous studies have quantified the influence of the mixing parameters on the dispersion of conductivity additives during the conventional-wet processing, be it for the batch mixing process [39, 40] or the continuous extrusion [41, 42].
On the contrary, the third possible mechanism of breakage visualized in Figure 2.4, called shattering occurs only at high levels of energy associate with the mixing process. Such energy levels are seldom reached in the wet mixing process but are characteristic to

intensive-dry mixing [43]. The process of shattering during dry mixing, leads not only to the deagglomeration of clusters of carbon black and binder but also to the comminution of carbon black aggregates into further smaller structures. Under the influence of further intensive mixing, these extremely fine particles can also mechanically fuse or latch on to the rough active material surface leading to the formation of a protective, conductive additive coating [44].
The mixing process in the conventional route of lithium-ion battery manufacturing is followed by the drying process, as discussed in Section 2.1.4. During the process of drying, as the solvent evaporates from the cathode slurry, the solid components of the slurry settle together, leading to the deposition of the passive components between and around the active material particles. As was suggested earlier, dependent on the volume ratio of carbon black to the polymeric binder, free-binder which is not immobilized by carbon black gets deposited on the active material surface leading to the coating of the active material by the inert binder [25]. Moreover, due to the evaporation of the solvent at the surface of the wet slurry a unidirectional force is generated in the direction of the evaporating solvent [45]. This forces the movement of the carbon black and binder particles to the heated interface of the slurry via a phenomenon called binder migration, leading to the de-mixing of cathode components [46].
The process of calendering LIB cathodes serves the purpose of compacting the cathode mixture before it gets assembled into the battery, intended at improving its volumetric performance. This compaction leads to a reduction in the pore space of the cathode microstructure. Conversely reduced pore space, increases proximity of the particles on account of the calendering pressure leading to an increase in the electrical contacts [43]. This interplay, has critical ramifications for the electrical as well as ionic conduction of the cathode. In addition, the calendering process influences the mechanical properties of the cathode in combination with the adhesion characteristics to the current-collector [47]. In the bounds of this work, the focus lies on its influence on the electrochemical characteristics, with emphasis on the role of conductivity additive and the binder [48], controlling the interplay of the conduction phenomena in the cathode.
In addition to the influence of individual processes, a strong interaction is observed between the manufacturing processes [11]. Depending on the degree of dispersion reached in the mixing process the rheological properties of the cathode slurries change considerably. This implies a significantly different result after the subsequent drying process e.g. Kremer et al. [49] observed that increased deagglomeration of carbon black and binder agglomerates, lead to an enhanced binder migration during drying. Moreover, Bockholt et al. [50] realized that intensive mixing lead to denser cathodes in comparison to the conventional-wet mixing. The compact dry mixed cathodes however exhibited poor contacting, which had to be rectified through calendering.

2.2.2 Influence on Microstructure

To represent the influence of the conductivity additive on the cathode microstructure, contemporary literature employs a variety of methods, including **experimental and numerical** approaches. In the experimental approach, the representation of the influence, is carried out by means of measurable quantities revealing insights into the conductivity additive structure. While in the numerical approach complete digital representative of the cathodes are generated followed by characterization through numerical simulations of performance related characteristics (elaborated in the following section).

In case of the mixing process a variety of quantities have been utilized for **experimental** tracking of the progress of conductivity additive dispersion. Haselrieder et al. suggested that rheological characteristics of cathode slurries are sensitive to change in formulation, hence parameter like viscosity are unsuited for the evaluation of the dispersion process [51, 52]. Instead, Dreger et al. [40] presented the analysis of particle size through light scattering and diffraction as a means of quality control. This method was adapted by Mayer et al [53], to study the influence of dispersion of carbon black while considering only the mean particle size. However, since the particle size distribution of carbon black in cathode slurries is usually bi-modal, the method was extend by Weber et al. [54] to accurately account for the particle size distribution for industrial applications, using the self defined parameter dispersion index. In close correlation to these contributions Asylbekov et al. [55, 39] used a combination of particle simulation and populations balances to numerically predict the particle size distribution resulting from the fragmentation of carbon black particles during mixing.

Alternatively, Mayer et al. [56] concluded that although particle size distribution analysis could reveal insights into the progress of deagglomeration during mixing, it is an insufficient parameter when the correlation to electrochemical performance is considered. Hence, they proposed a more comprehensive yet arduous experimental method of characterizing the conductivity additive by its inner porosity, measured by mercury intrusion. A more simplistic method to track the progress of conductivity additive comminution in intensive-dry mixing was proposed by Lischka et al. [57], by using bulk density measurement to characterize dry cathode blends intended for dry processed cathodes.

In experimental investigations concerning drying and calendering the focus has been on quantifying the influence of these processes on the global properties of the cathode rather than representation of carbon black and binder combination in the cathode microstructure. Therefore, previous studies have reported global parameters, such as adhesion strength [45] and the ratio of elastic-to-plastic work [48], rather than providing detailed insights into the specific impacts of these processes on carbon black and binder. The exception to this is imaging analysis, which has been utilized to qualitatively describe the influence of these processes [58].

For the **numerical** representation of the influence of conductivity additives, various methodologies have been employed. These methodologies can be categorized based on the approach used to generate the digital representation of the cathode. When tomographic imaging data from actual cathodes is utilized, the method is termed *reconstruction*. Alternatively, when the digital representation is generated through computational techniques, the method is referred to as *computational fabrication*.
The two prominent techniques used for *reconstruction* of cathodes are X-ray tomography [59] and focused ion beam scanning electron microscopy (FIB-SEM) tomography [60]. While the FIB-SEM tomography delivers a high resolution image of the cathode, it is field of view is restricted. Conversely, the X-ray tomography allows for non-destructive measurements of larger sections of the cathode but lacks the resolution needed to clearly distinguish the conductivity additive and binder combination from the pore space [61], leading to uncertainties in its position and structure. Consequently, Hein et al. [30] used X-ray tomography measurement to reconstruct the active material phase but relied on impedance measurements to artificially insert the passive phase (carbon black and binder). Similarly, numerous efforts have been made to overcome the shortcomings of these imaging methods. Zielke et al. [62] proposed a method combining the two tomographic techniques in this regard. While, Cooper et al [63] proposed improvements in the contrasts of the FIB-SEM technique by infiltrating the pore space of the cathode with platinum.
With a rising need to build a fundamental understanding of the LIB manufacturing processes, the approach of *computational fabrication* has gained prominence. In this approach, owning to the particulate nature of wet as well as dry cathode mixtures, particle simulations are used to mimic manufacturing processes. These particle simulation usually involve the modelling of constituent of the cathode mixture as spheres. Further, since resolving the structure of carbon black and binder polymer chains at the nanoscale is arduous, they are often treated as a composite material called the Carbon Binder Domain (CBD) (with the inclusion of even in the solvent in a molecular approach [64]). Moreover, in order to simulate relevant quantities of the cathode mixture using feasible computational resources, groups of associated particles and clusters in the cathode mixture are treated a single particle applying the coarse-graining technique, thus decreasing the computational effort by a reduction in the number of particles considered.
The simulation of manufacturing processes rely on modelling of the particle-particle as well as particle-wall interactions. Numerous instance of these can be found in literature. A fusion of Computational Fluid Dynamics (CFD) and the Discrete Element Method (DEM) was employed to simulate the effects of the drying process [65, 66]. The ensuing calendering process is detailed in Reference [67], utilizing the DEM approach. Following a Coarse Grained Molecular Dynamics (CGMD) [64] method, the influence of mixing [68], drying [69] and calendering [70] processes was characterized. In another investigation,

granular-colloidal method was used to systematically to vary the CBD in the cathode [31] revealing its influence on the microstructure.
The discussed means of digital representation of the cathode, either require expensive experimental setup or high computational resources. Hence a third method of generating digital cathodes through spatial *stochastic modelling*, is found in literature. The method is based on the tools of stochastic geometry [71], which evolves the generation of randomized spatial patterns. To ensure the comparability of these randomized geometries to real cathodes, realistic particles shapes [72] as well as comparison to tomographic data [73], is employed. Stochastic modelling enables expedited generation of a broad range of cathode microstructure, e.g. the method was used in the study of the influence of a variety of compaction loads on cathode microstructure [74].

2.2.3 Influence on Performance

This section elaborates on the link between the changes in the cathode microstructure inflicted by the processing of the conductivity additive and binder, discussed previously in Section 2.2.1 and quantified by the means in Section 2.2.2, on the indicators and determinants of cathode performance. In this dissertation, the term *performance indicator* is used to denote metrics that quantify microstructural change with potential to alter electrochemical performance. While, *performance determinant* refers to metrics that directly quantify the performance of the cathode.
Measurements on the conduction phenomena are an essential performance indicators as they indicate the efficiency of the transport pathways in the cathodes. In this regard, effective electrical conductivity of the cathode microstrucutre, provides insights into the transport of electrons through the electrical connections established during the manufacturing process. The effective electrical conductivity is an important performance indicator as it controls the distribution of potential and hence intercalation current in the cathode (see Section 2.1.1). Increased dispersion of the conductivity additives was found to increase the electrical conductivity [75, 43] by improvement in localized or short range electrical connections for the active material. However, it was found that very high levels of comminution of the conductivity additive achieved especially in the intensive mixing process, wherein a coating of the conductivity additive was formed on the active material, the conductivity decreased on account of loss of global or long range contacts [50]. The two contrasting trends in electrical conductivity with the dispersion of conductivity additive and their impact on cathode performance have been handled in Chapter 5 and 6 respectively.
In the quest for an indicator of the efficiency of transport of lithium-ions in porous cathodes, the diffusion phenomena is often evaluated. A popular means hereof, specially when considering the digital representation of cathodes is the tortuosity [76]. The diffu-

sive tortuosity is a measure of pore network connectivity and pore network arrangement established in the cathode [77]. Morphology of the CBD achieved from a combination of the applied manufacturing processes has strong impact on these quality parameters. High dispersion of the CBD achieved in the mixing process makes the pore network convoluted by making the pore size distributions narrower [56]. In addition, CBD particles breach continuous pore networks due to their deposition around the active surface during the drying process. Moreover, concentration of the CBD close to the top of the cathode microstructure resulting from the migration of the binder during drying, impedes the movement of lithium-ion in the thickness of the cathode [49]. Finally, although calendering increases effective electrical conductivity through improved long-range contacts, it decreases the porosity, increasing resistance to ionic movement [50].

A further indicator for transport phenomena and performance in LIBs is the impedance spectrum. Impedance spectrum denoted on a Nyquist plot represents a wide range of dynamics process occurring in the cathode [78]. The different frequency domains of the spectra correspond to transport phenomena at varying length and time scales, from ohmic resistance of the cathode components, to the interfacial resistance at the active surface as well as resistance to diffusion much further away from the site of the redox reactions. Numerous studies have quantified the influence of conductivity additives on the impedance of cathodes, examining their impact on diffusion due to morphology [79, 30] and their effect on interfacial resistance due to the coating of the active material [80].

Besides conduction-related performance indicators, the mixture of conductivity additive and binder also affects performance indicators linked to the structural properties of the microstructure. The specific active surface area available for intercalation, which directly influences the resistance to the charge conversion reaction taking place at the active surface, is effected by the presence of the CBD. Depending on the dispersion of the CBD agglomerates, the availability of the area varies as the active site are occupied by these particle inhibiting the movement of charge carriers to these sites [77].

A combination of the performance indicators mentioned, determine the influence of CBD on the performance of the lithium-ion battery. The most commonly used performance determinant is cell capacity. Capacity is defined as the amount of charge delivered by the battery in given range of voltage and under a given operational current [81]. Since the capacity of a battery fades over time due to degradation [82], often the performance determinant is evaluated over numerous cycles with emphasis on its retention. Since batteries are applied to electrical machines intended to carry out mechanical work, the energy and power output of lithium-ion battery are crucial performance determinants. In the context of e-mobility, specific energy as well as power are considered to be prominent performance parameters, driving innovations in the field of cathodes [83].

2.2.4 Challenges and Opportunities

Quantifying the influence of conductivity additives on the cathode microstructure and its consequent impact on cathode performance is beset by a series of challenges. To begin with, due to the interconnected nature of the processes involved in the manufacturing of lithium-ion battery cathodes, attributing the resulting structure to any single process is unfeasible. Thus, the extent to which each individual process influences the final structure remains indeterminate. Similarly, since each process step has an influence on the indicators of performance as well as its determinants, the measured value of a performance indicator or determinant for a fabricated cathode, does not bear a direct causality to the individual manufacturing processes.

Moreover, the microstructures of cathodes exhibit intricate combinations of their constituent components. Notably, carbon black agglomerates with the binder within the microstructure. Isolating carbon black for analysis thus requires complex separation processes. Additionally, the active material particles, which are larger than carbon black particles by an order of magnitude, also necessitate removal via separation techniques. This inherent complexity poses substantial challenges in accurately determining the particle size distributions, which are crucial for assessing the extent of carbon black dispersion, as discussed in Section 2.2.1. As an alternative to particle size measurements of the conductivity additive, the in-situ pore size distribution of the cathode can be measured using porosimetry techniques. These techniques however are infeasible for industrial application due to enormous experimental effort involved.

Alternatively, tomographic analysis is often applied to investigate the influence of conductivity additives on the cathode microstructure, especially for the investigation of the spatial distribution of carbon black resulting from drying and calendering. However, tomographic techniques are either restricted by ability to fully resolve the CBD or by the field of view (refer to Section 2.2.2). Additionally, segmentation techniques needed to process tomographic data, lead to non-negligible difference in the digital representation of the cathodes [61]. This poses a challenge for numerical investigation based on tomographic reconstructions as often the position and morphology of the conductivity additive has to be mathematically estimated in the digital cathode representation, leading to loss of relation to the manufacturing process or the misinterpreted of CBD and pore volume fractions due to segmentation errors.

Contrastingly, the approach of computational fabrication allows the investigation of intricate details of the influence of processes on the cathode microstructure, but digitally mimicking manufacturing processes requires rigorous experimentation and validation. Moreover, modeling assumptions are necessary to simplify the cathode microstructure in order to maintain computational feasibility. This often means sacrificing CBD morphology resolution to achieve the desired thickness of the digital representative.

In this work, the influence of conductivity additive in the cathode microstructure has been investigated using their digital representation. Consequently, the digital representations are subjected to electrochemical simulations of transport processes to numerically evaluate performance. Thus, driving process and microstructure development based on a direct analysis of the cathode performance. In order to generate the digital representation of the cathodes, stochastic method for generating randomized particle assemblies was chosen. This allows for the expedited representation of a wide range of microstructural changes that occur in the cathode microstructure during the manufacturing process through systematic variation in the shape and size of the conductivity additive (Chapter 4), contrary to the computation fabrication and reconstruction techniques. In order to adequately inform the stochastic microstructure generation method about the process, experimental evaluations (e.g particle size distribution) of the carbon black structure was employed. These insights could then also be incorporated into the investigation of contrasting strategies of cathode design: high-energy and high-power application design (Chapter 5), since the flexibility of stochastic modelling allows for ease of variation in cathode dimensions, constituent volume fractions and porosity. Furthermore, stochastic generation of particulate structure allows for the isolated investigation of the change in a single microstructural parameter (e.g. Bulk Density in Chapter 6) allowing to correlated it directly to cathode performance. Finally, by applying resolved simulation of the transport processes on the digital cathode representations, the influence of localized transport phenomena can be investigated on the global cathode performance.
In terms of opportunities in contemporary research concerning cathode manufacturing processes, the influence of the mixing process on the cathode performance has largely been ignored. This has do to with the long held notion, that passive elements do not have a significant impact on battery performance, which was considered to be predominantly restricted by the capacity of the active material. But as the research of active materials with every higher capacities reaches a bottleneck, due to the inherently bound chemical capacity of materials and increasing concern on the safety and cost of high capacity materials, the focus has shifted towards the optimization of the cathode microstructure. In this regard, the capabilities of mixing can be investigated far beyond the classical task of homogenisation of the cathode components. While the percolating behaviour of the conductivity additive and binder in the cathode resulting from the mixing process is clearly understood, there still remains a gap in the understanding of engineering the structure and location of passive materials to ensure feasible conduction pathways for the reactants and adequate surface area for the dis-/charge redox reactions. Thus in this work, recommendations are provided as conclusive remarks to the investigations on conductivity additives, addressing the optimum microstructure obtainable through the mixing process.

Chapter 3

Numerical Method

The following sections of this chapter, arranged in the chronological order of their execution, establish the **three-step** numerical framework adopted in this work, to investigate the influence of conductivity additives on the performance of lithium-ion batteries. In the presented three-step numerical method, at first, a means of generating computational half-cells capable of replicating changes in the cathode microstructure caused by the processing of conductivity additives is presented. Followed by, a numerical characterization step to quantify the extend of these changes on the cathode microstructure. Conclusively, scale resolving simulations of the transport processes in half-cells have been outlined as a means of linking the cathode microstructure to the performance of lithium-ion batteries.

3.1 Idealized Computational Half-Cell Generation

This section elaborates on the **first-step** of the numerical method, dealing with the generation of idealized half-cell computational domains alternatively referred to as idealized half-cell geometries or simply the half-cell, in this work. These computational domains are finite volume element (FVE) meshes, that capture the alterations occurring in the cathode microstructure during manufacturing processes. Idealized in this context, refers to the assumption that the constituent particles of the half-cell are assumed to be perfectly spherical, smooth and dense in nature. The generation of the half-cells is divided into two parts. In the first half, using a stochastic, mesh-free method, particulate structures are generated. These structures serve as the basis for the FVE meshes of the comprising regions of the half-cell namely, the cathode region also known as the solid region and the electrolyte region. Subsequently, the particulate structures from the first half are transformed into finite volume element meshes suitable for OpenFOAM based solvers intended for characterization and electrochemical simulations.

3.1.1 Generation of Particulate Structures

Owing to the particulate nature of the cathode constituents, the discrete element method (DEM) is suitable for the representation of their structural variations, during the lithium-ion battery manufacturing process. The DEM was initially proposed as an explicit numerical scheme called distinct element method by Cundall and Strack for research in the field of granular assemblies [84]. The method derives its name from the modelling of interactions as well as movement of particles of an assembly, individually. Such that the trajectory of motion under the influence of external forces for each particle, is individually evaluated based on the time integration of Newton's second law of motion. Wherein, the external forces are a result of particle-particle as well as particle-wall interactions. Wall in this regard refers to rigid, impenetrable surfaces.

For the purpose of generation of particulate structures in this work, simulations of particle assemblies were conducted using the open-source software LIGGGHTS®, made available by the CFDEM® Project [85]. These simulations consider a two component particle assembly, consisting of an active and a passive component. The active component, which refers to the material taking part in the redox reactions in the half cell as indicated in Section 2.1.3, is represented by a lithium-nickel-cobalt-manganese-oxide namely, $LiNi_{0.6}Mn_{0.2}Co_{0.2}O_2$ (NMC 622). Commercially produced NMC is spherical in nature, with an inner porosity of $< 4\%$ [86], hence non-porous, smooth and perfectly spherical particles where employed to emulate the active material in the particulate assemblies.

On the other hand, the passive component, which is inert to such electrochemical reactions, was modelled as a composite of the conductivity additive: carbon black and the polymeric binder: $(C_2H_2F_2)_n$ polyvinylidene difluoride (PVDF), called the carbon binder domain (CBD) as indicated in Section 2.2. Similar to the active component, the CBD was also modelled as spherical particles with no porosity. Moreover, as will be witnessed in the upcoming chapters, complex shapes of the CBD e.g. fractals were further constructed using idealized spheres in a multi-sphere approach (see Section 4.2).

To define the distribution of particles of the respective components in the particulate assembly a number based method (see LIGGGHTS® Documentation) using the number of particles of each component was utilized. Based on the method elaborated in Appendix B, volume fractions of the individual components could be calculated for a given cathode recipe (typically stated in wt-%) and half-cell porosity. The density of the materials used in these evaluations has been denote in Table 3.1. Subsequently, the number of particles for an individual component was calculated using the relation:

$$n_i = \frac{6 \cdot V_{\mathrm{HC}} \cdot \epsilon_i}{\pi \cdot d_i^3} \ . \tag{3.1}$$

Herein, n is the number of particles of a given component i, V_{HC} refers to the half-cell volume, ϵ_i represent the volume fraction of the component and d_i its diameter. In order to calculate the volume fraction of the CBD the evaluated volume fraction of the binder and carbon black were summed up.

Table 3.1: Density of the materials used in the components of the particulate structures [30].

Material	Density / kg m^{-3}
Active Material, NMC 622	4780
Carbon Black	1850
Binder, PVDF	1780

The quantities of the components hence determined were inserted at random points in a simulation box to give rise to the *initial suspension* state illustrated in Figure 3.1. Herein, the lateral dimension of the simulation box Δx and Δy correspond to the desired dimension of the half-cell, while the height is set sufficiently higher than the final cathode height H, to accommodate all the particles with out overlapping. The boundaries of the simulation box are periodic in the lateral direction (x and y) while the top and the bottom boundaries (z_{min} and z_{max}) are modelled as walls.
The choice of periodic boundaries in the lateral direction were inspired from the discussions in the preliminary work [1]. Performance determining phenomena in a lithium-ion battery occur at the microscale, however the length of a typical cathode roll in a cylindrical cell is a few meters [87]. Since a numerical evaluation on the entire cathode is bound to be computationally infeasible, periodically extendable microstructures are used in such investigations, as a means to ensure coherence between the contrasting length scales. The coupling of transport phenomena over the periodic boundaries of the cathode microstructure allow for the assumption of an infinite computational domain in the x and y directions, hence linking the evaluations at the microscale to the macroscale. In case of LIGGGHTS® simulations, periodic boundaries implies that particles partially extending out of the periodic boundaries are inserted back into the simulation box over the coupled boundary on the opposite side. For the sake of computational feasibility, only particles with their centers inside the simulation box were explicitly accounted for.
The randomized insertion of particles in the *initial suspension* is driven by a arbitrarily chosen prime number called the *seed number*. This number serves as an initialization of the randomized particle position generation algorithm (Park-Miller random number generator). It can be inferred from Figure 3.1, that the random insertion of particle in the simulation box leads to a relatively homogeneous distribution of the active and passive components. Hence, throughout the investigations made in this work the distribution of the cathode components in the half-cell is considered to be homogeneous.

Subsequent stages of the generation of the particulate structures have also been shown in Figure 3.1. The *dryed cathode* state, shown in the middle of the figure, is achieved by shrinking the simulation box at a constant rate to the final size of the half-cell, followed by relaxation to overcome the resulting overlapping between the particles. Herein, the Simplified Johnson-Kendall-Roberts (SKJR) model [88] was implemented to mimic the cohesion between the particles, while the particle-wall cohesion was neglected and the particle-particle as well as particle-wall contacts were modelled with the help of the Hertz-Mindlin contact model [89], in-built in LIGGGHTS®. The process imitates the drying of cathode suspensions as the solvent evaporates and the pore space between the particulate matter contracts. Herein the solvent, considered to be present in the empty spaces of the simulation box has not been modelled explicitly. Moreover, physical modelling of the solvent evaporation leading to migration of the binder under capillary forces were considered out of the scope of this work. Rather, the purpose of simulation was to imitate the active and passive component interaction as the surrounding pore space shrinks.

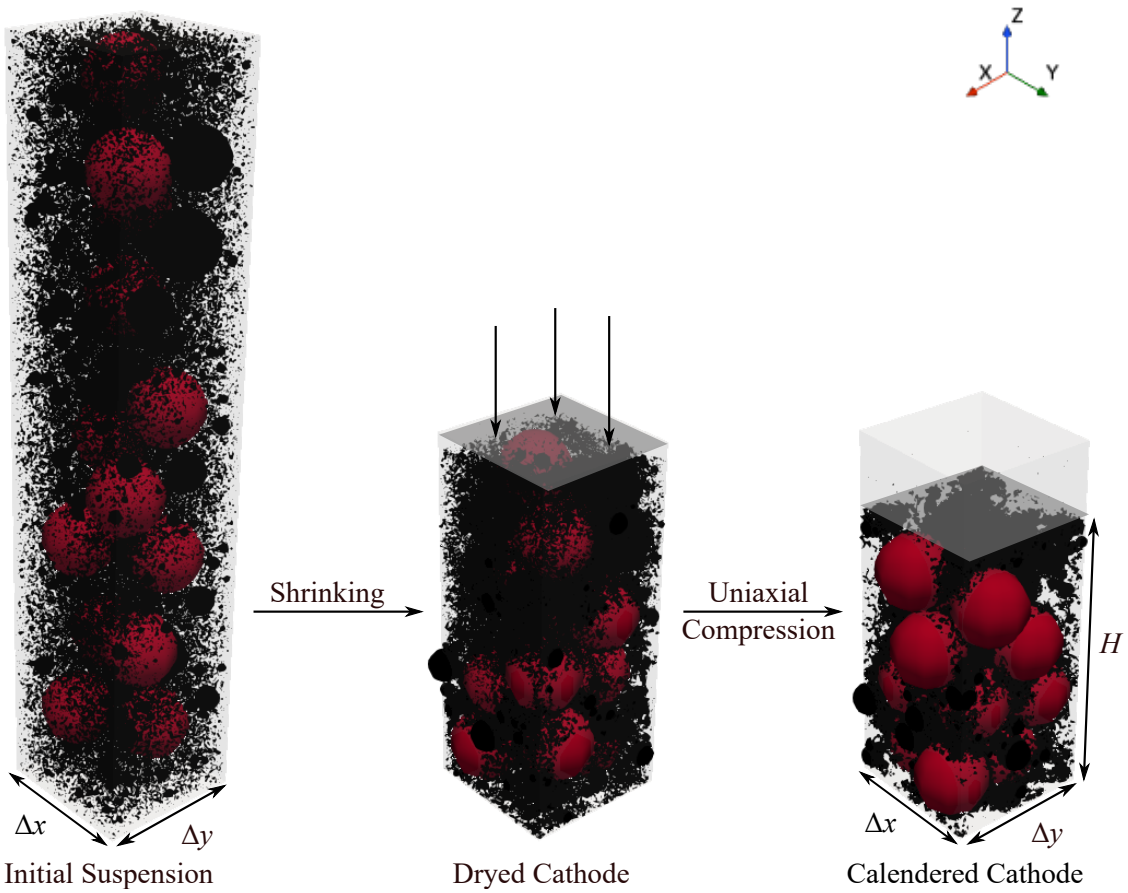

Figure 3.1: Stages in the generation of the stochastic particulate structures using DEM.

In a subsequent stage of the particulate structure generation to reach the *calendered cathode* state, the *dryed cathode* was subjected to uni-axial compression by a rigid surface moving in the negative z-direction with a constant speed, as shown in Figure 3.1. Thereafter, the particulate assembly was given sufficient relaxation time to overcome the overlaps between the particles. The purpose of this procedure is primarily to imitate the influence of compression on the contacting of the active and the passive components in the cathode during the calendering process. Additionally, it serves to regulate the final porosity achieved in the half-cell through fixation of the final cathode height H. During the procedure, deformation of the constituents under the force of the rigid surface is not considered. Consequently, the procedure is not devised to simulate the physical effects of calendering on the cathode's microstructure, such as particle deformation or fracture. Instead, its primary focus is on understanding how compression affects the electrical (contacts) and ionic (porosity) conduction in the half-cell.
In preliminary works [1, 90], DEM was utilized to generate periodic particulate structures as well. However, in these contributions the interaction of constituent particles was neglected and the followed procedure differs form one shown in Figure 3.1. Herein, the particulate assemblies were formed by dropping particles into an initially empty simulation box with periodic boundaries under the influence of gravity in the negative z-direction. Subsequently, the particles assembly was allowed to settle until a predefined minimum energy threshold was reached, followed by uni-axial compression as in the case of the procedure shown in Figure 3.1. The former procedure used in the preliminary works, was initially adopted for the investigations made in Chapter 4. However, notable disparities in the particulate structures, particularly evident in case of extremely small CBD sizes (see Chapter 5), revealed a significant limitation of the procedure when utilized for investigating conductivity additives. It was noted that under the assumption of no interaction between the active and passive components, the smaller CBD particles percolated through the larger pores surrounding the primary active material particles, resulting in a localized concentration of CBD at the bottom of the simulation box. This is an un-physical effect of the modelling, as in reality the combination of carbon and binder are know to stick to the surface of the active material observed through SEM images [25]. Hence, the methodology illustrated in Figure 3.1, was utilized in the remainder of the present work to imitate active material and conductivity additive interaction adequately.
Nonetheless, the presented method is not meant to digitally recreate the manufacturing of LIB cathodes. Instead of capturing transient microstructural changes, the focus herein is to reach a physically viable, stationary, end state capable of replicating the spatial distribution of the conductivity additive. The presented procedure hence, falls under the category of stochastic methods, discussed in Section 2.2.4. This implies that parameters chosen for the DEM simulations (Appendix A) were determined through trail and error.

3.1.2 Transformation to Finite Volume Element Mesh

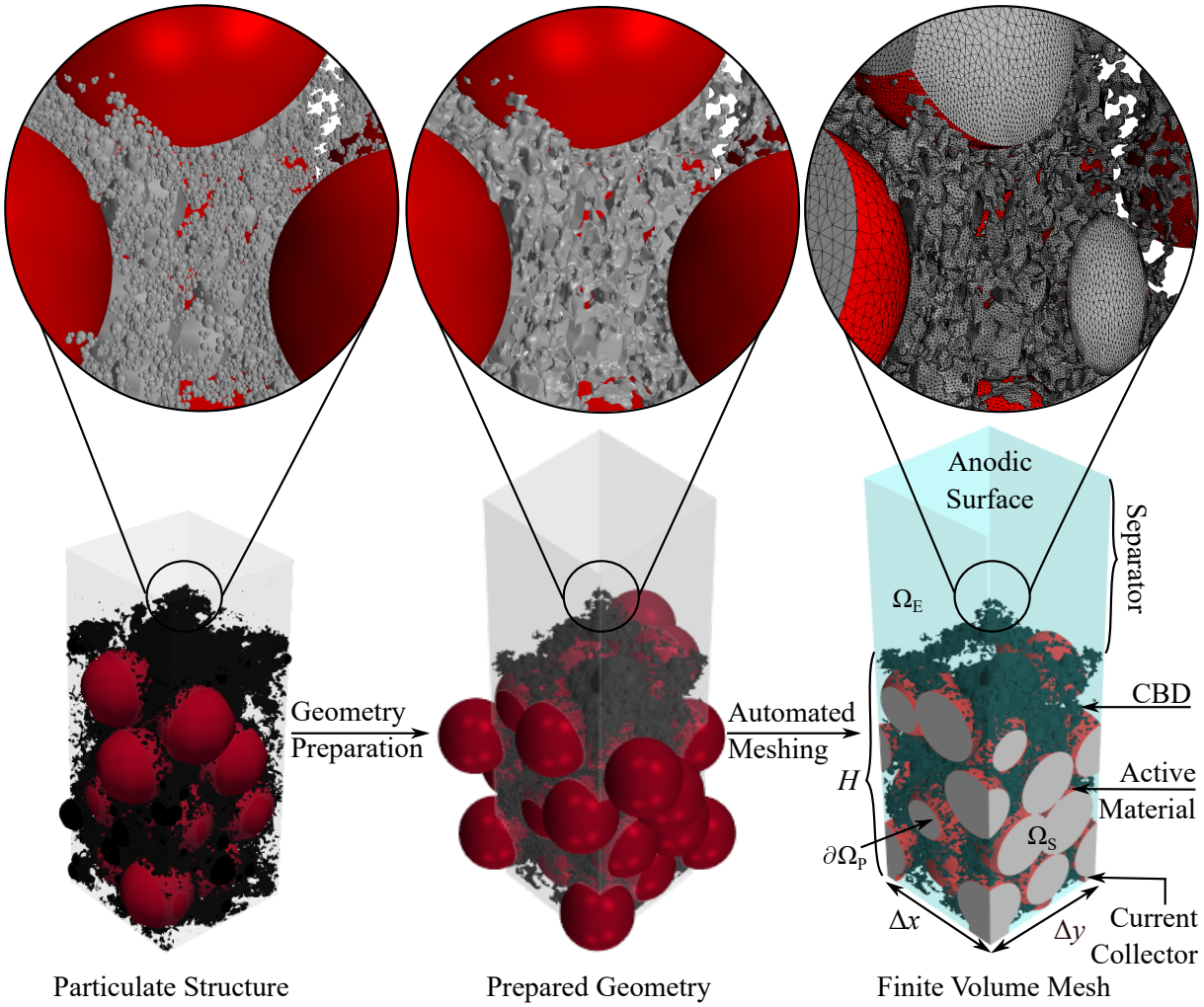

Figure 3.2: Illustration of the transformation of the periodic particulate structure into a periodic finite volume element mesh.

This section deals with the transformation of particulate structures into finite volume element meshes, intended for the numerical solvers described in the sections to follow. As shown in Figure 3.2, the particulate structure generated using DEM simulations, is at first, prepared for the meshing process with the help of geometry manipulations. This includes the addition of *periodic particles*, referring to the particles that partly penetrate the simulation box but their centers lie outside it. These particles were not explicitly accounted for in the DEM simulations, as mentioned in the previous section. Moreover, during the preparation, geometrical features leading to poor quality finite volume meshes are resolved. Hereby, slight adjustments are made to the particle positions as well as surface to ensure a smooth transition between the finite volume elements, discretizing the particulate structure. The prepared geometry is finally subjected to an automated meshing workflow to yield two non-overlapping domains with a conformal interface.

Geometry Preparation

In order to transfer the results of the DEM simulations to the geometry preparation process, the position and radii of the particles reached at the end of particle simulations were imported into MATLAB®. The imported list of particle in this state only contains the particles whose centers lie within the DEM simulation box (Figure 3.2 (far-left)). These particles will henceforth be referred to as *parent particles*. Using a self-written script in MATLAB®, originally developed by Kespe et al. [1], the positions of the *parent particles* were examined while considering the discretization of the computational domain. The discretization at the periodic boundary is of particular importance for the resolved electrochemical model presented in Section 3.3.1. Due to the interpolation of the model quantities as well as the coupling of mass transport over the periodic boundaries, significant numerical errors can arise due to a poor mesh. Moreover, the cathode surface, which is also the interface to the electrolyte region, and the cathode current-collector are crucial boundaries w.r.t. to post processing, necessitating their accurate representation.

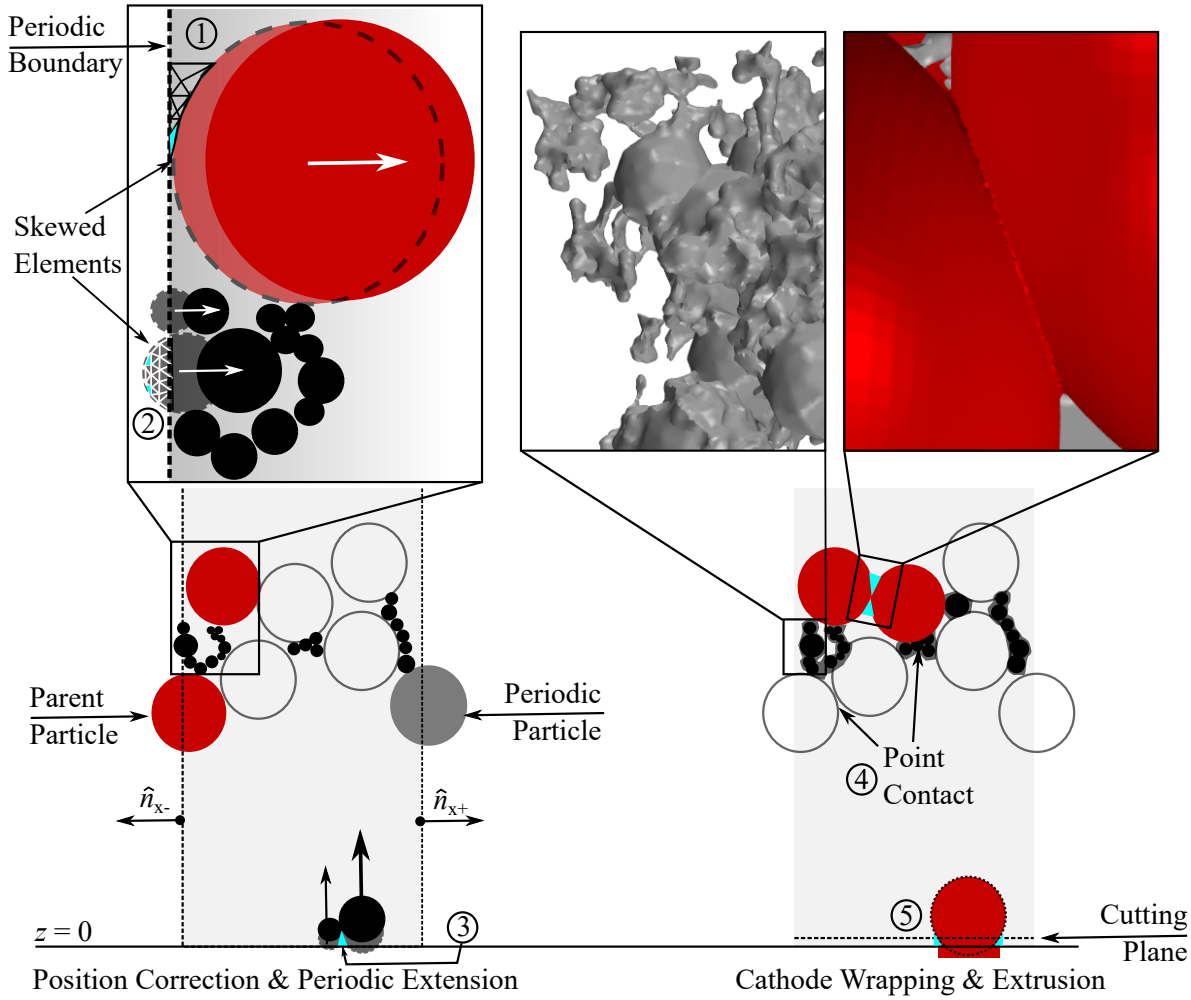

Figure 3.3: Visual representation of the problem areas and the means of geometry preparation.

Kespe et al. identified two fundamental problematic areas at the periodic boundary [1]. First, the proximity of the particles to the periodic boundary leading to a narrow region between the two, inevitably causing the formation of skewed triangular elements during discretization, denoted as ① in Figure 3.3. Skewness in this context refers to the deviation in the shape of the triangular elements compared to equilateral triangles. Second, in case only a small portion of a particle extrudes out of the simulation box, the corresponding small fraction of the *periodic particle* intruding into the simulation box (as elaborated later within this section) will have to be discretized by means of highly skewed elements denoted by ②, in Figure 3.3. In addition, a third problem area, linked to the explicitly consideration of the conductivity additives, in this work was identified at the bottom of the simulation box. Due to the small size of the passive component, the region between two contacting passive particles and the bottom of the simulation box becomes narrow with their proximity to the bottom of the simulation box, leading to highly skewed elements depicted by ③ in the figure.

To resolve these problem areas, small corrections to the particle positions were made based on an algorithm implemented in the aforementioned script. Herein, thresholds for the individual components were defined. These thresholds define the critical distance or the critical overlap between the outer most edge of a particle and a given boundary. With respect to the periodic boundary, the threshold for the active component was set to 10% of the particle diameter, as specified in the preliminary work [1]. In contrast, for the passive component, the threshold value is equal to the particle's radius. In both cases, i.e. when the overlap falls short of the threshold or the distance between a particle and the boundary is smaller than the critical value, the particles were pushed in the direction opposite to the surface normal of the respective boundary, as shown in Figure 3.3 (① & ②). For the passive component, as the threshold is equal to the particle radius, all the particles were pushed completely into the simulation box, ensuring no intersection with the periodic boundary. Since coupled periodic faces must coincide to avoid unwanted interpolation of the numerical solution, this approach helps to ensure that errors due to complicated contours of the periodic faces are avoided. Similarly, the passive component particles were also pushed in the positive z direction, away from the simulation box boundary to avoid possible intersections, denoted by ③ (Figure 3.3). The critical distance between the passive component and the bottom of the simulation box was set to 1 µm.

Followed by the corrections in particles positions, parent particles whose surface intersect with the simulation box boundary, were identified. For the finite volume mesh to be periodic in nature, for each parent particle extruding out of a periodic boundary of the simulation box a periodic particle must exist that intrudes into the simulation box at the coupled periodic boundary. In case of DEM simulation the opposite faces of the simulation box in the lateral direction are periodically coupled e.g. the periodic boundary with its

outward normal in the positive x-direction is coupled to the boundary with the outward normal in the negative x-direction, as shown in Figure 3.3. Consequently, for each parent particle intersecting the periodic boundary a periodic particle was added as shown in grey in the later figure. This concludes the particle position related modifications displayed on the left side of Figure 3.3.

In the subsequent steps of the geometry preparation process, the corrected position and radii of the particles was used to generate a computer-aided design (CAD) file in the stereolithography (STL) format using the software COMSOL Multiphysics®. The STL file was consecutively imported into Simcenter STAR-CCM+® for the preparation of the cathode surface. Significant issues to be resolved in the surface preparation process have been denoted as ④ and ⑤ in Figure 3.3. To tackle the issue of point contacts between the particles, leading to very narrow spaces close to the contact point as shown in the figure, the *surface wrap* utility available in Simcenter STAR-CCM+® was employed [91]. This utility bridges together points that are closer to each other than a predefined critical value, called the *wrapping threshold*, but not already connected through a surface. As a result a sort of wrap is formed around the discrete particle assembly, leading to the smooth continuous surface shown on the right hand side of Figure 3.3. Surface wrapping leads to alterations in the volume fractions of the components, hence the *wrapping threshold* was chosen carefully to make negligible changes in comparison to the volume fraction of the components and the porosity of the half-cell. In the subsequent step of surface preparation, a *cutting plane* was used to intersect the wrapped cathode, as shown in Figure 3.3 (right-bottom). The resulting cross-section was then extruded to extend out of the simulation box. This correction omits the possibility of skewed mesh elements at the cathode current-collector shown in the figure, at $z = 0$.

After the wrapping of the particulate assembly via the surface wrap utility, the newly generated surface was checked for errors and modified using the *surface repair* tool available in Simcenter STAR-CCM+®. Hereby, focus was laid on checking for and repairing pierced faces, face-proximity, free-edges and non-manifold edges. These categories of surface diagnostics have been elaborated in Simcenter STAR-CCM+® user-guide [92]. Figure 3.4, depicts these errors with help of simplified illustrations. The final result of the detailed process thus far, is the prepared geometry shown in the center of Figure 3.2.

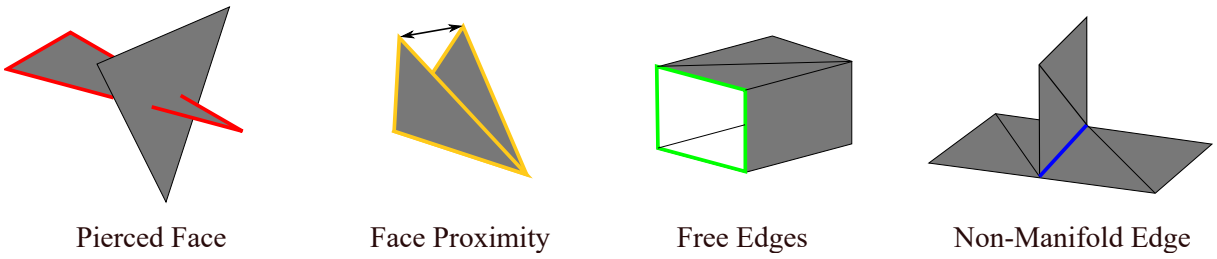

Figure 3.4: Visualization of surface errors as defined in STAR-CCM+® User-Guide [92].

Automated Meshing

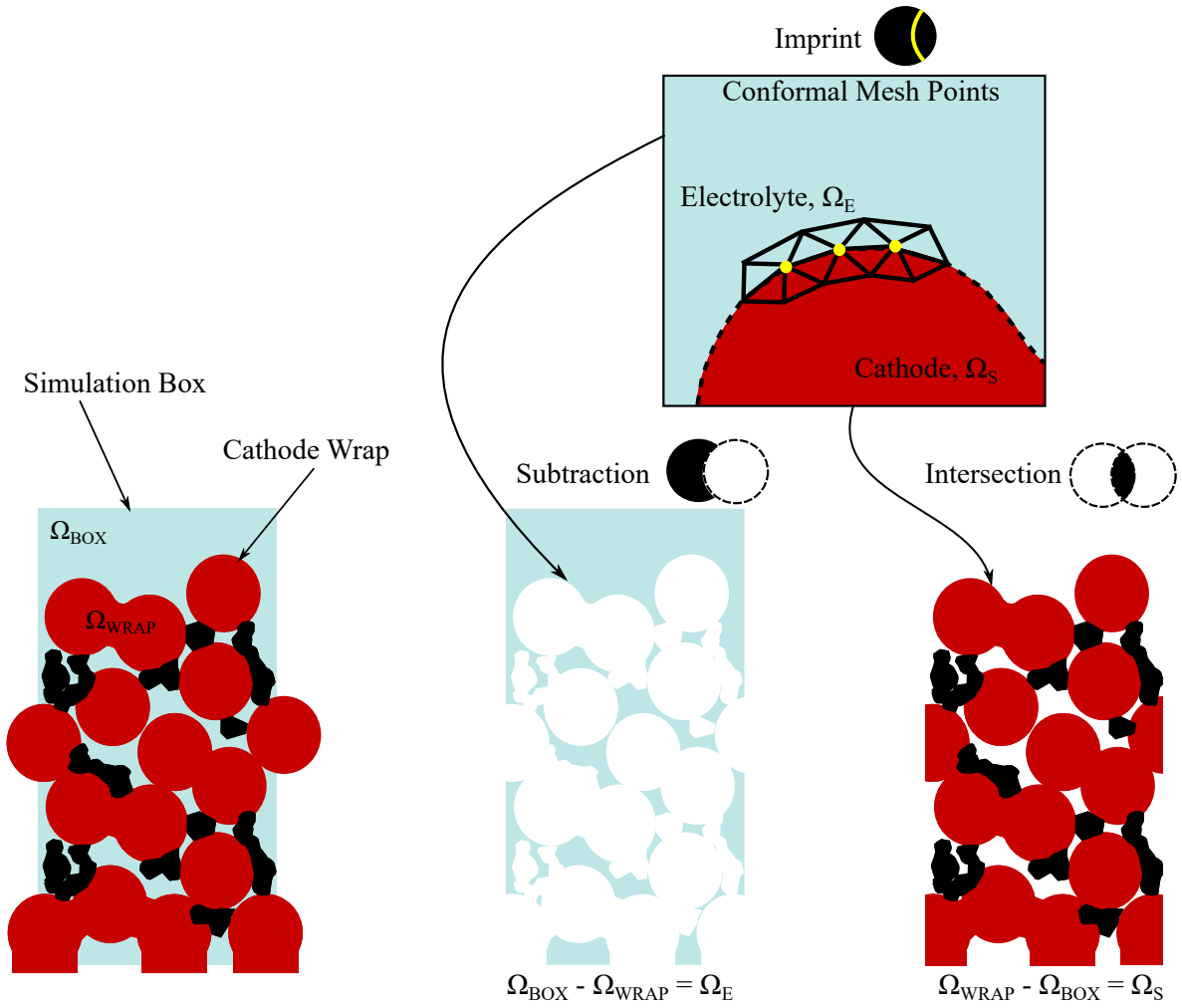

Figure 3.5: Mesh operations leading to the creation of electrolyte and cathode computational domains with a conformal mesh on the interface in Simcenter STAR-CCM+®.

The prepared geometry was transformed into a finite volume element mesh shown on the far right of Figure 3.2, using an automated workflow in Simcenter STAR-CCM+®. The automated work flow comprises of a series of linked operations. This work-flow starts with the prepared geometry as an input and culminates in producing surface meshes of two non-overlapping computational domains namely electrolyte and cathode, with a conformal interface as the output. Upon subsequent iterative surface check and repair, the surfaces meshes are eventually transformed into tetrahedral volume meshes.
At the start of the automated meshing workflow two independent geometrical boolean operations, subtraction and intersection are carried out as shown in Figure 3.5. For both these operations, the input parts are the prepared cathode geometry labelled as *cathode wrap*, Ω_{WRAP} and the simulation box , Ω_{BOX} corresponding to the dimensions of the simulation box in the DEM simulations, shown on the far left of the latter figure.

In case of the subtraction operation, the cathode wrap is subtracted from the domain of the simulation box. Since the simulation box is of the dimension of the cathode half-cell the resulting domain represents the void spaces filled with the electrolyte in the half-cell, displayed in the middle of the figure. Hence, this operation forms the basis for the outer surface of the electrolyte region, Ω_{E} shown in Figure 3.2. The dimensions of simulation box used for DEM simulations and hence the electrolyte region are based on the investigations on unit-cells with periodic boundaries in the preliminary work [1]. Herein, influence of the periodic boundary on the diffusion phenomenon was used to evaluate the smallest unit-cell cross-section necessary to minimize the numerical error associated with extremities of the half-cell. These evaluations lead to the choice of 20×20 µm as the minimum half-cell cross-section utilized in this work. Further, the height of the simulation box or the corresponding electrolyte region and hence the half-cell, is a sum of the cathode height H and the separator thickness as shown in Figure 3.2. The thickness of separator was chosen based on the parameterization carried out using LIB coin-cells in the preliminary work [1] and is set to 25 µm.

In the second boolean operation show on the far right of Figure 3.5, the intersecting domain between the simulation box and the *cathode wrap* is determined. This domain represents the *cathode wrap* trimmed at edges of the simulation box which coincide with the periodic boundary and the cathode current-collector (as labelled in Figure 3.2). The resulting domains hence, forms the basis for the outer surface of the periodic cathode region, Ω_{S} shown in Figure 3.2.

Following the independent generation of the respective surfaces, they were imprinted over one another as represented in the top part of Figure 3.5, using the merge and imprint tool [93] in Simcenter STAR-CCM+®. This operation patches the edges of the contacting surfaces of the electrolyte and cathode regions together and aligns the vertices on the opposites sides of the interface as shown in the figure, laying the foundation of a conformal mesh. Conformal meshes minimize the numerical error related to discretization by eliminating solution interpolation at the interface of the contacting regions.

In the final stages of the mesh generation process, at first, surface meshes for both the domains were generated. These meshes were then subjected to same check and repair process using the *surface repair* tool mentioned in the previous section. Subsequently, the surface meshes were converted into tetrahedral volume meshes within Simcenter STAR-CCM+® . Subject to quality criterion of the volume mesh i.e. maximum allowed cell skewness angle (70°) and minimum permissible cell quality (0.3), the surface meshes of the domains were manually repaired till the quality thresholds of the subsequent volumetric mesh were satisfied. Herein, cell skewness angle was used as a measure of diffusivity of the numerical quantities over adjacent cells without diverging. While, cell quality indicates the structural quality of the mesh elements w.r.t. a perfect tetrahedron [94].

3.2 Characterization

In this section the **second-step** of the three-step process developed in this work to investigate the influence of conductivity additives on the performance of lithium-ion batteries is elaborated. Previously, idealized half-cell computational domains we generated from particle simulations. In the chapters to follow, changing processing conditions are incorporated into the generation of these domains yielding distinct half-cell, hence forth referred to as variants. To quantify the differences between the variants, indicators of lithium-ion battery cathode performance: electrical conductivity, ionic conductivity and available active surface area, were put to use. As a measure of the electrical conductivity of the cathode microstructure, the effective electrical conductivity was chosen. Moreover, an evaluation of particle contacts in the half-cell was used as a means to assess the electrical connections. To asses the quality of ionic conductivity, tortuosity was employed. Together with effective electrical conductivity, tortuosity forms the combination of conduction phenomenon related characteristics simply referred to as conduction characteristics. In addition to conduction characteristics, the structural features of the half-cell were also compared using the structural characteristics: available volume specific active surface area as measure of the active surface and the porosity. In the forthcoming parts of this section the numerical method implemented for the characterization is explained in detail.

3.2.1 Effective Electrical Conductivity and Electrical Contacts

To obtain a measure of the bulk electrical conduction in the porous, heterogeneous cathode microstructure (composed of the active as well as the passive components), the effective electrical conductivity κ_{eff}, was chosen. Effective electrical conductivity is a global parameter that can either be measured in the plane of the cathode i.e in the direction parallel to the cathode current-collector (see Figure 3.2) using the four-point contact method [95, 51, 22] or in the perpendicular direction using the two-point contact method [96].The four-point contact method, in which all measurement probes are positioned on the top surface of the cathode sample, provides more accurate experimental results. It achieves this by eliminating contact resistances, such as those associated with the current-collector, and by reducing resistance spreading within the cathode plane. However, the two-point contact method, which involves contacting the cathode at opposite ends along a common axis, is more commonly used in numerical simulations due to its simpler modeling requirements. Numerical representations of this method can be found in literature in form of numerical evaluation of κ_{eff}, through resolved potential field in the cathode using finite element method (FEM) based solvers [28, 97], as well as resistor-network (RN) models [98, 99] using a network of resistor to map the conduction pathways.

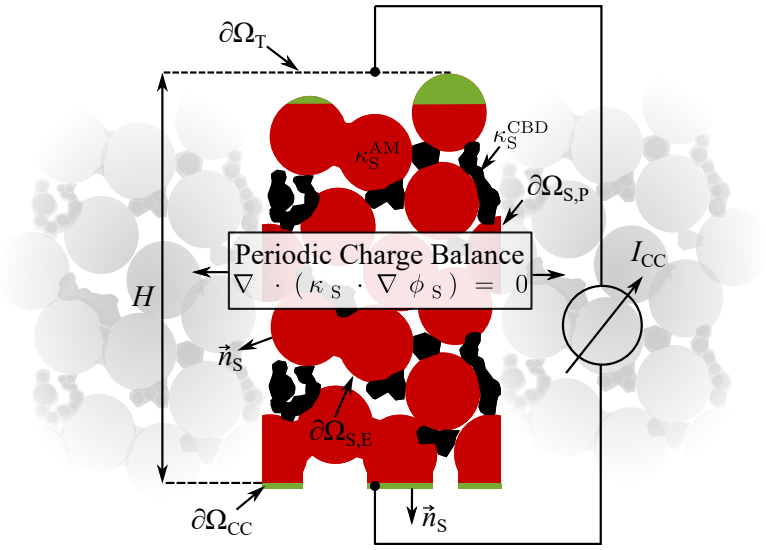

Figure 3.6: Schematic representation of the numerical solver used for the determination of effective electrical conductivity following the two-point contact method [1].

Following the methodology established in the preliminary work [1], a numerical solver based on finite volume method (FVM) written in the open source software OpenFOAM® Version 10 was used. The choice of FVM is based on the transferability of the cathode computational mesh from the characterization to the resolved electrochemical simulations elaborated in Section 3.3.1. The solver relies on the solution of the charge conservation equation

$$\nabla \cdot (\kappa_{\mathrm{S}} \cdot \nabla \phi_{\mathrm{S}}) = 0 \ , \tag{3.2}$$

under periodic coupling of the potential over the boundary $\partial\Omega_{\mathrm{S,P}}$, depicted in Figure 3.6. To imitate the two-point contacting measurement method, The potential $\phi_{\mathrm{S,T}}$, at top surface of the cathode $\partial\Omega_{\mathrm{T}}$, generated using *topoSet* and *createPatch* utilities in OpenFOAM® [100], was set to 1V. While, the potential $\phi_{\mathrm{S,CC}}$ at the current-collector $\partial\Omega_{\mathrm{CC}}$, was fixed at 0V. The potential difference across these two points leads to the evolution of a current $I_{\mathrm{S,CC}}$ at the current-collector

$$I_{\mathrm{S,CC}} = \int_{\partial\Omega_{\mathrm{CC}}} \vec{i}_{\mathrm{S}} \cdot \vec{n}_{\mathrm{S}} \ dS = \int_{\partial\Omega_{\mathrm{CC}}} (-\kappa_{\mathrm{S}} \cdot \nabla\phi_{\mathrm{S}}) \cdot \vec{n}_{\mathrm{S}} \ dS \ . \tag{3.3}$$

Herein, $\vec{i}_{\mathrm{S}}$ represents the current density and $\vec{n}_{\mathrm{S}}$ the outward normal at the cathode surface. Moreover, using the vector form of the Ohm's law, the current $I_{\mathrm{S,CC}}$ can be related to the solid potential gradient $\nabla\phi_{\mathrm{S}}$.

To ensure that the flowing current is restricted to the cathode domain, a *zeroGradient* boundary condition at the cathode interface to the electrolyte $\partial\Omega_{\mathrm{S,E}}$ (see Figure 3.6), was applied following the equation:

$$\nabla\phi_{\mathrm{S}} \cdot \vec{n}_{\mathrm{S}} = 0 \ . \tag{3.4}$$

Finally, reformulation of Equation 3.3 to extract κ_{eff} results in the relation:

$$\kappa_{\mathrm{eff}} = \frac{I_{\mathrm{S,CC}} \cdot \ H}{(\phi_{\mathrm{S,T}} - \phi_{\mathrm{S,CC}}) \ \cdot \ S_{\mathrm{CC}}} \ . \tag{3.5}$$

Herein, H represents the height of the cathode region as illustrated in Figure 3.6 and S_{CC} signifies the surface area of the cathode current-collector boundary $\partial\Omega_{\mathrm{CC}}$. The evaluated effective value κ_{eff} thus, accounts for the influence of the specific conductivity (reciprocal of electrical resistivity, which is a fundamental material specific property) of the individual components: $\kappa_{\mathrm{S}}^{\mathrm{AM}}$ and $\kappa_{\mathrm{S}}^{\mathrm{CBD}}$ along with the cathode microstructure.

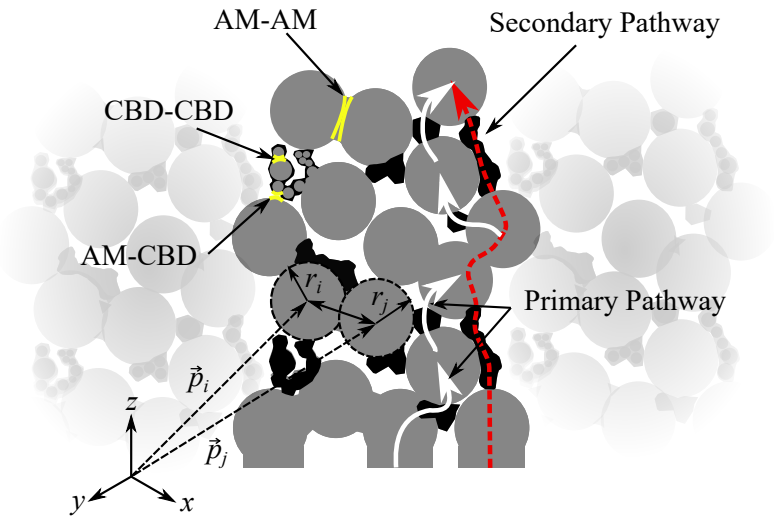

Figure 3.7: Visual representation of the classification of contacts and pathways in the cathode microstructure.

In addition to a macroscopic evaluation of the electrical conduction in the cathode microstructure, the contacts within the microstructure were evaluated to establish an understanding of the charge transport mechanisms. In doing so, three categories of contacts were established as shown in Figure 3.7. In the figure, the **AM-AM** contact represent the contact between two active material particles, **CBD-CBD** stands for the contact between the constituent particles of a CBD agglomerate or inter-agglomerate contact and **AM-CBD** denotes the contact between the active component and the passive component.

To determine these contacts, the mathematical description of contacting spheres was implemented in a MATLAB® script and executed on the particle position and radii information available after geometry preparation, explained in Section 3.1.2. A contact is thus considered to be formed in the cathode microstructure, if the norm of the difference of the positions of two individual particles $\vec{p_i}$ & $\vec{p_j}$ is less than or equal to the sum of their radii r_i & r_j (see Figure 3.7), following the relation:

$$\|\vec{p_i} - \vec{p_j}\| \leq r_i + r_j \ . \tag{3.6}$$

An alignment of these contacts in direction of the following current leads to the formation of conduction pathway, as indicated in Figure 3.7. Wenzel et al. [101] termed these pathways as primary and secondary pathways. Primary pathways are composed primarily of the **AM-CBD** contact. Hence, they establish a direct contact between the active component and the conductivity additive contained in the passive component, contributing directly to charge transfer between two active material particles. Since these contacts establish the interaction between immediate neighbours they are often referred to short-range pathways in contemporary literature. As is apparent from Figure 3.7, these contacts are formed by smaller fragments of the CBD lodged between active material particles. Hence, formation of short range contacts requires the significant fragmentation of the CBD to achieve higher dispersion. Increased dispersion in turn has a significant impact on the available active surface area and porosity in the cathode microstructure, as will be discussed at length in the chapters to follow.
Secondary pathways on the other hand are mainly composed of **CBD-CBD** contacts. These pathways act as shortcuts in the cathode allowing faster charge transfer over a larger thickness, as shown in Figure 3.7. Secondary, in this case suggests their coexistence with the direct contact between neighbouring active material particles via the primary or short-range contact. Moreover, these contacts form long chains within the cathode microstructure, as shown in the figure, to carry the charge from its source at the cathode current-collector all the way to top surface of the cathode closest to source of the lithium. For this reason, these pathways are also referred to as long-range pathways.
Due to the significant differences in the types of the contacts and the resulting pathways from their alignment, the analysis of contacts provides an essential tool to understand the difference in effective electrical conductivity of the variants investigated in this work. Moreover, these evaluation reveal information on the evolution of the cathode microstructure under processes such as compression (see Section 4.2.3) and intensive mixing (see Section 6.1.2).

3.2.2 Tortuosity

The tortuosity τ following the definition [102, 76]:

$$\frac{\kappa_{\mathrm{E,eff}}}{\kappa_{\mathrm{E}}} = \frac{D_{\mathrm{E,eff}}}{D_{\mathrm{E}}} = \frac{\epsilon}{\tau} = N_{\mathrm{M}} \ , \tag{3.7}$$

is used as an indicator of the ionic conductivity of the porous half-cells in this work. In this definition, κ_{E} & D_{E} signify the intrinsic value and $\kappa_{\mathrm{E,eff}}$ & $D_{\mathrm{E,eff}}$ the effective value of the ionic conductivity and the diffusion coefficient of the electrolyte, present in the pore room of the half-cell. Further, ϵ stands for porosity and N_{M} for the MacMullin number [103]. Hence, for a given ϵ, τ can be calculated from the stated definition, if $D_{\mathrm{E,eff}}$ or $\kappa_{\mathrm{E,eff}}$ is known. Experimental evaluation of τ is commonly based on the determination of effective diffusion coefficient for porous media, using techniques like the restricted-diffusion-method (RDM) [104, 105]. Hereby, a gradient is established in the salt concentration present in the pores of the medium and the diffusion phenomenon is observed under relaxation, as the concentration gradient is removed. This concept was modified and adopted to electrically conducting media such as battery material by Thorat et al. [106]. In addition, high frequency impedance response of symmetric cells is also used for similar evaluations. Nguyen et al. [107] argued that their numerical solver *TauFactor* based on this technique, leads to improved values of tortuosity, to be used in homogenized models like the pseudo 2-dimensional (P2D) model.

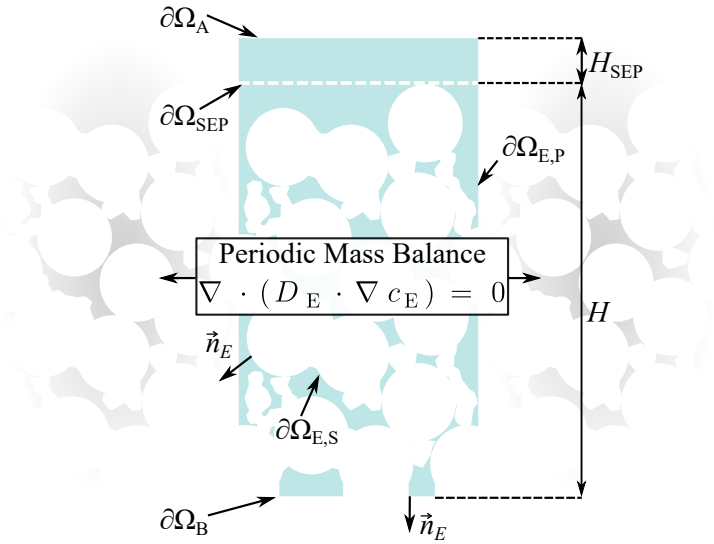

Figure 3.8: Schematic representation of the numerical solver used for the determination of effective diffusion coefficient following the preliminary work [1].

In this work however, on the one hand a resolved electrochemical model (see Section 3.3.1) is employed, while on the other, the evaluation on tortuosity serves only the pur-

pose of macrostructural characterization of ionic conduction in the half-cell, for which the RDM methodology is deemed sufficient. Hence, a finite volume method solver written in OpenFOAM® Version 10, identical to the preliminary work [1], was used to evaluate the effective diffusion coefficient, mimicking the RDM methodology. In doing so, a concentration gradient was established across the electrolyte region of the half-cell shown in Figure 3.8. The concentration $c_{\mathrm{E,A}}$ at top surface called the anodic surface $\partial\Omega_{\mathrm{A}}$ was set to 1 mol m^{-3} and the concentration $c_{\mathrm{E,B}}$ at the bottom most surface $\partial\Omega_{\mathrm{B}}$ was set to 0 mol m^{-3}. The solver is based on the solution of the steady state diffusion equation (Fick's law)

$$\nabla \cdot (D_{\mathrm{E}} \cdot \nabla c_{\mathrm{E}}) = 0 \ . \tag{3.8}$$

The boundaries of the electrolyte $\partial\Omega_{\mathrm{E,P}}$, are periodically coupled, such that mass transfer takes place across the lateral extremities of the electrolyte region. Further, to restrict the diffusive phenomenon to the electrolyte region a *zeroGradient* boundary condition

$$\nabla c_{\mathrm{E}} \cdot \vec{n}_{\mathrm{E}} = 0 \ , \tag{3.9}$$

similar to the previous section was implemented on the boundary $\partial\Omega_{\mathrm{E,S}}$ (see Figure 3.8). The established concentration gradient leads to the generation of material flux

$$\dot{N}_{\mathrm{E,B}} = \int_{\partial\Omega_{\mathrm{B}}} (-D_{\mathrm{E}} \cdot \nabla c_{\mathrm{E}}) \cdot \vec{n}_{\mathrm{E}} \ dS \ , \tag{3.10}$$

evaluated at the bottom surface $\partial\Omega_{\mathrm{B}}$. Wherein, ∇c_{E} represents the concentration gradient in the electrolyte and $\vec{n}_{\mathrm{E}}$ the outward normal at $\partial\Omega_{\mathrm{B}}$, as shown in Figure 3.8. In this work, the electrolyte region is modelled to include the separator region (see Section 3.3.1). Hence in order to exclude the influence of the separator region, the concentration immediately below the separator region $c_{\mathrm{E,SEP}}$, at the boundary $\partial\Omega_{\mathrm{SEP}}$, was evaluated as

$$c_{\mathrm{E,SEP}} = c_{\mathrm{E,A}} - \dot{N}_{\mathrm{E,B}} \frac{\tau_{\mathrm{SEP}}}{D_{\mathrm{E}} \cdot \epsilon_{\mathrm{SEP}}} \frac{H_{\mathrm{SEP}}}{\Delta x \cdot \Delta y} \ , \tag{3.11}$$

based on the Equation 3.7 & 3.8. Herein, τ_{SEP} and ϵ_{SEP} are values of tortuosity and porosity of the separator, while H_{SEP} is its thickness, as indicated in Figure 3.8. Finally, plugging the evaluated concentration in a similar reformulation of Equation 3.8, the effective diffusion coefficient in the electrolyte region was determined by the relation:

$$D_{\mathrm{E,eff}} = \dot{N}_{\mathrm{E,B}} \frac{1}{(c_{\mathrm{E,SEP}} - c_{\mathrm{E,B}})} \frac{H}{\Delta x \cdot \Delta y} \ . \tag{3.12}$$

3.2.3 Specific Available Active Surface Area and Porosity

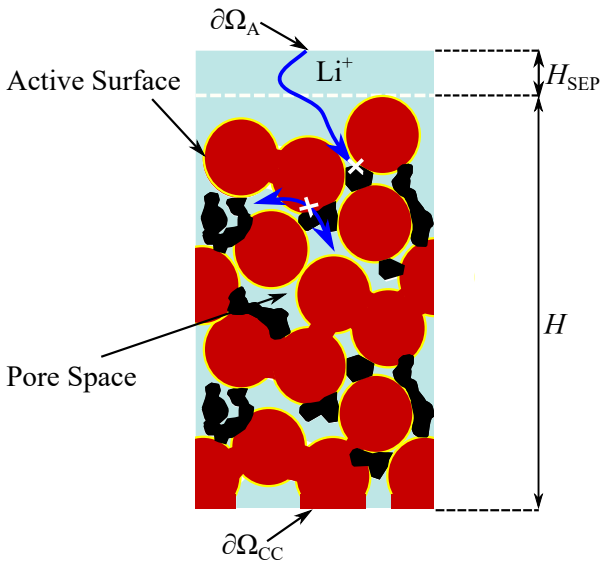

Figure 3.9: Visual representation of the structural characteristics of the half-cell along with their influence on lithium-ion transport.

The basis for the evaluation of structural characteristic in this work is formed by the active surface (yellow) and the pore space (blue) in Figure 3.9. The chosen structural property, specific available active surface area S_V, represents the volume specific surface area of the active material, available for intercalation in the half-cell. Alternatively S_V, has been referred to as the specific active surface area or simply, the active surface through the course of this work.

The availability of the active surface is directly linked to the distribution of the CBD in the half-cell, as can be seen in Figure 3.9. The CBD is considered to be completely dense in all considerations in this work. This implies, that at sites of the active material occupied by the CBD, no intercalation reaction can take place as the diffusion of the ions to the occupied surface is blocked by the CBD. Furthermore, since no lithium diffusion can take place across the CBD, it breaches the pore network of the electrolyte, hindering communication between pores, as indicated in the figure.

It was however found that the combination of the conductivity additive and the binder is nano-porous in nature [32]. Hence, contemporary studies [30, 108, 109] can be found with the diffusion in the CBD being modelled using the Equation 3.7. Such that the effective diffusion in the CBD is a function of the inner porosity and the tortuosity of the CBD. However, it was demonstrated by Mayer et al. [56], that the accurate determination of these parameter is non-trivial leading to notable inconsistencies in the electrochemical characterization. Moreover, Chouchane et al. [29] found in their study of different levels of diffusion restriction in the CBD that, completely restricted diffusion was able to replicate

the spatial distribution of intercalated lithium in the cathode. In addition, they concluded that the restricted diffusion modelling in the CBD was essential to account for its influence of the availability of the active surface. Thus, in this work fully redistricted diffusion in the CBD was opted for, to build a worst-case scenario analysis of the influence of the CBD.
To evaluate the volume specific available active surface area, the active surface area S_{AM}, resulting from the summation of the active part of the cathode boundary

$$S_{\mathrm{AM}} = \sum_{i \in \partial\Omega_{\mathrm{S,E}}^{\mathrm{AM}}}^{\partial\Omega_{\mathrm{S}}} S_i \ , \tag{3.13}$$

is divided by the volume of the solid region in the half-cell

$$V_{\mathrm{S}} = \sum_{i}^{\Omega_{\mathrm{S}}} V_i \ , \tag{3.14}$$

leading to the relation:

$$S_{\mathrm{V}} = \frac{S_{\mathrm{AM}}}{V_{\mathrm{S}}} \ . \tag{3.15}$$

These evaluations were carried out by the summation of the discretized volume and surface elements of the finite volume element mesh that represent the half-cell, in OpenFOAM®. Based on the solid volume, the porosity of the half-cell can be calculate as

$$\epsilon = 1 - \frac{V_{\mathrm{S}}}{\Delta x \cdot \Delta y \cdot H} \ . \tag{3.16}$$

Finally, using Equations 3.15 and 3.16, the relationship between porosity and available specific active surface area can be stated as

$$S_{\mathrm{V}} = \frac{S_{\mathrm{AM}}}{1 - \epsilon \cdot \Delta x \cdot \Delta y \cdot H} \ . \tag{3.17}$$

This equation, highlights the interrelation between the structural characteristics of the half-cell.

3.3 Performance Evaluation

This section deals with the **third and final-step** of the three-step numerical method explained in this chapter. In this step, the half-cells generated in the first-step and characterized in the second-step, are subjected to electrochemical simulations with help of a resolved model to simulate transport processes occurring during galvanostatic discharge at the microscale. The resolved simulations help to make an accurate prediction of the impact of the cathode microstructure on the electrochemical characteristics of the half-cell such as half-cell potential, intercalation current density and lithium concentration distribution. These characteristics have been presented as derivatives of the model. Subsequently, the model derivatives were used to compare the variants in the chapters to follow. In addition, these characteristics were used to evaluate common performance metric used to compare lithium-ion batteries namely energy density and power density, which are referred to as performance determinants in this work.

3.3.1 Resolved Electrochemical Model

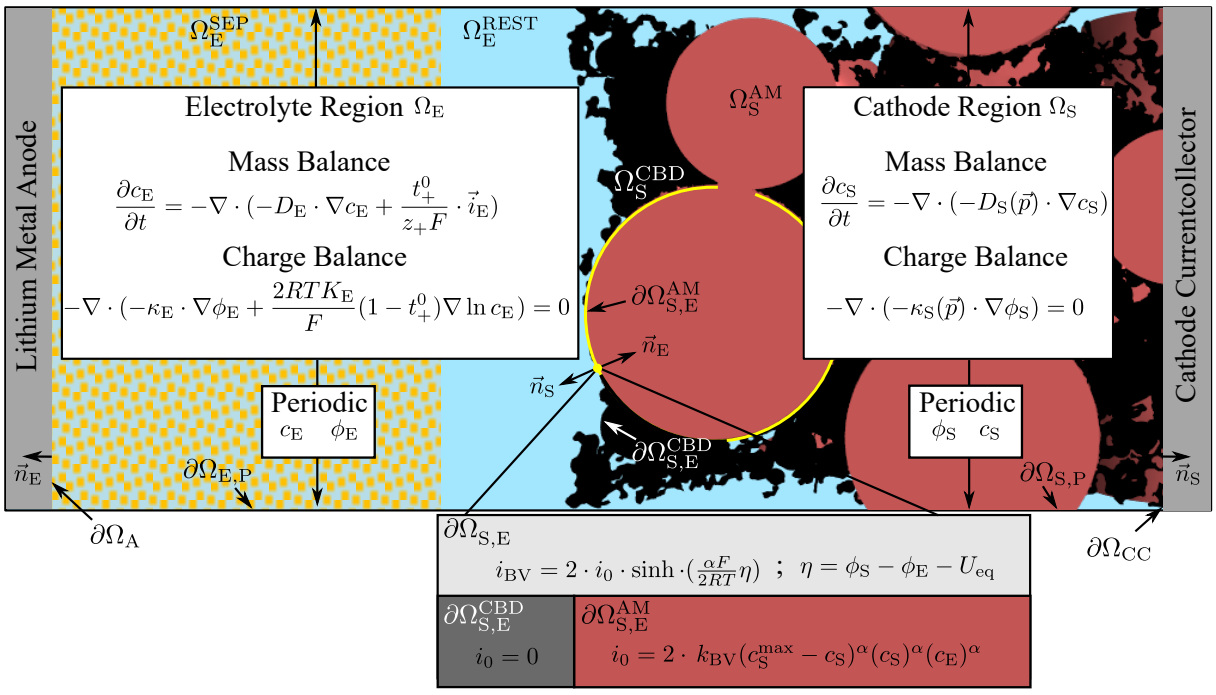

Figure 3.10: Resolved electrochemical model of the lithium-ion battery half-cell at the microscale, implemented in OpenFOAM® by Kespe et al. [110].

For the purpose of the resolved electrochemical simulations carried out in this work, the numerical model from the preliminary work [1], implemented in OpenFOAM® by Dr.-Ing. Michael Andreas Kespe, was extended to explicitly account for the passive materials in LIBs, comprising of conductivity additive and binder. A visual summary of the model

has been presented in Figure 3.10. In this representation, the half-cell shown is laid on the side after a 90 deg anti-clockwise rotation (compare Figure 3.2). The model accounts for two non-overlapping computational domains, also called regions, namely the cathode Ω_{S} and electrolyte Ω_{E} region. The cathode region, is further classified into the active material domain $\Omega_{\mathrm{S}}^{\mathrm{AM}}$ and the passive domain $\Omega_{\mathrm{S}}^{\mathrm{CBD}}$.

To explicitly account for the passive material, the *passive-material-bridges* interlinking active material particles in the preliminary work [1], were replaced by discrete particles reflecting the influences of manufacturing processes, as explained in step one and two (Section 3.1.2 and 3.1.1) of the numerical method. Subsequently the passive material, carbon binder domain, was considered as a composite of carbon black and binder in which the percolation threshold was reached, such that the achieved electrical conductivity (100 S m^{-1}) was an order of magnitude lower than pure carbon black (1000 S m^{-1}). Guy et al. [23] argued that carbon black aggregates in the CBD are not directly in contact, but separated by a polymer layer accounting for the difference. Percolation in this regard refers to tendency of carbon black aggregates to diffuse together in a polymer matrix at a critical threshold leading to formation of a electrical network [111, 112, 113]. In addition similar to the handling of the passive component in the preliminary work [1], the CBD domain was modelled to restrict the diffusion of lithium-ions as indicated in Section 3.2.3. To reflect this in the numerical model, boundaries of the CBD were modelled as walls for the electrolyte region and the diffusion coefficient in the CBD was chosen to satisfy $D_{\mathrm{S}}^{\mathrm{CBD}} << D_{\mathrm{S}}^{\mathrm{AM}}$ (see Table 3.3).

Similar to the preliminary work [1], the electrolyte region is classified into $\Omega_{\mathrm{E}}^{\mathrm{SEP}}$ and $\Omega_{\mathrm{E}}^{\mathrm{REST}}$, such that former represents the separator region modelled as a subdomain of the electrolyte region Ω_{E}, with help of effective transport properties following Equation 3.7 and the latter stands for the remaining electrolyte present in the pore space.

The boundary conditions as well as the solution implementation were inherited directly from the preliminary work [1]. The concentration and potential in both the regions is coupled over the periodic boundaries $\partial\Omega_{\mathrm{S,P}}$ & $\partial\Omega_{\mathrm{E,P}}$, as indicated in Figure 3.10. The anodic surface $\partial\Omega_{\mathrm{A}}$, shown as a plate on the far left of the figure is considered to be composed of pure lithium with constant potential of 0V, at all times during the discharge simulation. The cathode current-collector $\partial\Omega_{\mathrm{CC}}$, shown on the far right, is considered to composed of a perfect conductor such that no gradient in the cathode potential develops on this surface. Moreover, the cathode current-collector is modelled to ensure galvanostatic discharge, such that the current flowing through it remains constant at all times. The non-overlapping regions are coupled with help of an exchange current density, while simultaneously ensuring charge neutrality in the entire half-cell. The details thereof are addressed in the following section, where the governing equations of the model are stated. Finally, isothermal operation is considered at all times with temperature $T = 298$ K.

Governing Equations

The model uses charge and mass balance to simulate the transport of lithium-ions and electrons within the half-cell. The generalized differential forms of these balances are stated by the equations:

$$\frac{\partial c}{\partial t} = -\nabla \cdot \vec{n} \tag{3.18}$$

and

$$\frac{\partial q}{\partial t} = -\nabla \cdot \vec{i} \ . \tag{3.19}$$

Here, c denotes the concentration, q the charge, t the time, $\vec{n}$ the material flux and $\vec{i}$ the current density. The material flux and current densities for the individual domains have been denoted in Table 3.2.

Table 3.2: Mass flux and current densities in the cathode and electrolyte domain.

$\Omega_\mathrm{S} = \Omega_\mathrm{S}^\mathrm{AM} \cup \Omega_\mathrm{S}^\mathrm{CBD}$, $\partial\Omega_\mathrm{S} = \partial\Omega_\mathrm{S,E} \cup \partial\Omega_\mathrm{CC} \cup \partial\Omega_\mathrm{S,P}$		$\Omega_\mathrm{E} = \Omega_\mathrm{E}^\mathrm{REST} \cup \Omega_\mathrm{E}^\mathrm{SEP}$, $\partial\Omega_\mathrm{E} = \partial\Omega_\mathrm{E,S} \cup \partial\Omega_\mathrm{A} \cup \partial\Omega_\mathrm{E,P}$	
$\vec{n}_\mathrm{S} = -D_\mathrm{S}(\vec{p}) \cdot \nabla c_\mathrm{S}$	(3.20)	$\vec{n}_\mathrm{E} = -D_\mathrm{E} \cdot \nabla c_\mathrm{E} + \frac{t_+^0}{z_+ F} \cdot \vec{i_\mathrm{E}}$	(3.21)
$\vec{i}_\mathrm{S} = -\kappa_\mathrm{S}(\vec{p}) \cdot \nabla \phi_\mathrm{S}$	(3.22)	$\vec{i}_\mathrm{E} = -\kappa_\mathrm{E} \cdot \nabla \phi_\mathrm{E} + \frac{2RTK_\mathrm{E}}{F}(1 - t_+^0)\nabla \ln c_\mathrm{E}$	(3.23)

For the cathode or solid region Ω_S, shown in the left column of the table, in Equation 3.20, following the Fick's law, $\vec{n}_\mathrm{S}$ represents the flow of lithium in the intercalated state, c_s the lithium concentration in the active material and $D_\mathrm{S}(\vec{p})$ the spatially distributed diffusion coefficient dependent on particle position $\vec{p} = x\hat{i} + y\hat{j} + z\hat{k}$. Plugging this equation into Equation 3.18, leads to the solid mass balance equation shown in Figure 3.10. For the modelling of charge in the solid region, the left hand side of the Equation 3.19 is set to zero under the condition of charge neutrality [6]. The combination of Equation 3.22, representing the Ohm's law in differential form and Equation 3.19, leads to the solid charge balance equation shown in the latter figure. Here, $\vec{i}_\mathrm{S}$ is the electrical current density, ϕ_S the solid potential and $\kappa_\mathrm{S}(\vec{p})$ the spatially distributed electrical conductivity.
In case of the electrolyte region Ω_E, the transport modelling is based on the theory of concentrated solutions [6]. In Equation 3.21, $\vec{n}_\mathrm{E}$ represents the flow of lithium in the ionic state, c_E is its concentration in the electrolyte and D_E the spatially constant diffusion coefficient, modelled as a function of c_E by the polynomial expression [114]:

$$D_{\mathrm{E}} = 1.2 \cdot 10^{-21} \cdot {c_{\mathrm{E}}}^4 - 6.5 \cdot 10^{-18} \cdot {c_{\mathrm{E}}}^3 + \ 1.14 \cdot 10^{-14} \cdot {c_{\mathrm{E}}}^2 - 8.06 \cdot 10^{-12} \cdot c_{\mathrm{E}} + 2.24 \cdot 10^{-9} \ . \tag{3.24}$$

Further, t_+^0 denotes the transference number, which is a measure of the mobility of lithium-ions in the electrolyte, z^+ is the change number equal to 1 for Li^+ and F the Faraday's constant. In addition, $\vec{i}_{\mathrm{E}}$ signifies the ionic current density in the electrolyte given by Equation 3.23. Here, κ_{E} denotes the spatially constant ionic conductivity, modelled as function of c_{E} by the polynomial expression [114]:

$$\kappa_{\mathrm{E}} = \ - 2.39 \cdot 10^{-11} \cdot {c_{\mathrm{E}}}^4 + 1.21 \cdot 10^{-7} \cdot {c_{\mathrm{E}}}^3 - 2.89 \cdot 10^{-4} \cdot {c_{\mathrm{E}}}^2 + 0.32 \cdot c_{\mathrm{E}} - 2.789 \ . \tag{3.25}$$

In the equation describing the ionic current density (Equation 3.23), the electrolyte potential is denoted as ϕ_{E}, the universal gas constant as R and the temperature as T. The combination of Equations 3.21 and Equations 3.23, indicates the coupling of charge and mass in the electrolyte region. This is not the case in the solid region, due to the separation of charge (carried by the electron) and mass (intercalated lithium) in this domain. The final form of charge and mass balance for the electrolyte region after substituting the later equations from Table 3.2 into the generalized balances, under the condition of charge neutrality, has been shown in Figure 3.10
The modelling of the separator $\Omega_{\mathrm{E}}^{\mathrm{SEP}}$ region as a subdomain of the electrolyte was carried out by using effective transport properties (see Equation 3.7) such that the diffusion coefficient in the separator region is given by

$$D_{\mathrm{E,eff}}^{\mathrm{SEP}} = D_{\mathrm{E}} \cdot \frac{\epsilon_{\mathrm{SEP}}}{\tau_{\mathrm{SEP}}} \ , \tag{3.26}$$

and the ionic conductivity of the region is stated by

$$\kappa_{\mathrm{E,eff}}^{\mathrm{SEP}} = \kappa_{\mathrm{E}} \cdot \frac{\epsilon_{\mathrm{SEP}}}{\tau_{\mathrm{SEP}}} \ . \tag{3.27}$$

As was mentioned in the overview of the model, the two non-overlapping regions of the half-cell are coupled with an exchange current density. This exchange current density was modelled at the cathode-electrolyte interface $\partial\Omega_{\mathrm{S,E}}$, by a Butler-Volmer type relation.

The interface is divided into parts (see Figure 3.10) such that at any given point, the magnitude of the exchange current density is given by

$$i_{\mathrm{BV}} = \begin{cases} 2 \cdot \ k_{\mathrm{BV}}(c_{\mathrm{S,max}} - c_{\mathrm{S}})^{\alpha}(c_{\mathrm{S}})^{\alpha}(c_{\mathrm{E}})^{\alpha} \sinh\left(\frac{\alpha F}{2RT}\eta\right) & \text{on } \partial\Omega_{\mathrm{S,E}}^{\mathrm{AM}} \\ 0 & \text{on } \partial\Omega_{\mathrm{S,E}}^{\mathrm{CBD}} \end{cases} , \tag{3.28}$$

on the respective boundaries. Here, $c_{\mathrm{S}}^{\mathrm{max}}$ indicates the maximum stoichiometric lithium concentration, k_{BV} the Butler-Volmer reaction rate and α the apparent transfer coefficient are all material specific constants. The stated expression is a modification of the Butler-Volmer-equation under the consideration of symmetry i.e. anodic transfer coefficient α_{A} equals the cathodic transfer coefficient α_{C}, equals $\alpha = 0.5$ [105]. Further, in the expression, η refers to the overpotential stated as the difference between the galvanostatic potential difference $(\phi_{\mathrm{S}} - \phi_{\mathrm{E}})$ and the equilibrium potential U_{eq}, given by the relation:

$$\eta = \phi_{\mathrm{S}} - \phi_{\mathrm{E}} - U_{\mathrm{eq}} \tag{3.29}$$

(compare Equation 2.3). The equilibrium potential U_{eq}, specific to the active material NMC622, investigated in this work, indicates the half-cell potential at a given lithium concentration c_{S} in the cathode region, under consideration of no net flow of charge or mass across the cathode-electrolyte interface given by the expression [49]:

$$\begin{aligned} U_{\mathrm{eq}} = 13.49 - 10.96 \cdot c_{\mathrm{S}} \ + \ 8.2 \cdot {c_{\mathrm{S}}}^{1.36} \\ - 3.11 \cdot 10^{-6} \cdot \mathrm{e}^{(127.12 \cdot c_{\mathrm{S}} - 114.26)} \\ - 7.03 \cdot c_{\mathrm{S}}^{-0.03} \ . \end{aligned} \tag{3.30}$$

In order to maintain continuity in the half-cell the current densities at electrolyte and cathode side of the cathode-electrolyte interface ($\partial\Omega_{\mathrm{E,S}}$-$\partial\Omega_{\mathrm{S,E}}$) obey

$$-\vec{i}_{\mathrm{S}} \cdot \vec{n}_{\mathrm{S}} = \vec{i}_{\mathrm{E}} \cdot \vec{n}_{\mathrm{E}} \ . \tag{3.31}$$

Finally, the anodic surface and the cathode current-collector are modelled to ensure

$$-\int_{\partial\Omega_{\mathrm{A}}} \vec{i}_{\mathrm{A}} \cdot \vec{n}_{\mathrm{E}} \ dS = \int_{\partial\Omega_{\mathrm{CC}}} \vec{i}_{\mathrm{CC}} \cdot \vec{n}_{\mathrm{s}} \ dS = \int_{\partial\Omega_{\mathrm{S,E}}} i_{\mathrm{BV}} \cdot \vec{n}_{\mathrm{S}} \ dS \tag{3.32}$$

Parameterization

The parameterization carried out in this work is based on extensive literature research. For all the investigations carried out in this work NMC 622 was chosen as the active material, carbon-black as the conductivity additive and PVDF as the binder. The liquid electrolyte is modelled as a completely dissociated conducting salt, lithium hexafluorophosphate ($LiPF_6$) in a solvent consisting of a mixture of ethylene carbonate (EC) and ethyl-methyl carbonate (EMC). Further, the separator is consider to made of an ideal ceramic. The model parameter values as well as their sources have been indicated in the Table 3.3.

Table 3.3: Parameters for the resolved electrochemical model on the microscale.

	Value	Unit
Active Material - NMC 622		
Density, ρ_S^{AM}	4780 [30]	kg m^{-3}
Electrical Conductivity, κ_S^{AM}	1 [8]	S m^{-1}
Diffusion Coefficient, D_S^{AM}	$4.3032{\cdot}10^{-14}$ [49]	m^2 s^{-1}
Initial Lithium Concentration $c_{S,ref}^{AM}$	18409.57 [49]	mol m^{-3}
Maximum Lithium Concentration $c_{S,max}^{AM}$	50451 [49]	mol m^{-3}
Initial Cathode Potential, $\phi_{S,ref}$	4.3 [30]	V
Equilibrium Potential U_{eq}	Eq. 3.30 [49]	V
Carbon Binder Domain - Carbon Black & PVDF		
Density, ρ_S^{CB}	1850 [30]	kg m^{-3}
Density, ρ_S^{Binder}	1780 [30]	kg m^{-3}
Electrical Conductivity, κ_S^{CBD}	100 [23]	S m^{-1}
Diffusion Coefficient, D_S^{CBD}	$1{\cdot}10^{-20}$ [1]	m^2 s^{-1}
Lithium Concentration, $c_{S,ref}^{CBD}$	0 [1]	mol m^{-3}
Electrolyte - $LiPF_6$ in EC/EMC		
Electrical Conductivity, κ_E	Eq. 3.25 [114]	S m^{-1}
Coefficient of Diffusion, D_E	Eq. 3.24 [114]	m^2 s^{-1}
Initial Electrolyte Potential on $\partial\Omega_A$, $\phi_{E,ref}$	0 [1]	V
Transfer Number, t_+^0	0.4 [114]	-
Initial Lithium Concentration, $c_{E,ref}$	1000 [1]	mol m^{-3}
Separator		
Porosity, ϵ_{SEP}	0.85 [115]	-
Tortuosity, τ_{SEP}	1.5 [115]	-
Butler-Volmer Kinetics		
Butler-Volmer Reaction Rate Constant, k_{BV}	$1.4693 \cdot 10^{-6}$ [49]	A m$^{2.5}$ mol$^{-1.5}$
Cathodic/Anodic Transfer Coefficient, α_C/α_A	0.5 [49]	-

3.3.2 Model Derivatives

Electrochemical characteristics derived from the resolved electrochemical model have been termed as model derivatives in this work. These will be used to compare half-cell variants in the course of this work.

Half-cell Potential

The half-cell potential is the potential recorded across the terminals of the half-cell. Its value is extracted at the boundary $\partial\Omega_{\mathrm{CC}}$ (see Figure 3.10), with respect to the pure lithium metal anode, whose potential set at zero to serve as a reference.

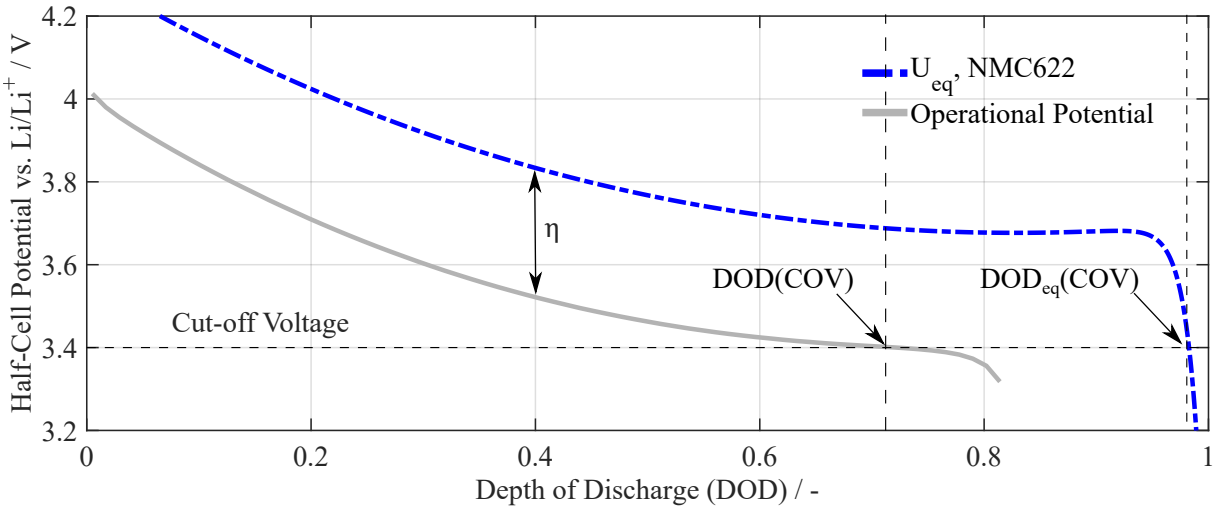

Figure 3.11: Schematic representation of the electrical potential related phenomena.

Figure 3.11, shows the half-cell potential under equilibrium operational condition plotted against the depth-of-discharge (DOD). The DOD is a dimensionless metric, indicative of discharge progress of the half-cell. Starting from an initial concentration $c_{\mathrm{S,ref}}$, the attained concentration at a given time t, $c_{\mathrm{S}}(\vec{p},t)$ can be used to determine the DOD following

$$\mathrm{DOD} = \frac{\int_{\Omega_{\mathrm{S}}} (c_{\mathrm{S}}(\vec{p},t) - c_{\mathrm{S,ref}})\ dV}{\int_{\Omega_{\mathrm{S}}} (c_{\mathrm{S,max}} - c_{\mathrm{S,ref}})\ dV}\ . \tag{3.33}$$

Therefore, DOD = 1 is indicative of a state of the half-cell where the concentration in the solid region has reached the maximum stoichiometric lithium concentration. This state however, is purely theoretical and reached only at no net current condition in the half-cell, or approached under at a very low current used to experimentally evaluate the equilibrium potential, shown in Figure 3.11. Under operational circumstances, when the current following across the active material is not zero, the half-cell potential lies lower than U_{eq} on account of the overpotential η, following the Equation 3.28 and 3.29.

Current

Under galavanostatic operational conditions the current flowing across the terminals of the half-cell is held constant. To quantify this current, the concept of C-rate is used. The C-rate in this work, is defined with respect to the maximum capacity of the cathode active material. A C-rate of 1C is the constant current necessary to exhaust the cathode capacity, within an hour. The cathode capacity in-turn, is dictated by the maximum lithium concentration that can be held by the cathode active material. Subsequently, the current following through the current-collector in dependence of the volume and maximum capacity $c_{\mathrm{S,max}}$ of the active material as well as C-rate is given by the relation:

$$I_{\mathrm{CC}} = \mathrm{C} \cdot \frac{F}{3600\frac{\mathrm{s}}{\mathrm{h}}} \cdot \int_{\Omega_{\mathrm{S}}^{\mathrm{AM}}} (c_{\mathrm{S,max}} - c_{\mathrm{S,ref}})\, dV \ . \tag{3.34}$$

The total current following through the current-collector is equal to the exchange current following normal to the cathode-electrolyte boundary according to Equation 3.32. However, the exchange current density is distributed heterogeneously over the thickness of the cathode. The local average intercalation current density in a section of the cathode electrolyte interface can be evaluated by the expression:

$$i_{\mathrm{BV}}^{\mathrm{avg}} = \frac{\int_{\partial\Omega_{\mathrm{S,E}}^{\mathrm{SEC}}} i_{\mathrm{BV}} \cdot \vec{n}_{\mathrm{S}}\, dS}{\int_{\partial\Omega_{\mathrm{S,E}}^{\mathrm{SEC}}} dS} \ . \tag{3.35}$$

This averaged local intercalation current density quantifies the distribution of current as well as the distribution of the overpotential driving the current in the thickness of the half-cell, following the Equations 3.28 and 3.29.

Spatial Lithium Concentration

To reveal deeper insights into the transport mechanisms of the half-cell, distribution of lithium in the both regions of the half-cell was investigated with help of 3D post-processing of the simulation results in the open-source software ParaView® e.g. Figure 4.4. In these representations, color coding indicating relative lithium concentration with respect to the maximum concentration is used to highlight the distribution of intercalated lithium in the cathode region. The passive cathode sub-region is always at a constant null lithium concentration, as it doesn't gain lithium concentration from the intercalation reaction, but is displayed in the color set at for lowest active material concentration. A similar color coding of the electrolyte region is used to indicate local lithium concentration changes w.r.t. to the initial concentration on account of the transport processes.

3.3.3 Performance Determinants

These properties form the basis of half-cell performance determination and comparison in the chapters to follow.

Utilizable Capacity

The utilizable capacity (UC), is the simplest performance determinant, derived from the definition proposed by Kespe et. al, in the preliminary work [1]

$$\mathrm{UC} = \frac{\int_{\Omega_\mathrm{S}} (c_{\mathrm{S,COV}} - c_{\mathrm{S,ref}})\ dV}{\int_{\Omega_\mathrm{S}} (c_{\mathrm{S,max}} - c_{\mathrm{S,ref}})\ dV}\ . \tag{3.36}$$

Here, the denominator represents the theoretical capacity of the half-cell and the nominator, the achieved capacity which could be utilized until a predefined cut-off voltage (COV). Lithium-ion batteries are typically discharged only up to a certain cut-off voltage to avoid degradation [116]. The maximum lithium concentration achieved until the COV, is not only limited by the theoretical capacity of the active material, but also by the constrains on transport of reactants involved in the electrochemical reactions. Hence, as show in Figure 3.11, the achieved DOD corresponding to the lithium concentration in the cathode at COV under operation condition, is less than that possible under equilibrium conditions. The ratio of DOD, thus reached at the COV for a given operational condition and the equilibrium, gives the performance determinant used in this work as

$$\mathrm{UC} = \frac{\mathrm{DOD(COV)}}{\mathrm{DOD_{eq}(COV)}} \cdot 100\ . \tag{3.37}$$

The utilizable capacity, is unsuitable to compare variants with different cathode mass (or volume at constant density). On the one hand, the maximum capacity of the cathode is dependent on its volume. While on the other, when comparing the galvanostatic performance at a given C-rate, the absolute current following through the cathode scales with the cathode mass, dictated by the Equation 3.34. Hence higher cathode mass leads to higher absolute current and thus higher intercalation current density following Equation 3.32, which eventually leads to a higher overpotential and lower half-cell potential following Equation 3.28 and 3.29, responsible for a lower DOD.
Moreover, the UC is only an indicator of the final cathode concentration reached at COV and doesn't account for the progression of the potential during the discharge process. Thus more generalized performance determinants are needed.

Utilizable Energy Density

The energy density is a common battery performance metric widely used to compare LIBs as well as other energy storage devices [83]. To determine the energy output of the half-cell from the resolved electrochemical simulations the definition proposed by Dr.-Ing. Susanne Kespe née Cernak in the preliminary work [90], was used to determine the utilizable energy (UE) following the equation:

$$\mathrm{UE} = \int_{\mathrm{t(0)}}^{\mathrm{t(COV)}} \phi_{\mathrm{S,CC}}(t) \cdot I_{\mathrm{CC}}(t) dt \ . \tag{3.38}$$

Here, $t(0)$ and $t(\mathrm{COV})$ indicate the time at beginning and end of the discharge. To facilitate the comparison of energy output of variants with different cathode mass, specific UE was evaluated corresponding to the cathode volume and mass. An approach similar to the volumetric approach followed Cernak et. al [117] was used to calculate the volume specific energy density, termed as volumetric utilizable energy density ($\mathrm{UED_V}$)

$$\mathrm{UED_V} = \frac{\mathrm{UE}}{V_{\mathrm{HC}} \cdot 3600 \frac{\mathrm{s}}{\mathrm{h}}} \ , \tag{3.39}$$

And the gravimetric approach following Cernak et. al [117]

$$\mathrm{UED_G} = \frac{\mathrm{UE}}{\rho_{\mathrm{S}} \cdot V_{\mathrm{S}} \cdot 3600 \frac{\mathrm{s}}{\mathrm{h}}} \ , \tag{3.40}$$

for the evaluation of mass specific energy density, termed as gravimetric utilizable energy density ($\mathrm{UED_G}$). Essentially, the expressions represent energy per unit volume of the half-cell V_{HC} or per unit volume of the cathode region V_{S} (at constant cathode density ρ_{S} calculated using Appendix B). Thus, $\mathrm{UED_V}$ is of significance when the cell-volume is restricted, while $\mathrm{UED_G}$ is relevant for restrictions on the active material.

Utilizable Power Density

Following the definition put forward in the preliminary work [90]. The volumetric-/gravimetric utilizable power density is evaluated by averaging the respective specific energy density over the entire time of discharge, regulated either by the achievement of COV (see Section 5.3.1) or by the numerical instability of the electrochemical simulations (see 5.3.2), following the relation:

$$\mathrm{UPD_{G/V}} = \frac{\mathrm{UED_{G/V}} \cdot 3600 \frac{\mathrm{s}}{\mathrm{h}}}{t(\mathrm{COV/END}) - t(0)} \ . \tag{3.41}$$

Chapter 4

Investigations on Conductivity Additive Size and Fractal Dimension

This chapter presents an investigation on the influence of the theoretical size and shape of the conductivity additive, produced during manufacturing of lithium-ion battery cathodes, on their performance. For this purpose, the following results have been divided into two studies namely, the impact of size and the impact of fractal dimension. The exterior diameter of the conductivity additive and binder agglomerates has been used as a measure of their size and the concept of fractal dimension employed to replicate the branched structure of common additives like carbon black. In both the studies, an analysis of the performance indicators reveals the impact of the size and shape on the cathode microstructure, followed by the performance evaluation revealing insights into the influence on transport processes at the microscale. This chapter therefore, addresses the **first objective** of this work, of establishing the **influence of conductivity additive size and shape** on the cathode performance. Moreover, it serves as a theoretical basis for establishing a link between the state of the conductivity additive, the resulting cathode microstructure and the half-cell performance. The fundamentals established in this chapter on the dependence of cathode performance on its microstructure as well as entailing electrochemical phenomenon are used throughout the course of this work.

4.1 Impact of Size

In order to study the influence of the conductivity additive size, idealized computational half-cell geometries were generated as explained in Section 3.1. These, comprise of two components namely, the active material and a combination of the conductivity additive and the binder referred to as the carbon binder domain (CBD), following Section 3.1.1. Both the components are modelled as smooth dense spheres with distinct diameters based

on the outer dimension of the respective particles found in contemporary literature. In case of the active material, the diameter of the modelled spherical particle was set to 10 µm, based on particle size distribution measurements for NMC 622 [118]. Furthermore, a similar order of magnitude can be found for lithium-ion battery active material particles modelled as spheres in contemporary numerical studies [119, 31]. However, for the fictitious particle CBD, such a direct estimation of the size cannot be made. Dreger et al. [40, 42] reported, that carbon black particles in cathode suspensions fall into two broad categories: aggregates, characterized by permanently bound primary particles in the range of 0.05-0.9 µm and agglomerates formed by weak attraction among aggregates in the range of 1-9 µm. Herein, primary particle refers to the smallest building unit of the aggregate, found to be ≈ 30 nm [96] in diameter. A further reference for the CBD size can be found in imaging analysis of the LIB cathodes as was discussed in Section 2.2.2, where it is clear that the binder and carbon black form agglomerates well in the range of few micrometers, specially in the case of conventional-wet mixing processes.

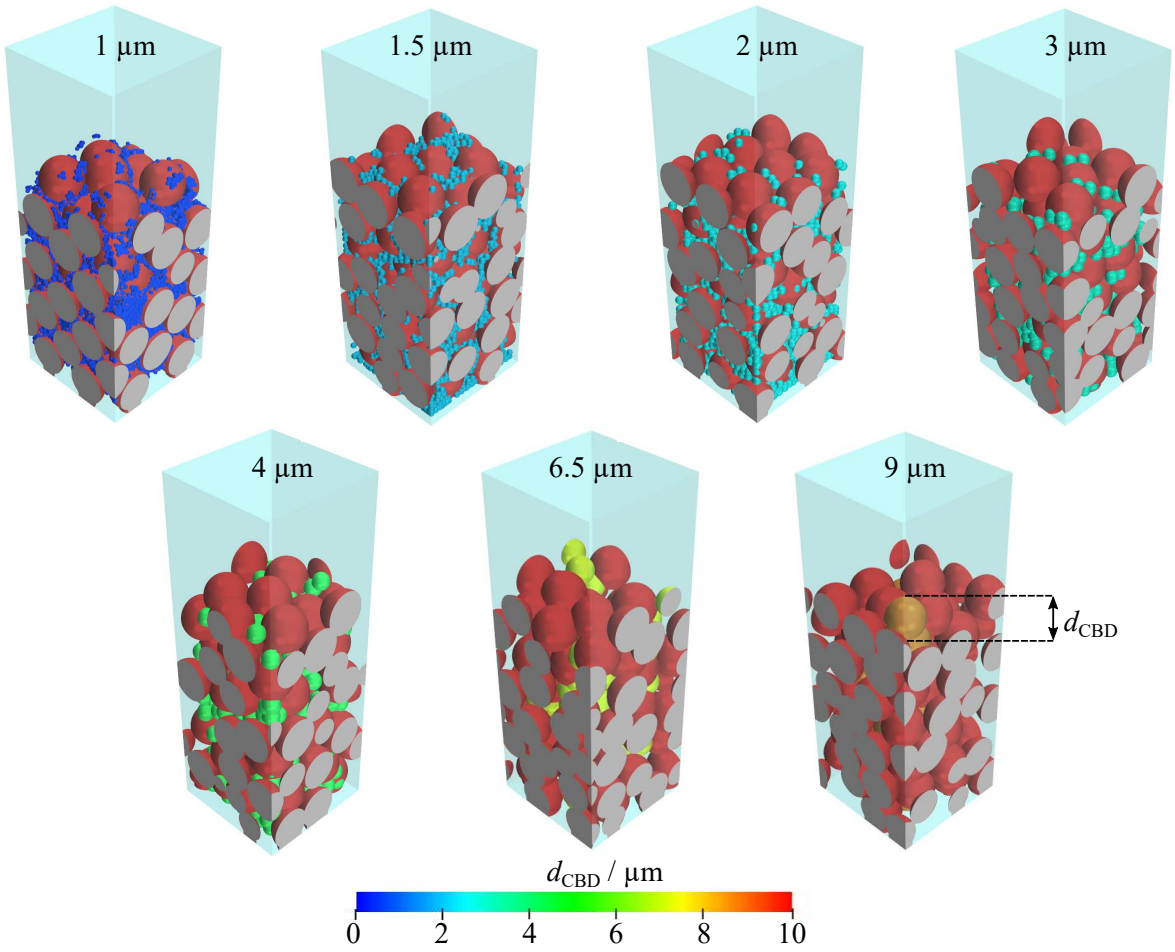

Figure 4.1: Idealized half-cell geometries of the CBD size variants with variation in CBD diameter d_{CBD}. The color-bar (bottom) highlights the systematic variation in size [120].

Thus, within the framework of this study, the diameter of the CBD particles d_{CBD} was varied in the range of the category of the agglomerates $1 \leq d_{\mathrm{CBD}} \leq 9\,\mu\mathrm{m}$, proposed by Dreger et al. [40]. It was further assumed that all the binder content in the cathode suspension was absorbed by the carbon black aggregates to form agglomerates on account of their high specific surface area. Hence, a state with no free aggregates and no excess binder in the suspension to interact with the active material was presumed, following the approach outlined by Bauer et al. [25]. The domain of the investigated variants with variation in the CBD diameter has been shown in Figure 4.1. The depicted computational domains arranged in the ascending order of the CBD diameter in the figure are constructed to the same mass ratio of the components 94:3:3 (active material:carbon black:binder) wt-% and the diameter of the active material is always held constant.
For the purpose of the DEM simulations the mass ratio was transformed into volumetric ratio via the method denoted in Appendix B and the sum of the volume fraction of carbon black and the binder were adopted as the volume fraction of the CBD. The volumetric composition of the variants attained after half-cell generation has been tabulated in Table 4.1. The roman numerals (I and II) in the table have been used to denominate the repetitions of randomized structure generation, carried out to rule out the influence of the variance caused by the initialization of the DEM simulations via the *seed number* as mentioned in Section 3.1.1. The height of the solid domain of the cathode Ω_{S} was fixed to 58 µm via uni-axial compression elaborated in Section 3.1.1, to achieve a half-cell porosity of $\approx$ 34 vol-%. The cross-section of the domain is restricted to 30×30 µm with periodic boundaries in the lateral direction as dictated by Section 3.1.

Table 4.1: Volumetric composition of the half-cell domains for the size study achieved by means of DEM simulations.

	Size I	Size II
Active Material / vol-%	57±0.7	57±0.8
CBD / vol-%	9±0.8	9±0.8
Porosity / vol-%	34±1.4	34±1

Characterization

A visual inspection of the size study variants from Figure 4.1, reveals an increase in the dispersion of the CBD with decreasing diameter. Since the mass of the CBD is constant in all the variants, a reduction in the size leads to increase in the number of its particles. Conversely, the active material particles remain same in number due to the unchanged diameter. The increment in the number of particles with reducing CBD diameter is specially steep toward the lower end of the investigated variants, such that

an increase from 1396 CBD particles at $d_{\mathrm{CBD}} = 2\,\mu\mathrm{m}$ to 11,166 particles at $d_{\mathrm{CBD}} = 1\,\mu\mathrm{m}$ is observed for the same volume fraction in the half-cell. Subsequently, owing to the homogeneous distribution of the CBD particles in the half-cell resulting from their randomized positioning in the DEM simulations as indicated in Section 3.1.1, an increased dispersion results. The implication of this change is reflected in the characteristics of the half-cell variants, as plotted in Figure 4.2. In the figure, the error bars represent the maximum and minimum value respectively, calculated for the half cell variant from structure generation repetitions (I and II). The solid line represents the trend in the characteristics by joining the average values over the entire domain of investigation. It is evident from the figure, that the variance in the characteristics due to the repetitions in structure generation is negligible in comparison to the trends observed with change in CBD diameter.

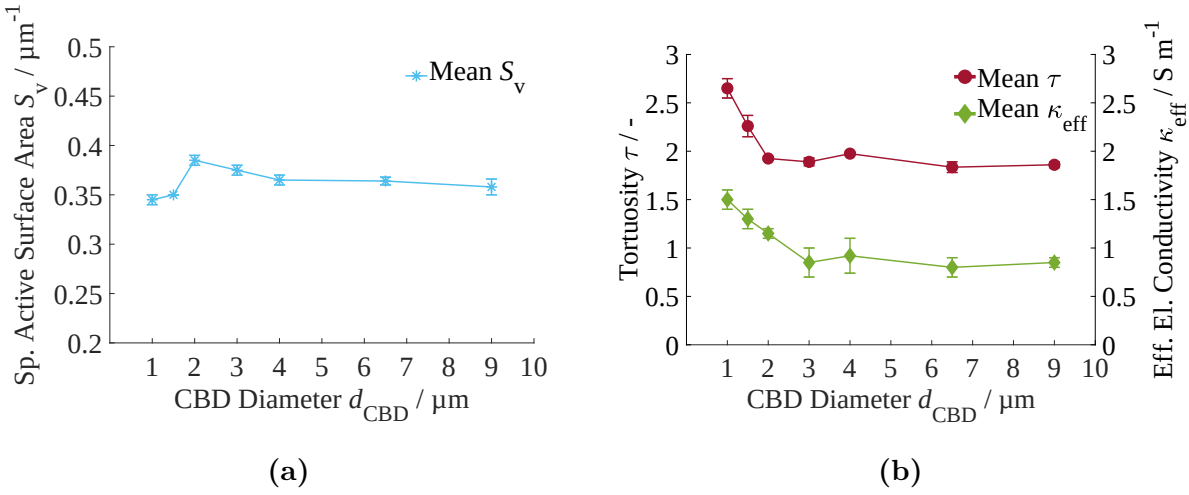

(a) **(b)**

Figure 4.2: Characterization of the CBD size variants [120]: (a) Available specific active surface area (b) Tortuosity (left axis) and effective electrical conductivity (right axis).

In Figure 4.2a, it can be observed that with decreasing CBD diameter, the available specific active surface area S_{V} gradually increases, till a maximum is reached at $d_{\mathrm{CBD}} = 2\,\mu\mathrm{m}$. Below this diameter however, a sharp decrease in the available surface area is observed, as the CBD diameter reduces further. An initial increase in the available surface despite the increasing dispersion of the CBD suggests, that the area of contact between individual CBD and active material particles decreases. Thus, in the direction of reducing CBD diameter, the sum of the active area blocked (see Section 3.2.3) by the CBD particles contacts with smaller diameter (despite being more in number) is less than that of the higher diameters, in the domain $d_{\mathrm{CBD}} \geq 2\,\mu\mathrm{m}$. Below this diameter however, the increased dispersion of the CBD outweighs the influence of the reduced diameter, such that an extensive coverage of the active surface takes place. This effect is especially visible through the diminished active surface shown in red, in Figure 4.1 for the variant $d_{\mathrm{CBD}} = 1\,\mu\mathrm{m}$.

In Figure 4.2b, the influence of CBD size on the conduction characteristics in the half-cell has been depicted. Complementary to the observations made in the case of S_V, the tortuosity τ plotted on the left hand axis of the figure, changes only marginally in the domain $2 \leq d_{CBD} \leq 9\,\mu m$. However for variants $d_{CBD} \leq 2\,\mu m$, a sharp increase in the number of particles and the resulting dispersion leads to a linear increase in the tortuosity with the CBD diameter. The increased dispersion on account of the numerous smaller CBD particles leads to infiltration of the pores of the half-cell, breaching the pore network necessary to transport lithium-ions, thereby deteriorating ionic conductivity. On the other hand, the value of effective electrical conductivity of the half-cell κ_{eff}, plotted on the right axis of the figure, is evaluated close to the intrinsic conductivity of the active material 1 S m^{-1} (see Table 3.3) in the domain $3 < d_{CBD} \leq 9\,\mu m$, but at $d_{CBD} = 3\,\mu m$, a percolation of the electrical contacts owing to the increased dispersion with decreasing CBD diameter, leads to a linear increase in the electrical conductivity as shown in the figure. The contrasting trends observed in the half-cell characteristics influencing the rate of fundamental oxidation-reduction reactions in LIBs underscore their interdependence. This relationship presents a recurring challenge in prioritizing one characteristic over the other, a dilemma that will be addressed throughout this work.

Performance Evaluation

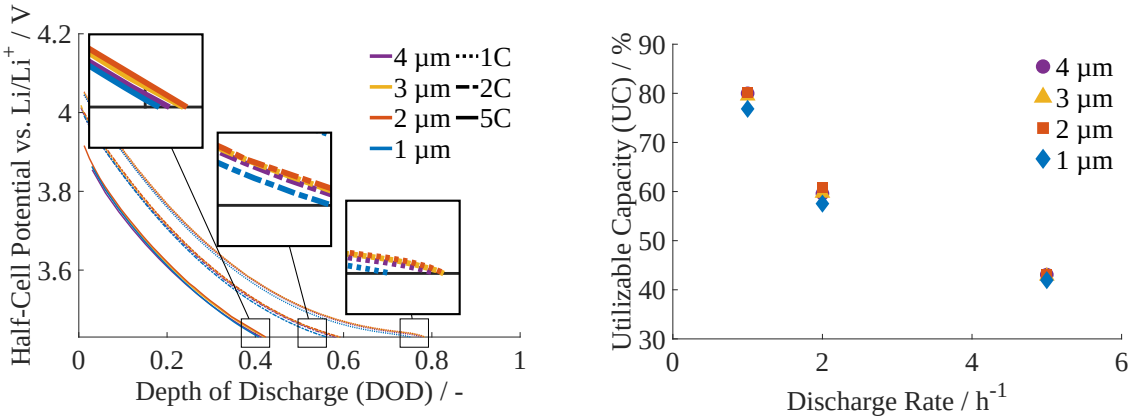

(a) **(b)**

Figure 4.3: Performance evaluation of the chosen CBD size variants [120]: (a) Half-cell potential w.r.t. lithium metal (b) Utilizable capacity as a percentage of maximum theoretical capacity.

Since significant changes in the half-cell characteristics were only observed in the domain $1 \leq d_{CBD} \leq 4\,\mu m$, variants within this domain were selected for performance evaluations. The results thereof have been summarized in Figure 4.3. In Figure 4.3a, the potential at the current-collector of the chosen half-cell variants has been displayed over the depth

of discharge (DOD), for a range of different C-rates: 1C, 2C and 5C. The C-rates were chosen to represent a wide range of LIB operational conditions highlighted in Section 2.1.2. Lower currents are closer to the state of equilibrium wherein no net current is assumed to flow through the current-collector (Section 2.1.2). Hence, they are associate with lower overpotentials and higher half-cell potential (see Equation 3.29). Thus, the half-cell potential recorded at the current-collector scales inversely with the C-rate, as can be seen from the latter figure. Further, it is apparent from the figure that the variant with $d_{\mathrm{CBD}} = 2\,\mu\mathrm{m}$ exhibits the highest half-cell potential across all C-rates, while the potential of the $d_{\mathrm{CBD}} = 1\,\mu\mathrm{m}$ always lies the lowest. No noticeable differences can be seen for the variants $d_{\mathrm{CBD}} = 3$ & $4\,\mu\mathrm{m}$ over the C-rate range, nonetheless their half-cell potential lies closer to the upper limit of the recorded potentials. The differences in potentials observed specially at the lowest C-rate (1C) are an outcome of the difference in the available active surface area of the variants. Owing to the maximum of S_{V} being achieved at $d_{\mathrm{CBD}} = 2\,\mu\mathrm{m}$, the intercalation current density of the variant at a given C-rate is the lowest. Therefore, it operates at the lowest overpotential and hence the highest half-cell potential following Equations 3.28 and 3.29.

At higher C-rates however, the differences in the half-cell potentials of the variants diminish proportional to the rising C-rate, as seen from the magnified regions of Figure 4.3a. The scaling of the differences in the half-cell potentials is quantified by means of the performance determinant, Utilizable Capacity (UC), in Figure 4.3b. The figure displays the achieved capacity of the chosen variants under changing C-rates, as a percentage of the maximum theoretical capacity of NMC 622 subjected to equilibrium conditions (see Section 3.3.3). Due to the drop in the half-cell potential with increment in C-rate as was discussed earlier, the evaluated UC for the lower currents is always closer to maximum achievable capacity (UC = 100 %), as evident from the figure. The data in the figure reveals that the evaluated UC of the chosen variants converges towards each other as the C-rate increases. The observed outcome can be attributed on the one hand to the rising importance of the effective electrical conductivity at higher C-rates, known to influence cathode performance [121], improving the relative performance of the $d_{\mathrm{CBD}} = 1\,\mu\mathrm{m}$ variant and on the other hand to the tendency of LIB cathodes to operate at a diffusion limited state at higher C-rates [122], such that limitations on lithium-ion diffusion restrict the capacity of all the variants.

In the course of the performance evaluations, an analysis of the resolved lithium concentration distribution in the cathode and electrolyte regions, reveals insights into the transport mechanisms of the reactants involved in the redox reactions of the half-cell. These transport mechanisms determine the spatial distribution of lithium in the half-cell. Since they are usually more pronounced at higher C-rates, the end stages of discharge at 5C have been displayed in Figure 4.4, in an exemplary manner. In the figure, the concentration

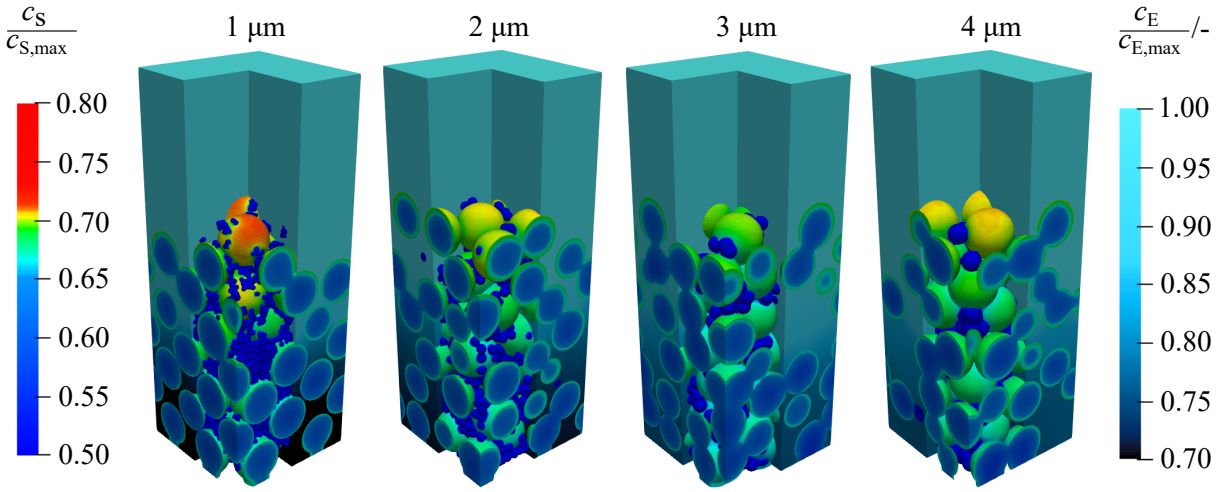

Figure 4.4: Relative lithium concentration distribution in the cathode (left color-bar) and electrolyte domain (right color-bar) of the selected CBD size variants after 310 s of galvanostatic discharge at 5C [120].

distribution in the regions of the half-cell is represented by means of separate color-bars displayed on the left and right hand side of the figure, respectively. Furthermore, the electrolyte region has been split open at the midpoint of the width of the half-cell, to reveal the cathode. It is discernible from the figure that electrolyte concentration of the variant with $d_{\mathrm{CBD}} = 1\,\mu\mathrm{m}$ has depleted up to $\approx 30\%$ close to the current-collector by the end of 5C discharge, as shown by the black colored region in the figure, where the lithium concentration has dropped to $\approx 70\%$ of the initial concentration in the electrolyte. The cause of this depletion is the high tortuosity of the variant. Since the porosity of all the investigated variants is the same, high tortuosity of the variant indicates poor ionic conduction (see Section 3.2.2). Thus, specially at the higher C-rate, the lithium in the pores of this half-cell variant close to the current-collector is consumed faster than it can be replenished by the anodic source, leading to its depletion.

Consequently, a preferential intercalation of lithium-ions at the top of the surface of the cathode takes place, close to the anodic source as show in the latter figure, as the movement of lithium-ions through the electrolyte is heavily restricted. Thus a gradient of intercalated lithium concentration develops, increasing in the direction of the anodic source. As the tortuosity of the half-cell decreases with increasing diameter of the CBD, both the stated phenomenon are mitigated such that depleted region becomes smaller in size and a homogeneous distribution of lithium across the height of the cathode is observed, as shown for the variants $d_{\mathrm{CBD}} \geq 2$.

4.2 Impact of Fractal Dimension

Cathode slurries associated with conventional-wet process are usually regarded as colloidal suspensions [31, 123]. Particles (aggregates/agglomerates) in such systems are often described based on a mass scaling proposed by Forrest & Witten [124] in the form of the power law:

$$n_{\mathrm{p}} = k_{\mathrm{f}} \left(\frac{d_{\mathrm{g}}}{d_{\mathrm{p}}} \right)^{\mathrm{d_f}} , \tag{4.1}$$

wherein n_{p} represents the number of primary particles, i.e. smallest building block that comprise the particulate structure and d_{p} refers to the diameter of these primary particles. The gyration diameter d_{g}, in Equation 4.1 is a measure of size of the structure, defined with the help the geometrical relation:

$$d_{\mathrm{g}} = \sqrt{\frac{2}{n_{\mathrm{p}}^2} \sum_{i,j=1}^{\mathrm{n_p}} (p_i - p_j)^2} , \tag{4.2}$$

such that p_i and p_j represent the positions of the ith and jth primary particle centers. Half the value of d_{g} for a fractal structure, signifies the radial distance from an axis of rotation where the moment of inertia would be equivalent to that of the entire structure, assuming the entire mass of the structure were concentrated at that specific point. Finally, the fractal dimension d_{f} in Equation 4.1, varies from 1 (linear structure) to 3 (spherical structure), controlling the arrangement of the primary particles, while k_{f} is the factor of proportionality, known to be a function of fractal dimension itself [125]. To facilitate clarity in this study, the factor k_{f} was held constant.

In addition to the colloidal nature of cathode suspensions, aggregates of common conductivity additive: carbon black, have been known to posses a fractal structure, through characterization by means of light scattering [126]. Moreover, studies on the variation in the fractal dimension of carbon black aggregates in flame synthesis [34] as well as in colloidal suspensions [127], indicate the potential of tailoring their structure through process control. However, it remains to be seen if a distinctive dependence of the cathode characteristics can be established on the fractal dimension of the conductivity additive and binder composites, as is widely known for polymers with fillers [128].

The following study on the impact of fractal dimension on cathode performance, has been split into two sub-studies. At first, the influence of fractal dimension was investigated together with the effect of uni-axial compression (Section 3.1.1), similar to the size study. Based on the outcome of the compressed variants however, it was decided to expand the domain of the investigation and withdraw the effect of compression in the second sub-study to establish a direct link between the fractal dimension and the half-cell characteristics.

4.2.1 Compressed Variants

For the purpose of exploring the influence of the fractal dimension of conductivity additives on the half-cell performance, idealized computational half-cell geometries comprising active material and CBD were generated by the method explained in Section 3.1. Similar to the size study, size and shape of the active material was held constant for all the variants, to a smooth sphere of 10 µm diameter. However, unlike the size study where CBD agglomerates were modelled as a single smooth sphere, the concept of multi-spheres was used in the following sub-studies, wherein the shape of CBD agglomerates was approximated with the help of partially overlapping and permanently connected spheres [90]. Consequently, each agglomerate posses a distinct shape governed by the primary particles n_p, their diameter d_p, the gyration diameter d_g and the fractal dimension d_f interlinked by Equation 4.1.

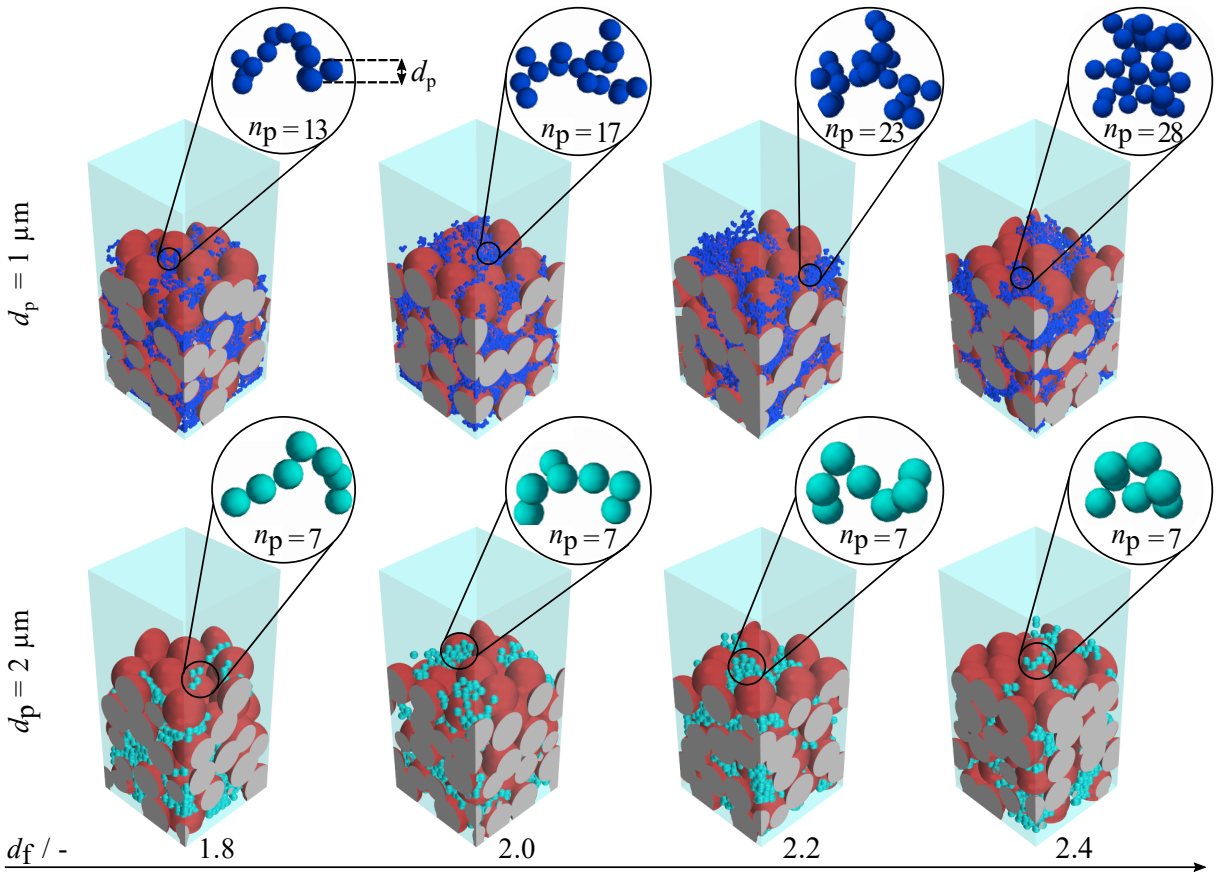

Figure 4.5: Idealized half-cell geometries of the CBD fractal dimension variants with variation in fractal dimension d_f and primary particle diameter d_p at constant diameter of gyration d_g = 4 µm [120].

The generation of the fractal structures was carried out by Mr. Ermek Asylbekov, M.Sc. at the Institute of Mechanical Process Engineering and Mechanics, Karlsruhe Institute of Technology, using a self developed algorithm following the Tunable Dimension Method

(TDM) [35], which allows for the generation of structures with a predefined fractal dimension using a combination of spheres [55]. Subsequently, the fractal structures were incorporated in the DEM simulations intended for the generation of half-cell geometries. The resulting domain of half-cells at constant size i.e., $d_g = 4\,\mu m$ and variation in d_f and d_p generated for the investigations on fractal dimension including the influence of uni-axial compression have been depicted in Figure 4.5.
The recipe of the half-cell variants was adopted from the size study such that the mass of the components follows the ratio 94:3:3 (active material:carbon black:binder) and the volume fractions of the constituent was calculated using Appendix B. The height of the solid domain was held at 40 µm such that the resulting porosity amounted to ≈ 34 vol-% and the cross-section of 30×30 µm was inherited from the size study. The obtained volume fraction of the components of the half-cell after the DEM simulations has been tabulated in Table 4.2. Similar to the size study the roman numerals I and II represent the repetitions in randomized structure generation for the variants.

Table 4.2: Volumetric composition of the half-cell domains for the fractal dimension sub-study involving uni-axial compression, achieved by means of DEM simulations.

	Fractal Dimension I ($d_p = 1\,\mu m$)	Fractal Dimension II ($d_p = 1\,\mu m$)	Fractal Dimension I ($d_p = 2\,\mu m$)	Fractal Dimension II ($d_p = 2\,\mu m$)
Active Material / vol-%	58±0.4	58±0.1	57±1.0	58
CBD / vol-%	9±0.4	9	8±0.2	8±0.1
Porosity / vol-%	33±0.6	33±0.9	35±1	34±0.2

Characterization

Upon close examination of the variants shown in the first row of Figure 4.5, it is apparent that for variants with $d_p = 1\,\mu m$, an increase in the fractal dimension leads to increase in the concentration of mass in an individual agglomerate, evident from the increase in n_p. Since the total mass of CBD is same in all the variants fixed by the chosen recipe, it can be inferred that the degree of dispersion of the CBD is lower for variants with higher fractal dimension, as with increasing n_p, the number of such agglomerates in the half cell decreases for the same gyration diameter. In contrast, for variants with $d_p = 2\,\mu m$, shown in the second row of Figure 4.5, the mass of the CBD is concentrated in the primary particles leading to no change in n_p and dispersion over the entire range of fractal dimension as shown in the figure.

The influence of this scaling of mass of the CBD agglomerates on the characteristics of the half-cell variants has been illustrated in Figure 4.6. Here, Figures 4.6a and 4.6b correspond to the variants in the first row of Figure 4.5, with $d_p = 1$ µm. The invariance of the specific active surface area in Figure 4.6a with changing fractal dimension, indicates that the increase in the dispersion associated with increment in the fractal dimension is not as high as the increased dispersion associated with reduction in CBD agglomerate diameter (see Figure 4.2a). Furthermore, changes in tortuosity plotted on the left axis and effective electrical conductivity denoted on right axis in Figure 4.6b are only discernible upon a magnification of the scale of the respective characteristics in comparison to Figure 4.2b. Nonetheless, the conductivity phenomena follow contrasting trends, as discussed in the size study, such that an increase in dispersion leads to blockage of the half-cell pores increasing tortuosity and hence reducing ionic conductivity while simultaneously increasing the contacts between the components of the cathode leading to an increment in the effective electrical conductivity.

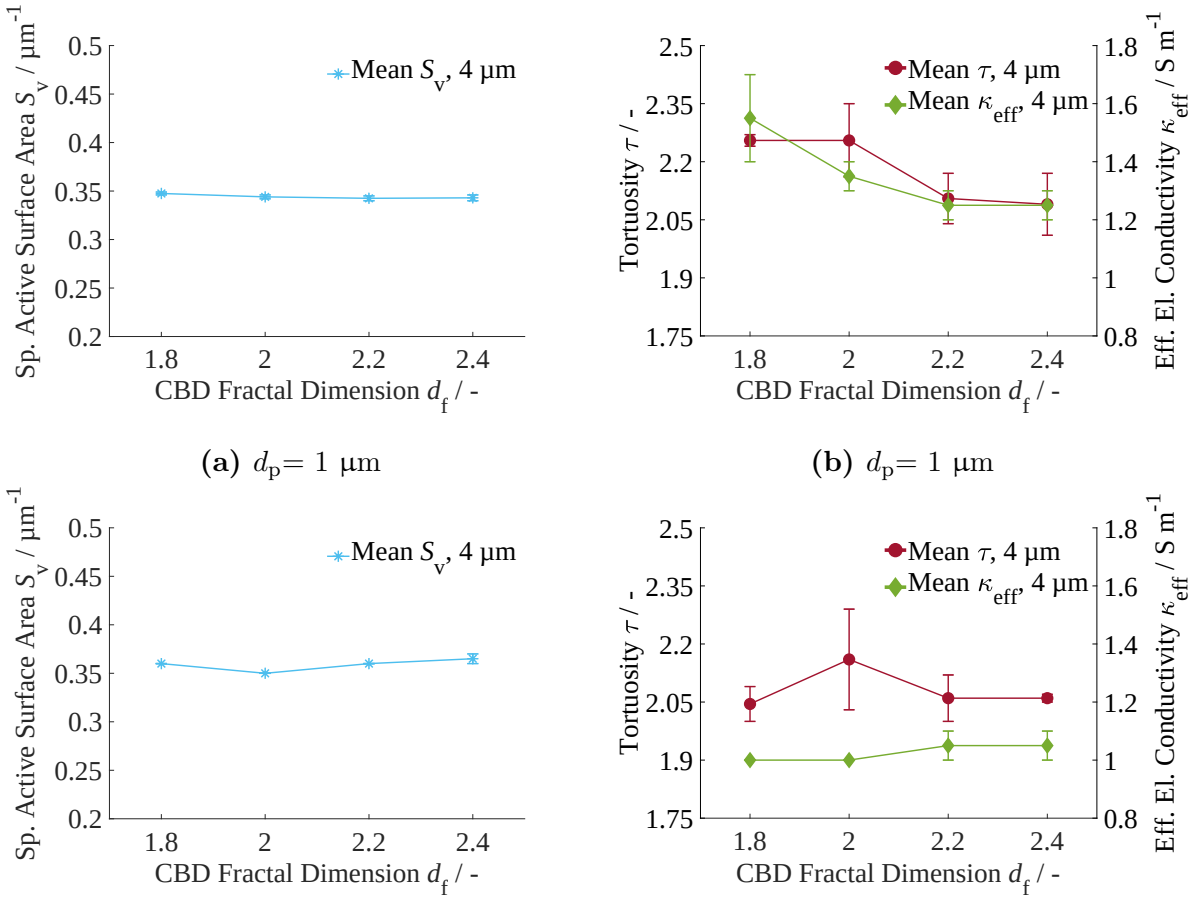

(a) d_p= 1 µm **(b)** d_p= 1 µm

(c) d_p= 2 µm **(d)** d_p= 2 µm

Figure 4.6: Characterization of the CBD fractal dimension variants including the influence of uni-axial compression [120].

Figures 4.6c and 4.6d correspond to variants in the second row of Figure 4.5, with $d_p = 2\,\mu m$. While the available specific active surface area remains constant for the variants as conveyed by Figure 4.6c, a slight increment as compared to the $d_p = 1\,\mu m$ variants can be seen, such that for all the variants, $S_V \geq 0.35\,\mu m^{-1}$ (compare 4.6a). This could be attributed to the concentration of CBD mass in the primary particles of the agglomerates, such that with increased diameter the number of agglomerates of CBD in the half-cell decrease at same fractal dimension, leading to decreased occupation of the active surface via CBD. This in turn is in accordance with the observations made in the size study, wherein an increase in the CBD agglomerate diameter was associated with reduced dispersion and higher S_V in the range $1 \leq d_{CBD} \leq 2\,\mu m$. A lack of increase in dispersion with increasing d_f for the variants is also visible from Figure 4.6d, where no influence on the conduction characteristics is identifiable. Concurrent with the variation of S_V with d_p, the recorded tortuosity and effective electrical conductivity of the variants, is in turn lower than that of $d_p = 1\,\mu m$ variants, as can be deduced by comparison with Figure 4.6b.

Performance Evaluation

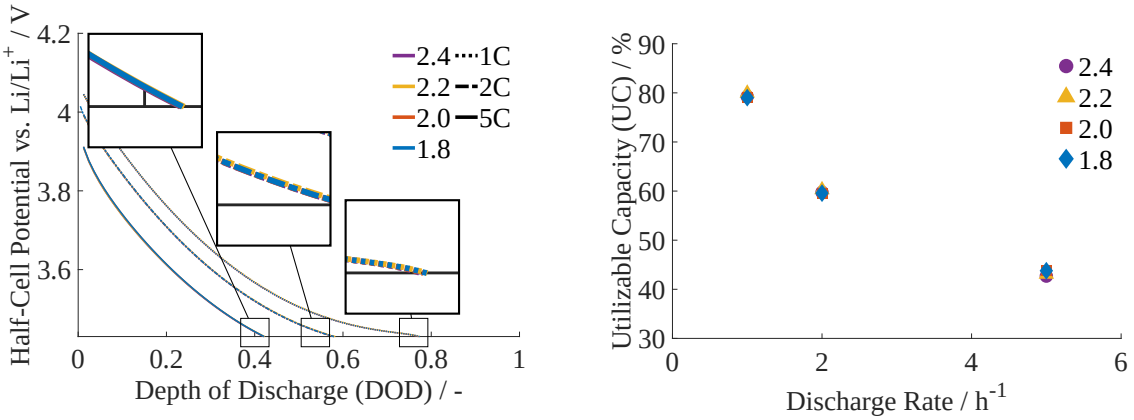

Figure 4.7: Performance evaluation of the chosen CBD fractal dimension variants [120]: (a) Half-cell potential w.r.t. lithium metal (b) Utilizable capacity as a percentage of maximum theoretical capacity.

Based on the characterization results, only the variants with $d_p = 1\,\mu m$, wherein the impact of the fractal dimension was noticeable, were subjected to performance evaluations. The results of the evaluations exhibited in Figure 4.7, however suggest that the structural changes caused by the changing fractal dimension were unable to influence performance of the half-cell. It is thus hypothesized that owing to the compression of the variants to achieved the common porosity, the changes in the structural properties were subjugated.

Subsequently, in the following sub-study (Section 4.2.2) the investigated domain of fractal dimension was expanded along with variation in the gyration diameter, to account for a wider range of CBD agglomerate shapes and the compression step was excluded from the computational half-cell generation.

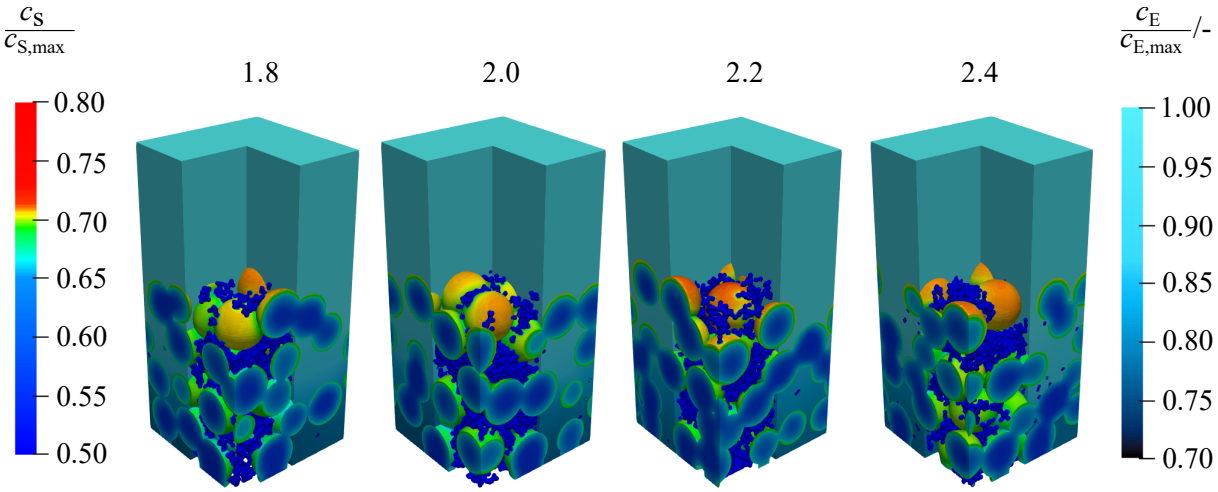

Figure 4.8: Relative lithium concentration distribution in the cathode (left color-bar) and electrolyte (right color-bar) domain of the selected CBD fractal dimension variants (compressed) after 310 s of galvanostatic discharge at 5C [120].

Nonetheless, in Figure 4.7a and 4.7b, the reduction in the half-cell potential as well as the performance property UC, with increased C-rate due to the rising overpotential in the half-cell (similar to Figure 4.3) is evident. In addition, a detailed look into the transport phenomena in the half-cell variants via analysis of the lithium concentration in the half-cell regions in Figure 4.8, reveals no depletion of the electrolyte, in contrast to what was observed for $d_{CBD} = 1\,\mu m$ variant in the size study. Thus it can be inferred, that diffusion limited state has not been reached for these variants, even at the highest C-rate (5C). Considering the fact that the fractal dimension variants are smaller than the size variants, it can be concluded that height of the half-cell variants regulates the diffusion length of lithium-ions in the half-cell (from their origin at the anodic surface to the opposite end at the current-collector) thereby impacting the onset of the diffusion limited state. Conversely, all the compressed fractal dimension variants exhibit a preferential deposition of lithium closed to the anodic surface, owing to the higher tortuosity of the variants in comparison to size variant possessing uniform lithium distribution. Comparing Figure 4.6b and 4.2b, it is evident that for $d_{CBD} \geq 2\,\mu m$, $\tau < 2$, while all the fractal dimension variants with $d_p = 1\,\mu m$, exhibit $\tau > 2$.

4.2.2 Uncompressed Variants

An expansion of the investigated domain of the variants to $1.4 \leq d_f \leq 2.8$, in this sub-study, is intended at achieving pronounced changes in the cathode microstructure through variation in the CBD, absent in the previous sub-study. Furthermore, an analysis of the uncompressed state of these variants will be used to establish a direct correlation of the shape as well as mass dispersion of the CBD to the performance of half-cells in the following sections. The investigated domain of the uncompressed variants with $d_g = 4\,\mu m$ has been displayed in Figure 4.9. For the sake of brevity, the final half-cell domains resulting by using the shown variants as multi-spheres in the idealized half-cell geometry generation process (see Section 3.1), have not be explicitly shown in the figure.

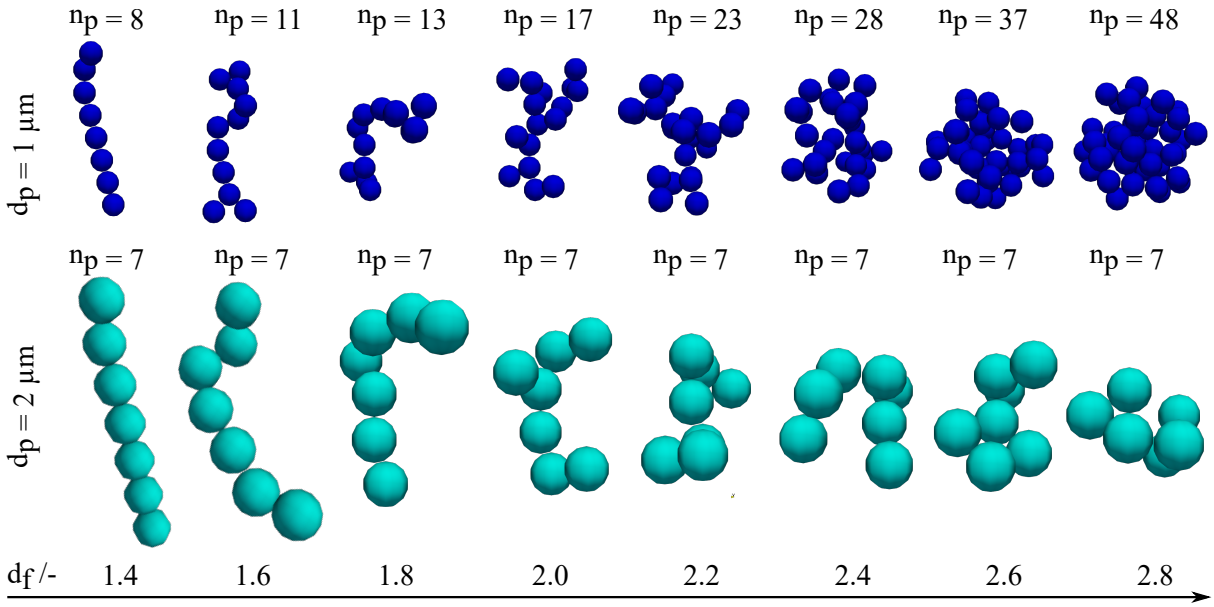

Figure 4.9: CBD fractal dimension multi-spheres with variation in fractal dimension d_f and primary particle size d_p, at constant diameter of gyration $d_g = 4$ µm.

In Figure 4.9, the top row corresponds to $d_p = 1\,\mu m$ and the bottom row to $d_p = 2\,\mu m$. It is clear from the top row of the figure that as the value of d_f approaches 1 the agglomerates of CBD posses lesser primary particles (n_p) at constant d_g (see Equation 4.1) and exhibit a near linear configuration, while close to 3 an almost spherical configuration is achieved due to the concentration of mass around the axis of rotation of the agglomerate. Hence, these variants significantly expand the scope of investigations in this sub-study (compare Figure 4.5). Conversely, owing to the concentration of mass in the primary particle with its increased diameter, a change in the number of primary particles (Equation 4.1), is still not achieved for the agglomerates of CBD with $d_p = 2\,\mu m$, even after the extension of the investigated domain (compare Figure 4.5). Nonetheless, a significant change in the arrangement of the particles is visible also in the second row.

Table 4.3: Volumetric composition of the half-cell domains for the fractal dimension sub-study without uni-axial compression at $d_g = 4\,\mu m$, achieved my means of DEM simulations.

	Fractal Dimension I ($d_p = 1\,\mu m$)	Fractal Dimension II ($d_p = 1\,\mu m$)	Fractal Dimension I ($d_p = 2\,\mu m$)	Fractal Dimension II ($d_p = 2\,\mu m$)
Active Material / vol-%	58±0.02	58±0.02	58±0.02	58±0.02
CBD / vol-%	9±0.005	9±0.005	9±0.005	9±0.005

The calculated volume fractions of the half-cell components at $d_g = 4\,\mu m$ has been tabulated in Table 4.3. Like the previous investigations, the change in volume fraction with structure generation repetitions I and II are minimal. Moreover, the exclusion of the compression step leads to a further reduction in the variance by reduction in agglomerate overlaps (compared Table 4.2).

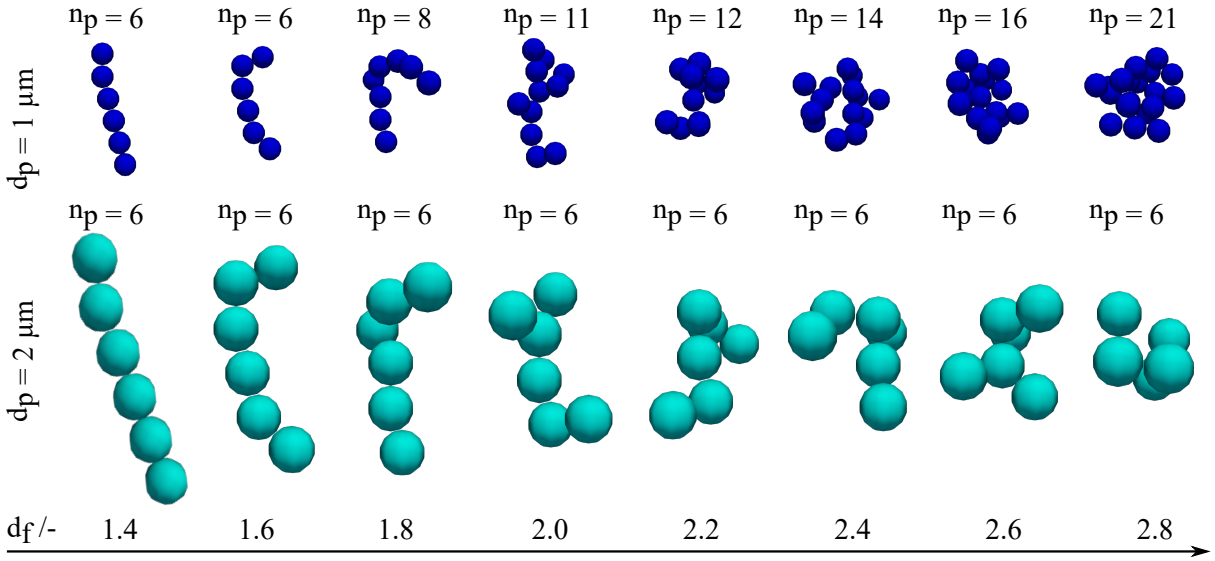

Figure 4.10: CBD fractal dimension multi-spheres with variation in fractal dimension d_f and primary particle size d_p at constant diameter of gyration $d_g = 3\ \mu m$.

With a motive of further increasing the dispersion in the half-cell, the gyration diameter d_g of the CBD was reduced to 3 µm. As a consequence, n_p of the CBD multi-spheres decreases following Equation 4.1. This, in turn, implies the redistribution of CBD mass away from an individual multi-sphere, resulting in greater dispersion of the CBD throughout the half-cell. The multi-spheres hence generated have been sorted in two rows in increasing order of primary particle diameter in Figure 4.10. On comparison of the latter with Figure 4.9, it is observed that with reduction in d_g, n_p reduces at the same d_f, leading to an increase in the number of agglomerates of CBD in the half-cell and hence increased dispersion. This increased dispersion in the half-cell with reduction in size via the gyration diameter however, comes at the cost of reduced concentration of mass about the axis of

rotation of the agglomerates, such that the variance in n_p with variation in d_f is lesser in comparison to the $d_g = 4\,\mu m$ variants. The effect is even more pronounced at the higher d_p, such that the primary particle number remains unchanged for the $d_g = 3\,\mu m$, despite the extended d_f domain (also observed in the second row of Figure 4.9). Nevertheless, the arrangement of the primary particles is noticeably effected by the fractal dimension, as was the case for the higher gyration radius (4 µm).

Table 4.4: Volumetric composition of the half-cell domains for the fractal dimension sub-study without uni-axial compression at $d_g = 3\,\mu m$, achieved my means of DEM simulations.

	Fractal Dimension I ($d_p = 1\,\mu m$)	Fractal Dimension II ($d_p = 1\,\mu m$)	Fractal Dimension I ($d_p = 2\,\mu m$)	Fractal Dimension II ($d_p = 2\,\mu m$)
Active Material / vol-%	58±0.02	58±0.02	58±0.02	58±0.02
CBD / vol-%	9±0.005	9±0.005	9±0.005	9±0.005

Similar to the previous studies, the variance in the particulate structures with repetitions in the generation process have been documented in Table 4.4. Considering the consistently minimal variations in repetitive structure generation, it's reasonable to infer at this point, that the stochastic variations have a limited impact on the microstructural outcome.

Characterization

Quantification of the influence of the multi-sphere variants discussed in the previous sub-section on cathode characteristics has been denoted in Figure 4.11. Herein, the structural characteristics i.e. volume specific active surface area (left axis) and porosity (right axis) of the half-cell have been shown in a single diagram, while the characteristics concerning the conduction phenomenon have been clubbed together in a single representation such that tortuosity is depicted on the left axis and effective electrical conductivity on the right. The first row of the figure containing Figures 4.11a and 4.11b represents influence of the CBD agglomerates shown in the top row of the Figures 4.9 and 4.10 with $d_p = 1\,\mu m$. While the bottom row, containing Figures 4.6c and 4.11d corresponds to the agglomerates of CBD show in the bottom row of the figures showing the CBD agglomerate variants in the previous section with $d_p = 2\,\mu m$.

Impact of Gyration Diameter

Inspection of Figures 4.11a and 4.11b reveals insights into the impact of the variation in size of the CBD agglomerates via the gyration diameter. As previously discussed, a decrease in d_g at constant fractal dimension leads to increased dispersion of the CBD agglomerates in the half-cell due to reduced n_p, but these variants exhibit lesser change

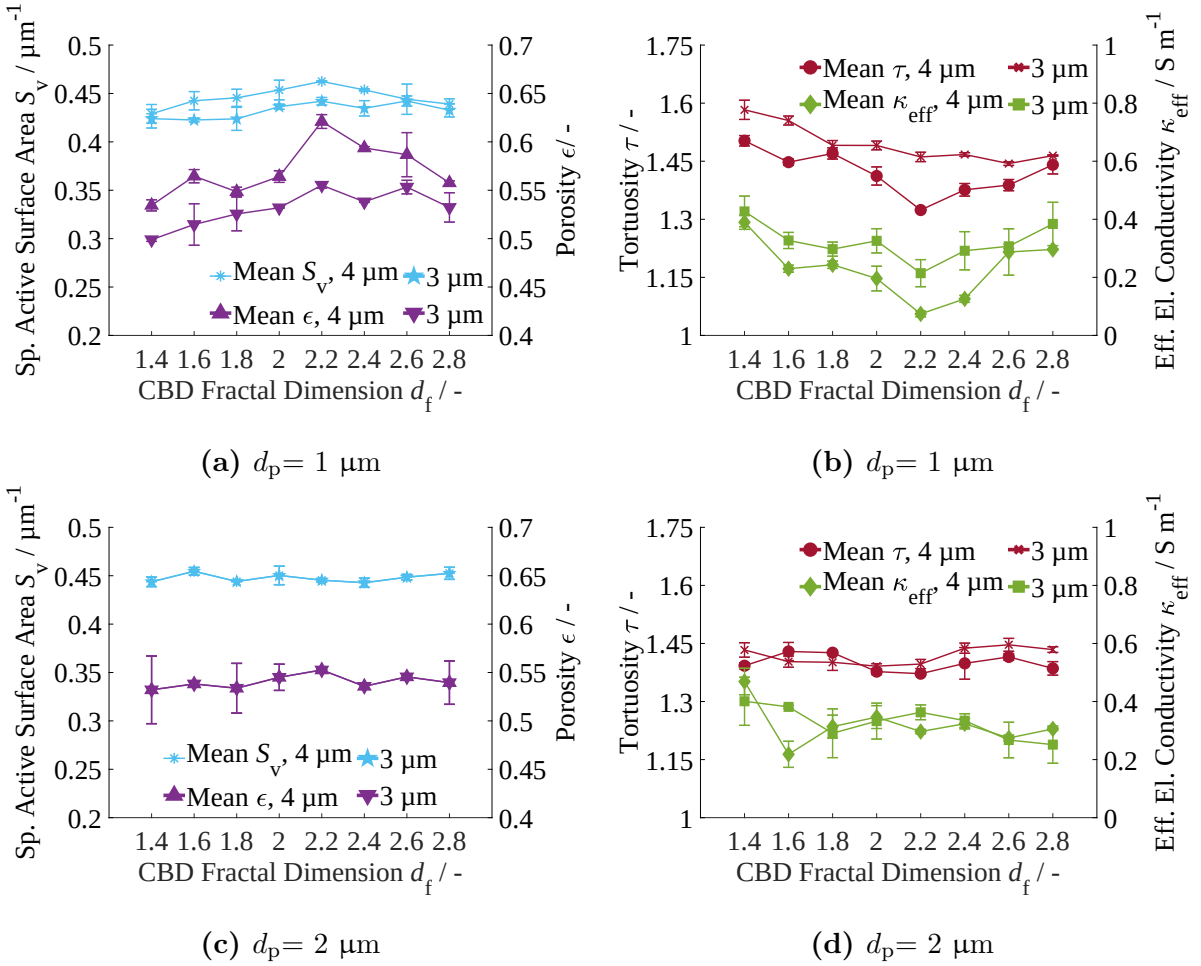

(a) d_p= 1 µm **(b)** d_p= 1 µm

(c) d_p= 2 µm **(d)** d_p= 2 µm

Figure 4.11: Characterization of the CBD fractal dimension variants without the influence of uni-axial compression, performed by Mr. Salvatore Vella, M.Sc.: (a) Structural Characteristics at $d_p = 1\,\mu m$ (b) Conduction Characteristics at $d_p = 1\,\mu m$ (c) Structural Characteristics at $d_p = 2\,\mu m$ (d) Conduction Characteristics at $d_p = 2\,\mu m$

with variation in d_f, apparent from the comparison of the top rows of the Figures 4.10 and 4.9. As a consequence, the specific active surface area as well as the porosity of the variants recorded for the variants with $d_g = 3\,\mu m$ is lesser than the $d_g = 4\,\mu m$ variants, shown in figure 4.11a. Moreover, the characteristics remain fairly constant over the entire d_f, due to the lack of significant difference caused by d_f to the CBD agglomerates at $d_g = 3\,\mu m$. Concurrently, higher dispersion of the $d_g = 3\,\mu m$, leads to higher tortuosity and effective electrical conductivity for these variants at constant d_f, as plotted in Figure 4.11b, such that the curves representing the trend in characteristics for the latter lie above the higher gyration diameter curves in Figure 4.11b, for the entire d_f domain.

Impact of Fractal Dimension

The influence of fractal dimension is most apparent for CBD agglomerates constructed under the conditions, $d_g = 4\,\mu m$ and $d_p = 1\,\mu m$, see Figure 4.11a and 4.11b. The data from characterization simulations carried out for these conditions, illustrates an increase in the available active surface area as well as decrease in tortuosity and effective electrical conductivity, with decreased dispersion of the CBD, caused by increasing n_p in the domain $1.4 \leq d_f \leq 2.2$, till a maximum of specific active surface area in Figure 4.11a and minimum of the conduction characteristics in Figure 4.11b, is reached respectively at $d_f = 2.2$. Such a change in microstructural properties with reduced dispersion of the CBD, was linked in all the previous investigations, to the declining interaction of the CBD with the active material as the dispersion in the half-cell reduced. However, it falls short of explaining the trends seen in the characteristics in the range $2.2 < d_f \leq 2.8$.
As is discernible from Figures 4.11a and 4.11b, at $d_g = 4\,\mu m$ and $d_p = 1\,\mu m$, S_V decreases and κ_{eff} and τ increase in the said domain, despite the reduced dispersion. Thus it can be inferred, that even at low levels of dispersion, sufficient CBD-active material interaction is achievable with higher fractal dimension of the CBD agglomerates, evident specially from the increase in the effective electrical conductivity and decrease in the available specific active surface area, in this range. The observations confirm the hypothesis suggested by Bauer et al. [25], that a less dispersed state of carbon black and binder combination in a fractal morphology could prove to be beneficial with regard to microstructural properties. The increased effective conductivity in this domain could also be linked to the connections formed within CBD agglomerates, with the increase in the concentration of mass about the axis of their rotation. Such connections were identified by Wenzel et al. as secondary pathways (see Section 3.2.1). They argued, that these pathways co-exist with the primary pathways established through CBD-active material interactions, essential for the conduction of electrons in the half-cell [75].
Subsequently, the increased interaction in the half-cell, be it through primary or secondary connections leads to an increase in the tortuosity as seen in Figure 4.11b. In the range $2.2 < d_f \leq 2.8$, the increasing secondary constants breach the pore network hampering ionic conduction. While in the range $1.4 \leq d_f \leq 2.2$, the increased primary contacts obstruct the movement of lithium-ions.
Finally, the influence of fractal dimension on porosity also becomes apparent form Figure 4.11a. The porosity is seen to increase most evidently for the variant with $d_g = 4\,\mu m$ till $d_f = 2.2$, where a maximum is reached coincident with the decrease in tortuosity and effective electrical conductivity. In the domain $1.4 \leq d_f \leq 2.2$, the increased porosity is due to the decreased dispersion and the elongated shape of the particles. Beyond $d_f = 2.2$ however, the reduced dispersion of the CBD is countered by the compactness of the agglomerates with higher d_f, such that a decrease in porosity is evidenced again.

Impact of Primary Particle Diameter

An increase in the primary particle diameter leads to concentration of the CBD mass in the primary particles. This in turn suppresses the changes in the agglomerates caused by the fractal dimension and the gyration diameter. As is evident from the bottom rows of Figures 4.9 and 4.10, n_p remains unchanged with variance in d_f and the CBD agglomerates grow only by a single particle as d_g is raised from 3 to 4 µm. As a consequence, no significant change in the characteristics is observed in Figures 4.11c and 4.11d. Nonetheless, a comparison Figures 4.11a and 4.11c reveals the influence of reduced dispersion due to increased d_p, such that a higher S_V is observed over the entire investigated domain of d_f, for the $d_p = 2\,\mu m$ variants.

Performance Evaluation

The trends in characteristics of the half-cell variants can be suitably represented by the variants $d_f = 1.4, 2.2$ and 2.8. Moreover, as was discussed in the previous section, these trends are the most pronounced at the higher gyration diameter (4 µm). Hence, the evaluations made in this section are restricted only to the three mentioned variants. The half-cell potential and the utilizable capacity of the half-cell variants derived from these evaluations have been depicted in Figure 4.12.

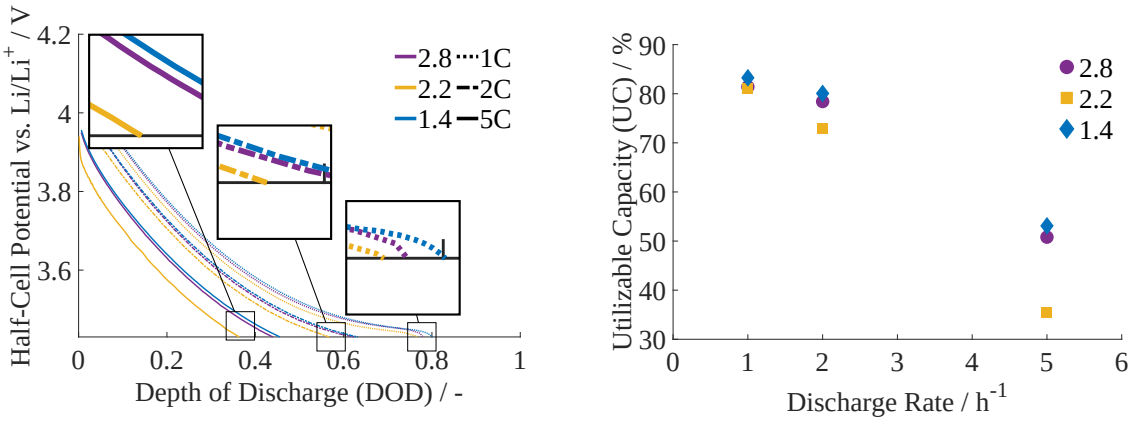

(a) **(b)**

Figure 4.12: Performance evaluation of the chosen CBD fractal dimension variants without the influence of compression: (a) Half-cell potential w.r.t. lithium metal (b) Utilizable capacity as a percentage of maximum theoretical capacity.

From Figure 4.12a it evident that the variant $d_f = 2.2$ exhibits the lowest half-cell voltage over all the C-rates. While the variants $d_f = 1.4$ and 2.8 display similar half-cell potentials, lying above the $d_f = 2.2$ variant irrespective of the C-rate. The low effective electrical conductivity of the $d_f = 2.2$ variants as shown in 4.11a, specially at $d_g = 4\,\mu m$ leads to

higher ohmic losses in the variant. Since the drop in potential occurs in the direction of the current (opposite to the direction of the flow of electrons) the potential achieved at the cathode current-collector is reduced. Subsequently, since the $d_f = 1.4$ and 2.8 variants posses equivalent effective electrical conductivity higher than $d_f = 2.2$ variant, the ohmic losses experienced by them are similar and lower than the $d_f = 2.2$ variant.
Since the ohmic losses scale with current applied at the current-collector, following the Ohm's law, the half-cell potential curves of the variants drift apart as the C-rate increases, as seen in the Figure 4.12a. This effect is quantified in Figure 4.12b, by means of the utilizable capacity, as the UC scales with the half-cell potential reached at the cut-off voltage. As is apparent from the latter figure, the UC of the $d_f = 2.2$ variant drifts away from the variants $d_f = 1.4$ and 2.8 proportional to the differences in half-cell potential, as the C-rate increases. This emphasizes the critical role of effective electrical conductivity at higher C-rates, which is delved into further in the following investigations of this work, especially in context of high-current applications.

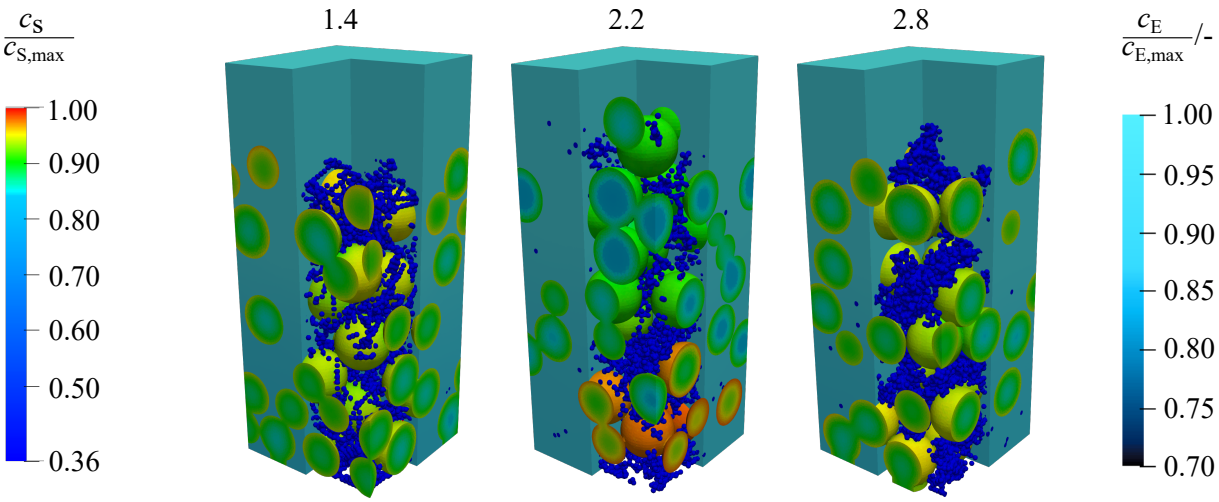

Figure 4.13: Relative lithium concentration distribution in the cathode (left color-bar) and electrolyte domain (right color-bar) of the selected uncompressed CBD fractal dimension variants after 600s of galvanostatic discharge at 5C.

The consequence of the higher ohmic losses and lower half-cell potential for the $d_f = 2.2$ variant on the lithium concentration distribution in the half-cell become apparent from the analysis of Figure 4.13. Due to the reduction in the potential close to the current-collector, the overpotential in this region increases. Increased overpotential on the other hand, leads to an increase in the intercalation current density (see Equation 3.28). Subsequently, as seen in the figure, the region close to the current-collector for the said variant (closest to the source of electrons) exhibits much higher lithium concentration than rest of the cathode. A similar effect is absent in the remaining variants owing to a comparatively uniform distribution of potential and hence intercalation current density.

In the size study as well as the compressed variant sub-study, performance evaluation was restricted to the sole performance property, utilizable capacity. Since, the mass fractions, half-cell volume and porosity of the variants in these studies was the same, an analysis of the UC was sufficient, as the maximum theoretical capacity in each of these cases remained constant over the variants. In case of the uncompressed variants however, although the mass fractions of the constituents of the half-cell is the same, dictated by the recipe adopted from the compressed variants, the achieved porosities, half-cell volume and volume fractions of the cathode constituents are different. Furthermore, following the calculations shown in Appendix B, it is clear that the variants selected for the performance evaluation posses different densities. Consequently the performance property, utilizable energy density (UED) was employed to complement the evaluations.

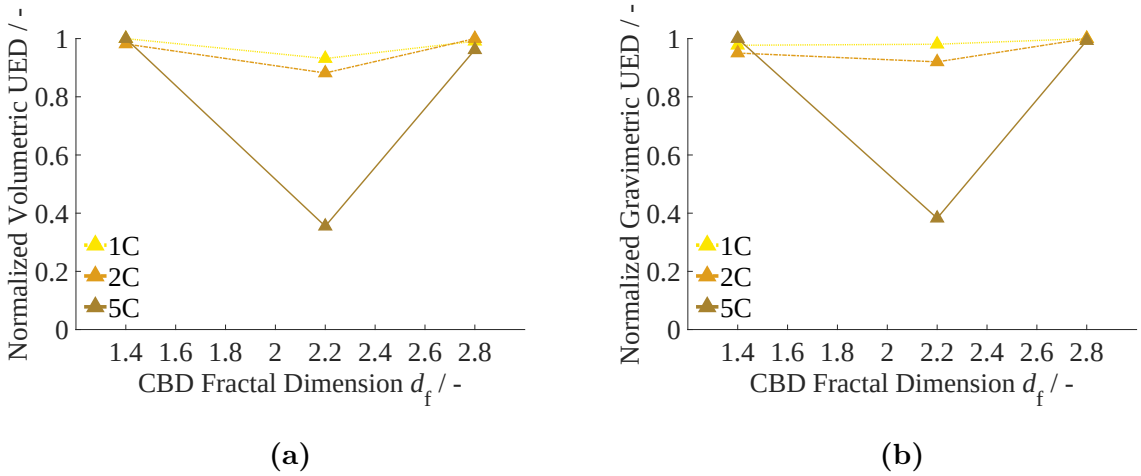

Figure 4.14: Energy density evaluations of the uncompressed CBD fractal dimension variants: a) Volumetric utilizable energy density normalized based on the highest value achieved at the respective C-rate b) Gravimetric utilizable energy density normalized based on the highest value achieved at the respective C-rate.

For the evaluations shown in Figure 4.14a, the highest thickness recorded at 65 µm, which was achieved by the variant $d_f = 2.2$, with cross-section same as the previous studies, was used to set the reference volume ($30 \times 30 \times 65$ µm^3) for the volumetric analysis (see Section 3.3.3). In case of the gravimetric analysis show in Figure 4.14b, the density of the variants was calculated using Equation B.1 from Appendix B. The results depicted in the figure for the respective analysis have been normalized using the highest energy density achieved for a given C-rate. Absolute values of the utilizable energy densities achieved have been denoted in Appendix C, Section C.1. Complementary to the observations made in Figure 4.12b, the UED for the variant $d_f = 2.2$, is the lowest owing to its half-cell potential irrespective of the type of analysis. In addition, the UEDs scales in the same fashion as UC such that the difference in the performance property are enlarged with increasing C-rate.

4.2.3 Comparison

In this section, an assessment of the contacts formed within the half-cell along with their dependence on fractal dimension and compression has been presented. Additionally, a recapitulation of the findings from the characterization of both compressed and uncompressed sub-studies is provided, facilitating a direct comparison. This comparison is complemented by an elaboration on the trends seen in characteristics of the half-cells with changing fractal dimension using the contact evaluations. The findings of this section suggest, that though compression has an impact on the number of contacts as well as the characteristics of the half-cell, the fundamental trend in the characteristics are governed by the fractal dimension of the CBD agglomerates and remains the same despite the scaling caused by compression.

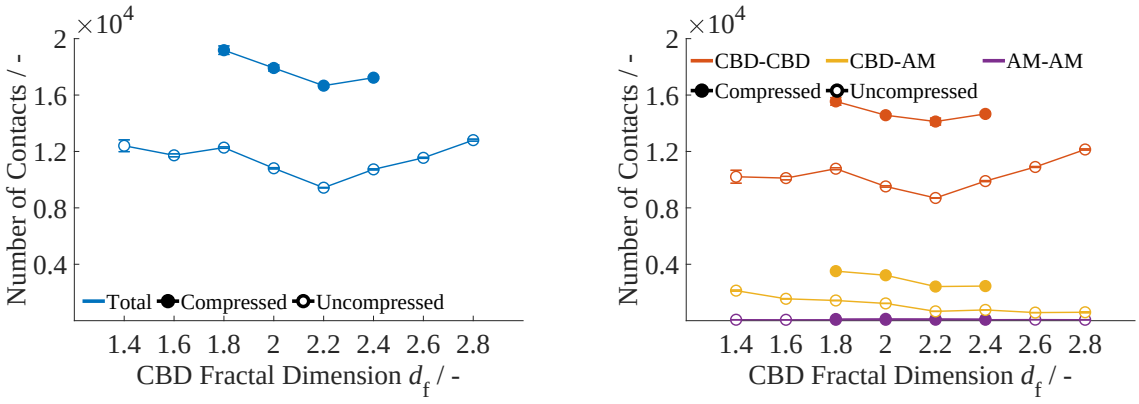

Figure 4.15: Contact Evaluation: (a) Total Contacts (b) Composition of contacts in the half-cell.

In Figure 4.15, the contacts formed within the half-cell have been plotted against the changing fractal dimension of the CBD agglomerates. The definition of a contact in this context as well as its evaluation have been elaborated in Section 3.2.1. The data points shown in the figure correspond to CBD agglomerates constructed under the conditions $d_p = 1\,\mu m$ and $d_g = 4\,\mu m$. Furthermore, the domain of the compressed variants is restricted to $1.8 \leq d_f \leq 2.4$ (see Section 4.2.1).

Figure 4.15a depicts the sum of all contacts, while Figure 4.15b shows the individual types of contacts that compose the total contacts in the half-cell. Herein, **CBD-CBD** contacts represent contacts formed within CBD agglomerates as well the inter-agglomerate contacts formed between two CBD agglomerates. **CBD-AM** contacts signify the contacts formed between CBD agglomerates and active material particles, while **AM-AM** contacts denote the inter-active material particle contacts.

An evaluation of the total contacts of the uncompressed variants (hollow-circles) in Figure 4.15a, reveals a decline in their number in the half-cell with increasing d_f, till a minimum is reached at $d_f = 2.2$, followed by an increment on further increase in the fractal dimension. Insights into this trend can be found in Figure 4.15b, where the total contacts are decomposed. It is evident from the data corresponding to uncompressed variants in the latter figure, that CBD-CBD contacts decrease with increasing d_f in the domain $1.4 \leq d_f \leq 2.2$. In this domain, as the fractal dimension increases, n_p increases at constant d_g, as was discussed earlier. This leads to a decrease in CBD dispersion in the half-cell such that lesser inter-agglomerate contacts are formed. The reduced dispersion also effects the CBD-AM contacts negatively, as seen from the figure, leading to an overall loss of total contacts. Beyond this domain i.e. $d_f > 2.2$, the increased contacts formed within CBD agglomerates due to the rising concentration of mass about their axis of rotation, overcome the loss in inter-CBD-agglomerate contacts as well CBD-AM contacts, resulting from the decreasing dispersion of CBD in the half-cell, such that an overall increase in the total contacts is observed again. As is to be expected the AM-AM contacts remain the same since no change is made to the active material in the entire domain of d_f investigation.
Remarkably, both figures reveal that the qualitative trends in contacts persist under compression. All the constituent contacts (except the AM-AM contacts) and hence the total contact indicate a shift towards higher values upon compression while simultaneously exhibiting the same dependence on fractal dimension. This finding is of considerable significance, as it indicates that the quality of the network of pores and electrical connections in the cathode microstructure is solely dependent on the configuration of the CBD and should scale only in intensity under the influence of compression.

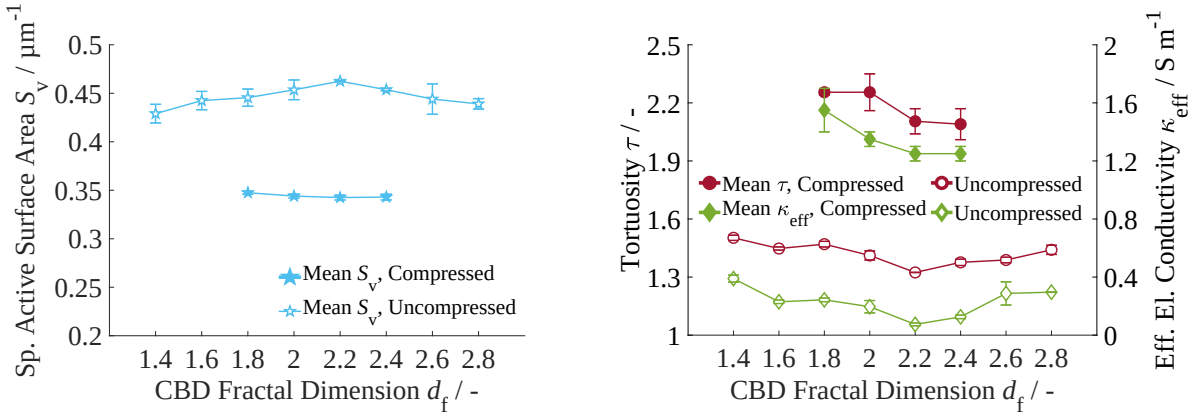

Figure 4.16: Comparison of half-cell characteristics: (a) Specific Active Surface Area (b) Tortuosity (left axis) and Effective Electrical Conductivity (right axis)

Finally, Figure 4.16 shows a direct comparison of the characteristics of the compressed and uncompressed variants with $d_p = 1\,\mu m$ and $d_g = 4\,\mu m$. It is evident that with compression

as the number of contacts increase, as was indicated in Figure 4.15a, the available active surface area decreases and the tortuosity and effective electrical conductivity increase. Despite the increment however, the trend in the characteristics over d_f remains the same as was suggested by the evaluation of contacts. Moreover, the relative change in the characteristics with change in d_f is identical, apparent from near parallel progression of the characteristics in the figure.
Further insights into the evolution of characteristics with fractal dimension can be extracted from the contact evaluations of the uncompressed variants. For these variants, the decline in κ_{eff} and τ shown in Figure 4.16b, in the domain $1.4 \leq d_f \leq 2.2$, is due to the decreased dispersion of the CBD and hence decreased CBD-CBD as well as CBD-AM contacts. While the absence of contacts deteriorates electron conduction and due to lack of sufficient conduction pathways, it reduces tortuosity due to the absence of obstruction encountered by lithium-ions in the pore space. The decrease in CBD-AM contacts specially impacts the available active surface, which increases in the absence of these contacts.
Beyond $d_f > 2.2$, however κ_{eff} increases, due to the increase in the CBD-CBD contacts, also regarded as secondary pathways of electron conduction in the previous sub-section, as depicted in Figure 4.15b. Furthermore, a stagnation of reduction in CBD-AM contacts (primary conduction pathway) with increasing d_f, is apparent in the latter figure. Herein, reduced dispersion of the CBD is countered by the enhanced contacting ability of CBD agglomerates with higher fractal dimension, leading to a slight increase in the CBD-AM contacts (suppressed in the figure due to the dominance of CBD-CBD contacts). Since, both the CBD-CBD and CBD-AM contacts act as an obstruction for the lithium-ions, τ increases as a consequence. Furthermore, an increase in CBD-AM contacts leads to reduction of S_V, due to the increased occupation of active material surface by the CBD.

4.3 Recommendations

A decrease in size, while considering equal amounts of the conductivity additive, be it of the carbon-black-binder agglomerate as a whole (size study) or of the primary particles (fractal dimension study), leads to an increase in conductivity additive dispersion in the cathode microstructure. As a result, an increase in the connections made between the active material and the conductivity additive are observed. The increased connections improve the electrical conductivity but reduce the area available for intercalation, by occupation of the active surface. At constant porosity, it was observed that variants with higher surface area performed better despite their inferior electrical conductivity at lower currents. However, with increase in the C-rate, the effect of available surface diminished and effect of the electrical conductivity increased. During the manufacturing process of cathodes, higher energy must be input into the mixing process to decrease the size of

carbon-black binder agglomerates by breaking them through mechanical stressing. Thus, increased energy input during mixing to facilitate deagglomeration of the conductivity additive, is only justified when electrical conductivity of the cathode is the predominant performance limiting factor. A detailed examination of this hypotheses is carried out in Chapter 5. While in a conventional-wet process, increased conductivity comes at the cost of reduced ionic conductivity due to the increased dispersion, modern intensive-dry mixing process can be exploited to mechanically coat the active material with the conductivity additive thereby retaining the quality of the pores space but with a more enhanced impact on the surface. This is explored in Chapter 6.

An improvement in electrical connections within the cathode microstructures is possible not only through increased dispersion, but also through lesser disperse and highly fractal shapes ($d_\mathrm{f} \rightarrow 3$) of the conductivity additive agglomerates. As was shown by the fractal dimension study, the shape of the conductivity additive can be manipulated in a manner such that, despite the reduced dispersion on account of the increased concentration of mass in individual agglomerates, the connectivity is improved. This implies that rather than investing large sums of energy in the mixing process to increased conductivity additive dispersion, which comes at a cost of the active surface, it could prove to be beneficial to synthesise the conductivity additive in highly fractal shapes. The potential of process in manipulation of carbon-black morphology has already been demonstrated in literature [34], furthermore efforts have been made to replace the conventional carbon-black-binder composite with hetero-aggregates of carbon-black with adjustable dimension, formed using silica [129].

Finally, based on the comparison of the compressed and uncompressed variants, it was observed that the quality of the electrical network i.e. proportion of primary and secondary contacts established in the half-cell was strongly influenced by the agglomerates shape and that compression only lead to scaling of these connections. Thus it can be suggested that the connections formed in a cathode and hence the electrical conductivity are a result of the size and shape of the conductivity additives. Furthermore, the calendering process in cathode manufacturing only serves to magnify the order of magnitude of the contacts formed and the electrical conductivity as long as the conductivity additives retain their shape and size. Conversely, the compression during calendering has a significant impact on the ionic conductivity. On the one hand the diffusion length reduces, due to a decrease in the height of the cathode under the influence of calendering pressure, improving the permeability of the cathode microstructure. On the other hand the porosity reduces, leading to increased tortuosity, resulting in a deficiency of lithium-ions, specially in the smaller pores.

Chapter 5

Investigations on Conductivity Additive Dispersion in a Conventional-Wet Process

This chapter deals with the dispersion of the conductivity additive in lithium-ion battery cathodes, manufactured using the conventional processes. The influence of carbon black particle size distribution, achieved in the dispersion process, is evaluated at first with respect to its influence on the cathode microstructure, followed by the implications thereof on the electrochemical performance of the computational half-cells, generated under consideration of wet processing. Moreover, contrasting cathode design strategies and operating conditions have been investigated to derive guidelines, specific to high-power or high-energy applications of modern batteries. As a key insight, the interplay of electrical conductivity, ionic conductivity and active surface area with changing degree of dispersion, has been presented. Hence, the chapter addresses, the **second objective** of this work by presenting an application dependent **optimum of the active surface area**.

5.1 Particle Size Distribution

In Section 2.2.2, measurement of particle size distribution was presented as a means of experimental characterization of the conductivity additive in lithium-ion battery cathodes. Since the size of the conductivity additive strongly influences the cathode microstructure, as was elaborated in the previous chapter, particle size distributions are an essential means of quality control for lithium-ion battery electrode suspensions [40]. Subsequently, Mayer et al. [53] used the particle size distributions of carbon black in cathode suspensions to quantify the changing degree of dispersion of the former in the cathode microstructure and linked it to the electrochemical cell performance, through experimentation. Further-

more, they found that the median size of the carbon black particles, evaluated from the particle size distributions, could be correlated to the specific energy input into the mixing process evaluated w.r.t. the circumferential velocity of the mixing tool called tip speed t_s, hence establishing a link between the cathode processing and the performance of the cells constructed thereafter [54].

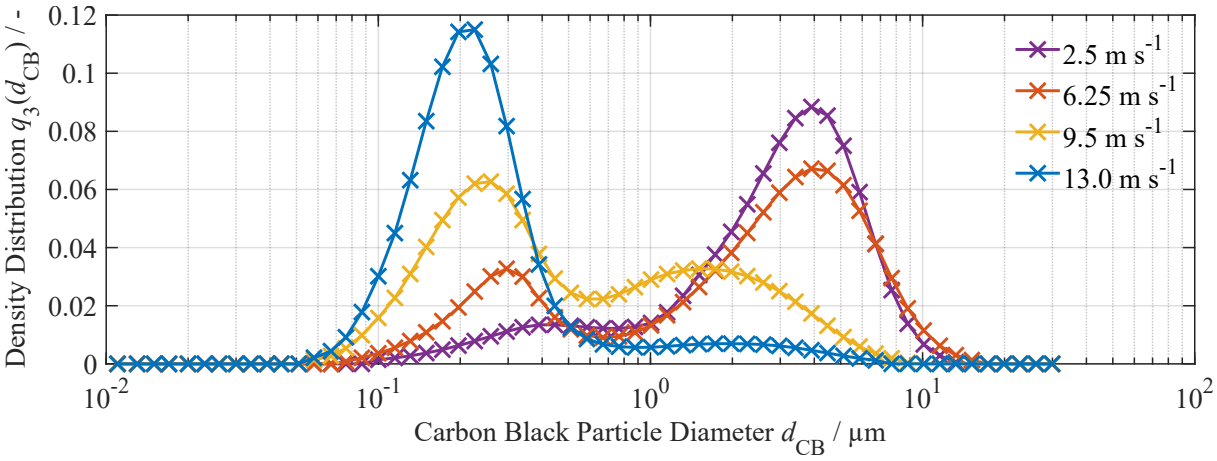

Figure 5.1: Measured carbon black particle size distribution (courtesy Mayer et al.) represented as a density distribution function $q_3(d_{CB})$ at varying tip speeds of the mixing tool.

For further exploration of the implication of carbon black particle size on performance of lithium-ion battery cathodes using a numerical method, measurements made at the Institute of Particle Technology, Braunschweig, were kindly made available by Dr.-Ing. Julian Burmeister née Mayer, for the investigations presented in the following sections. These measurements visualized in Figure 5.1, show the density distribution function $q_3(d_{CB})$, of carbon black particle diameters d_{CB}, achieved after mixing with active material and binder, for a constant time period but changing tip speed of the mixing tool. Details on the extraction of the shown data can be found in Reference [39]. It is apparent from the figure that the function is bimodal in nature. Mayer et al. [53] labelled the mode at the smaller carbon black diameter as the aggregate peak and the mode at the larger diameter as the agglomerate peak. Herein, agglomerate refers to clusters of carbon black particles held together by weak forces of attraction, while the aggregates, that are building blocks of agglomerates, comprise of primary particle of carbon black fused together.
The change in the density distribution function with changing tip speed in Figure 5.1, indicates an increase in the proportion of carbon black particles with smaller diameter as the tip speed increases, due to the increased energy input in the same time, at higher speeds. In order to realize the change in the cathode microstructure associate with such a change in dispersion of the conductivity additive, the measured carbon black diameters were incorporated into the method elaborated in Section 3.1. In doing so, it was assumed that carbon black and binder existed in equal quantities in the half-cell. Furthermore, it

was assumed that all the binder was absorbed by carbon black during the wet dispersion, leaving no surplus binder that could attach itself to the active surface. Moreover, it was assumed that forces evolved in the conventional mixing process where not high enough to coat carbon black on the active material surface.
Constituents of the cathode: active material and CBD (carbon black and binder), were modelled as smooth, dense spheres as in the previous chapter. The size of the active material, NMC 622, was held constant at 10 µm. Conversely, the size of the CBD was derived from the density distribution functions. The number of particles of the CBD for the particle simulations described in Section 3.1.1, were calculated using the relation:

$$n_{\mathrm{CBD}}(d_{\mathrm{CB}}) = \frac{6 \cdot V_{\mathrm{HC}} \cdot \epsilon_{\mathrm{CBD}} \cdot q_3(d_{\mathrm{CB}})}{\pi \cdot d_{\mathrm{CB}}^3} \ . \tag{5.1}$$

Here, $n_{\mathrm{CBD}}(d_{\mathrm{CB}})$ signifies the number of CBD particles as function of the carbon black particle diameter, V_{HC} represents the half-cell volume and ϵ_{CBD} is the sum of the volume fraction of carbon black and the binder. Similarly, to calculate the number of NMC 622 particles, the active material fraction of the half-cell volume $V_{\mathrm{HC}} \cdot \epsilon_{\mathrm{AM}}$ was divided by the volume of a single NMC 622 particle. The volume fractions needed for the previous evaluations were calculated from mass based recipe of cathodes using Appendix B. Subsequently, particulate structures generated by the particle simulations were transformed into half-cell computational domains following the method presented in Section 3.1.2.

5.2 Impact of Degree of Dispersion

The following sections are dedicated to exploring the most suited degree of dispersion of the conductivity additive, quantified by the particle size distribution achieved at a given tip speed of the mixing device in Figure 5.1, for contrasting applications of lithium-ion battery cathodes. Owing to the diverse application of lithium-ion batteries, from consumer electronics to electrical vehicles, their design strategy as well as operation condition is often cratered to a specific application. Lain et al. [130] identified two broad categories of these applications based on the trade-off between energy and power. High-power applications, wherein faster transport of lithium-ions as well as electrons is essential; and high-energy cathodes, which trade slower transport of the reactants for higher energy. Consequently, achieving an ideal dispersion of conductivity additives becomes challenging due to the differing requirements between these applications. As discussed in the preceding chapter, enhanced conductivity additive dispersion typically enhances electrical conductivity, albeit at the expense of reduced surface area and increased tortuosity. The importance of these characteristics varies depending on the specific application. Therefore, the ensuing sections address the pursuit of optimal dispersion individually.

5.2.1 High-Power Cathode

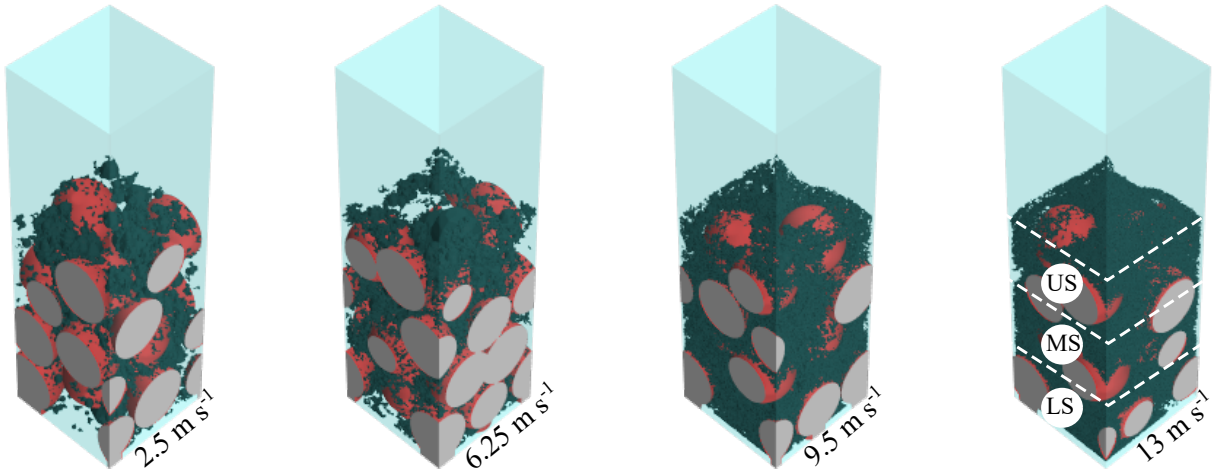

Figure 5.2: Idealized half-cell geometries of the high-power variants at varying tip speeds, with dotted lines marking volumetrically equal upper (US), middle (MS) & lower sections (LS) [131].

High-power cathodes are designed to ensure high current output and faster charging. Thus, these cathodes exhibit comparatively higher porosity to ensure good ionic conduction as well as high conductivity additive content to enhance the electrical conductivity. Furthermore, to reduce diffusion lengths in the half-cell, the thickness of these cathodes is kept small by using lower coating weights [130]. High-power cathodes are prone to poor ionic diffusion, due to the high current throughput, but are limited by reaction rate at the active surface. Figure 5.2, shows the domain of investigated high-power cathode variants representing four different degrees of dispersion labelled using the mixing tool tip speed. The chosen recipe for all these variants is 90:5:5 (active material:carbon black:binder) wt-%. The half-cell porosity is set to 40% and the thickness of the cathode is set to 40 µm with a cross-section of 20×20 µm.

Characterization

A visual inspection of the variants shown in Figure 5.2, puts into perspective the influence of the particle size distribution at changing tip speeds on the cathode microstructure. While much larger agglomerates of CBD are visible at 2.5 m s^{-1} due to the significant agglomerate peak of the density distribution function at this tip speed, as shown in Figure 5.1, only smaller particles in the range of aggregate size are visible at 13 m s^{-1}, where the agglomerate peak of the density distribution is diminished, as seen in the latter figure. The consequences of this increased dispersion are apparent from the illustration of the half-cell variants. As the tip speed rises, the active surface, depicted by the red area in Figure 5.2, gradually diminishes in visibility. Additionally, the pores in variants with lower tip speeds seem to be notably larger compared to those at higher tip speeds.

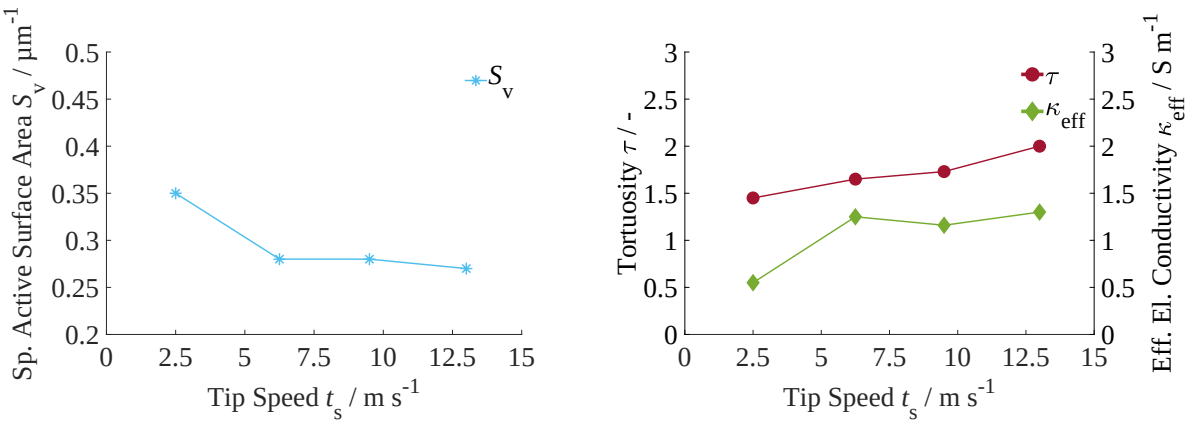

(a) **(b)**

Figure 5.3: Characterization of the high-power cathode variants [131]: a) Specific active surface area b) Tortuosity (left axis) and Effective electrical conductivity (right axis).

To quantify these observations, characterization simulations using the numerical models explained in Section 3.2, were carried out. In Figure 5.3a, the available volume specific active surface area of the variants has been plotted against the tip speed. It can be seen from the figure that with increased dispersion of the CBD, as the tip speed increases, S_V decreases sharply but converges to a constant value beyond 6.25 m s^{-1}. The drastic initial decrease in S_V is caused by the aggregate peak of the density distribution function which becomes apparent starting from 6.25 m s^{-1} (see Figure 5.1). Consequently, the smaller CBD particles represented by the aggregate peak, increase in number with increasing tip speed, as the volume of the CBD in the variants remains constant. Subsequently, these particle attach themselves to the active surface, reducing S_V. With further increase in the aggregate peak along with increasing tip speed a saturation of this effect is reached, leading to no further change in S_V.

The consequences of increased dispersion in the half-cell for the conduction characteristics has been plotted in Figure 5.3b. As evident from the right axis of the graph, the effective electrical conductivity κ_{eff} of the half-cell exhibits a sharp increase until 6.25 m s^{-1}, with increased dispersion, followed by an asymptotic decay. This percolation behaviour is to be expected from a combination of carbon black and binder, as found by Guy et al. [23]. Moreover, the maximum of κ_{eff} correlates with the minimum of S_V, indicating a trade-off between the two, with increasing tip speed and conductivity additive dispersion. Conversely, the left axis of Figure 5.3b shows a consistent rise in the tortuosity of the variants with higher tip speed. This underscores the clash between electrical and ionic conductivity, as depicted in Figure 4.2b. However here, the increase in the electrical conductivity stagnates, while the tortuosity rises steadily with increasing tip speed. This is because the increased contacts on account of the increased dispersion contribute directly to the obstructions to ionic movement, but not to the conduction pathways.

Performance Evaluation

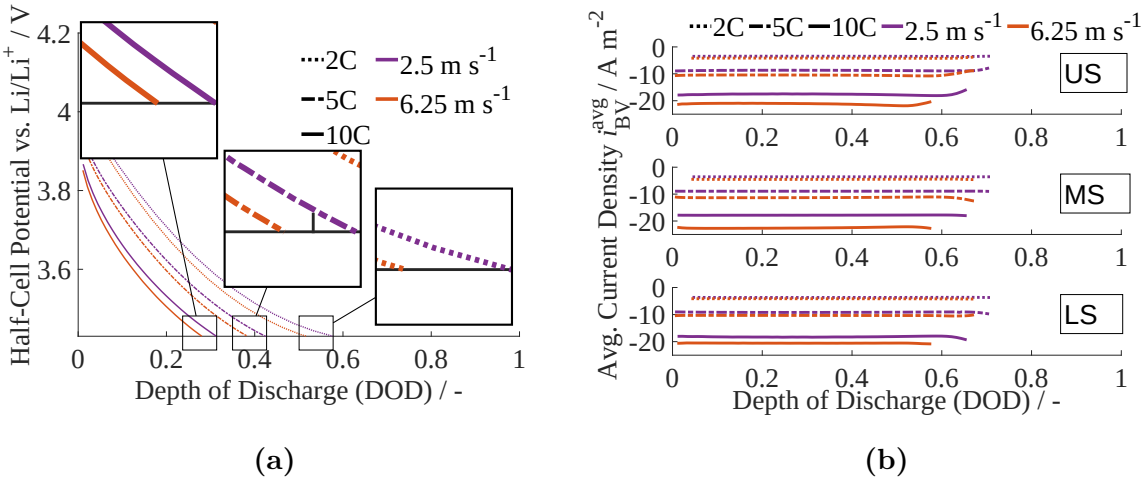

(a) **(b)**

Figure 5.4: Performance evaluation of the chosen high-power cathode variants: a) Galvanostatic discharge curves at varying discharge rates b) Average intercalation current density in the upper section (top) middle section (middle) and lower section (bottom).

Owing to the time and cost intensive nature of the scale resolving simulations using the numerical method explained in Section 3.3, only the high-power cathode variants: 2.5 and 6.25 m s^{-1}, wherein relevant differences in microstructural properties were observed, were examined further. Figure 5.4a, shows the half-cell potential of the high-power variants with respect to pure lithium anode at increasing galvanostatic current arising from the C-rates 2C, 5C and 10C. It is discernible from the figure that the 2.5 m s^{-1} variant, exhibits higher half-cell voltage over the entire DOD irrespective of the C-rate. This observation is a consequence of the substantially higher specific active surface area possessed by the variant. Subsequently, due to the greater surface area, the intercalation current density at given C-rate is lower for the variant and hence following Equation 3.28, it operates at a lower overpotential.

To verify this, the surface average intercalation density $i_{\mathrm{BV}}^{\mathrm{avg}}$ (see Equation 3.35), arising in three volumetrically equal sections of the cathode, has been depicted in Figure 5.4b. These represent the upper(US), middle(MS) and lower(LS) section of the half-cell, as indicated in Figure 5.2. The data in the latter figure illustrates, that the higher surface area of the 2.5 m s^{-1} variant indeed leads to lower intercalation current density, irrespective of the C-rate, in all the sections of the half-cell. It is to be noted that $i_{\mathrm{BV}}^{\mathrm{avg}}$ is considered to be negative due to the sign convention adopted in this work, wherein flux in the direction opposite to the normal vector at a surface is considered negative. The lower overpotential hence achieved through the higher active surface, dominates in case of high-power cathodes, such that the influence of improved electrical conductivity of the 6.25 m s^{-1} variant is overshadowed by its lower S_{v}, at all C-rates. Nonetheless, with increasing C-rate, the

half-cell potential curves of the variants converge together (see Figure 5.4a) despite the increasing differences in $i_{\mathrm{BV}}^{\mathrm{avg}}$ in all the sections (compare Figure 5.4b), indicating that the influence of electrical conductivity becomes apparent as the C-rate increases. This leads to the inference that the lower ohmic losses due to the higher effective electrical conductivity of the 6.25 m s^{-1}, increasingly make up for its reduced active surface as the C-rate increases.

Drawing attention to the progression of $i_{\mathrm{BV}}^{\mathrm{avg}}$ with DOD in Figure 5.4b, reveals further insights into high-power cathodes. Comparing the magnitude of $i_{\mathrm{BV}}^{\mathrm{avg}}$ for the individual variants, at a given C-rate, across the sections of the half-cell at small DOD, reveals no significant variation in the current. Since, the surface area of the individual section is expected to be equal, due to the homogeneous distribution of the CBD, it can be inferred that for both the variants, the electrical conductivity is high enough to ensure low ohmic losses, leading to an even distribution of potential and identical intercalation current at the beginning of discharge. Consequently, lithium concentration distribution in both the regions of the half-cell variants show no sharp gradients, as shown in an exemplary manner, at DOD = 0.09 for a 5C discharge, in Figure 5.5. In this figure, the cathode and electrolyte domain have been presented separately next to each other. The electrolyte domain has been clipped to reveal deeper layers of the half-cell.

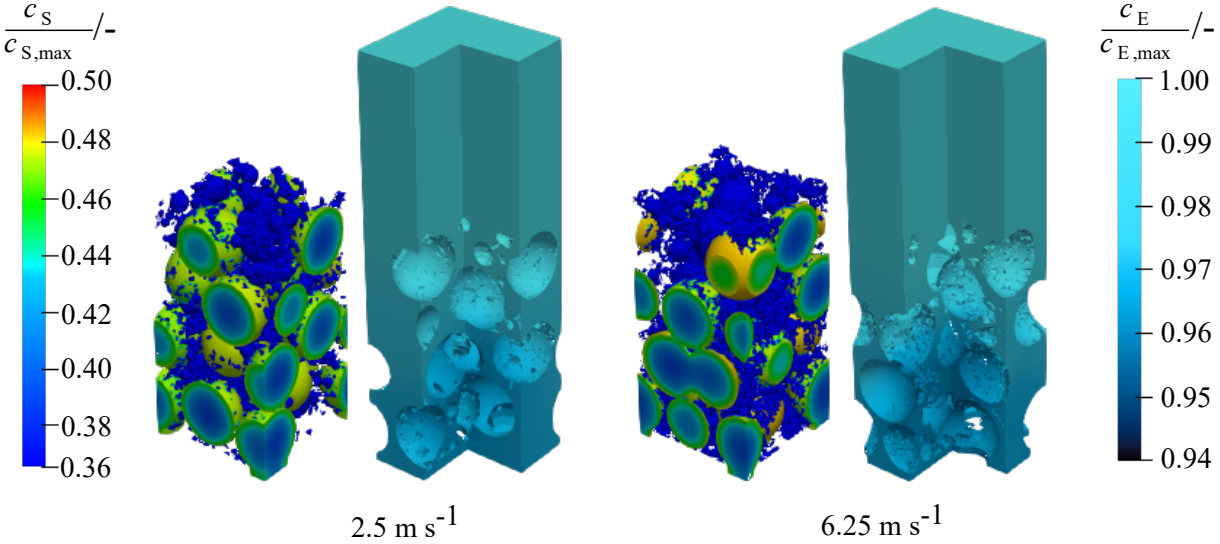

Figure 5.5: Relative lithium concentration distribution in the high-power cathode (left color-bar) and electrolyte domain (right color-bar) of the 2.5 m s^{-1} variant and 6.25 m s^{-1} variant at DOD = 0.09 for galvanostatic discharge at 5C [131].

In contrast, towards the end of the discharge at DOD = 0.65, the current in the upper section (US) seems to reduce at the expense of the increasing current in the remaining sections, most evidently for the higher C-rates, for both the variants, as seen in Figure 5.4b. Since the total current in a galvanostatic discharge process must remain the same, this observation indicates a shift of the lithium intercalation current from the top to the

bottom two section. This shift is caused by the saturation of lithium concentration (as c_s approaches $c_{s,max}$) in the top third of the cathode close to the source of the lithium-ions, leading to reduction in the current, following Equation 3.28. The phenomenon is easily verified by the analysis of lithium concentration distribution at DOD = 0.65 during the 5C discharge, shown in Figure 5.6. It is evident from the figure, that due to the restriction

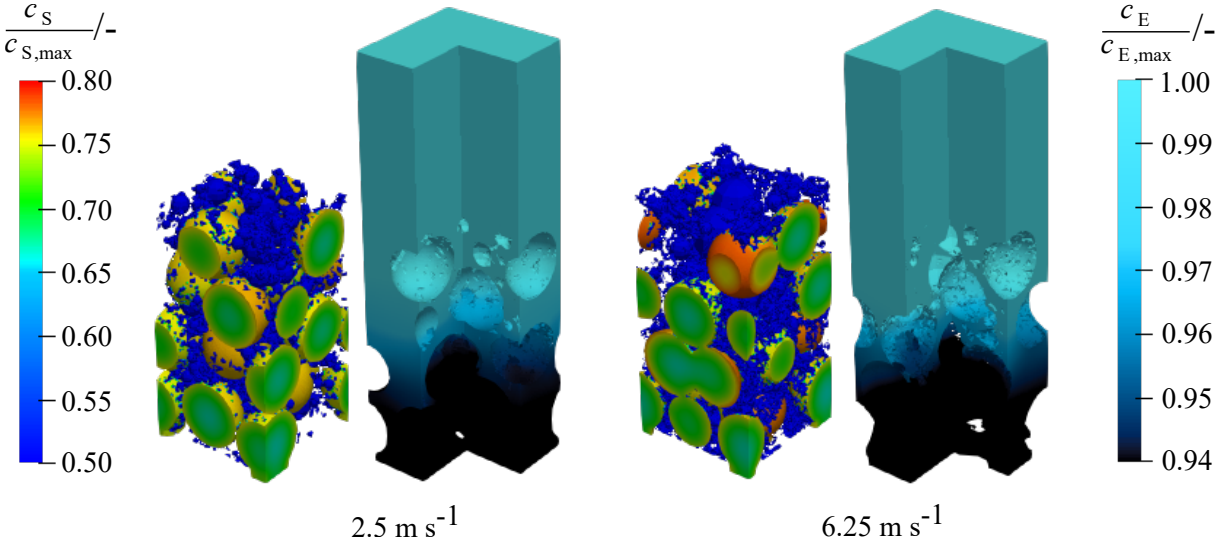

Figure 5.6: Relative lithium concentration distribution in the high-power cathode(left color-bar) and electrolyte(right color-bar) domain of the 2.5 m s^{-1} variant and 6.25 m s^{-1} variant at DOD = 0.65 for galvanostatic discharge at 5C [131].

on lithium transport at the high C-rate, the lithium-ions get preferentially intercalated at the top of the cathode due to its proximity to their anodic source. Consequently, the top third of the cathode gains lithium concentration the fastest, as seen most evidently for the 6.25 m s^{-1} variant in the latter figure, wherein the top layer exhibits a much higher lithium concentration than the rest of the cathode. Subsequently, the intercalation current is redirected to the remaining parts of the cathode.

As a consequence of the accumulation of the ionic flux at the top of the cathode, the region close to the current-collector exhibits depletion of the lithium concentration in the electrolyte, indicated by the black spots in the electrolyte domains of Figure 5.6. Similar effect was also observed at the highest current for size variants in Figure 4.4. The occurrence of this phenomenon underscores the nature of high-power cathodes. Despite the smaller thickness and higher porosity of these cathodes, the rate of lithium consumption in the intercalation reaction at higher C-rates, is so fast that lithium diffusion in the electrolyte cannot keep up, specially at the regions far away from the source of lithium-ions. Thus at a certain diffusion limited C-rate (DLC) [132], wherein the performance is solely dominated by the ionic transport, the availability of the active surface, found to be crucial for the investigated high-power cathodes, is bound to become irrelevant.

5.2.2 High-Energy Cathode

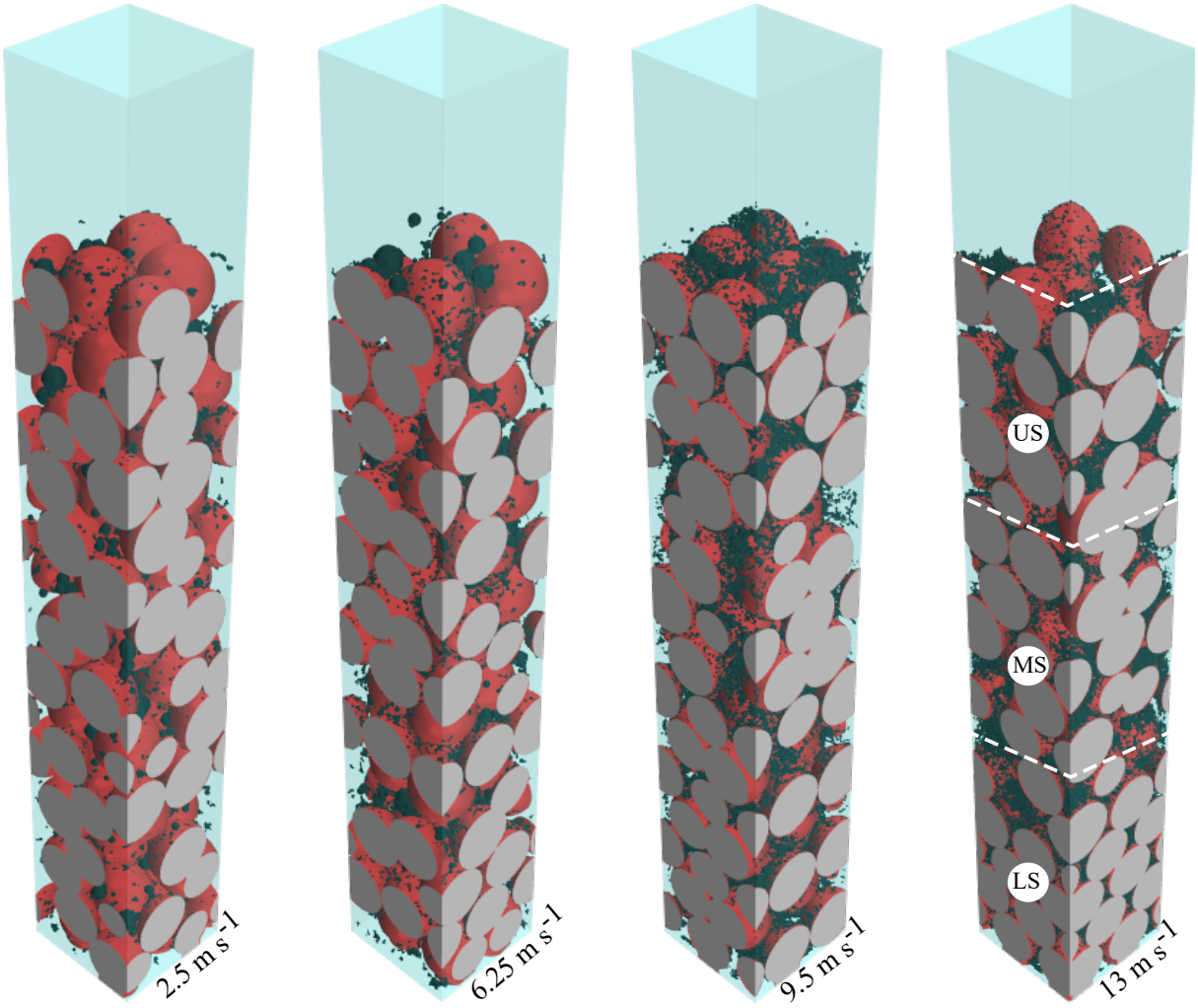

Figure 5.7: Idealized half-cell geometries of the high-energy variants at varying tip speeds, with dotted lines marking volumetrically equal upper (US), middle (MS) & lower sections (LS) [131].

High-energy cathode design strives for high energy density. These cathodes sacrifice power output for capacity. Key design aspect of these cathodes involves the maximization of energy density through increased active material content, increased thickness or coating weights, reduced porosity and reduced passive materials such as conductivity additive and binder. As a result such cathodes are operated under low current to avoid ionic diffusion limitations. Moreover, due to their low conductivity additive content these cathodes are limited by their insufficient electrical connections. Figure 5.7 shows the domain of investigated high-energy cathode variants, representing four different degrees of dispersion labelled using the mixing tool tip speed. The chosen recipe for all these is 98:1:1 (active material:carbon black:binder) wt-%. The half-cell porosity is set to 30% and the thickness of the cathode is set to 120 µm with a cross-section of 20×20 µm.

Characterization

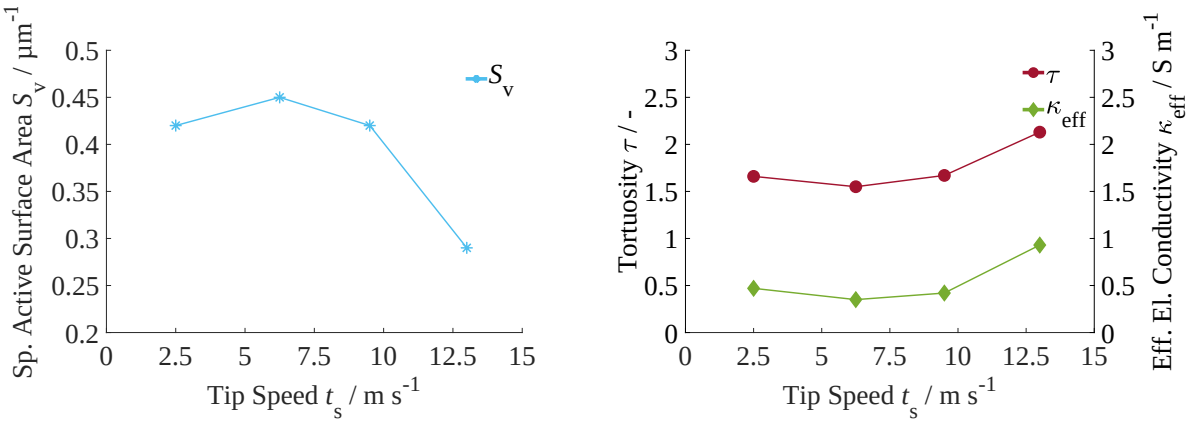

(a) **(b)**

Figure 5.8: Characterization of the high-energy cathode variants [131]: a) Specific active surface area b) Tortuosity (left axis) and Effective electrical conductivity (right axis).

Similar to the observations made for the high-power cathode, the influence of the increasing aggregate peak with increasing tip speed (see Figure 5.1), is reflected in the microstructure of the high-energy cathode variants shown in Figure 5.7. While bigger agglomerates of the CBD are still clearly visible until 9.5 m s^{-1}, these completely disappear at 13 m s^{-1}. However, the visual appearance of high-energy cathode is dominated by their high active material content. Consequently, the influence of the increased dispersion of the CBD, present in considerably lesser quantity than in high-power cathode, is not evident through a visual inspection alone. Quantification of the influence of the increased tip speed and the entailing increased CBD dispersion, has been made in Figure 5.8.
Contrary to the high-power variants, the rising peak of aggregates in the high-energy half-cells until 9.5 m s^{-1}, is not sufficient to cause a significant change in the half-cell characteristics as seen from Figure 5.8a and 5.8b. Subsequently, it is only at the tip speed 13 m s^{-1}, where all agglomerates have been fragmented into aggregates, that a notable change in the half-cell characteristics can be seen. At the highest tip speed, ergo highest degree of dispersion, the high-energy cathode exhibits a drastic decrease in S_V accompanied by a sharp increase in κ_{eff} and τ. This is to be expected on account of the previously presented discussions on the influence of CBD dispersion on half-cell characteristics. The shift in electrical percolation threshold to a higher tip speed for high-energy cathode is because of their three times larger thickness and significantly lower CBD content, which warrants much higher dispersion to achieve sufficient electrical connections. Moreover, upon comparison with Figure 5.3, it can be contemplated that with further increase in the tip speed, S_V and κ_{eff} would converge to a constant value, similar to the high-power cathodes, resulting in S-shape typical for percolation.

Performance Evaluation

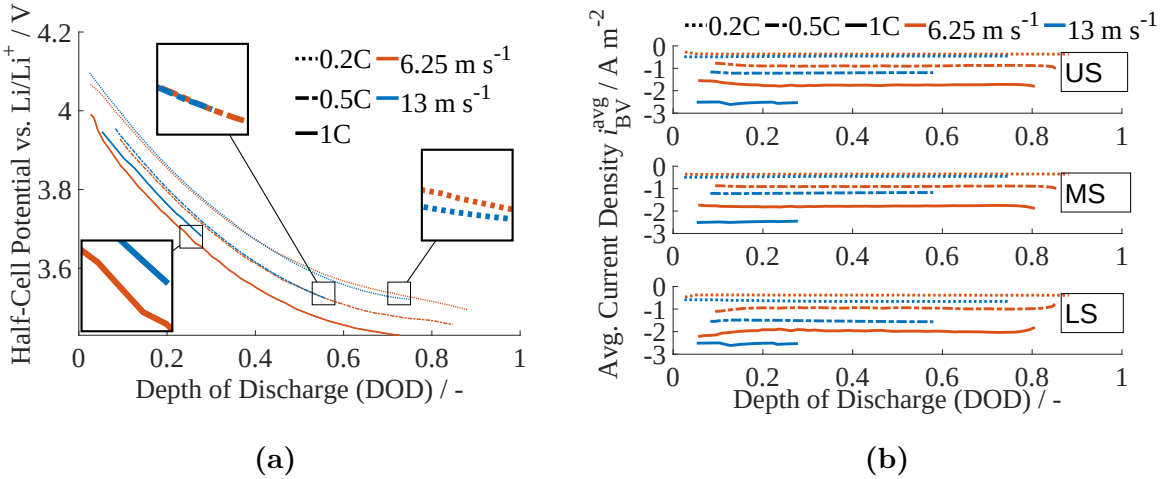

(a) **(b)**

Figure 5.9: Performance evaluation of the chosen high-energy cathode variants: a) Galvanostatic discharge curves at varying discharge rates b) Average intercalation current density in the upper section (top) middle section (middle) and lower section (bottom).

The increased thickness of the high-energy variants increases the size of the finite volume computational domain needed for the numerical evaluations immensely, making scale resolving electrochemical evaluations for all the variants highly infeasible. Hence, only variants 6.25 and 13 m s^{-1} were chosen for these evaluations. Figure 5.9a, shows the half-cell potential of the chosen variants, evaluated at the cathode current-collector w.r.t. pure lithium metal at increasing C-rates: 0.2C, 0.5C and 1C. In contrast to the high-power variants, where the variant with the higher specific active surface area always exhibited the highest half-cell potential, irrespective of the C-rate (see Figure 5.4a), a dominance of the electrical conductivity with increasing galvanostatic current is evident for the high-energy variants. Consequently, at the lowest C-rate 0.2C, the 6.25 m s^{-1} variant exhibits slightly higher half-cell potential due to its higher S_V (see Figure 5.8a), but at 0.5C, the higher electrical conductivity of the 13 m s^{-1} variant compensates for its lower S_V, in Figure 5.9a. Finally, at the highest C-rate 1C, the poor electrical conductivity of the 6.25 m s^{-1} variant becomes decisive, leading to high ohmic losses and significantly lower half-cell potential than the 13 m s^{-1} variant, with higher κ_{eff} (see Figure 5.8b). This observation, despite the increased i_{BV}^{avg} and the related overpotential for the 13 m s^{-1} at the highest current, as shown in Figure 5.9b is a clear sign of the dominance of the electrical conductivity in high-energy cathodes, particularly at higher C-rates.

Similar to the high-power cathodes the progress in i_{BV}^{avg} with DOD delivers important insights into the transport mechanism of the high-energy cathodes. As is evident from Figure 5.9b, most evidently at the higher currents, the distribution of the intercalation current at the beginning of the discharge in the different sections of the cathode is not

uniform. Particularly, in case of the 6.25 m s^{-1} variant, a higher average intercalation current is observed in the lower section, indicated by the deflection of the i_{BV}^{avg}-curve towards a higher magnitude at low DOD < 0.2. This is due to the inadequate electrical conductivity of the variant, leading to high ohmic losses and hence drop in potential in direction of current i.e opposite to the movement of electron flow, as dictated by convention. Consequently, the potential close to the current-collector is the lowest and the overpotential the highest. Hence, following Equation 3.28 the intercalation current in LS is higher than the remaining sections.

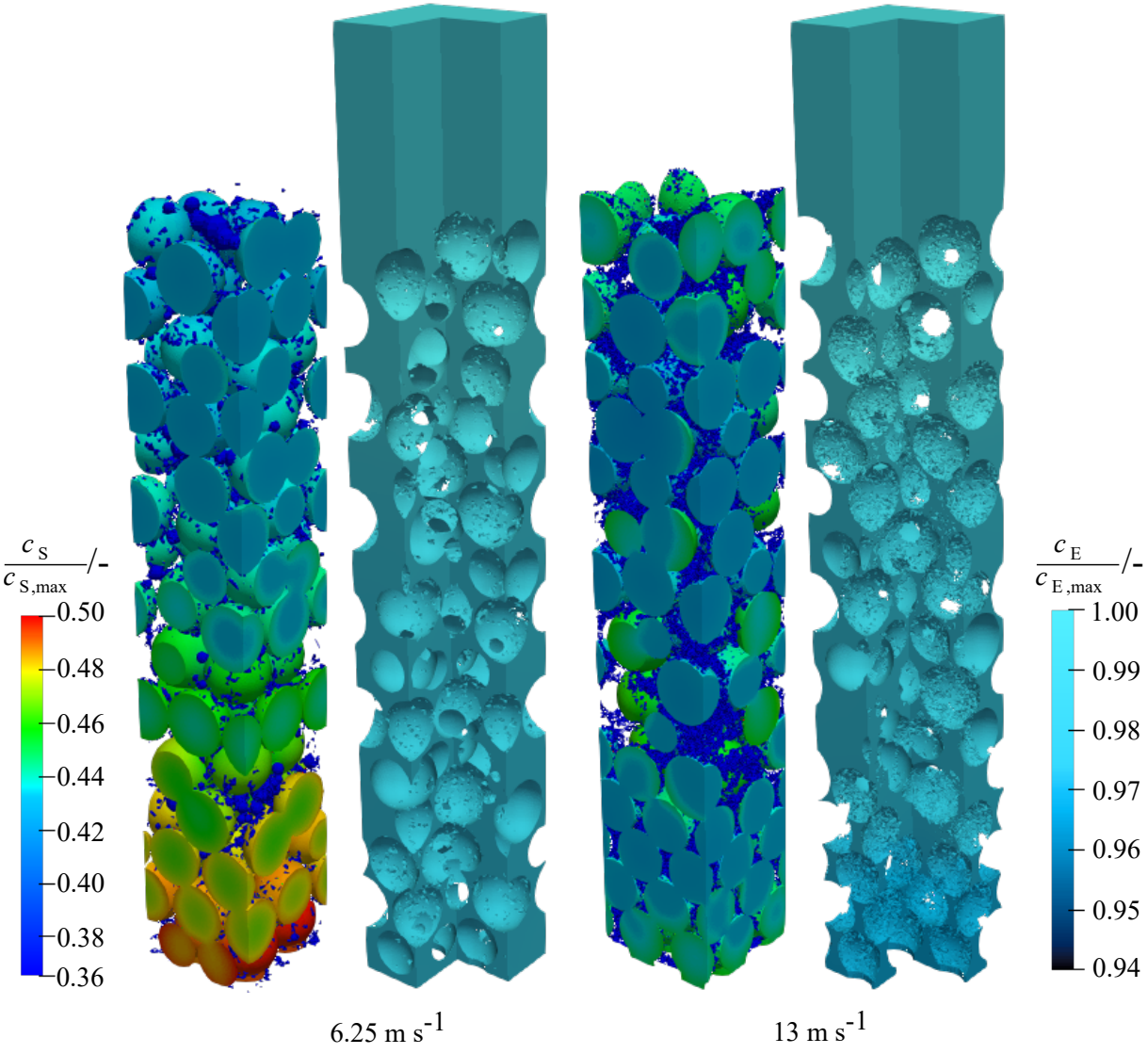

Figure 5.10: Relative lithium concentration distribution in the high-energy cathode and electrolyte domain of the 6.25 m s^{-1} variant (left) and 13 m s^{-1} variant (right) at DOD = 0.15 for galvanostatic discharge at 0.5C [131].

The consequences of this disparity in potential and current is clearly visible in Figure 5.10, showing the lithium concentration in both the regions of the half-cell variants during a

0.5C discharge, in an exemplary manner. Owing to the accumulation of intercalation current in the lower section of the 6.25 m s^{-1} variant, lithium concentration in this region of the cathode, rises the fastest leading to the concentration gradient observed in the figure. This sharp rise in lithium in the LS leads to a saturation of lithium at DOD ≈ 0.2, on account of which the intercalation current decreases, following Equation 3.28. As can be seen from Figure 5.9b, the current from the lower section is diverted to the remaining section, such that $i_{\mathrm{BV}}^{\mathrm{avg}}$ converges to the nearly the same magnitude in all the sections, for DOD > 0.2.

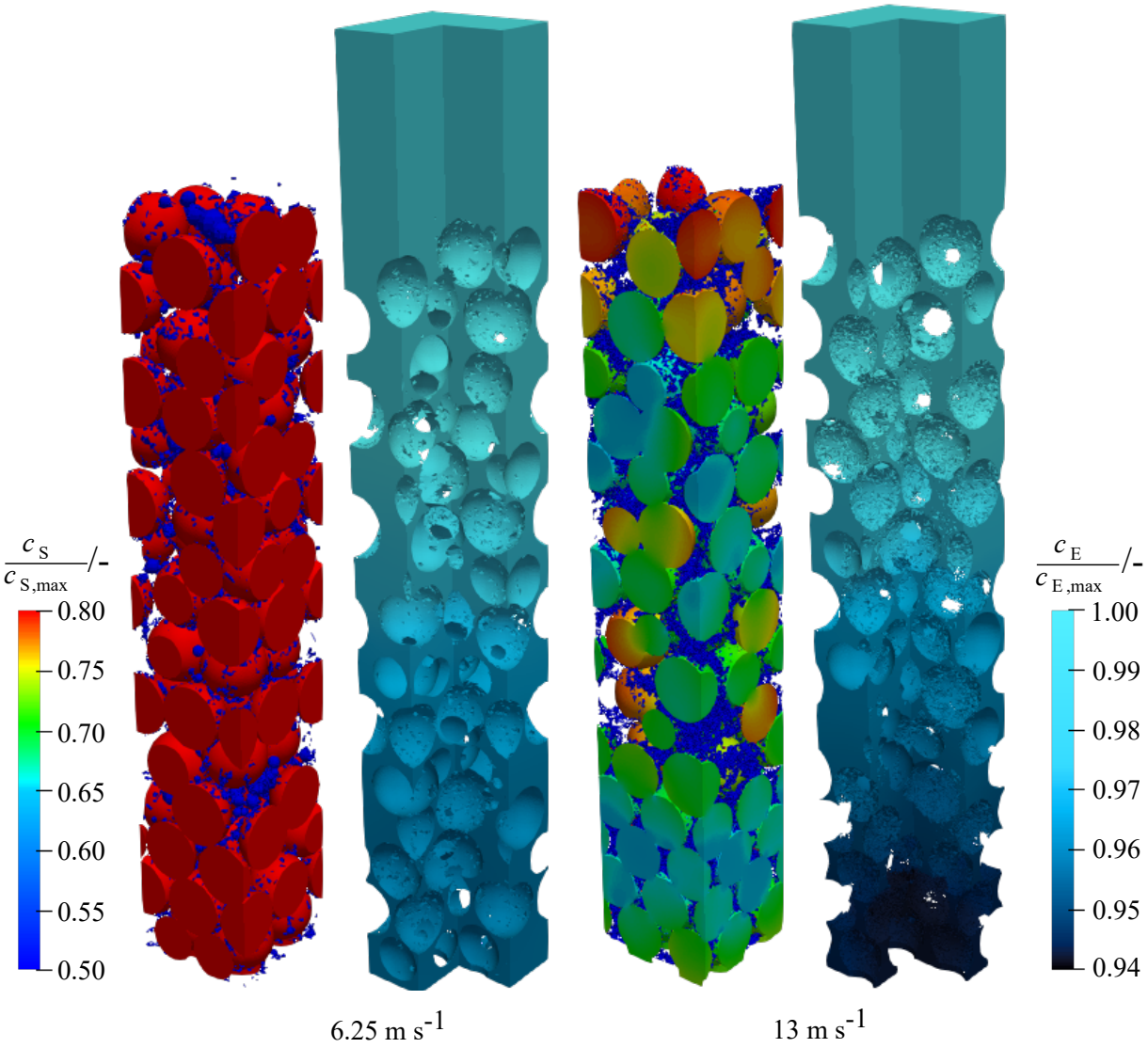

Figure 5.11: Relative lithium concentration distribution in the high-energy cathode and electrolyte domain of the 6.25 m s^{-1} variant (left) and 13 m s^{-1} variant (right) at end stages of galvanostatic discharge at 0.5C [131].

A similar behaviour is absent for the 13 m s^{-1} variant. On the one hand, it posses sufficient electrical conductivity to minimize the differences caused by the ohmic losses.

On the other hand, due to its high tortuosity, limiting the ionic conduction, it is incapable of redirecting the intercalation current as was observed for the 6.25 m s^{-1} variant, leading to a constant progression over DOD as is seen in Figure 5.9b and an uniform distribution of lithium concentration at an early stage of discharge, displayed in Figure 5.10.
The effects of the ionic limitation of the 13 m s^{-1} variant become apparent especially towards the end of the discharge. Figure 5.11, shows the state of lithium concentration distribution in both the half-cell variants at the end stages of a 0.5C discharge. Observation of the cathode domain of the 13 m s^{-1} variant, in the figure, clearly reveals an accumulation of lithium concentration at the top of the cathode due to the preferential lithium intercalation in this region, caused by the limitation on ionic transport. Moreover, due to the large size of the high-energy cells the absence of intercalation current at the current-collector leads to the depletion of lithium in the pores spaces of the lower section as shown by the black region in the electrolyte domain of the 13 m s^{-1} variant.
As is to be expected this behaviour is absent in the 6.25 m s^{-1}. The leveling of the intercalation current beyond DOD ≈ 0.2 in Figure 5.9b, leads to a uniform distribution of lithium concentration in the cathode region towards the end of discharge. Subsequently, as is shown in Figure 5.11, the entire thickness of the cathode region of the of the 6.25 m s^{-1} variant has achieved a uniform lithium concentration above 80% of the maximum capacity. On the contrary only the top layer of the 13 m s^{-1} variant is seen to have made the maximum of its capacity by the end of discharge. This is clearly reflected in the DOD reached by the latter variant at the end of a 0.5C discharge, in Figure 5.9b. The data in the figure suggests that while the 13 m s^{-1} could only reach a DOD of ≈ 0.57 in during the entire discharge process, the 6.25 m s^{-1} variant was able to achieve ≈ 0.84 discharge depth. These evaluations put in to perspective, the major limitation posed by ionic diffusion in high-energy cathodes.
It is to be noted that the end of discharge in this case is not indicated by temporal end of the discharge or the achievement of the cut-off voltage, but by the numerical stability of the electrochemical simulations. In order for the 13 m s^{-1} to reach higher DOD, the current must be directed to the lower section of the half-cell, to access the unused capacity. However, since movement to the LS is highly restricted, this would require a rapid drop in potential to increase the intercalation current, following Equation 3.28. Numerical representation of this rapid potential drop leads, on the one hand to computationally infeasible simulations on account of the smaller time discretization. On the other hand, numerical instabilities especially in the electrolyte region where the potential and concentration are coupled restrict further stable simulation. Thus, at the onset of this rapid drop in potential the discharge process is presumed to be over with the assumption that for a real cell the discharge process under similar circumstances must also be stopped to avoid damage.

5.3 Application Dependence of the Optimal Active Surface

In the previous chapter, utilizable capacity (UC) was used as the predominant performance determinant. This performance metric however is unsuitable for the comparison of the contrasting cathode design strategies presented in this chapter. Partly, because of the differences in the recipes and dimension of the resulting half-cells leading to comparison of unequal active material mass in the cathode. But more evidently, because the metric only provides information on the normalized capacity of the half-cell utilized at end of discharge. As was indicated in Section 5.2.2, the high-energy variants were not able to reach the cut-off voltage, hence an evaluation of UC for these variants according to the definition following Equation 3.37, is not possible. Hence, the performance determinants utilizable energy density (UED) and utilizable power density (UPD) were employed for the analysis presented in the following sections of this chapter. Not only do these metrics provide an adequate means of comparison, but they also enable the evaluation of the measure of performance for which the contrasting design strategies are tailor-made. In the sections to follow, when comparing the variants of a given application, only the gravimetric analysis of the performance determinants has been made. This is on account of the identical volume of the cathodes catering to a given application. The results of the analysis reveal the best suited state of dispersion of the conductivity additive in relation to the available active surface, in dependence of the chosen application.

5.3.1 High-Power Application

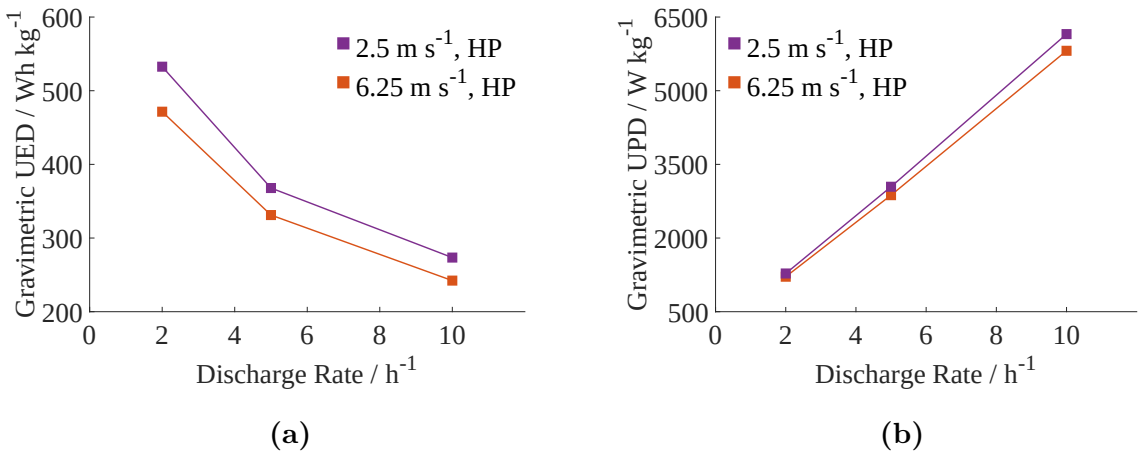

Figure 5.12: Performance determinants for the high-power application variants: a) Gravimetric utilizable energy density b) Gravimetric utilizable power density.

This section deals with the performance evaluation of the high-power cathode variants. In Figure 5.12, the specific values of the performance determinants evaluated using the gravimetric analysis have been plotted against the increasing high-power application C-rates: 2C, 5C and 10C. It can be seen from Figure 5.12a, that the energy density of the variant with the higher available specific active surface area, representing the lower degree of dispersion ($S_{V,2.5\ ms^{-1}} > S_{V,6.25ms^{-1}}$, see Figure 5.3a), is higher irrespective of the C-rate. The reason behind this observation is the higher half-cell potential of the 2.5 m s^{-1} variant (as shown in Figure 5.4a) and identical absolute galvanostatic current dictated by the C-rate. A reduction in the UED with increasing C-rate for both variants, as shown in the figure, is associate with lower operational half-cell voltage and higher overpotential associated with the increased galvanostatic current at higher C-rates.
As was the case for the half-cell potential shown in in Figure 5.4a, with rising C-rate the value of the utilizable energy density of the variants seem to converge together. This effect is caused by the increasing influence of the electrical conductivity as was argued earlier. Similar observation was made in Figure 4.3a, confirming the trade-off between surface area and electrical conductivity in dependence of the galvanostatic current. On the contrary, it can be argued, based on the analysis of Figure 5.6, that upon a further increase in current, the UED of the variants is likely to converge even closer. At a significantly high C-rate called the diffusion limited C-rate (DLC), the rate of the intercalation reaction at the active material surface is bound to no longer be the limiting factor for the utilizable energy, rather the restricted ionic diffusion in the pore space of the half-cell.
Figure 5.12b, shows the utilizable power density (UPD) of the variants chosen for performance evaluation. An increase in the power density with increasing current is expected, due to the increase in absolute galvanostatic current with the C-rate. Further, due to the higher half-cell potential achieved for the 2.5 m s^{-1} on account of its higher available active surface area, it is capable of delivering higher power. Moreover, the difference in the UPD increase with increase in the C-rate despite the reduced difference in the half-cell potential of the variants, as the half-cell power is an outcome of the multiplication of the potential and the increased galvanostatic current.
Conclusively, a higher specific active surface area, available at a lesser dispersed state of the conductivity additive indicated by the tip speed 2.5 m s^{-1} in Figure 5.1, is favourable for the high-power cathode. The higher availability of active surface at the lesser dispersed state, ensures lower overpotential and higher half-cell potential leading to better energy output at all investigated C-rates. Moreover, as is evident from the higher power density of the variant, the achieved electrical conductivity of the variant is sufficient. This further suggests that the energy expended in the mixing process to thoroughly disperse conductivity additives within the cathode microstructure of the high-power cathode variants examined in this study is unwarranted.

5.3.2 High-Energy Application

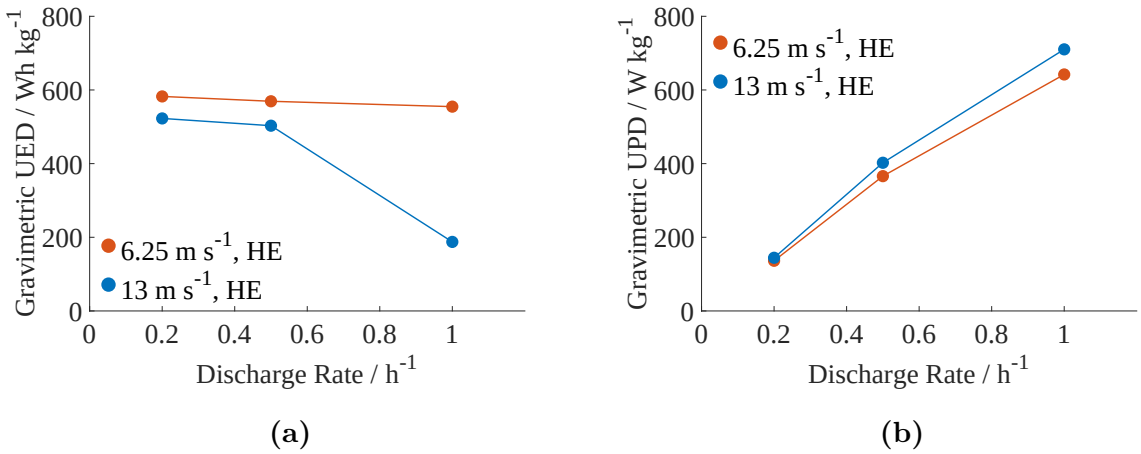

Figure 5.13: Performance determinants for the high-energy application variants: a) Gravimetric utilizable energy density b) Gravimetric utilizable power density.

In this section, the gravimetric performance analysis of the high-energy cathode variants has been presented. Figure 5.13, depicts the progression in gravimetric performance determinants, with increasing C-rates adequate for high-energy application: 0.2C, 0.5C and 1C. In Figure 5.13a, the UED of the investigated variants with significantly contrasting characteristics, $S_{\mathrm{V,6.25\ m\ s^{-1}}} > S_{\mathrm{V,13\ m\ s^{-1}}}$ and $\kappa_{\mathrm{eff,6.25\ m\ s^{-1}}} < \kappa_{\mathrm{eff,13m\ s^{-1}}}$ (see Figure 5.8a), is depicted. It can be inferred from the figure that until C-rate $\leq$ 0.5, the difference in the UED of the variants is comparatively small. Similarly in Figure 5.13b, only minor differences in the UPD can be seen until 0.5C. The observed differences are small, due the to the ability of the 13 m s^{-1} variant to make up for the increased overpotential on account of its smaller active surface than the 6.25 m s^{-1} variant, with its significantly better electrical conductivity. This is evident from the near identical half-cell potentials of these variants in Figure 5.9a, until 0.5C. Nonetheless, the observed differences in UED, are on account of the lower DOD reached for the 13 m s^{-1} in comparison, leading to low energy output following Equations 3.38 and 3.40. Conversely, its slightly higher UPD, is a result of its higher half-cell potential (see Figure 5.9a).

At the highest C-rate for the high-energy application (1C) however, a sharp decline in the UED of the 13 m s^{-1} variant can be seen in Figure 5.13a. This is because under the latter operational mode, the variant is driven into a diffusion limited state as is evident from the lithium concentration distribution in its regions, shown in Figure 5.11. Consequently, a large portion of its capacity remains un-utilized due to the considerably low DOD achieved, as was seen in Figure 5.9a. Thus despite is higher half-cell potential at 1C (see Figure 5.9a), it is able to deliver much lesser energy than the 6.25 m s^{-1} variant. On the contrary, an increase in the UPD of the 13 m s^{-1} variant is evident from Figure 5.13b.

The increased power here, is however indeed a result of the higher half-cell potential of the variant leading to an increase in the the product of half-cell potential and galvanostatic current, which scales with increase in the C-rate. Finally, the overall decrease in the UED and increase in UPD with increasing current as seen in Figure 5.13, for both the variants, is a consequence of the increasing galvanostatic current and the consequent lower half-cell potential, as argued for the high-power application.
Summarizing these findings with regard to the optimal state of dispersion or active surface availability for the high-energy application, the following argument can be made: Although the 13 m s^{-1} variant, exhibiting the highest degree of dispersion, always achieved the lowest DOD and the combination of the highest C-rate with the highest degree of dispersion lead to a diffusion limited state, this can be mitigated simply by increasing the porosity of the half-cell. However, given the scarcity of the conductivity additive, which is inherent to high-energy cathode design, achieving uniform dispersion throughout the full thickness of the half-cell is essential. This can be accomplished by using higher tip speeds during mixing, which promotes adequate electrical conductivity through enhanced dispersion. This will ensure that at lower range of the high-energy application C-rates ($\leq$ 0.5C) the loss of surface will be compensated by the electrical conductivity, while at higher currents the loss of energy due to ohmic losses can be kept under check. In the context of high-energy cathodes, where there is a significantly higher content of active material, ample active surface area is available. Therefore, the increased dispersion, which compromises some active surface area to enhance electrical conductivity through greater energy input in the mixing process, is justified, contrary to high-power applications.

5.4 Recommendations

Under the assumption of the operation of high-power cathodes at C-rates lower than the diffusion limited C-rate (DLC), the availability of the active surface is the most significant limiting criterion as discussed in Section 5.2.1. Hence, a lower degree of dispersion of the conductivity additive ensuring more surface area per unit volume of the active material is favorable for this application. Moreover, the evaluations in Section 5.2.1 demonstrate that the effective electrical conductivity of the cathode variant with the lowest dispersion degree remains sufficient even at the highest C-rate. This indicates that electrical conduction is assured in high-power cathodes due to the ample presence of the conductivity additive. Thus, even with the rising importance of electrical conduction at the higher currents the variant with higher specific active area but lower conductivity performs the best. Therefore, increased energy input into the mixing process to increase dispersion of the conductivity additive in the cathode microstructure, is not justified in the case of high-power cathodes.

In case of the high-energy application however, it was observed that the surface area plays a subordinate role and the performance of the investigated variants was limited by the transport limitations. Evidence based on the progression of half-cell potential of the high-energy variants, suggests that under the consideration of improved ionic diffusion e.g. with increased porosity, such that significant quantity of the cathode capacity doesn't remain un-utilized, the improvement in the electrical conductivity of the cathode at the expense of the specific active surface area could prove to be beneficial. Thus for the high-energy application, where the cathode design grants abundant active surface, higher degree of dispersion to improve the electrical conductivity, is more desirable. This implies that investing higher energy in the mixing process to establish a well dispersed electrical network is crucial for high-energy cathodes.

Thus dependent on application, the performance determining reactions at cathode active material surface are either limited by the availability of the active surface or by the transport of the reactants to the active surface. In a bid to improve the latter, numerous publications [49, 133] have pointed out that ionic transport in the pores space of the cathode can be improved by a favourable gradient in the distribution of the conductivity additive in the thickness of the cathode. Herein, by increasing the conductivity additive content in the direction of the current-collector, the size of pores close to the anodic source can be increased, allowing for an easier passage for the lithium-ions through the thickness of the cathode. Subsequently, in order to achieve improved electrical percolation in cathodes, without significantly increasing the passive material content, to preserve the active surface, conductivity additives with high aspect ratios and hence lower percolation threshold e.g. Graphite have been employed in recent years [22].

Finally, the diffusion limited state, is governed by the diffusion limited current (DLC) in close relation to the porosity of the half-cell. The following chapter hence, explores the influence of mixing process on the porosity of the half-cell in combination with changing galvanostatic current.

Chapter 6

Investigations on Conductivity Additive Comminution in Intensive-Dry Mixing

In this chapter, intensive-dry mixing of cathode components has been investigated with regard to its influence on the microstructure and the electrochemical performance, using the numerical method established in this work. To ensure a direct causality of the mixing process, a completely solvent-free means of cathode production was assumed, such that only the dry mixing of components had an influence on the investigated cathode microstructures. The influence of intensive-dry mixing on cathode microstructure was quantified by means of the easily measurable property: bulk density, representing the progress of the conductivity additive comminution in a mixer. In addition, a coating factor accounting for the dry coating of the conductivity additive on the active material surface, was also considered. At first, the groundwork for half-cell variants depicting different stages of intensive-dry mixing has been established. Followed by, characterization and performance evaluations dictated by the numerical method. Lastly, evaluations on energy density and power density of the variants were employed to initiate discussion on the **third objective** of this work, the **determination of optimal half-cell porosity**.

6.1 Numerical Modelling of the Mixing Process

This section deals with the method adopted to transfer the implication of experiments on intensive-dry mixing of active material and conductivity additive to a numerical model. At first, a method for the generation of coarse grained particulate structures, representing possible states of deagglomeration of the conductivity additive during intensive-dry mixing with the active material has been presented. Followed by, discussions on a param-

eterization aimed at reflecting the consequences of the mixing procedure on the numerical characterization and performance evaluation established in Chapter 3.

6.1.1 Coarse Grained Particulate Structures

In order to characterize the behavior of dry mixtures of cathode components: active material (NMC 622) and conductivity additive (carbon black) subjected to intensive dry mixing, Ms. Jasmin Lisann Kappes, M.Sc., conducted experiments at Maschinenfabrik Gustav Eirich GmbH & Co. KG, Hardheim. The experiments were performed in an Eirich-Intensive-Mixer, with varying mixing intensities (adjusted by changing the tool speed) and different sizes of the mixing apparatus (by varying the volume). The bulk density of the dry mixture was measured at regular intervals to track the progress of carbon black comminution in the mixer.
Consistent with the observations made by Bockholt et al. [43] and Mayer et al. [56], an increase in the bulk density of the dry mixture related to the breakage of carbon black particles (aggregates/agglomerates) with increasing time and intensity, could be recorded in these experiments. Moreover, a visual proof of the occurrence of the phenomenon was presented in form of SEM images. In their publication elaborating on these findings, Lischka et al. [57] showed, that the progression of bulk density was self-similar across different mixing intensities and mixer sizes, such that an empirical relationship could be established between variable mixing parameters and the attained bulk density of the dry mixture. Thus, it could be argued that the bulk density of the dry mixture, achievable through different set of mixing parameters (e.g. time, tool-speed), represents a characteristic state of carbon black in the mixture, which in turn can be correlated to the specific energy input into mixing [57].
In order to model this state of the conductivity additive and its impact on the cathode microstructure, a DEM workflow was developed in cooperation with Mr. Clemens Lischka, M.Sc.. It is essential to note, that the following DEM workflow differs from the particulate structure generation method established previously (see Section 3.1.1) and was used only for the investigations presented in this chapter. Owing to the extremely small size of carbon black particles [96], it is computationally infeasible to account for all the conductivity additive particles needed for the construction of a cathode of realistic thickness, in DEM simulations. Thus, 200 particles were considered to comprise a single particle in the following evaluations. This ratio between the size of the bigger virtual particle and the real particle is often called the coarse graining factor and has been used extensively in the study of cathodes microstructures, as elaborated in Section 2.2.2.
Subsequently, in order to obtain particulate structures resembling cathodes microstructures for the purpose of the following investigations, the constituents where filled into a simulation box of the dimension $22 \times 22 \times 22$ mm, as illustrated in Figure 6.1. The box

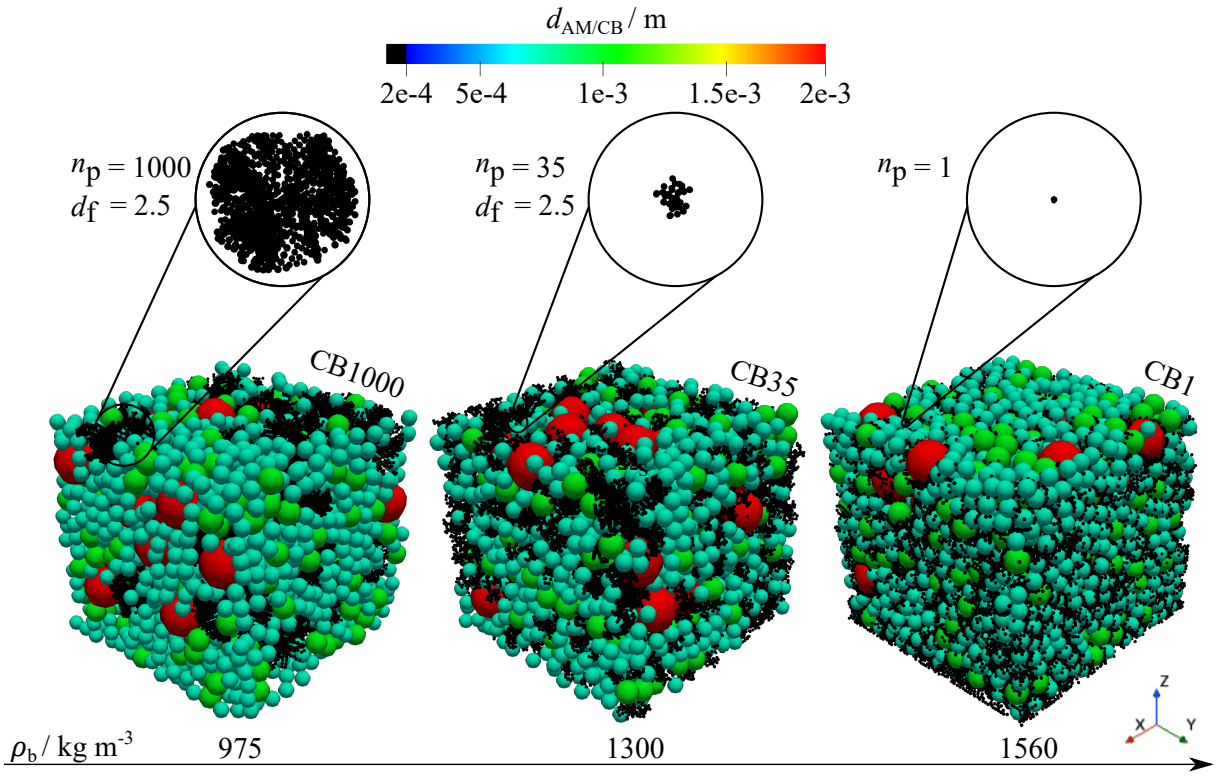

Figure 6.1: Coarse grained particulate structures generated by Lischka et al. [57]. The simulation box (22 × 22 × 22 mm) has been omitted for the sake of clarity. The color-bar (top) represents the coarse grained particle size distribution (scaled by a factor of 200) of the active material. Carbon black particle shown in black, posses the same coarse grained primary particle diameter.

was completely filled with the mixture, ensuring a mass fraction ratio of 98:2 wt-% for the active material to carbon black, using the commercial software Altair EDEM 2022®. The active material particles were modelled as smooth dense spheres as in the previous chapters, however in this chapter a particle size distribution was implemented for them [57], evident from the color-bar in the latter figure. Moreover, the density of these particles was adjusted to account for the coarse graining, such that the bulk density of coarse grained active material particles in a given volume is same as that of real NMC 622 particles, resulting in the coarse grained density $\rho_{AM}^{CG} = 3112$ kg m^{-3}. On the other hand, the carbon black particles were modelled using multi-spheres, generated by means of the tunable dimension method to form fractal shapes, elaborated in Section 4.2. Hereby, d_f was set to 2.5, $d_p = 1\mu$m or 0.2 mm upon coarse graining and n_p was varied resulting in three distinct variants, depicting different stages of carbon black comminution. The nomenclature of these variants: CB1000, CB35 & CB1, has been chosen to reflect the number of primary particles that comprise an individual carbon black agglomerate (see Figure 6.1). The coarse grained density of carbon black determined similar to the active material, amounts to $\rho_{CB}^{CG} = 738$ kg m^{-3}.

Table 6.1: Structural properties of the coarse-grained cathode geometries generated by the filling simulations [57].

Variant Name	Bulk Density / kg m^{-3}	Porosity / %	Total Particles / -	Tortuosity / -	Sp. Active S. Area / mm^{-1}	Eff. El. Conductivity / S m^{-1}
CB1000	975	60	31639	1.33	2.73	0.16
CB35	1300	57	35059	1.35	2.68	0.18
CB1	1560	29	52136	2.41	1.44	1.53

The interaction of the dry mixture components among themselves as well as with the simulation box, in the filling simulations, was modelled based on friction coefficients. These friction coefficients dictate the flow behaviour of the cathode mixture in DEM simulations. Calibration of these coefficients was carried out using the methodology published by Lischka et al. [118]. Details on the calibration experiments and ascertained values of the DEM parameters can be found in Reference [57].
In the final step of the structure generation process, the particulate structures, generated from the filling simulations, were compressed under the identical pressure conditions. It is to be noted that the applied pressure in this case, is very moderate and carried out only to emulate pressure conditions to which the dry blends were subjected to in the electrical conductivity experiments, after the measurement of bulk density in Reference [57].
Characteristics of the cathode geometries hence generated, have been tabulated in Table 6.1. It is evident from the data that as the carbon black particle size decreases with reductions in its primary particle number, the bulk density increases and the porosity decreases. Smaller particles seep readily into pore spaces, leading to a denser packing. The bulk densities hence achieved numerically adequately cover domain of the bulk densities observed during experiments under varying mixing conditions in Reference [57].
Since the volume of the simulation box in all cases is the same, the increasing bulk density leads to an increase in the mass of the cathode and hence total number of particles (active material and carbon black), as denoted in Table 6.1. The last three columns of the table, display the results of characterization simulations according to Section 3.2, published in Reference [57]. As is to be expected from the discussion in previous chapters, the tortuosity increases with increase in the bulk density and decrease in porosity. In addition, the increased dispersion of the conductivity additive, as n_{p} reduces, leads to a reduction in the available specific active surface area due to the increased carbon black and active material interaction. Finally, the increased dispersion accompanied by increased mass of both the mixture constituents leads to an increase in the numerically evaluated effective electrical conductivity, due to the rising electrical contacts, when using the parameterization denoted in Table 3.3.

6.1.2 Parameterization

In order to asses the quality of the connections established in the cathode mixture after intensive-dry mixing, Ms. Kappes carried out conductivity measurements on the dry blends. The details on these experiments have been elaborated in Reference [57]. In Figure 6.2a, the conductivity measurements for the domain of the mixture bulk density relevant for this study have been depicted. It is evident from the figure, that the powder conductivity representing the effective conductivity of the bulk, decreases with increase in the bulk density, irrespective of the mixing tool speed. Similar observation was also made by Bockholt et al. [50] for uncalendered cathodes, who are argued that the loss of conductivity was due to a loss of secondary contacts at cost of primary contacts, referred to as long range and short range contacts respectively by the author. The concept of primary and secondary contacts as well as their significance was previously highlighted in Section 3.2.1. Concurrently, it is apparent from the analysis of the contacts of the cathode geometries generated previously (see Figure 6.1) that the CB-CB contacts or secondary contacts reduce and the CB-AM or the primary contacts increase, with the increased bulk density as shown in Figure 6.2b. In the figure, the number of contacts have been normalized by the total number of particles to ensure comparability among variants with difference in total particle count (see Table 6.1). As is to be expected, the AM-AM contacts per particle remains the same, as no fractioning of the active material takes place.

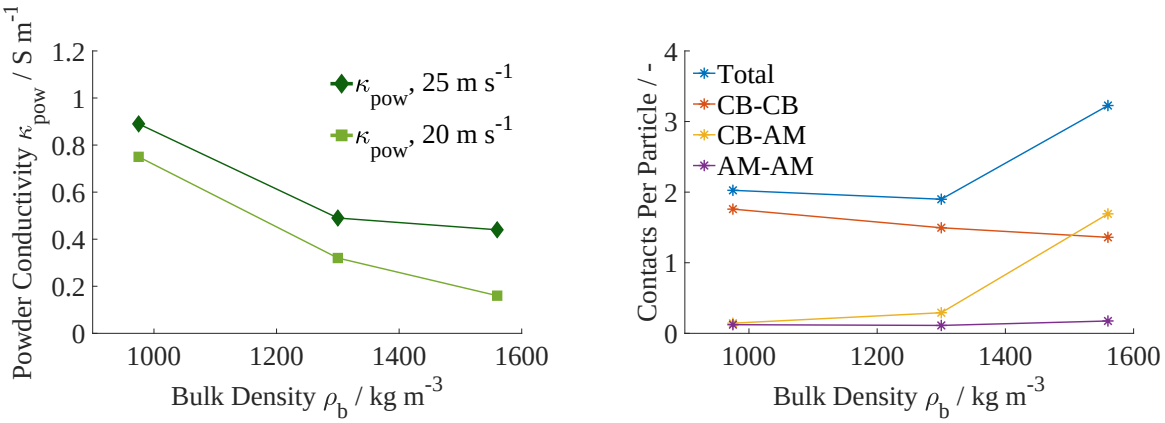

Figure 6.2: Evaluation of electrical connections [134]: (a) Measured powder conductivity (Courtesy Lischka et al.) (b) Contacts evaluated per particle in the particulate structure from DEM simulations.

Hence, the generated particulate structures are capable of mimicking the progression of contacts in cathode component mixtures subjected to intensive-dry mixing. However, as can be read from Table 6.1, the effective electrical conductivity evaluations carried

out for these structures, using the parameterization and numerical method established in Chapter 3, exhibited an increase in the conductivity with increased bulk density. The reason for the observed discrepancy between the experimental and numerical results, is two-fold. Firstly, for the computationally generated variants, the mass of the cathode components increases with increase in the bulk density due to the identical volume occupied by the variants, contrary to the electrical conductivity measurement where the mass of the powders was held constant. The increased mass leads to an increase in the total contacts (see Figure 6.2b), which enhances the electrical conductivity. Finally, the numerical method established in Section 3.2.1, does not account for the contact resistances of the individual contacts. It can contemplated that the resistance to current flow at CB-CB contacts, connecting particles with superior conductivity, is significantly lower than the CB-AM contacts, that link a conducting (CB) and a partially insulating material (AM). Hence, the loss in conductivity due to increased conduction through primary pathways (see Figure 3.7), involving both the active material and the conductivity additive, instead of secondary pathways comprised of only the conductivity additive, are not reproducible as the bulk density increases. Moreover, the numerical evaluation of the effective electrical conductivity was carried out using the parameterization denoted in Table 3.3, which may not be valid universally under all mixing conditions.

Furthermore, a notable increase in the measured powder conductivity was observed with increasing intensity of mixing (increasing tool speed), as shown in Figure 6.2a. This enhancement in conduction can be attributed to the phenomenon of coating of the conductivity additive on the active material during intensive-dry mixing, known to improve the conduction properties of cathode active materials [135]. Given that the proportion of conductivity additive coated on the active material is small, a noticeable change in the electrical conductivity is achieved by improvement of the localized electrical conduction of the active material without a considerable change in the bulk density. Since, the development of a new model accounting for the aforementioned phenomena along with a mixer specific parameterization were not feasible given the time constraint of this work, the measured value of the bulk density was adopted as an initial approximation of the intrinsic conductivity of the bulks investigated.

Finally, in order to account for the influence of changing intensity on the performance of the half-cells, to be constructed from the previously generated particulate structures, a coating factor f_c, was introduced. Although, the coating phenomenon leads to an increase in the electrical conductivity, evidence can be found in contemporary literature [44, 136] that at a certain threshold, the coated conductivity additive could significantly impede the intercalation process taking place on the active material surface. Thus, the factor f_c, was modelled as a mixing intensity dependent parameter, fitted to reflect the adverse effects of active material coating in the performance evaluations. In doing so, the fractional

change in powder conductivity extracted from Figure 6.2a, at constant bulk density but increased intensity was adopted as an estimate for the coating phenomenon. Hence, the coating factor at the higher intensity is stated as:

$$f_{\mathrm{c}}^{\rho_{\mathrm{b},25}} = \frac{\kappa_{\mathrm{pow}}^{\rho_{\mathrm{b},25}}}{\kappa_{\mathrm{pow}}^{\rho_{\mathrm{b},20}}} \tag{6.1}$$

Herein, $\kappa_{\mathrm{pow}}^{\rho_{\mathrm{b},25}}$ represents the powder conductivity measured at tool speed 25 m s^{-1} and $\kappa_{\mathrm{pow}}^{\rho_{\mathrm{b},20}}$ the powder conductivity at tool speed 20 m s^{-1} at a given bulk density ρ_{b}. It was further assumed that no significant coating takes place for the lower intensity, such that $f_{\mathrm{c}}^{\rho_{\mathrm{b},20}}$ is always unity. The values of the coating factor have been tabulated in Table 6.2. Subsequently, the factor f_{c}, was applied to scale the Butler-Volmer reaction rate k_{BV} (see Table 3.3) in Equation 3.28, thereby inversely scaling the intercalation reaction at the active material surface, in dependence of the coating at a given bulk density and intensity, as denoted in the table. Hence, at higher intensities, k_{BV} decreases proportionally to the increase in the powder conductivity, while at lower intensities, its value remains constant.

Variant Name	Bulk Density/ kg m^{-3}	$f_{\mathrm{c}}^{\rho_{\mathrm{b},25}}$ / -	$k_{\mathrm{BV}}^{\rho_{\mathrm{b},25}} = \frac{k_{\mathrm{BV}}}{f_{\mathrm{c}}}$ / A m$^{2.5}$ mol$^{-1.5}$	$f_{\mathrm{c}}^{\rho_{\mathrm{b},20}}$ / -	$k_{\mathrm{BV}}^{\rho_{\mathrm{b},20}} = \frac{k_{\mathrm{BV}}}{f_{\mathrm{c}}}$ / A m$^{2.5}$ mol$^{-1.5}$
CB1000	975	1.18	$1.24{\cdot}10^{-6}$	1	$1.47{\cdot}10^{-6}$
CB35	1300	1.53	$9.6{\cdot}10^{-7}$	1	$1.47{\cdot}10^{-6}$
CB1	1560	2.75	$5.24{\cdot}10^{-7}$	1	$1.47{\cdot}10^{-6}$

Table 6.2: Coating factor as a function of bulk density and intensity

6.2 Impact of Solvent-Free Intensive-Dry Mixing

In this section, at first, assumptions required to transform particulate structures derived from the numerical modeling of the mixing process in the preceding section, into computational half-cells are introduced. These transformations are aimed at the generation of half-cell variants, suitable for the numerical method established in Chapter 3. Subsequently, the results of the characterization following Section 3.2 and the performance evaluations following Section 3.3, are discussed.

In order to account for microstructural changes inflicted solely by the mixing process, the half-cells were numerically constructed under the consideration of a solvent-free process [15]. This allows the exemption of microstructural changes caused by the migration of the binder during the drying process [137]. The solvent-free manufacturing processes, partic-

ularly involving the use of binder fibrillation are associated with very low binder content [18]. Moreover, under the assumption of fully fibrillated state, i.e. when all the binder particles have been stretched into long thin filaments during mixing, their influence on the cathode microstructure is marginal. This is exemplified by the thinly stretched binder filaments and active material particles, shown in Figure 6.3. Contrary to the composites of carbon black and binder formed in the conventional-wet process (see Figure 2.2), modelled as the CBD in previous chapters, binder filaments are not expected to significantly influence microstructural characteristics. Therefore, it can be reasonably inferred that the presence of the binder in such a state, does not exert a noteworthy influence on the cathode performance. Consequently, no compelling requirement to explicitly account for the binder in the performance evaluation of half-cells was assumed. In addition, the investigations were restricted to the study of uncalendered cathodes, avoiding the consideration of microstructural changes caused by the calendering process.

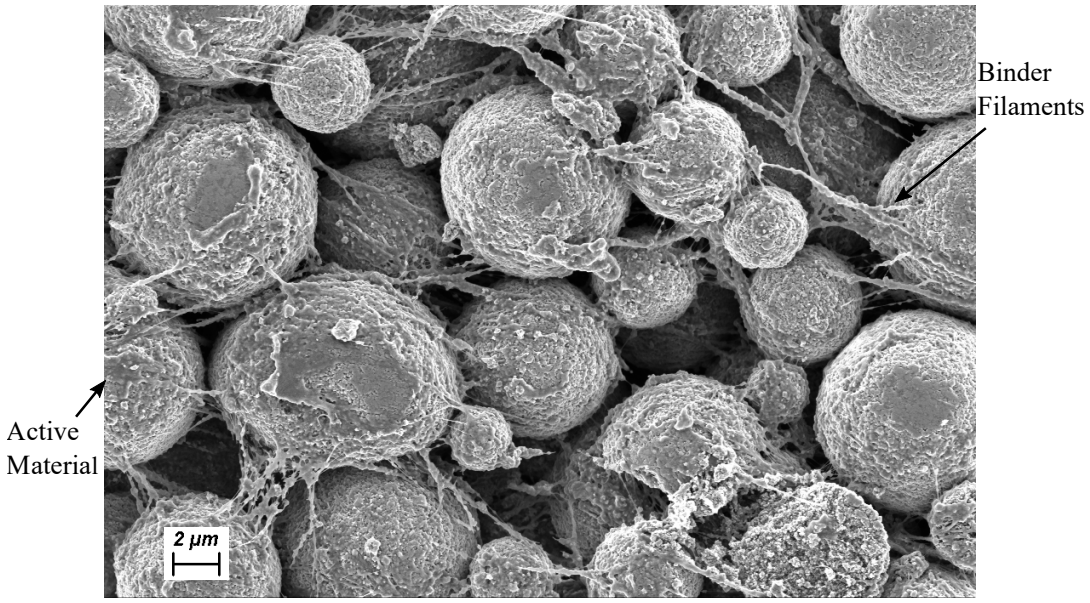

Figure 6.3: Exemplary visualization of binder filaments and active material particles. The SEM image was taken in cooperation with Institute of Applied Materials - Energy Storage Systems, Karlsruhe Institute of Technology.

Thus, under the stated assumptions, the particulate structures resulting from the intensive-dry mixing of the active material and carbon black discussed in the previous section, could be directly transformed into half-cell geometries following the procedure stated in Section 3.1.2. However, investigations on transport process in the computational domains of the half-cell variants, using the resolved electrochemical model presented in Section 3.3, necessitated a downsizing to the microscale. This adjustment was deemed necessary because achieving resolved concentration and potential distributions at the coarse-grained scale would demand impractical computational resources. Thus, scaling the half-cell back to the microscale was considered a pragmatic compromise.

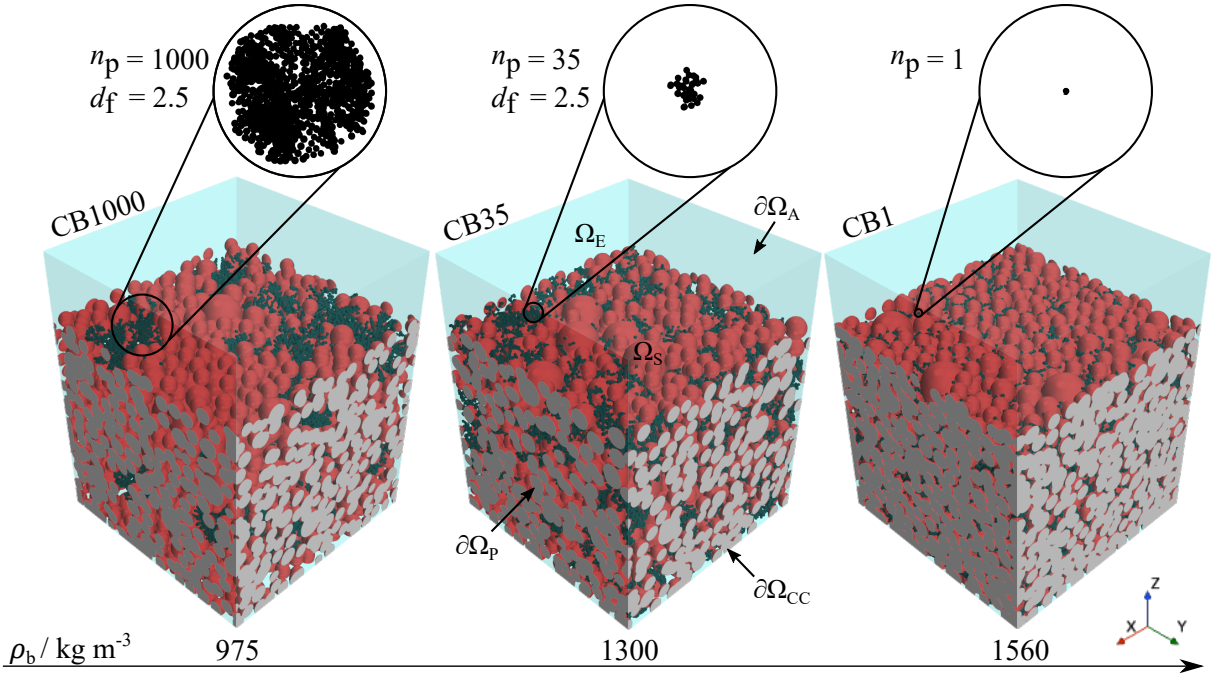

Figure 6.4: Idealized half-cell computational domains with variation in bulk density ρ_b. The areas marked with circles are zoomed into, to show the carbon black agglomerate structure at a given bulk density. The red and black spheres comprise the solid region and the electrolyte region is present in the pores of the solid and above it shown in blue [134].

The computational domains with variation in bulk density hence constructed, have been visualized in Figure 6.4. In the figure, all the active material particles exhibit the same color contrary to Figure 6.1, to highlight the active surface. The shown domains, posses an identical lateral dimension of 110×110 µm. However, the height of the cathode domain, attained after moderate compression to match the electrical conductivity measurements, is dependent on the bulk density, as documented in Table 6.3. Despite the increase in the dispersion of the conductivity additive in the half-cell with increasing bulk density, a decrease in the volume specific total surface area can be observed from the data in the table, due to the increased mass and hence volume of the solid mixture in the filling simulation box.

Table 6.3: Structural properties of the half-cell computational domains scaled back to the microscale.

Variant Name	Bulk Density / kg m^{-3}	Cathode Height / µm	Total Sp. Surface Area / µm^{-1}	Cathode Volume / µm^3
CB1000	975	105.33	0.73	502501
CB35	1300	103.57	0.71	539254
CB1	1560	102.64	0.51	878083

In order to represent different mixing intensities using the computational domains shown in Figure 6.4, the measured powder conductivities from Figure 6.2a were incorporated as spatially constant electrical conductivities in the cathode domain Ω_S of the half-cells. Contrary to the previous chapters, wherein the conductivities of carbon black and active material (from Table 3.3) were used to assign values to their respective particles, leading to a spatially inhomogeneous distribution of the electrical conductivity in the cathode domain, the experimental powder conductivity was assigned as the homogeneous conductivity of the entire bulk, in this chapter.

Thus, depending on the assigned spatially constant conductivity, each of the variants in Figure 6.4 represents two different dry mixing intensities characterized by the tool speed: 25 m s^{-1} and 20 m s^{-1}. It is to be noted here, that a particular combination of spatially constant conductivity and bulk density (see Figure 6.2a) was achieved at a different time interval during the mixing process, depending on the intensity of mixing. Owing to the correlation between the energy input into mixing and the achieved bulk density of the dry mixture [57], the higher intensity is able to achieve a higher bulk density in a given time on account of the higher energy input.

Moreover, the achieved conductivity at the higher intensity is higher, as was discussed in Section 6.1.2. Thus, at the higher intensity of mixing, a coating factor f_c was employed, in addition. Since, no physical quantification of the coating phenomenon could be carried out within the scope of this work, both cases of explicit consideration of the coating factor and the absence thereof have been considered to retain objectivity.

Therefore, the three half-cell variants with changing bulk density based on the state of the conductivity additive along with two intensities and consideration of coating factor for three variants at the higher intensity, constitute the nine variants investigated in this chapter.

Characterization

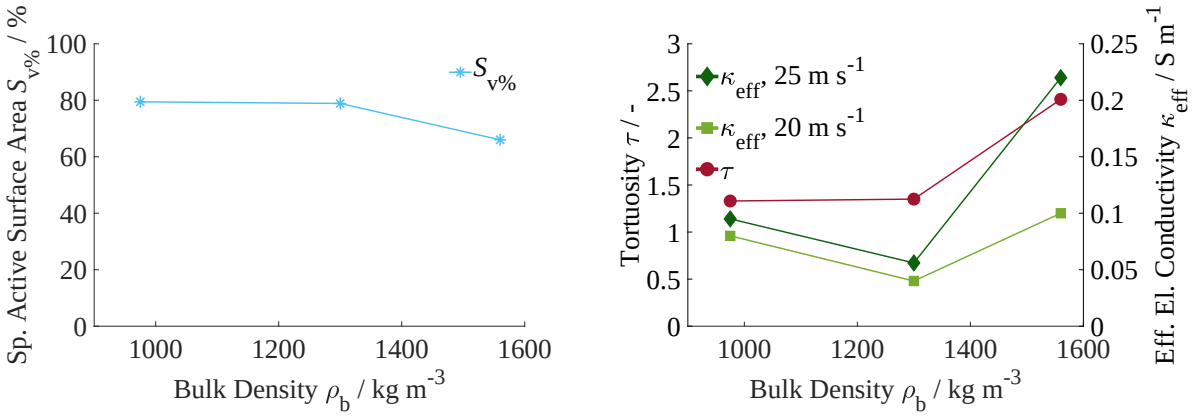

Figure 6.5: Characterization of the half-cells [134]: a) Available active surface area as a percentage of the total surface area (Table 6.3) b) Tortuosity (left axis) and effective electrical conductivity (right axis) at changing tool speeds.

In Figure 6.5a, decrease in the percentage of total specific surface area available for intercalation, as a consequence of the increased dispersion of the conductivity additive with increasing bulk density in the half-cell, has been displayed. Due to the increased dispersion, the interaction between the conductivity additive and the active material increases, confirmed by the increasing CB-AM contacts shown in Figure 6.2b. In turn, increased CB-AM contacts imply the coverage of the active surface by the conductivity additive, leading to a reduction in the available active surface.

Similarly, the trends in the conduction characteristics can also be elucidated by means of the contact analysis presented in Figure 6.2b. The increased total contacts associated with increased dispersion at higher bulk density, present increased obstruction to the movement of lithium-ions. Moreover, at higher bulk density the porosity is lower. Thus an increase in the tortuosity is observed on the left axis of Figure 6.5b. Since the structure of the variants remains same at changing intensity, three data points are sufficient to represent the entire domain of investigation with regard to τ and $S_{V\%}$.

Conversely, the increased total contacts have a positive impact on the effective electrical conductivity. However, since the spatially constant conductivity of the half-cells, dictated by the powder conductivity, decreases with increasing bulk density (see Figure 6.2), a decrease in κ_{eff} is seen at first, with increasing bulk density upto $\rho_b \leq 1300$ kg m^{-3} on the right axis of Figure 6.5b. Yet, the sharp increase in the total contacts eventually overcomes the decreasing κ_{pow} leading to a considerable increase in κ_{eff}. Finally, the increment in κ_{eff} seen at the increased intensity, shown by the 25 m s^{-1} variant, is a consequence of the coating phenomenon, complementary to the increment in κ_{pow} in Figure 6.2a.

Performance Evaluation

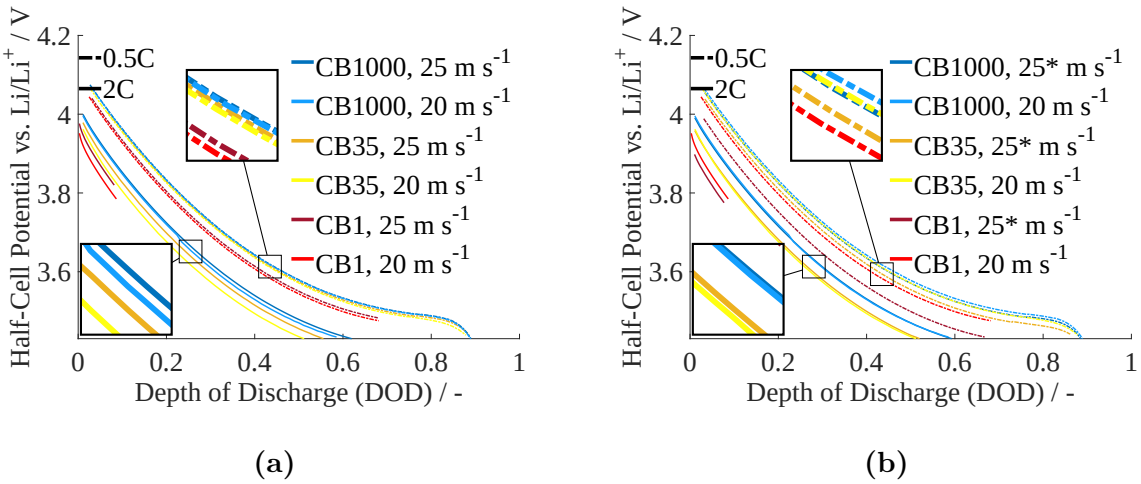

Figure 6.6: Half-cell potential at the cathode current-collector [134]: a) Coating factor not accounted for b) Coating factor accounted for by scaling the Butler-Volmer reaction rate constant.

Leveraging the resolved electrochemical model presented in Section 3.3, the half-cell potentials, evaluated at the current-collector of the investigated half-cells, have been plotted over the depth of discharge (DOD), in Figure 6.6. In the figure, distinct colors represent potential curves associated with the bulk density variants: CB1000, CB35 and CB1. Moreover, within each color category, differing shades represent varying intensities, with darker shade indicating the higher intensity (at a tool speed of 25 m s^{-1}) and lighter shades indicating the lower intensity (at a tool speed of 20 m s^{-1}).
In the Figure 6.6a, the influence of coating has been disregarded. Thus, the spatially constant conductivity taken from Figure 6.2a, is the only differentiating parameter in this figure. In contrast, the potential curves shown in Figure 6.6b, have been evaluated under explicit consideration of the coating phenomenon. Such that, along with the variation in the spatially constant conductivity following Figure 6.2a, the coating factor f_c differentiates the variants. The value of f_c used, can be read from Table 6.2. Since the value of f_c is always unity at 20 m s^{-1}, the potential curves shown for the intensity, are same in both the sub-figures of Figure 6.6. Consequently, the potential curves at 25 m s^{-1}, in Figure 6.6b, with explicit consideration of coating have been demarcated with an asterisk symbol (*) to set them apart from the data at the same tool speed in Figure 6.6a.
The performance evaluations were carried out under two different galvanostatic operational conditions. The C-rate 0.5C was chosen to exemplify high-energy application, depicted as dotted lines in Figure 6.6. While, the C-rate 2C was chosen to represent a high-power application, shown as solid lines in the figure. At lower C-rates, closer to equilibrium potential, there's consistently lower overpotential and higher half-cell potential

(Equation 3.29). Hence, in the Figure 6.6a and 6.6b, the dotted lines always lie above the solid lines. Further, under all C-rates and intensities as well as consideration of the coating factor show in Figure 6.6, the half-cell potential recorded for the lower bulk density variants is higher over the entire depth of discharge. The higher absolute current at a given C-rate due to the larger volume of the higher bulk density variants (see Equation 3.34), along with the increased current density due to the reduced available active surface area (see Figure 6.5a), leads to a higher overpotential according to Equation 3.28. Consequently, the half-cell potential at higher bulk densities is lower (Equation 3.29).
Moreover, it is evident from the half-cell potential evaluations, that despite the considerably improved effective electrical conductivity of the CB1 variant (see Figure 6.5b), its half-cell potential is always the lowest, irrespective of the operational condition, intensity and coating consideration. Hence, it can be inferred that the electrical conductivity plays a subordinate role at constant intensity. With variation in intensity but constant bulk density however, the influence of the electrical conductivity becomes noticeable.
From Figure 6.6a, it is apparent that the lower intensity variants, shown in the lighter shade of the color at a given bulk density, exhibit a lower half-cell potential due to their lower effective electrical conductivity. Poor electrical conductivity in the half-cell, leads to higher resistance to current flow and hence, higher ohmic losses. The loss of potential occurs in direction of the current i.e. the direction opposite to the movement of the electrons. Hence, a lower half-cell potential is recorded, at the current-collector, for the lower intensity variants. Furthermore, since the drop in potential is proportional to the applied current, according to the Ohm's law, an enhanced difference in the half-cell potential curves at changing intensity can be seen at the higher C-rate (2C).
In comparison, the half-cell potential shown in Figure 6.6b, is influenced by a combination of effective electrical conductivity and the Butler-Volmer reaction rate dictated by the coating factor. At the lower C-rate (0.5C), the reduction of the Butler-Volmer reaction rate proportional to the coating factor dominates. Reduced k'_{BV}, implies an increase in the overpotential to keep up the same intercalation current density following Equation 3.28. This in turn reduces the half cell potential. The domination of this effect implies that for the 25* m s^{-1} variants, shown in the darker shade of the color at a given bulk density, the improved conductivity at higher intensity is overcome by the negative influence of the coating and hence the half-cell potential is recorded lower that the 20 m s^{-1} variants, shown in the lighter shade. On the other hand, at the higher C-rate (2C) the influence of the effective electrical conductivity dominates, such that the negative influence of coating with variation in intensity, is compensated by the reduction in the ohmic losses occurring in the half-cell. Therefore, the potential curves of the higher intensity variants coincide with those of the lower intensity variants, except at the highest bulk density where the reduced ohmic loses overcompensate the negative influence of coating.

In order to gain further insights into the transport mechanisms of the investigated half-cells and their dependence on the state of the conductivity additive, lithium concentration in the non-overlapping regions of the half-cell: cathode and electrolyte was investigated. Spatial distribution of lithium in the half-cell is strongly dependent on the interlinked conduction phenomenon. On the one hand sufficient ionic conductivity is essential to conduct the lithium-ions in the electrolyte region from their origin at the anode to the farthest end of the half-cell at the current-collector. On the other hand, adequate electrical conductivity is imperative in the cathode region for the transport of the electrons in the opposite direction starting at the current-collector.

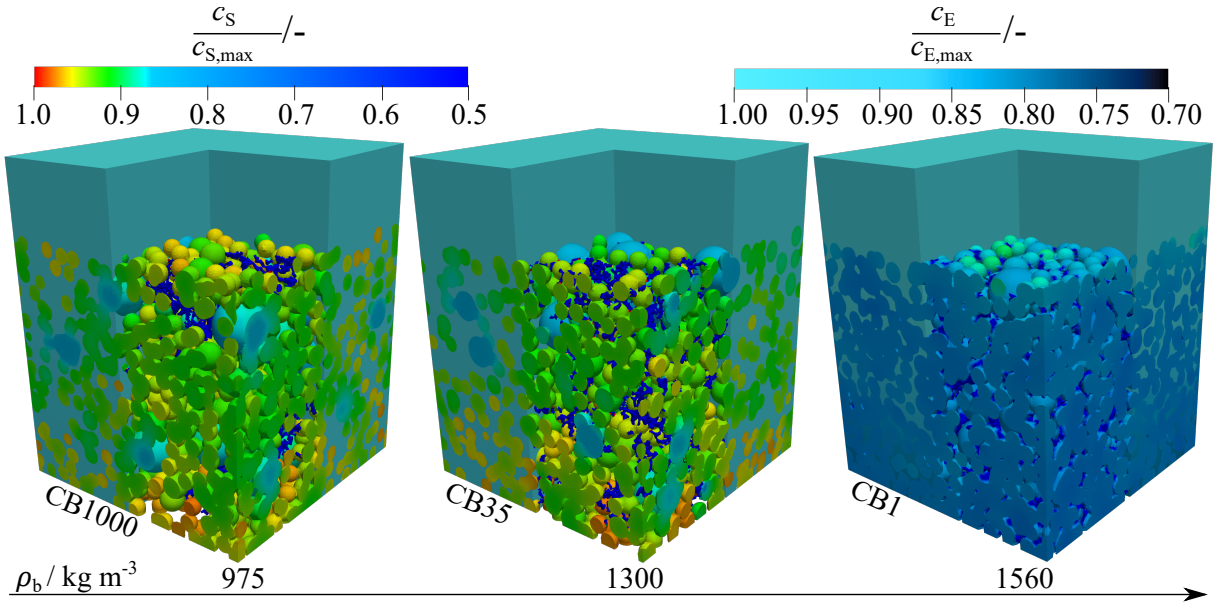

Figure 6.7: Relative lithium concentration distribution in the half cell variants at tool speed 25 m s^{-1}. The electrolyte domain is opened up to reveal the cathode surface. The instance represents the end stages of discharge at 0.5C at an identical DOD = 0.84. Solid concentration is shown on the top left and electrolyte concentration on the top right [134].

To highlight the limitation on the ionic transport in the investigated variants, lithium distribution in the cathode and electrolyte domains of the half-cells, at the tool speed 25 m s^{-1}, has been shown at an instance close to the end of a 0.5C discharge in Figure 6.7. Since, the influence of the electrical conductivity is insignificant at the lower C-rate and the influence of coating is spatially constant, the chosen instance is ideal to emphasise the importance of the ionic conduction. It is apparent from the figure, that while variants CB1000 and CB35 exhibit a rather uniform distribution of lithium along the thickness of the cathode, the CB1 variant shows an increased concentration of lithium at the top of the cathode. Due to the significantly lower porosity of the CB1 variant, denoted in Table 6.1, along with the increased dispersion of the conductivity additive, it exhibits the highest tortuosity among the variants (see Figure 6.5b). Consequently, the lithium-ions

struggle to penetrate the entire thickness of the variant swiftly, leading to a preferential lithium intercalation at the top of the cathode domain. Subsequently, a large portion of the thickness of the CB1 variant remains un-utilized during the discharge. Thus, despite the superior electrical properties of the CB1 variant it performs inferior to the CB1000 and CB35, which posses substantially better ionic conduction indicated by their higher porosity and lower tortuosity. In addition, it is evident from the figure, that smaller active material particles show higher lithium concentration for all the variants. This phenomenon, also observed by Kespe et al. [110], results from increased specific active surface area and reduced diffusion length in smaller particles.

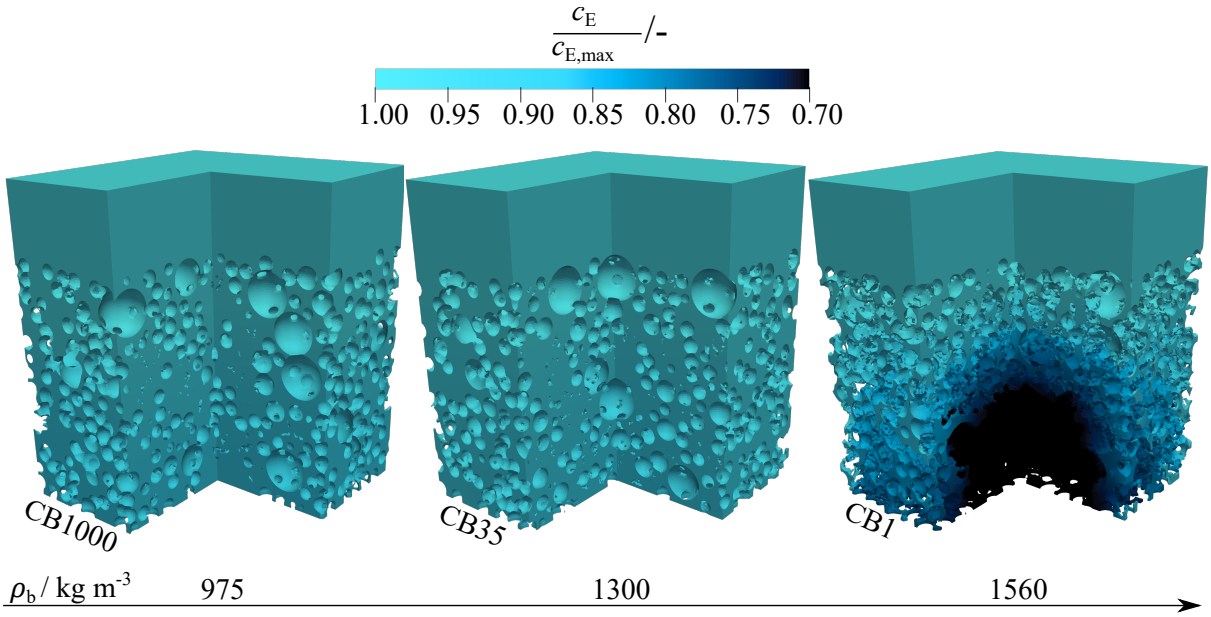

Figure 6.8: Analysis of the resolved lithium concentration distribution at C-rate 2C and tool speed 25 m s^{-1} in the electrolyte region: Lithium depletion caused by the narrow pores of the CB1 variant at DOD = 0.08.

Another consequence of restriction to lithium-ion movement in the CB1 variant, has been displayed in Figure 6.8. As depicted by the black region in the figure, the relative lithium concentration in the CB1 variant, close to the current-collector, appears to have dropped below 30% of the initial concentration. This reduction of the electrolyte concentration in the early stages of a 2C discharge is due to the low porosity and high tortuosity of the CB1 variant. Consequently, instead of relying on the lithium-ions originating at the anodic source, transported through the electrolyte, the intercalation reaction at the active material surface close to the current-collector, consumes the lithium present in electrolyte solution in the narrow pores surrounding it. This consumption of lithium, at higher C-rate take place faster than the replenishment through the ionic flux, leading to depletion. A similar depletion for remaining to variants is absent due to the visibly bigger pores shown in the figure.

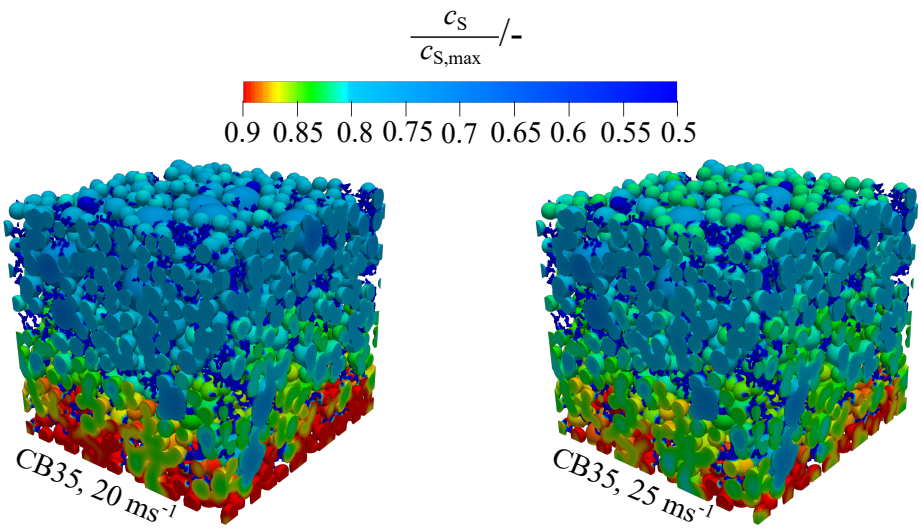

Figure 6.9: Analysis of the resolved lithium concentration distribution at C-rate 2C in the cathode region: Influence of changing conductivity for the variant CB35 with variation in intensity at same the DOD = 0.66.

To highlight the significance of electrical conductivity, lithium concentration in the cathode region of the CB35 variant has been displayed at different intensities in Figure 6.9, at the discharge rate 2C. As was mention in the discussion of the half-cell potentials, the impact of electrical conductivity with variation in bulk density but constant intensity, is insignificant in comparison to conductivity additive dispersion and half-cell porosity. However, at constant bulk density, the increased conductivity with increased intensity leads to a noticeable improvement in the half-cell potential at the higher C-rate. Thus, to emphasise the importance of the electrical conductivity, the comparison in the figure, is limited to the higher C-rate (2C) and the mid-range bulk density variant CB35.
The consequences of improved conduction in the half-cell with increased conductivity can be clearly seen in Figure 6.9. It is evident, that at the higher intensity (25 m s^{-1}), a relatively uniform distribution of lithium takes place in the half-cell in comparison to the lower intensity (20 m s^{-1}). The differences in the lithium concentration of the two variants shown in the figure, are most apparent by a comparison of the concentration attained in the smaller active material particles. While at the higher intensity numerous particles have reached relative lithium concentration ≥ 0.8 across the entire thickness of the cathode, for the lower intensity variant, lithium concentration seems to be concentrated close to the current-collector. This is due to the improved ability of the variant at higher intensity to conduct electrons to the top of the cathode. The improved conductivity ensures lower ohmic losses, hence, a more uniform distribution of the intercalation current (see Equation 3.28). Conversely, for the lower intensity variant, a much higher overpotential exists close to the current-collector. Hence, the intercalation current is concentrated at the current-collector of the half-cell, leading to an accumulation of lithium in this region.

6.3 Application Dependence of Optimal Porosity

The analysis presented in Section 6.2, gives the impression that the lowest bulk density variant (CB1000) performs the best under all operating conditions. Since, bulk density and porosity are inversely related (see Table 6.1), this could lead to the rash conclusion that performance of cathodes always improves with increased porosity. However, it must be noted that the mass as well as the volume of the cathode variants investigated in this chapter, are not the same (see Table 6.3). Since, the absolute current flowing through the current-collector (see Equation 3.34) as well the maximum theoretical capacity of the variants, are both a function of the active material mass, the investigations made until now are inadequate for a direct comparison revealing optimal bulk properties. Thus in the following sections, the volumetric and gravimetric approaches elaborated in Section 3.3.3, were employed to transfer the results of the performance evaluations in the previous section, to identical cell volume and active material mass respectively, ensuring compatibility. In doing so, common performance properties used to compare lithium-ion batteries: utilizable energy density (UED) and utilizable power density (UPD), have been deployed to reveal the application dependent nature of the optimal half-cell porosity, related to the bulk density of the dry cathode mix.

6.3.1 Utilizable Energy Density

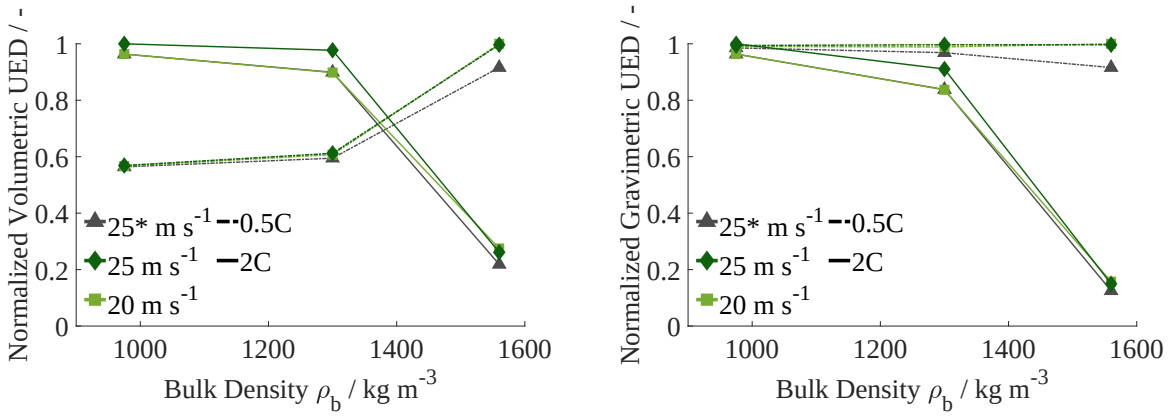

(a) **(b)**

Figure 6.10: Energy density evaluations [134]: a) Volumetric utilizable energy density normalized based on the highest value achieved at the respective C-rate b) Gravimetric utilizable energy density normalized based on the highest value achieved at the respective C-rate.

In this section, evaluations concerning energy density have been presented. In Figure 6.10, normalized values of the utilizable volumetric energy density and utilizable gravimetric energy density have been displayed over the bulk density. The data points in

the illustrations, connected by solid lines, correspond to the C-rate 2C, representing the high-power application and the data points representing the high-energy application at 0.5C, are connected by dotted lines. Further, the normalization was carried out using the highest UED achieved at the respective C-rate. The absolute value of the UEDs evaluated following both the approaches can be found in Appendix C, under Section C.2. Finally, the different intensities indicated by the tool speed in the diagrams have been shown in different shades of the color green, such that the higher intensity is indicated by the darker shade. Moreover, the data points involving the influence of the coating factor at the higher intensity have been shown in gray to set them apart.

In Figure 6.10a, under the consideration of identical volume, following the volumetric approach, it is evident that at the high-energy application (0.5C), UED increases with increase in bulk density and decrease in porosity. This is due to the increased absolute current following through the current-collector, proportional to increased mass of the cathode in the same cell volume with increasing bulk density. The increased current at higher bulk densities overcomes the reduced half-cell potential shown in Figure 6.6, leading to a net increase in the utilizable energy (UE) (see Equation 3.38). Alternatively, denser variants exhibit higher theoretical capacity due to the higher active material content. Subsequently, the increased theoretical capacity compensates for ionic limitations at the higher bulk density variant (CB1) leading to an overall increased UED. Since the influence of electrical conductivity is minor at the lower C-rate, no differences in UED at changing intensities can be seen. Conversely, reduction in half-cell potential on account of coating reduces the UED.

Under high-power conditions at the C-rate 2C however, the ionic transport limitations become significant. Subsequently, the reduced porosity with increasing bulk density leads to severe diffusion limitation in the half-cell, as was indicated in Figure 6.8. As a consequence, the utilizable fraction of increased theoretical capacity at higher bulk densities decreases, leading to a loss in volumetric UED. Since, the influence of ohmic losses also becomes apparent at the higher current the differences in the effective electrical conductivities, at changing intensity, are reflected in the UEDs. Moreover, the UEDs at the higher intensity with inclusion of coating (25^* m s^{-1}) coincide with the lower intensity (20 m s^{-1}), except at the highest bulk density, as was observed for the half-cell potential curves corresponding to 2C discharge, in Figure 6.6b.

These observations are in line with the findings made by Cernak et al. [117]. In their investigations on the optimal porosity of active material particles, Cernak et al. found that, the optimal porosity, corresponding to the highest volumetric UED, shifted to higher values at higher C-rates. Moreover, they identified the occurrence of both the limiting mechanism stated previously: theoretical capacity and diffusion limitation, at a given operational condition by sufficient manipulation of the porosity. Hence, it can be argued

that, the investigated domain of variants at 0.5C are limited by the theoretical capacity, such that the highest bulk density variant exhibits the highest UED, but at even higher bulk density and hence lower porosity, the diffusion limitations will start to dominate due to the spare pore space, leading to reduction in the UED. Similarly, the domain of investigated variants are diffusion limited at the C-rate 2C, such that the lowest bulk density variant produces the highest UED. However, with further decrease in the bulk density the theoretical capacity is bound to dominate, due to the reduced active material content. The bulk density and porosity variations discussed in this chapter can be reproduced using an intensive mixer. Consequently, prior conclusions were predominantly drawn from theoretical considerations.

In contrast to the trends observed in volumetric UED, the highest gravimetric UED is always achieved at the lowest bulk density and hence highest porosity, as shown in Figure 6.10b. Following the gravimetrical approach, the results of the performance evaluations were transferred to identical mass of the active material. Therefore, the theoretical capacity represented by all the data points in the figure at a given C-rate is the same. Since, the utilization of the available capacity at higher bulk density and lower porosity is restricted by diffusion limitation, the best utilization of the capacity always take place at the lower bulk density and higher porosity irrespective of the operational condition. Finally, similar to the volumetric UED, the difference between different intensities only becomes evident at the higher C-rate and the gravimetric UED achieved at 25* m s^{-1} coincides with the gravimetric UED at 20 m s^{-1}.

6.3.2 Utilizable Power Density

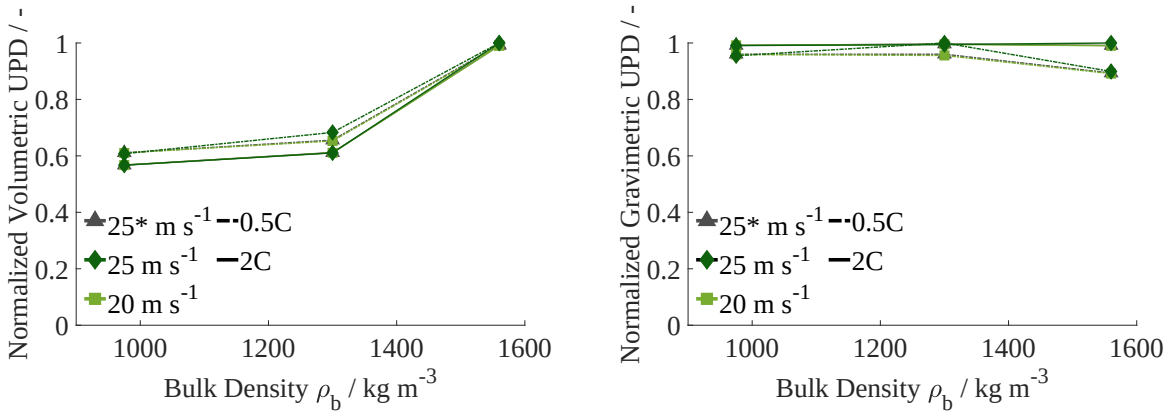

Figure 6.11: Power density evaluations [134]: a) Volumetric utilizable power density normalized based on the highest value achieved at the respective C-rate b) Gravimetric utilizable power density normalized based on the highest value achieved at the respective C-rate.

In this section evaluations pertaining to power density have been discussed. Similar to Figure 6.10, normalized values of utilizable power density with respect to highest UPD achieved at a given C-rate, have been depicted over the bulk density, in Figure 6.10b, using the same color scheme. Moreover, the high-power application data points (2C discharge) have been connected with solid lines and the high-energy application data points (0.5C discharge) via dotted lines. Finally, the absolute value of the evaluated UPDs have also been denoted in Appendix C, under Section C.3.

It is discerned from Figure 6.11a that, UPD increases with increase in bulk density irrespective of the application. Under consideration of constant cell volume, with increase in the bulk density, the active material mass (or volume, since density is constant), and the resulting current increases. Subsequently, there is an increase in power, as power in the half-cell is a product of current and voltage. This increase in current is proportional to the C-rate (see Equation 3.34). Hence, at the higher C-rate the current compensates for the changes in potential caused by intensity and coating, such that UPD increases with increase in bulk density and the data points at different intensities and coating coincide. Conversely, at the lower C-rate, minor differences in UPD are apparent.

While applying the gravimetrical approach, the performance evaluation are transferred to identical mass of the cathode. Hence, in the data points shown in Figure 6.11b, the mass of active material in all the variants is considered to be equal. Equal mass implies equivalent current, following the discussions made previously. At the high-power application, the scaling of current with the mass overcomes the difference in half-cell potential of the variants shown in Figure 6.6. Thus, UPD remains constant at the high-power (2C) discharge. In contrast, differences in UPD can be seen at the high-energy application, when accounting for coating and changing intensity. These minor differences at 0.5C discharge, can be attributed to the differences in half-cell potentials discussed in Section 6.2.

Conclusively, condensing the findings presented, into design principles for cathode manufacturing reveals the application dependent nature of the optimal half-cell porosity. When considering equal cell volume, lower porosity and thus higher active material content, leads to the optimal performance for high-energy application, indicated by the highest UED and UPD attained by the highest bulk density variant at 0.5C. On other hand for high--power application at 2C, the highest porosity variant exhibited the highest UED, while the lowest porosity variant lead to the highest UPD, when considering identical cell volumes. This presents a challenge on determining the ideal porosity. The dilemma as state in Chapter 4, arises from the preferential choice of ionic or electrical conductivity. In case of faster dis-/charging requirement lower porosity and improved electrical conductivity should be preferred. While, improved ionic conduction and higher porosity are desirable to ensure improved energy output. Finally, the highest porosity is always the best suited when identical mass of the active material is take into consideration.

6.4 Recommendations

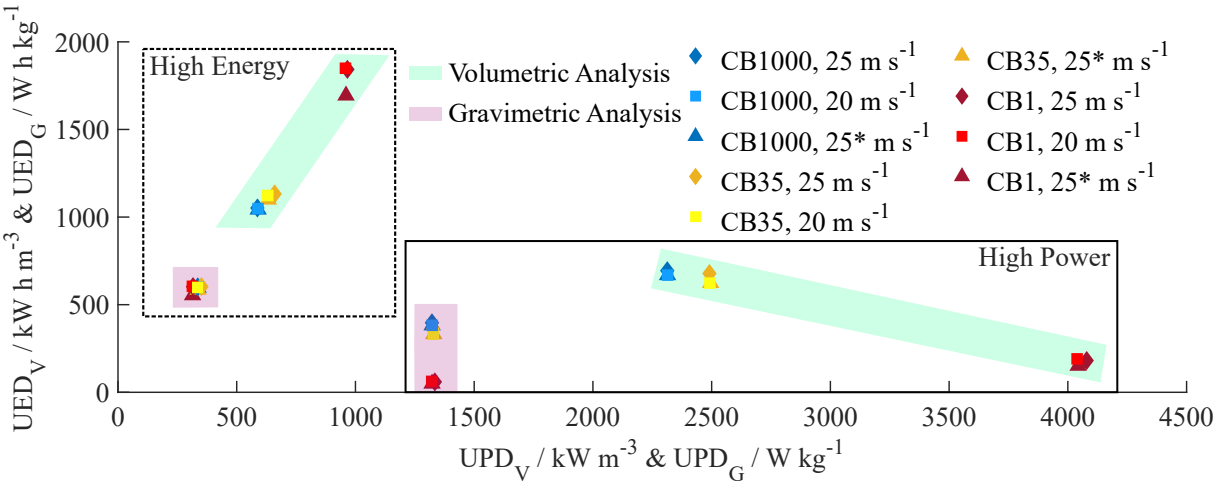

Figure 6.12: Ragone plot showing volume and mass specific performance determinants: energy and power density, for contrasting applications.

The Ragone plot [83], typically used for comparing performance of lithium-ion batteries as well as other energy-storage devices, as shown in Figure 6.12, displays the specific energy and specific power density of the variants investigated in this chapter. The top left of the figure represents the domain of lower current and high-energy application, indicated by the dotted box. While at the right bottom of the plot, the solid box belongs to the high-power application and higher currents. In each of these boxes, the green region represents the volumetric analysis and the pink region, the gravimetric analysis. Finally, the colors scheme as well the labelling of the data points corresponding to the bulk density variants, is identical to Figure 6.6.

Summarizing the findings presented previously, it can be stated that, when the maximum mass of active material that can be used in the cathode is limited, the means of extraction of maximum energy from the cathode constituents is through an increase in half-cell porosity and hence improvement in ionic conductivity. Such consideration are of particular interest due to the raw material scarcity faced by the battery industry [138]. It can be clearly seen in Figure 6.12, within the pink region of the high-power applications, where the specific energy increases with decrease in bulk density at the same specific power, that increased porosity enhances the energy output. The effect is most prominent for the high-power application as with increasing C-rate, the relevance of the ionic limitations increases. Consequently, in the pink region of the high-energy application the data points at changing bulk densities coincide.

On the other hand, if the cell volume is the limiting factor. Which could be possible in case of design of an electric vehicle (EV) battery system designed for longer driving range, but where the volume allocated for it, is fixed. To maximize the energy as well as power

for the high-energy application, the active material and hence the cathode mass should be increased in the allocated space, by an increased bulk density, provided the raw material is abundant. This can be achieved, either by mixing at lower intensity for longer period of time or mixing at very high intensity for a comparatively lesser time, to ensure the deagglomeration of the conductivity additive and hence a denser packing. Subsequently, as seen from green region of the high-energy application in Figure 6.12, a simultaneous increase in specific energy and power density is seen, with increase in bulk density.
Conversely, for identical volume and higher current output, shown in the green region of the high-power application, the highest specific energy is recorded at the lowest bulk density, while the highest specific power results from the highest bulk density. Thus, the increased energy input in the mixing stage, to mix for longer periods of time or with a higher tool speed, is only justified under high-power applications, when power output is preferred over energy. Such might be the case for power tools that require higher power but can be quickly recharged regularly in short intervals. On the contrary if power can be compromised at the cost of energy, as is the case for implantable electronic medical devices that are expected to have a considerably long life while requiring very low power, less denser bulks that can be produced at much lesser mixing effort are suitable.
Moreover, with regard to increasing the specific power output without a significant compromise in specific energy, the intensity of mixing could be exploited. As indicated in discussion of Figure 6.2a, increased intensity increases the conductivity of the blend without an influence on the bulk density. Subsequently, the coating phenomenon could be used to enhance the electrical conductivity of the dry blend without a significant impact on the ionic conductivity, as the porosity remains identical. Although no correlation could be made with the intensity variation investigated in this chapter, it can be theoretically considered that improvement in electrical conductivity of variants with lower bulk density could overcome their inherent low power output. Thus, shorter mixing times and highly intense mixing could lead to the best combination of electrical (due to enhanced active material conductivity via coating) and ionic properties (higher porosity and lesser bulk density, due to lower fragmentation of the conductivity additive) in cathodes. This inference is however theoretical and subject to further investigations.

Chapter 7

Conclusion and Outlook

Conclusion

In this work, the impact of the conductivity additive: carbon black, has been quantified on the performance of lithium-ion batteries using scale resolving electrochemical simulations, performed on the positive half of the lithium-ion battery: the cathode. Hereby, emphasis has been laid on the characterization of modifications made by the conductivity additive on the cathode's microstructure and the entailing effect of these microstructural changes on the performance. For this purpose, a **three-step** numerical method was devised. In the **first-step**, stochastic particulate structures where generated via particle simulations to mimic the cathode microstructure with active component: active material (NMC622) and passive components: carbon black and binder (PVDF). Subsequently, these particulate structures were transformed into two non-overlapping finite volume element domains (cathode domain and electrolyte domain) comprising the idealized computational half-cell, wherein the active and passive components are modelled as perfectly smooth and dense spheres. The stochastic method allows for numerous variations in the cathode microstructure through a change in the conductivity additive size and shape hence, in the **second-step** of the numerical method, the change in the cathode microstructure inflicted by the variations in the conductivity additive were characterized using *performance indicators*. The indicators of performance: effective electrical conductivity, tortuosity and available volume specific active surface area were chosen based on their close correlation to the cathode performance. Finally in the **third-step**, the half-cell was subjected to resolved electrochemical simulations. This allowed for the evaluation of the half-cell potential resulting from the intricate transport processes in the half-cell. Moreover, localized influence of the microstructural change in the cathode could also be observed via the spatial lithium concentration distribution derived from the electrochemical simulations. Furthermore, the performance of the cathode variants was quantified in the form of

performance determinants commonly used to compare energy storage systems: utilizable capacity, utilizable energy density and utilizable power density. The numerical method hence developed allowed for the following investigations:

Fundamental investigations on the influence of conductivity additive size and fractal dimension on cathode performance

In these investigations presented in Chapter 4, the possible change in the shape and size of carbon black, with its impact on the performance indicators and determinants was studied. The alterations in these geometrical characteristics of carbon black were inspired from the quantitative (measured particle size distributions) as well as qualitative (tomographic imaging) analysis of the mixing process found in literature.
In case of the analysis of **size**, the outer diameter of the agglomerates of carbon black and the binder was utilized. In the conventional-wet process considered in this investigation, carbon black forms clusters with the binder during the mixing process, on account of its high specific active surface area. Hence, the two passive materials were modelled together as the so called carbon binder domain (CBD). In the investigations, the composition of the cathode was held constant and size of the CBD agglomerates was varied. It was found, that with decreasing size of the CBD agglomerates, their dispersion in the cathode increases. This lead to an increase in the performance indicator, effective electrical conductivity on account of increased contacts between the CBD and the active material. However, the downside of increased CBD dispersion is the obstruction to ionic conduction evident from the increased tortuosity. Hence, it is concluded that the impact of carbon black dispersion on the two conduction phenomena is interdependent, such that the improvement in one lead to the depreciation of the other. Furthermore, it was observed that the increased dispersion lead to a decrease in the available specific active surface area on account of the active surface occupation by the CBD. The implication of these trends in the performance indicators were reflected in the performance analysis such that the half-cell variant with sufficient dispersion to allow improved electrical conductivity without severely compromising the ionic conduction and active surface, lead to the highest values for the performance determinant: utilizable capacity. Further, varying significance of the different performance indicators with variation in current could be observed. At higher currents the performance was dictated by the transport phenomena while at lower currents the surface area determined performance.
In order to mimic the branched **shape** of carbon black, the concept of fractal dimension was employed. By varying the diameter and number of primary particles, as well as the gyration radius, of the particulate CBD structure while keeping the cathode composition the same, different levels of CBD dispersion were achieved. However, no significant influence on the performance indicators and determinants was observed in the investigation of

compressed half-cells. Moreover, a clear trend in the performance indicators with variation in the fractal dimension was not evident. As a result, the investigations were extended to account for a wider range of fractal shapes while simultaneously removing the influence of compression. Through these investigations, it was shown that, unlike in the study of CBD size where higher dispersion was directly linked to increased effective electrical conductivity, the effective electrical conductivity in the cathode can also be improved using less dispersed, fractal CBD structures. This supports the hypothesis proposed by Bauer et al. [25] that highly fractal structures can enhance electrical conductivity in lithium-ion battery cathodes. Furthermore, a comparison of the electrical connections in the cathode through an analysis of the contacts in both the compressed and uncompressed states revealed that the quality of the network, as indicated by the type of contacts formed in the cathode, remained unchanged. This suggests that the quality of the electrical network is strongly linked to the shape and size of the CBD, formed during the mixing process. Moreover, that the compression enhances electrical conductivity by increasing the number of contacts, rather than changing the inherent quality of the network.

Investigations on conductivity additive dispersion in a conventional-wet process revealing an application dependent optimal available active surface area

In Chapter 5, four incremental degrees of carbon black dispersion derived from particle size distribution were investigated. Furthermore, a conventional-wet process of cathode manufacturing was assumed, with **erosion** and **rupture** as the primary agglomerate breakage mechanisms during mixing and no coating of the active material by the conductivity additive. As was the case in the previous investigations, carbon black was modelled together with the binder as CBD. The investigations focused on the suitability of the varying degrees of CBD dispersion for contrasting designs strategies of lithium-ion battery cathodes catering to specific application: high-power cathode and high-energy cathode.
From the performance analysis of **high-power cathodes** under increasing C-rate, it was found that owing to their porous design, composition (higher carbon black content) and reduced thickness, the availability of the active surface area is the predominant limiting factor on their performance. Accordingly, the lowest degree of dispersion leading to the least occupation of the active material surface through the conductivity additive was found to deliver the highest energy density as well as power density for them. Based on these findings, it is recommended that high energy mixing, which can lead to increased dispersion and loss of active surface area, be avoided in the manufacture of high power cathodes. Nonetheless, as the C-rate increases, the utilizable energy density of high-power cathodes with varying degrees of dispersion was found to converge, indicating that transport limitations eventually dominate at further higher C-rates.

On the contrary, findings on the influence of carbon black dispersion on the performance of **high-energy cathodes** under varying C-rate revealed, that their performance is dominated by limitations on transport of the reactants of the electrochemical reactions, taking place in the cathode. To maximize the energy output of high-energy cathodes, they are packed with more active material leading to low porosity and greater thickness. Moreover, the composition of these cathodes allows for only very small quantities of the carbon black and binder. Consequently, the enhanced availability of the active surface, coupled to the reduced dispersion of carbon black and the binder, does not significantly benefit this cathode design strategy, contrary to what was observed for the high-power cathodes. Instead, optimizing transport phenomena is essential for improved performance. To enhance ionic conduction, it is proposed to implement a gradient in the concentration of the carbon black and binder (CBD). By increasing the CBD concentration from the separator towards the current-collector within the cathode, the microstructure's permeability to lithium ions can be improved. Additionally, a higher degree of dispersion of carbon black within the high-energy cathode design was shown to enhance performance by minimizing ohmic losses through improved electrical conductivity. Therefore, increased energy input in the mixing process was found to be imperative for high-energy cathodes.

Investigations on conductivity additive comminution in an intensive-dry solvent-free process revealing an application dependent optimal porosity

In Chapter 6, various degrees of carbon black communition, resulting from **shattering** during intensive-dry mixing, were characterized using the bulk density of the dry cathode mix, followed by its correlation (through the half-cell porosity) to the performance of the cathode. Moreover, a coating factor was introduced to account for the coating of the active material through carbon black, in the intensive-dry mixing process. The half-cells investigated, were computationally fabricated under the assumption of a solvent-free process and left uncalendered. Furthermore, it was assumed that the binder exists in a completely fibrillated state, with no significant influence on the cathode microstructure.
In the evaluations on performance, two different approaches: volumetric and gravimetric, were used to evaluate the specific value of the performance determinants. In addition, two different application scenarios: high-energy (low-current) and high-power (high-current), were investigated using variation in the C-rate.
When comparing the performance of identical volumes of the cathode variants in the **volumetric approach**, it was found that under **high-energy application** (low current) the cathode variant with the highest investigated bulk density and lowest porosity lead to the highest utilizable energy density, as more material translated into more energy in this application scenario. This enhancement in the energy however is not expected to be continuous. Based on the findings made by Cernak et al. [117], with further decrease in

porosity resulting from the increasing active material mass, the transport limitation are bound to restrict performance.
The trends observed in high-energy application were reversed under **high-power application** (high-current), where the transport limitations dominate, leading to the highest energy being achieved at the highest porosity (lowest investigated bulk density), due to the better utilization of the active material. Similar to considerations made at the lower current, a continuous increase in porosity at the higher current would not directly translate into improved performance. This is because increasing porosity reduces the active material content in the same volume, leading to decreased cathode performance due to its declining theoretical capacity. In case of the utilizable power density, an increase associated with decreased porosity and higher active material content was observed under both application scenario following the volumetric approach.
Thus, when considering the high-energy application, where the battery is operated under lower current, the lowest investigated porosity was found to be optimal, leading to an improvement in both the performance determinants: energy and power density. Conversely, under the higher current of high-power applications, where transport limitations dictate performance, a compromise between performance determinants dictates the optimal porosity. In this scenario, the highest energy is achieved at the highest porosity, while the highest power is attained at the lowest porosity.
In the **gravimetric approach**, considering equal mass of the cathodes, it was found that the highest porosity always lead to higher energy. This is due to the more efficient use of the active material. However, the power output remained the same across different variants because the mass of the active material was identical. Hence, when the mass of the active material used in a battery is limited, a higher porosity allowing for the best utilization of the active material through ample pore space proves to be beneficial.

Outlook

The insights gained from this work provide a foundation for future research and advancements in the optimization of the cathode microstructure to enhance its performance, using numerical methods. The following suggestions outline potential directions for these efforts.
The investigation presented in this work covered how conductivity additive dispersion as well as comminution influences the cathode microstructure and its performance. However, coating of the conductivity additive on the active material and its explicit impact on the performance remains to be quantified. Extending the model to explicitly account for the conductivity coating phenomena could lead to valuable insights on the interplay between the electric and ionic conductivity at the active material surface. Additionally, this study

assumed ideal electrical contacts with no resistance to current flow. Including contact resistance in the model could allow for precise simulations of how variations in conductivity additives affect electrical conductivity trends. Moreover, the cathode microstructure considered in this study was assumed to remain static during discharge. However, it is widely recognized that mechanical stresses and degradation cause the rearrangement of battery components within the microstructure. Thus, extending the resolved electrochemical model used in this work to include mechanical degradation and rearrangement of the cathode components could provide further meaningful insights.

In the course of this work, the binder was not explicitly accounted for in the cathode microstructure. Development of future cathodes however warrants attention to this long overlooked component. Modern binders are capable of much more than maintaining the structural integrity of the cathode and ensuring the adhesion to the current-collector [139]. This opens the possibility of a variety of investigations on the structural as well as electrochemical influence of the binder on the cathode performance. Additionally, due to increasing ecological concerns regarding binders used in lithium-ion batteries, which often fall under the category of per- and polyfluoroalkyl substances (PFAS), it is essential to evaluate alternative binding materials. Furthermore, modern methods of cathode manufacturing have substantial implications for the structure of the binder compared to conventional processes. Therefore, to accurately understand the influence of these manufacturing processes on the cathode microstructure, it is imperative to resolve the structure of the binder.

Finally, within the framework of this dissertation the influence of the mixing process could be quantified on the conductivity additive structure, followed by the evaluation thereof on cathode performance. This methodology can be extended to the remaining process steps in the manufacturing of lithium-ion batteries: coating and calendering. Such a comprehensive quantification of the influence of all the processes on the cathode microstructure, will allow for the digital representation of the entire process chain involved in lithium-ion battery manufacturing, followed by the evaluation of its implications on performance. Through such a performance based optimization of the digital representations, the enhancements in the cathode microstrucutre as well as processes involved in its manufacturing can be streamlined.

Appendix A

DEM Parameters

The DEM parameters denoted in Table A.1 do not bear a physical meaning. The value of these parameters was determined through trail and error and plugged into the particle simulation tool LIGGGHTS® to generated stochastic particle heaps, capable of mimicking the particulate nature of lithium-ion battery cathodes. The focus hereby, was not on modelling particle-particle and particle-wall interactions, but generating stochastic particulate structures with varying geometric characteristics in a computationally feasible manner. The values thus tabulated, serve the purpose of ensuring the reproducibility of the structures investigated in this work.

Table A.1: Parameter used in the LIGGGHTS®.

Parameter Name	Value	Unit
Young's Modulus	$1{\cdot}10^{12}$	$\mathrm{kg\,m^{-1}\,s^{-2}}$
Poissons Ratio	0.3	-
Coefficient of Restitution	0.3	-
Coefficient of Friction	0.5	-
Cohesion Energy Density	$3{\cdot}10^{10}$	$\mathrm{J\,m^{-3}}$
Time Step	$1{\cdot}10^{-6}$	s

Appendix B

Calculation of Volume Fractions

The elaborated method follows Hein et al. [30]. To calculate the density of the cathode $\rho_{\mathrm{C}}^{\mathrm{S}}$, the following relation was used:

$$\rho_{\mathrm{C}}^{\mathrm{S}} = \frac{1}{\sum_i \frac{w_i}{\rho_i}} \ . \tag{B.1}$$

Herein, w_i represents the mass fraction of the a given cathode constituent and ρ_i its density. The value of w_i is taken from the recipe of the investigated cathode and the densities of the cathode constituents can be found in Table 3.3. The volume fraction of the all the solid constituent comprises the cathode volume fraction ϵ_{C}, which is simply the total volume (of the half-cell) minus the pore volume expressed in form of volume fractions as:

$$\epsilon_{\mathrm{C}} = 1 - \epsilon \ . \tag{B.2}$$

Finally, using the values from Equations B.1 and B.2, the volume fraction ϵ_{i} of the the individual cathode components can be calculated by the relation:

$$\epsilon_i = \frac{w_i}{\rho_i} \cdot \rho_{\mathrm{C}}^{\mathrm{S}} \cdot \epsilon_{\mathrm{C}} \ . \tag{B.3}$$

Appendix C

Performance Determinants

C.1 Utilizable Energy Density from Chapter 4

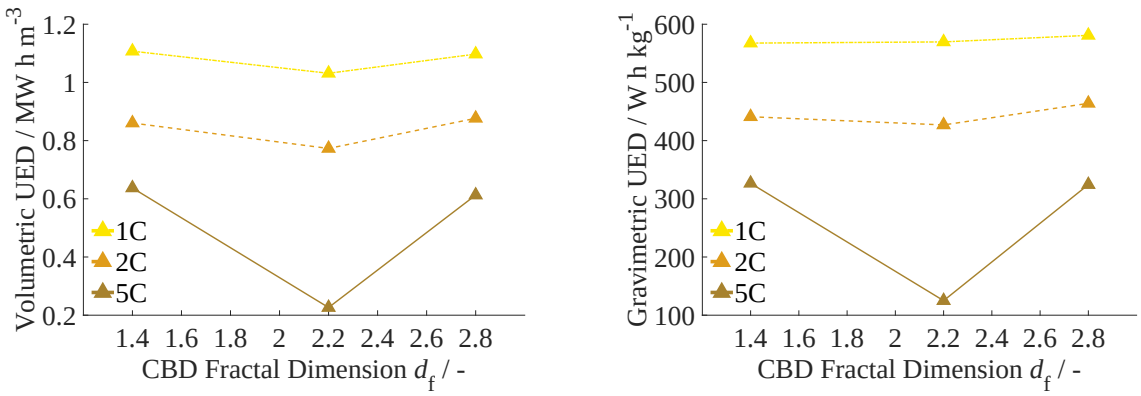

(a) **(b)**

Figure C.1: Utilizable energy density evaluations. a) Volumetric b) Gravimetric.

	d_f / -	1C	2C	5C
Volumetric / MW h m^{-3}	1.4	1.11	0.86	0.63
	2.2	1.03	0.77	0.22
	2.8	1.1	0.87	0.61
Gravimetric / W h kg^{-1}	1.4	567.57	441.04	326.67
	2.2	569.62	426.94	124.99
	2.8	580.87	464.07	324.40

Table C.1: Absolute values of utilizable energy density evaluated using the volumetric and gravimetric approach.

C.2 Utilizable Energy Density from Chapter 6

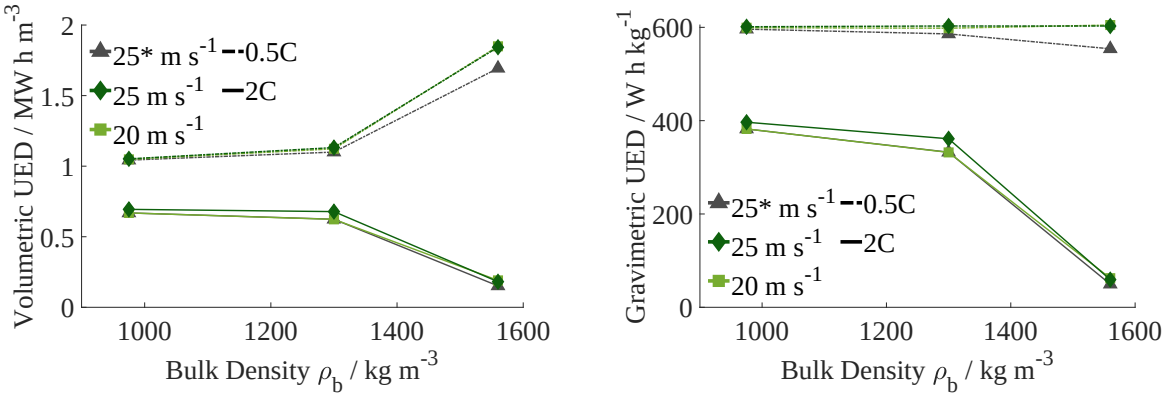

(a) **(b)**

Figure C.2: Utilizable energy density evaluations. a) Volumetric b) Gravimetric.

	ρ_b / kg m^{-3}	25* / MW h m^{-3}	25 / MW h m^{-3}	20 / MW h m^{-3}
0.5C	975	1.04	1.05	1.05
	1300	1.10	1.13	1.12
	1560	1.69	1.84	1.85
2C	975	0.67	0.69	0.67
	1300	0.62	0.68	0.62
	1560	0.15	0.18	0.19

Table C.2: Absolute values of volumetric utilizable energy density.

	ρ_b / kg m^{-3}	25* / W h kg^{-1}	25 / W h kg^{-1}	20 / W h kg^{-1}
0.5C	975	596.12	601.27	599.19
	1300	585.90	602.90	598.19
	1560	554.03	602.79	604.93
2C	975	382.16	396.66	382.26
	1300	332.39	361.18	331.96
	1560	49.60	59.31	62.39

Table C.3: Absolute values of gravimetric utilizable energy density.

C.3 Utilizable Power Density from Chapter 6

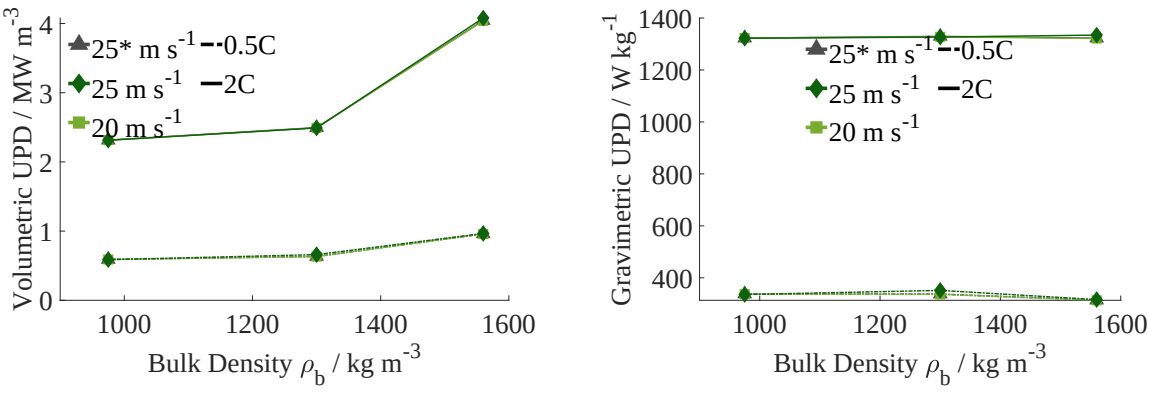

(a) **(b)**

Figure C.3: Utilizable power density evaluations. a) Volumetric b) Gravimetric

	ρ_b / kg m^{-3}	25* / MW m^{-3}	25 / MW m^{-3}	20 / MW m^{-3}
0.5C	975	0.59	0.58	0.59
	1300	0.63	0.66	0.63
	1560	0.96	0.97	0.96
2C	975	2.31	2.31	2.31
	1300	2.50	2.49	2.49
	1560	4.04	4.08	4.04

Table C.4: Absolute values of volumetric utilizable power density.

	ρ_b / kg m^{-3}	25* / W kg^{-1}	25 / W kg^{-1}	20 / W kg^{-1}
0.5C	975	337.43	335.60	337.05
	1300	337.48	351.49	335.96
	1560	314.09	316.00	313.34
2C	975	1322.90	1322.20	1323.20
	1300	1329.60	1326.80	1327.80
	1560	1322.60	1334.40	1321.20

Table C.5: Absolute values of gravimetric utilizable power density.

Nomenclature

Latin Notations

[A]	Anode Host Lattice	–
[C]	Cathode Host Lattice	–
Δx	Lateral Dimension of the Half Cell	m
Δy	Lateral Dimension of the Half Cell	m
$\dot{N}_{\mathrm{E,B}}$	Material Flux at the Bottom Electrolyte Boundary	$\mathrm{mol\,s^{-1}}$
$\hat{i}, \hat{j}, \hat{k}$	Unit Vectors	–
COV	Cutoff Voltage	V
C	Rate of Discharge	–
DOD	Depth of Discharge	–
UC	Utilizable Capacity	%
$\mathrm{UED_G}$	Gravimetric Utilizable Energy Density	$\mathrm{J\,kg^{-1}}$
$\mathrm{UED_V}$	Volumetric Utilizable Energy Density	$\mathrm{J\,m^{-3}}$
UE	Utilizable Energy	J
$\mathrm{UPD_G}$	Gravimetric Utilizable Power Density	$\mathrm{J\,s^{-1}\,kg^{-1}}$
$\mathrm{UPD_V}$	Volumetric Utilizable Power Density	$\mathrm{J\,s^{-1}\,m^{-3}}$
$\vec{\dot{n}}$	Material Flux Density	$\mathrm{mol\,m^{-2}\,s^{-1}}$
$\vec{\dot{n}}_{\mathrm{E}}$	Material Flux Density in the Electrolyte	$\mathrm{mol\,m^{-2}\,s^{-1}}$
$\vec{\dot{n}}_{\mathrm{S}}$	Material Flux Density in the Cathode	$\mathrm{mol\,m^{-2}\,s^{-1}}$
$\vec{i}$	Current Density	$\mathrm{A\,m^{-2}}$
$\vec{i}_{\mathrm{A}}$	Ionic Current Density at the Anodic Surface	$\mathrm{A\,m^{-2}}$
$\vec{i}_{\mathrm{E}}$	Ionic Current Density	$\mathrm{A\,m^{-2}}$
$\vec{i}_{\mathrm{S}}$	Electrical Current Density	$\mathrm{A\,m^{-2}}$
$\vec{i}_{\mathrm{CC}}$	Electrical Current Density at the Current Collector	$\mathrm{A\,m^{-2}}$
$\vec{n}_{\mathrm{E}}$	Outward Normal on the Electrolyte Surface	–

$\vec{n}_{\mathrm{S}}$	Outward Normal on the Cathode Surface	–
$\vec{p}$	Position Vector	m
c	Concentration of a Species	$\mathrm{mol\,m^{-3}}$
$c_{\mathrm{E,A}}$	Lithium Concentration at the Anodic Boundary	$\mathrm{mol\,m^{-3}}$
$c_{\mathrm{E,B}}$	Lithium Concentration at the Bottom Boundary of the Electrolyte	$\mathrm{mol\,m^{-3}}$
$c_{\mathrm{E,max}}$	Maximum Lithium Concentration in the Electrolyte	$\mathrm{mol\,m^{-3}}$
$c_{\mathrm{E,ref}}$	Initial Lithium Concentration in the Electrolyte	$\mathrm{mol\,m^{-3}}$
$c_{\mathrm{E,SEP}}$	Lithium Concentration Immediately below the Separator	$\mathrm{mol\,m^{-3}}$
c_{E}	Lithium Concentration in the Electrolyte	$\mathrm{mol\,m^{-3}}$
$c_{\mathrm{S,max}}$	Maximum Lithium Concentration in the Cathode	$\mathrm{mol\,m^{-3}}$
$c_{\mathrm{S,max}}^{\mathrm{AM}}$	Maximum Lithium Concentration in the Active Material	$\mathrm{mol\,m^{-3}}$
$c_{\mathrm{S,ref}}$	Initial Lithium Concentration in the Cathode	$\mathrm{mol\,m^{-3}}$
$c_{\mathrm{S,ref}}^{\mathrm{AM}}$	Initial Lithium Concentration in the Active Material	$\mathrm{mol\,m^{-3}}$
$c_{\mathrm{S,ref}}^{\mathrm{CBD}}$	Initial Lithium Concentration in the CBD	$\mathrm{mol\,m^{-3}}$
c_{S}	Lithium Concentration in the Cathode	$\mathrm{mol\,m^{-3}}$
d	diameter	m
$D_{\mathrm{S}}^{\mathrm{AM}}$	Diffusion Coefficient of Lithium in the Active Material	$\mathrm{m^2\,s^{-1}}$
$D_{\mathrm{S}}^{\mathrm{CBD}}$	Diffusion Coefficient of Lithium in the CBD	$\mathrm{m^2\,s^{-1}}$
D_{E}	Spatially Variable Diffusion Coefficient of Lithium in the Electrolyte	$\mathrm{m^2\,s^{-1}}$
d_{f}	Fractal Dimension	–
d_{g}	Diameter of Gyration	m
d_{p}	Primary Particle Diameter	m
D_{S}	Spatially Variable Diffusion Coefficient of Lithium in the Cathode	$\mathrm{m^2\,s^{-1}}$
d_{CBD}	CBD Cluster Diameter	m
d_{CB}	Carbon Black Diameter	m
$D_{\mathrm{E,eff}}$	Effective Diffusion Coefficient of Lithium in the Electrolyte	$\mathrm{m^2\,s^{-1}}$
$D_{\mathrm{E}}^{\mathrm{SEP}}$	Effective Diffusion Coefficient of Lithium in the Separator	$\mathrm{m^2\,s^{-1}}$
F	Faraday's Constant	$96485.33\,\mathrm{A\,s\,mol^{-1}}$
f_{c}	Coating Factor	–
H	Cathode Height	m
H_{SEP}	Separator Height	m
I	Electrical Current	A
i_0	Exchange Current Density	$\mathrm{A\,m^{-2}}$
i_{BV}	Intercalation Current Density	$\mathrm{A\,m^{-2}}$

$i_{\mathrm{BV}}^{\mathrm{avg}}$	Averaged Intercalation Current Density	$\mathrm{A\,m^{-2}}$
$I_{\mathrm{S,CC}}$	Current at the Cathode Current Collector	A
k_{f}	Fractal Proportionality Constant	–
k_{BV}	Butler-Volmer Reaction Rate Constant	$\mathrm{A\,m^{2.5}\,mol^{-1.5}}$
N_{M}	MacMullin Number	–
n_{p}	Number of Primary Particles	–
$n_{\mathrm{CBD/AM}}$	Number of Particles of the Cathode Constituents	–
P	Power	$\mathrm{J\,s^{-1}}$
q_3	Density Distribution Function	–
R	Universal Gas Constant	$8.314\,\mathrm{J\,mol^{-1}\,K^{-1}}$
r	Radius	m
S_{V}	Volume Specific Available Active Surface Area	$\mathrm{m^{-1}}$
S_{AM}	Total Active Surface Area	$\mathrm{m^2}$
S_{CC}	Surface Area of the Current Collector	$\mathrm{m^2}$
S_{i}	Surface Area of a Finite Volume Element	$\mathrm{m^2}$
$S_{\mathrm{V\%}}$	S_{V} as a Percentage of the Total Specific Surface Area	%
T	Temperature	K
t	Time	s
t_+^0	Transference Number	–
t_{s}	Tip Speed	$\mathrm{m\,s^{-1}}$
U_{eq}	Equilibrium Potential	V
V	Voltage	V
V_{HC}	Half-Cell Volume	$\mathrm{m^3}$
V_{i}	Volume of a Finite Volume Element	$\mathrm{m^3}$
V_{S}	Total Cathode Volume	$\mathrm{m^3}$
x	Scaling Factor	–
x, y, z	Spatial Coordinates	m
z_+	Charge Number	–
z_{max}	Maximum z-Coordinate of the Half Cell	m
z_{min}	Minimum z-Coordinate of the Half Cell	m

Greek Symbols

α	Charge Transfer Coefficient	–

$\Delta\phi$	Potential Difference	V
ϵ	Porosity	–
$\epsilon_{\mathrm{AM/CBD}}$	Volume Fraction of the Cathode Constituents	–
ϵ_{SEP}	Separator Porosity	–
η	Overpotential	V
κ_{E}	Ionic Conductivity of the Electrolyte	$\mathrm{S\,m^{-1}}$
κ_{S}	Spatially Variable Electrical Conductivity of the Cathode	$\mathrm{S\,m^{-1}}$
$\kappa_{\mathrm{S}}^{\mathrm{AM}}$	Intrinsic Electrical Conductivity of the Active Material	$\mathrm{S\,m^{-1}}$
$\kappa_{\mathrm{S}}^{\mathrm{CBD}}$	Intrinsic Electrical Conductivity of the CBD	$\mathrm{S\,m^{-1}}$
κ_{eff}	Effective Electrical Conductivity of the Cathode	$\mathrm{S\,m^{-1}}$
$\kappa_{\mathrm{E}}^{\mathrm{SEP}}$	Effective Ionic Conductivity of the Separator	$\mathrm{S\,m^{-1}}$
κ_{pow}	Electrical Conductivity of the Dry Cathode Mix	$\mathrm{S\,m^{-1}}$
$\Omega_{\mathrm{E}}^{\mathrm{REST}}$	Subdomain of the Free Electrolyte	–
$\Omega_{\mathrm{E}}^{\mathrm{SEP}}$	Separator Subdomain of the Electrolyte	–
$\Omega_{\mathrm{S}}^{\mathrm{AM}}$	Active Subdomain of the Cathode	–
$\Omega_{\mathrm{S}}^{\mathrm{CBD}}$	Passive (CBD) Subdomain of the Cathode	–
Ω_{BOX}	Domain of the DEM Simulation Box	–
Ω_{E}	Electrolyte Domain	–
Ω_{S}	Solid (Cathode) Domain	–
Ω_{WRAP}	Domain of the Wrapped Cathode Geometry	–
$\partial\Omega_{\mathrm{S,E}}^{\mathrm{AM}}$	Active Subdomain of the Cathode-Electrolyte Interface	–
$\partial\Omega_{\mathrm{S,E}}^{\mathrm{CBD}}$	Passive Subdomain of the Cathode-Electrolyte Interface	–
$\partial\Omega_{\mathrm{S,E}}^{\mathrm{SEC}}$	Section of the Cathode-Electrolyte Boundary	–
$\partial\Omega_{\mathrm{A}}$	Anodic Boundary	–
$\partial\Omega_{\mathrm{B}}$	Boundary at the Bottom of the Electrolyte	–
$\partial\Omega_{\mathrm{T}}$	Boundary at the Top of the Cathode	–
$\partial\Omega_{\mathrm{CC}}$	Boundary at the Current Collector	–
$\partial\Omega_{\mathrm{E,P}}$	Electrolyte Periodic Boundary	–
$\partial\Omega_{\mathrm{E,S}}$	Boundary at the Cathode-Electrolyte Interface (Electrolyte Side)	–
$\partial\Omega_{\mathrm{E}}$	Complete Electrolyte Boundary	–
$\partial\Omega_{\mathrm{S,E}}$	Boundary at the Cathode-Electrolyte Interface (Cathode Side)	–
$\partial\Omega_{\mathrm{S,P}}$	Cathode Periodic Boundary	–
$\partial\Omega_{\mathrm{SEP}}$	Boundary Immediately Below the Separator	–
$\partial\Omega_{\mathrm{S}}$	Complete Solid (Cathode) Boundary	–

ϕ_{E}	Electrolyte Potential	V
ϕ_{N}	Negative Electrode Potential	V
ϕ_{P}	Positive Electrode Potential	V
ϕ_{S}	Solid (Cathode) Potential	V
$\phi_{\mathrm{E,ref}}$	Initial Electrolyte Potential	V
$\phi_{\mathrm{S,CC}}$	Potential at the Cathode Current Collector	V
$\phi_{\mathrm{S,ref}}$	Initial Cathode Potential	V
$\phi_{\mathrm{S,T}}$	Solid (Cathode) Potential at the Top Boundary	V
$\rho_{\mathrm{AM}}^{\mathrm{CG}}$	Coarse Grained Density of the Active Material	$\mathrm{kg\,m^{-3}}$
ρ_{b}	Bulk Density	$\mathrm{kg\,m^{-3}}$
$\rho_{\mathrm{CB}}^{\mathrm{CG}}$	Coarse Grained Density of Carbon Black	$\mathrm{kg\,m^{-3}}$
$\rho_{\mathrm{S}}^{\mathrm{AM}}$	Density of the Active Material	$\mathrm{kg\,m^{-3}}$
$\rho_{\mathrm{S}}^{\mathrm{Binder}}$	Density of the Binder	$\mathrm{kg\,m^{-3}}$
$\rho_{\mathrm{S}}^{\mathrm{CB}}$	Density of Carbon Black	$\mathrm{kg\,m^{-3}}$
τ	Tortuosity	–
τ_{SEP}	Separator Tortuosity	–

Indices

i,j,k	Counting Indexes
A	Anode
B	Bottom
C	Cathode
c	Coating
CB	Carbon Black
CC	Current Collector
CG	Coarse Grained
E	Electrolyte
eq	Equilibrium
HC	Half Cell
max	Maximum
min	Minimum
P	Periodic
p	Related to the Primary Particle of an Aggregate

pow	Powder
S	Solid
SEC	Section
SEP	Separator
T	Top

Abbreviations

2D	Two Dimensional
3D	Three Dimensional
AM	Active Material
CAD	Computer Aided Design
CAM	Cathode Active Material
CB	Carbon Black
CBD	Carbon Binder Domain
CFD	Computational Fluid Mechanics
CGMD	Coarse Grained Molecular Dynamics
CMC	Carboxymethylcellulos
DEM	Discrete Element Method
DLC	Diffusion Limited C-Rate
EC	Ethylene Carbonate
EMC	Ethyl Methyl Carbonate
EV	Electric Vehicle
FEM	Finite Element Method
FIB	Focused Ion Beam
FVE	Finite Volume Element
FVM	Finite Volume Method
HAADF	High Angle Annular Dark Field
IHP	Inner Helmholtz Plane
LFP	Lithium Ferrophosphate
LIB	Lithium-Ion battery
LS	Lower Section
MS	Middle Section
NMC	(Lithium-)Nickel-Manganese-Cobalt(-Oxide)

NMP	N-Methyl-2-pyrrolidone
OCV	Open Circuit Voltage
OHP	Outer Helmholtz Plane
P2D	Pseudo 2D (Model)
PFAS	Per- and Polyfluoroalkyl Substances
PVDF	Polyvinylidene Difluoride
RDM	Restricted Diffusion Method
RN	Resistor Network
SBR	Styrene-Butadiene Rubber
SEI	Solid Electrolyte Interface
SEM	Scanning Electron Microscope
SKJR	Simplified Johnson-Kendall-Roberts (Model)
STEM	Scanning Transmission Electron Microscopy
STL	Stereolithography
TDM	Tunable Dimension Method
US	Upper Section

Mathematical Operators

ln	Natural Logarithm
sinh	Hyperbolic Sine

Bibliography

[1] M. A. Kespe. *Simulation von Transportvorgängen in Lithium-Ionen Batterien auf der partikulären Ebene*. PhD thesis, Karlsruher Institut für Technologie (KIT), 2019.

[2] N. G. Özcan Taşkin, G. Padron and A. Voelkel. Effect of particle type on the mechanisms of break up of nanoscale particle clusters. *Chemical Engineering Research and Design*, 87(4): 468–473, 2009.

[3] S. P. Rwei, I. Manas-Zloczower and D. L. Feke. Observation of carbon black agglomerate dispersion in simple shear flows. *Polymer Engineering & Science*, 30(12): 701–706, 1990.

[4] J. Newman and W. Tiedemann. Porous-electrode theory with battery applications. *AIChE Journal*, 21(1): 25–41, 1975.

[5] M. Ender. *Mikrostrukturelle Charakterisierung, Modellentwicklung und Simulation poröser Elektroden für Lithiumionenzellen*. PhD Thesis, Karlsruher Institut für Technologie (KIT), 2014.

[6] J. Newman and K. E. Thomas-Alyea. *Electrochemical Systems*. Wiley-Interscience, 3. Edition, 2012.

[7] E. Fontes. Does the current flow backwards inside a battery?, 2015. Accessed: 2024-06-20.

[8] R. Amin and Y.-M. Chiang. Characterization of Electronic and Ionic Transport in $Li_{1-x}Ni_{0.33}Mn_{0.33}Co_{0.33}O_2$ (NMC 333) and $Li_{1-x}Ni_{0.50}Mn_{0.20}Co_{0.30}O_2$ (NMC 523) as a Function of Li Content. *Journal of The Electrochemical Society*, 163(8): 1512–1517, 2016.

[9] H. Li, J. Li, X. Ma and J. R. Dahn. Synthesis of Single Crystal $LiNi_{0.60}Mn_{0.20}Co_{0.20}O_2$ with Enhanced Electrochemical Performance for Lithium Ion Batteries. *Journal of The Electrochemical Society*, 165(5): A1038, 2018.

[10] J. Kaiser, V. Wenzel, H. Nirschl, B. Bitsch, N. Willenbacher, M. Baunach, M. Schmitt, S. Jaiser, P. Scharfer and W. Schabel. Prozess- und Produktentwicklung von Elektroden für Li-Ionen-Zellen. *Chemie Ingenieur Technik*, 86(5): 695–706, 2014.

[11] H. Bockholt, M. Indrikova, A. Netz, F. Golks and A. Kwade. The interaction of consecutive process steps in the manufacturing of lithium-ion battery electrodes with regard to structural and electrochemical properties. *Journal of Power Sources*, 325: 140–151, 2016.

[12] M. Haarmann, D. Grießl and A. Kwade. Continuous Processing of Cathode Slurry by Extrusion for Lithium-Ion Batteries. *Energy Technology*, 9(10): 2100250, 2021.

[13] H. Dreger, H. Bockholt, W. Haselrieder and A. Kwade. Discontinuous and Continuous Processing of Low-Solvent Battery Slurries for Lithium Nickel Cobalt Manganese Oxide Electrodes. *Journal of Electronic Materials*, 44(11): 4434–4443, 2015.

[14] M. Schmitt. *Slot die coating of lithium-ion battery electrodes*. PhD Thesis, Karlsruher Institut für Technologie (KIT), 2016.

[15] Y. Zhang, S. Lu, Z. Wang, V. Volkov, F. Lou and Z. Yu. Recent technology development in solvent-free electrode fabrication for lithium-ion batteries. *Renewable and Sustainable Energy Reviews*, 183: 113515, 2023.

[16] A. Gyulai, W. Bauer and H. Ehrenberg. Dry Electrode Manufacturing in a Calender: The Role of Powder Premixing for Electrode Quality and Electrochemical Performance. *ACS Applied Energy Materials*, 6(10): 5122–5134, 2023.

[17] B. Ludwig, Z. Zheng, W. Shou, Y. Wang and H. Pan. Solvent-Free Manufacturing of Electrodes for Lithium-ion Batteries. *Scientific Reports*, 6(1): 23150, 2016.

[18] F. Hippauf, B. Schumm, S. Doerfler, H. Althues, S. Fujiki, T. Shiratsuchi, T. Tsujimura, Y. Aihara and S. Kaskel. Overcoming binder limitations of sheet-type solid-state cathodes using a solvent-free dry-film approach. *Energy Storage Materials*, 21: 390–398, 2019.

[19] D. Oehler. *Bestimmung der thermischen Transporteigenschaften poröser Elektroden von Lithium-Ionen Batterien*. PhD Thesis, Karlsruher Institut für Technologie (KIT), 2021.

[20] V. I. Becker. *Modellierung der Mechanik und der effektiven Transporteigenschaften von partikulären Kathoden sowie deren Einfluss auf die elektrochemische Performance von Lithium-Ionen-Batterien*. PhD Thesis, Karlsruher Institut für Technologie (KIT), 2022.

[21] M. Park, X. Zhang, M. Chung, G. B. Less and A. M. Sastry. A review of conduction phenomena in Li-ion batteries. *Journal of Power Sources*, 195(24): 7904–7929, 2010.

[22] Y.-H. Chen, C.-W. Wang, G. Liu, X.-Y. Song, V. S. Battaglia and A. M. Sastry. Selection of Conductive Additives in Li-Ion Battery Cathodes. *Journal of The Electrochemical Society*, 154(10): 978, 2007.

[23] D. Guy, B. Lestriez, R. Bouchet and D. Guyomard. Critical Role of Polymeric Binders on the Electronic Transport Properties of Composites Electrode. *Journal of The Electrochemical Society*, 153(4): 679, 2006.

[24] D. Stauffer and A. Aharony. *Introduction To Percolation Theory: Second Edition*. Taylor & Francis, London, 2 Edition, 2017.

[25] W. Bauer, D. Nötzel, V. Wenzel and H. Nirschl. Influence of dry mixing and distribution of conductive additives in cathodes for lithium ion batteries. *Journal of Power Sources*, 288: 359–367, 2015.

[26] G. Liu, H. Zheng, A. S. Simens, A. M. Minor, X. Song and V. S. Battaglia. Optimization of Acetylene Black Conductive Additive and PVDF Composition for High--Power Rechargeable Lithium-Ion Cells. *Journal of The Electrochemical Society*, 154(12): A1129, 2007.

[27] G. Inoue and M. Kawase. Numerical and experimental evaluation of the relationship between porous electrode structure and effective conductivity of ions and electrons in lithium-ion batteries. *Journal of Power Sources*, 342: 476–488, 2017.

[28] Y.-H. Chen, C.-W. Wang, X. Zhang and A. M. Sastry. Porous cathode optimization for lithium cells: Ionic and electronic conductivity, capacity, and selection of materials. *Journal of Power Sources*, 195(9): 2851–2862, 2010.

[29] M. Chouchane and A. A. Franco. Deconvoluting the impacts of the active material skeleton and the inactive phase morphology on the performance of lithium ion battery electrodes. *Energy Storage Materials*, 47: 649–655, 2019.

[30] S. Hein, T. Danner, D. Westhoff, B. Prifling, R. Scurtu, L. Kremer, A. Hoffmann, A. Hilger, M. Osenberg, I. Manke, M. Wohlfahrt-Mehrens, V. Schmidt and A. Latz. Influence of Conductive Additives and Binder on the Impedance of Lithium-Ion Battery Electrodes: Effect of Morphology. *Journal of The Electrochemical Society*, 167(1): 013546, 2020.

[31] I. Srivastava, D. S. Bolintineanu, J. B. Lechman and S. A. Roberts. Controlling Binder Adhesion to Impact Electrode Mesostructures and Transport. *ACS applied materials & interfaces*, 12(31): 34919–34930, 2020.

[32] S. R. Daemi, C. Tan, T. Volkenandt, S. J. Cooper, A. Palacios-Padros, J. Cookson, D. J. L. Brett and P. R. Shearing. Visualizing the Carbon Binder Phase of Battery Electrodes in Three Dimensions. *ACS Applied Energy Materials*, 1(8): 3702–3710, 2018.

[33] F. Beguin and E. Frackowiak (Hrsg.). *Carbons for Electrochemical Energy Storage and Conversion Systems*. CRC Press, Boca Raton, 2009.

[34] G. A. Kelesidis, S. Benz and S. E. Pratsinis. Process design for carbon black size and morphology. *Carbon*, 213: 118255, 2023.

[35] U. Kätzel, R. Bedrich, M. Stintz, R. Ketzmerick, T. Gottschalk-Gaudig and H. Barthel. Dynamic Light Scattering for the Characterization of Polydisperse Fractal Systems: I. Simulation of the Diffusional Behavior. *Particle & Particle Systems Characterization*, 25(1): 9–18, 2008.

[36] E. D. Shchukin. *Colloid and surface chemistry*, volume 12 of *Studies in interface science*. Elsevier, New York, 1st ed. Edition, 2001.

[37] S. P. Rwei, I. Manas-Zloczower and D. L. Feke. Characterization of agglomerate dispersion by erosion in simple shear flows. *Polymer Engineering & Science*, 31(8): 558–562, 1991.

[38] S. P. Rwei, I. Manas-Zloczower and D. L. Feke. Analysis of dispersion of carbon black in polymeric melts and its effect on compound properties. *Polymer Engineering & Science*, 32(2): 130–135, 1992.

[39] E. Asylbekov, J. Mayer, H. Nirschl and A. Kwade. Modeling of Carbon Black Fragmentation During High-Intensity Dry Mixing Using the Population Balance Equation and the Discrete Element Method. *Energy Technology*, p. 2200867, 2022.

[40] H. Dreger, M. Huelsebrock, L. Froboese and A. Kwade. Method Development for Quality Control of Suspensions for Lithium-Ion Battery Electrodes. *Industrial & Engineering Chemistry Research*, 56(9): 2466–2474, 2017.

[41] J. F. Meza Gonzalez and H. Nirschl. Numerical Investigation of the Local Shear Rate in a Twin-Screw Extruder for the Continuous Processing of Li-Ion Battery Electrode Slurries. *Energy Technology*, 11(6): 2201517, 2023.

[42] H. Dreger, W. Haselrieder and A. Kwade. Influence of dispersing by extrusion and calendering on the performance of lithium-ion battery electrodes. *Journal of Energy Storage*, 21: 231–240, 2019.

[43] H. Bockholt, W. Haselrieder and A. Kwade. Intensive Dry and Wet Mixing Influencing the Structural and Electrochemical Properties of Secondary Lithium-Ion Battery Cathodes. *ECS Transactions*, 50(26): 25–35, 2013.

[44] G. Kaur and B. D. Gates. Review—Surface Coatings for Cathodes in Lithium Ion Batteries: From Crystal Structures to Electrochemical Performance. *Journal of The Electrochemical Society*, 169(4): 043504, 2022.

[45] S. Jaiser, L. Funk, M. Baunach, P. Scharfer and W. Schabel. Experimental investigation into battery electrode surfaces: The distribution of liquid at the surface and the emptying of pores during drying. *Journal of Colloid and Interface Science*, 494: 22–31, 2017.

[46] B. Westphal, H. Bockholt, T. Günther, W. Haselrieder and A. Kwade. Influence of Convective Drying Parameters on Electrode Performance and Physical Electrode Properties. *ECS Transactions*, 64(22): 57, 2015.

[47] M. Abdollahifar, H. Cavers, S. Scheffler, A. Diener, M. Lippke and A. Kwade. Insights into Influencing Electrode Calendering on the Battery Performance. *Advanced Energy Materials*, 13(40): 2300973, 2023.

[48] E. N. Primo, M. Chouchane, M. Touzin, P. Vazquez and A. A. Franco. Understanding the calendering processability of Li(Ni0.33Mn0.33Co0.33)O2-based cathodes. *Journal of Power Sources*, 488: 229361, 2021.

[49] L. S. Kremer, A. Hoffmann, T. Danner, S. Hein, B. Prifling, D. Westhoff, C. Dreer, A. Latz, V. Schmidt and M. Wohlfahrt-Mehrens. Manufacturing Process for Improved Ultra -Thick Cathodes in High-Energy Lithium-Ion Batteries. *Energy Technology*, 8(2): 1900167, 2020.

[50] H. Bockholt, W. Haselrieder and A. Kwade. Intensive powder mixing for dry dispersing of carbon black and its relevance for lithium-ion battery cathodes. *Powder Technology*, 297: 266–274, 2016.

[51] J. Entwistle, R. Ge, K. Pardikar, R. Smith and D. Cumming. Carbon binder domain networks and electrical conductivity in lithium-ion battery electrodes: A critical review. *Renewable and Sustainable Energy Reviews*, 166, 2022.

[52] W. Haselrieder, S. Ivanov, H. Y. Tran, S. Theil, L. Froböse, B. Westphal, M. Wohlfahrt-Mehrens and A. Kwade. Influence of formulation method and related processes on structural, electrical and electrochemical properties of LMS/NCA-blend electrodes. *Progress in Solid State Chemistry*, 42(4): 157–174, 2014.

[53] J. K. Mayer, L. Almar, E. Asylbekov, W. Haselrieder, A. Kwade, A. Weber and H. Nirschl. Influence of the Carbon Black Dispersing Process on the Microstructure and Performance of Li-Ion Battery Cathodes. *Energy Technology*, 8(2): 1900161, 2020.

[54] M. Weber, J. K. Mayer and A. Kwade. The Carbon Black Dispersion Index DI CB : A Novel Approach Describing the Dispersion Progress of Carbon Black Containing Battery Slurries. *Energy Technology*, p. 2201299, 2023.

[55] E. Asylbekov, R. Trunk, M. J. Krause and H. Nirschl. Microscale Discrete Element Method Simulation of the Carbon Black Aggregate Fracture Behavior in a Simple Shear Flow. *Energy Technology*, p. 2000850, 2021.

[56] J. K. Mayer, H. Bockholt and A. Kwade. Inner carbon black porosity as characteristic parameter for the microstructure of lithium-ion electrodes and its effect on physical and electrochemical properties. *Journal of Power Sources*, 529: 231259, 2022.

[57] C. Lischka, S. Gerl, J. Kappes, A. Chauhan and H. Nirschl. Experimental & simulative assessment of mixing quality for dry Li-Ion cathode production in an Eirich intensive mixer. *Powder Technology*, 431: 119072, 2024.

[58] M. Müller, L. Pfaffmann, S. Jaiser, M. Baunach, V. Trouillet, F. Scheiba, P. Scharfer, W. Schabel and W. Bauer. Investigation of binder distribution in graphite anodes for lithium-ion batteries. *Journal of Power Sources*, 340: 1–5, 2017.

[59] X. Lu, A. Bertei, D. P. Finegan, C. Tan, S. R. Daemi, J. S. Weaving, K. B. O'Regan, T. M. M. Heenan, G. Hinds, E. Kendrick, D. J. L. Brett and P. R. Shearing. 3D microstructure design of lithium-ion battery electrodes assisted by X-ray nano-computed tomography and modelling. *Nature communications*, 11(1): 2079, 2020.

[60] L. Almar, J. Joos, A. Weber and E. Ivers-Tiffeé. Microstructural feature analysis of commercial Li-ion battery cathodes by focused ion beam tomography. *Journal of Power Sources*, 427: 1–14, 2019.

[61] B. Prifling, M. Neumann, S. Hein, T. Danner, E. Heider, A. Hoffmann, P. Rieder, A. Hilger, M. Osenberg, I. Manke, M. Wohlfahrt-Mehrens, A. Latz and V. Schmidt. Quantitative Comparison of Different Approaches for Reconstructing the Carbon-Binder Domain from Tomographic Image Data of Cathodes in Lithium-Ion Batteries and Its Influence on Electrochemical Properties. *Energy Technology*, 11(5): 2200784, 2023.

[62] L. Zielke, T. Hutzenlaub, D. R. Wheeler, C.-W. Chao, I. Manke, A. Hilger, N. Paust, R. Zengerle and S. Thiele. Three-Phase Multiscale Modeling of a LiCoO 2 Cathode: Combining the Advantages of FIB-SEM Imaging and X-Ray Tomography. *Advanced Energy Materials*, 5(5): 1401612, 2015.

[63] S. J. Cooper, S. A. Roberts, Z. Liu and B. Winiarski. Methods-Kintsugi Imaging of Battery Electrodes: Distinguishing Pores from the Carbon Binder Domain using Pt Deposition. *Journal of The Electrochemical Society*, 169(7): 070512, 2022.

[64] M. M. Forouzan, C.-W. Chao, D. Bustamante, B. A. Mazzeo and D. R. Wheeler. Experiment and simulation of the fabrication process of lithium-ion battery cathodes for determining microstructure and mechanical properties. *Journal of Power Sources*, 312: 172–183, 2016.

[65] M. Lippke, T. Ohnimus, T. Heckmann, D. Ivanov, P. Scharfer, W. Schabel, C. Schilde and A. Kwade. Simulation of structure formation during drying of lithium-ion battery electrodes using discrete element method. *Energy Technology*, 2022.

[66] S. Wolf, M. Lippke, A. Schoo, A. Kwade and C. Schilde. A Computational Fluid Dynamics-Discrete Element Method Model for Physics-Based Simulation of Structure Formation during Battery Electrode Drying. *Energy Technology*, p. 2301004, 2024.

[67] C. Sangrós Gimeńez, B. Finke, C. Schilde, L. Froböse and A. Kwade. Numerical simulation of the behavior of lithium-ion battery electrodes during the calendaring process via the discrete element method. *Powder Technology*, 349: 1–11, 2019.

[68] D. Zapata Dominguez, J. Xu, Y. Boudjema, S. Ben Hadj Ali, F. M. Zanotto and A. A. Franco. Influence of the mixing speed in the rheology of NMC622-based Li-ion battery electrode slurries. *Journal of Power Sources Advances*, 26: 100141, 2024.

[69] T. Lombardo, A. C. Ngandjong, A. Belhcen and A. A. Franco. Carbon-Binder Migration: A Three-Dimensional Drying Model for Lithium-ion Battery Electrodes. *Energy Storage Materials*, 43: 337–347, 2021.

[70] A. C. Ngandjong, T. Lombardo, E. N. Primo, M. Chouchane, A. Shodiev, O. Arcelus and A. A. Franco. Investigating electrode calendering and its impact on electrochemical performance by means of a new discrete element method model: Towards a digital twin of Li-Ion battery manufacturing. *Journal of Power Sources*, 485: 229320, 2021.

[71] S. N. Chiu, D. Stoyan, W. S. Kendall and J. Mecke. *Stochastic geometry and its applications*. John Wiley & Sons, 2013.

[72] J. Joos, A. Buchele, A. Schmidt, A. Weber and E. Ivers-Tiffeé. Virtual Electrode Design for Lithium-Ion Battery Cathodes. *Energy Technology*, 2021.

[73] D. Westhoff, I. Manke and V. Schmidt. Generation of virtual lithium-ion battery electrode microstructures based on spatial stochastic modeling. *Computational Materials Science*, 151: 53–64, 2018.

[74] B. Prifling, D. Westhoff, D. Schmidt, H. Markötter, I. Manke, V. Knoblauch and V. Schmidt. Parametric microstructure modeling of compressed cathode materials for Li-ion batteries. *Computational Materials Science*, 169: 109083, 2019.

[75] V. Wenzel, H. Nirschl and D. Nötzel. Challenges in Lithium-Ion-Battery Slurry Preparation and Potential of Modifying Electrode Structures by Different Mixing Processes. *Energy Technology*, 3(7): 692–698, 2015.

[76] D. Kehrwald, P. R. Shearing, N. P. Brandon, P. K. Sinha and S. J. Harris. Local Tortuosity Inhomogeneities in a Lithium Battery Composite Electrode. *Journal of The Electrochemical Society*, 158(12): 1393, 2011.

[77] B. L. Trembacki, A. N. Mistry, D. R. Noble, M. E. Ferraro, P. P. Mukherjee and S. A. Roberts. Mesoscale Analysis of Conductive Binder Domain Morphology in Lithium-Ion Battery Electrodes. *Journal of The Electrochemical Society*, 165(13): 725–736, 2018.

[78] D. Andre, M. Meiler, K. Steiner, C. Wimmer, T. Soczka-Guth and D. U. Sauer. Characterization of high-power lithium-ion batteries by electrochemical impedance spectroscopy. I. Experimental investigation. *Journal of Power Sources*, 196(12): 5334–5341, 2011.

[79] A. Shodiev, E. N. Primo, M. Chouchane, T. Lombardo, A. C. Ngandjong, A. Rucci and A. A. Franco. 4D-resolved physical model for Electrochemical Impedance Spectroscopy of Li(Ni1-x-yMnxCoy)O2-based cathodes in symmetric cells: Consequences in tortuosity calculations. *Journal of Power Sources*, 454: 227871, 2020.

[80] M. Gaberscek, R. Dominko and J. Jamnik. Is small particle size more important than carbon coating? An example study on LiFePO4 cathodes. *Electrochemistry Communications*, 9(12): 2778–2783, 2007.

[81] R. Korthauer (Hrsg.). *Lithium-Ion Batteries: Basics and Applications*. Springer, Berlin, Heidelberg, 2018.

[82] J. S. Edge, S. O'Kane, R. Prosser, N. D. Kirkaldy, A. N. Patel, A. Hales, A. Ghosh, W. Ai, J. Chen, J. Yang, S. Li, M.-C. Pang, L. B. Diaz, A. Tomaszewska,

M. Waseem Marzook, K. N. Radhakrishnan, H. Wang, Y. Patel, B. Wu and G. J. Offer. Lithium ion battery degradation: what you need to know. *Physical Chemistry Chemical Physics*, 23(14): 8200–8221, 2021.

[83] D. V. Ragone. Review of Battery Systems for Electrically Powered Vehicles. SAE Technical Paper 680453, SAE International, Warrendale, PA, 1968.

[84] P. A. Cundall and O. D. L. Strack. A discrete numerical model for granular assemblies. *Géotechnique*, 29(1): 47–65, 1979.

[85] C. Kloss, C. Goniva, A. Hager, S. Amberger and S. Pirker. Models, algorithms and validation for opensource dem and cfd-dem. *Progress in Computational Fluid Dynamics, An International Journal*, 12(2/3): 140, 2012.

[86] A. M. Dreizler, N. Bohn, H. Geßwein, M. Müller, J. R. Binder, N. Wagner and K. A. Friedrich. Investigation of the Influence of Nanostructured $LiNi_{0.33}Co_{0.33}Mn_{0.33}O_2$ Lithium-Ion Battery Electrodes on Performance and Aging. *Journal of The Electrochemical Society*, 165(2): A273, 2018.

[87] S. Baazouzi, N. Feistel, J. Wanner, I. Landwehr, A. Fill and K. P. Birke. Design, Properties, and Manufacturing of Cylindrical Li-Ion Battery Cellsâ€"A Generic Overview. *Batteries*, 9(6): 309, 2023.

[88] K. Johnson, K. Kendall and A. D. Roberts. Surface energy and the contact of elastic solids. *Proceedings of the Royal Society of London. A. Mathematical and Physical Sciences*, 1971.

[89] R. D. Mindlin. Compliance of elastic bodies in contact. *Journal of Applied Mechanics*, 16(3): 259–268, 1949.

[90] S. Cernak. *Numerische Untersuchungen zum Einfluss der Aktivmaterialpartikelmorphologie auf die stofflichen Transportvorgänge in Lithium-Ionen Batterien.* Karlsruher Institut für Technologie (KIT), 2021.

[91] Siemens Digital Industries Software. Simcenter STAR-CCM+ User Guide, version 2206. In *Surface Wrapping the Geometry*, p. 2440–2454. Siemens, 2022.

[92] Siemens Digital Industries Software. Simcenter STAR-CCM+ User Guide, version 2206. In *Surface Repair Error Categories*, p. 2024–2029. Siemens, 2022.

[93] Siemens Digital Industries Software. Simcenter STAR-CCM+ User Guide, version 2206. In *Merge and Imprint Tool*, p. 2102–2111. Siemens, 2022.

[94] Siemens Digital Industries Software. Simcenter STAR-CCM+ User Guide, version 2206. In *Mesh Metrics*, p. 2971–2977. Siemens, 2022.

[95] H. Zheng, G. Liu, X. Song, P. Ridgway, S. Xun and V. S. Battaglia. Cathode Performance as a Function of Inactive Material and Void Fractions. *Journal of The Electrochemical Society*, 157(10): 1060, 2010.

[96] M. E. Spahr, D. Goers, A. Leone, S. Stallone and E. Grivei. Development of carbon conductive additives for advanced lithium ion batteries. *Journal of Power Sources*, 196(7): 3404–3413, 2011.

[97] A. Awarke, S. Lauer, S. Pischinger and M. Wittler. Percolation-tunneling modeling for the study of the electric conductivity in LiFePO4 based Li-ion battery cathodes. *Journal of Power Sources*, 196(1): 405–411, 2011.

[98] O. Birkholz, Y. Gan and M. Kamlah. Modeling the effective conductivity of the solid and the pore phase in granular materials using resistor networks. *Powder Technology*, 351: 54–65, 2019.

[99] C. Sangrós Gimeńez, L. Helmers, C. Schilde, A. Diener and A. Kwade. Modeling the Electrical Conductive Paths within All-Solid-State Battery Electrodes. *Chemical Engineering & Technology*, 43(5): 819–829, 2020.

[100] C. Greenshields. *OpenFOAM v10 User Guide*. The OpenFOAM Foundation, London, UK, 2022.

[101] V. Wenzel, R. S. Moeller and H. Nirschl. Influence of Mixing Technology and the Potential to Modify the Morphological Properties of Materials used in the Manufacture of Lithium-Ion Batteries. *Energy Technology*, 2(2): 176–182, 2014.

[102] D.-W. Chung, M. Ebner, D. R. Ely, V. Wood and R. Edwin GarcÃa. Validity of the Bruggeman relation for porous electrodes. *Modelling and Simulation in Materials Science and Engineering*, 21(7): 074009, 2013.

[103] R. B. MacMullin and G. A. Muccini. Characteristics of porous beds and structures. *AIChE Journal*, 2(3): 393–403, 1956.

[104] H. S. Harned and D. M. French. A Conductance Method for the Determination of the Diffusion Coefficients of Electrolytes. *Annals of the New York Academy of Sciences*, 46(5): 267–284, 1945.

[105] J. S. Newman, S. D. Thompson and J. S. Newman. Differential Diffusion-Coefficients of Sodium Polysulfide Melts. *Journal of the Electrochemical Society*, 136(11): 3362–3369, 1989.

[106] I. V. Thorat, D. E. Stephenson, N. A. Zacharias, K. Zaghib, J. N. Harb and D. R. Wheeler. Quantifying tortuosity in porous Li-ion battery materials. *Journal of Power Sources*, 188(2): 592–600, 2009.

[107] T.-T. Nguyen, A. Demortiére, B. Fleutot, B. Delobel, C. Delacourt and S. J. Cooper. The electrode tortuosity factor: why the conventional tortuosity factor is not well suited for quantifying transport in porous Li-ion battery electrodes and what to use instead. *Computational Materials*, 6(1): 1–12, 2020.

[108] M. Chouchane and A. A. Franco. About the Consideration of the Inactive Materials and the Meshing Procedures in Computational Models of Lithium Ion Battery Electrodes. *ChemElectroChem*, 9(21): 202200692, 2022.

[109] R. Ge, A. M. Boyce, Y. Sun, P. R. Shearing, P. S. Grant, D. J. Cumming and R. M. Smith. Numerical Design of Microporous Carbon Binder Domains Phase in Composite Cathodes for Lithium-Ion Batteries. *ACS Applied Materials & Interfaces*, 15(23): 27809–27820, 2023.

[110] M. Kespe and H. Nirschl. Numerical simulation of lithium-ion battery performance considering electrode microstructure. *International Journal of Energy Research*, 39(15): 2062–2074, 2015.

[111] S. P. Rwei, F.-H. Ku and K.-C. Cheng. Dispersion of carbon black in a continuous phase: Electrical, rheological, and morphological studies. *Colloid & Polymer Science*, 280(12): 1110–1115, 2002.

[112] K. Vuillaume, B. Haidar and A. Vidal. Adsorption of monodisperse polybutadienes on carbon black, 1 Adsorption from dilute and semi-dilute solutions. *e-Polymers*, 3(1), 2003.

[113] K. Miyasaka, K. Watanabe, E. Jojima, H. Aida, M. Sumita and K. Ishikawa. Electrical conductivity of carbon-polymer composites as a function of carbon content. *Journal of Materials Science*, 17(6): 1610–1616, 1982.

[114] G. B. Less, J. H. Seo, S. Han, A. M. Sastry, J. Zausch, A. Latz, S. Schmidt, C. Wieser, D. Kehrwald and S. Fell. Micro-Scale Modeling of Li-Ion Batteries: Parameterization and Validation. *Journal of The Electrochemical Society*, 159(6): 697–704, 2012.

[115] M. Ender, J. Joos, T. Carraro and E. Ivers-Tiffée. Three-dimensional reconstruction of a composite cathode for lithium-ion cells. *Electrochemistry Communications*, 13(2): 166–168, 2011.

[116] Z. Zhao, Z. Wen, C. Li, Y. Ding, Y. Jiang, F. Wu, B. Wu, S. Chen and D. Mu. Effects of different charge cut-off voltages on the surface structure and electrochemical properties of $LiNi_{0.60}Mn_{0.20}Co_{0.2}O_2$. *Electrochimica Acta*, 353: 136518, 2020.

[117] S. Cernak, F. Schuerholz, M. Kespe and H. Nirschl. Three-Dimensional Numerical Simulations on the Effect of Particle Porosity of Lithium-Nickel-Manganese-Cobalt-Oxide on the Performance of Positive Lithium-Ion Battery Electrodes. *Energy Technology*, p. 2000676, 2020.

[118] C. Lischka and H. Nirschl. Calibration of Li-Ion Cathode Materials for Discrete Element Method Simulations. *Energy Technology*, 11(5): 2200849, 2023.

[119] A. C. Ngandjong, A. Rucci, M. Maiza, G. Shukla, J. Vazquez-Arenas and A. A. Franco. Multiscale Simulation Platform Linking Lithium Ion Battery Electrode Fabrication Process with Performance at the Cell Level. *The journal of physical chemistry letters*, 8(23), 2017.

[120] A. Chauhan, E. Asylbekov, S. Kespe and H. Nirschl. Influence of carbon binder domain on the performance of lithium-ion batteries: Impact of size and fractal dimension. *Electrochemical Science Advances*, p. 2100151, 2022.

[121] M. Kespe, M. Gleiß, S. Hammerich and H. Nirschl. Numerical optimization of the spatial conductivity distribution within cathode microstructures of lithium-ion batteries considering the cell performance. *International Journal of Energy Research*, 41(14): 2282–2296, 2017.

[122] W. Du, A. Gupta, X. Zhang, A. M. Sastry and W. Shyy. Effect of cycling rate, particle size and transport properties on lithium-ion cathode performance. *International Journal of Heat and Mass Transfer*, 53(17-18): 3552–3561, 2010.

[123] W. Bauer and D. Nötzel. Rheological properties and stability of NMP based cathode slurries for lithium ion batteries. *Ceramics International*, 40(3): 4591–4598, 2014.

[124] S. R. Forrest and T. A. Witten. Long-range correlations in smoke-particle aggregates. *Journal of Physics A: Mathematical and General*, 12(5): 109–117, 1979.

[125] C. M. Sorensen and G. C. Roberts. The Prefactor of Fractal Aggregates. *Journal of Colloid and Interface Science*, 186(2): 447–452, 1997.

[126] C. M. Sorensen. Light Scattering by Fractal Aggregates: A Review. *Aerosol Science and Technology*, 35(2): 648–687, 2001.

[127] S. Lazzari, L. Nicoud, B. Jaquet, M. Lattuada and M. Morbidelli. Fractal-like structures in colloid science. *Advances in Colloid and Interface Science*, 235: 1–13, 2016.

[128] M. Q. Zhang, J. R. Xu, H. M. Zeng, Q. Huo, Z. Y. Zhang, F. C. Yun and K. Friedrich. Fractal approach to the critical filler volume fraction of an electrically conductive polymer composite. *Journal of Materials Science*, 30(17): 4226–4232, 1995.

[129] S. Buchheiser, F. Kistner, F. Rhein and H. Nirschl. Spray Flame Synthesis and Multiscale Characterization of Carbon Black–Silica Hetero-Aggregates. *Nanomaterials*, 13(12): 1893, 2023.

[130] M. J. Lain, J. Brandon and E. Kendrick. Design Strategies for High Power vs. High Energy Lithium Ion Cells. *Batteries*, 5(4): 64, 2019.

[131] A. Chauhan and H. Nirschl. Numerical Investigation of Conductivity Additive Dispersion in High-Power and High-Energy NMC-Based Lithium-Ion Battery Cathodes: Application-Based Guidelines. *Energy Technology*, p. 2300281, 2023.

[132] C. Heubner, M. Schneider and A. Michaelis. Diffusion-Limited C-Rate: A Fundamental Principle Quantifying the Intrinsic Limits of Li-Ion Batteries. *Advanced Energy Materials*, 10(2): 1902523, 2020.

[133] T. Danner, M. Singh, S. Hein, J. Kaiser, H. Hahn and A. Latz. Thick electrodes for Li-ion batteries: A model based analysis. *Journal of Power Sources*, 334: 191–201, 2016.

[134] A. Chauhan, C. Lischka and H. Nirschl. Analysis of Solvent-Free Intensive-Dry-Mixed NMC-Based Lithium-Ion Battery Cathodes: Numerical Investigations on Performance Determinants. *Batteries & Supercaps*, 7(7), 2024.

[135] S.-J. Sim, S.-H. Lee, B.-S. Jin and H.-S. Kim. Use of carbon coating on LiNi0.8Co0.1Mn0.1O2 cathode material for enhanced performances of lithium-ion batteries. *Scientific Reports*, 10(1): 11114, 2020.

[136] R. Dominko, M. Bele, M. Gaberscek, M. Remskar, D. Hanzel, S. Pejovnik and J. Jamnik. Impact of the Carbon Coating Thickness on the Electrochemical Performance of $LiFePO_4$/C Composites. *Journal of The Electrochemical Society*, 152(3): 607, 2005.

[137] J. H. Chang, M. W. Pin, I. Kim, S. Kim, S. Kim, S. Moon, J. Cho, S. Choi, B. Heo, Z. A. Chandio, Y. Kim, J. Y. Cheong, D. Zide, M. Madondo, B. J. Bladergroen, M. Eldessouki, M. M. Escandell and H.-J. Jeon. Binder migration: Frequently

observed yet overlooked phenomena in electrode processing for lithium-ion batteries. *Journal of Energy Storage*, 83: 110729, 2024.

[138] A. R. Quinteros-Condoretty, S. R. Golroudbary, L. Albareda, B. Barbiellini and A. Soyer. Impact of circular design of lithium-ion batteries on supply of lithium for electric cars towards a sustainable mobility and energy transition. *Procedia CIRP*, 100: 73–78, 2021.

[139] F. Zou and A. Manthiram. A Review of the Design of Advanced Binders for High--Performance Batteries. *Advanced Energy Materials*, 10(45): 2002508, 2020.